

Facultad de Física
Departamento de Física Atómica, Molecular y Nuclear



VNIVERSITAT
DE VALÈNCIA

TRITIUM: Design, Construction and Commissioning of an In-Water Tritium Detector

Marcos Martínez Roig

PhD in Physics
2nd May 2022

Under the supervision of:

José Díaz Medina
Nadia Yahlali Haddou

*Dedicated to
my family*

Sometimes it is the people no one imagines anything
of who do the things that no one can imagine.

"Alan Turing"

I

Acknowledgements

Muchas personas han colaborado a lo largo de estos cuatro años para hacer posible este trabajo. En primer lugar me gustaría agradecer enormemente a mis tutores, Jose Díaz Medina y Nadia Yahlali Haddou, por intentar transmitirme en todo momento tantos conocimientos como les ha sido posible. También agradecer su tiempo ya que, a pesar de sus obligaciones, siempre han encontrado un hueco en sus agendas para ayudarme rápidamente con cualquier problema. Estoy muy agradecido por su cercanía y sus consejos, tanto en el mundo laboral como en la vida personal, los cuales me han ayudado a llegar a donde estoy ahora. Gracias de todo corazón por todo, nada de esto hubiera sido posible sin vosotros.

En segundo lugar me gustaría agradecer a mis compañeros de laboratorio Andrea Esparcia Córcoles, Ana Bueno Fernández, Marcos Llanos Expósito y sobre todo a Mireia Simeo Vinaixa, con quienes los largos e interminables trabajos de laboratorio han sido mucho más fáciles, ayudandome en todo momento a comprender y mejorar los resultados experimentales obtenidos. También me gustaría agradecer a los técnicos e investigadores del LARAM, Clodoaldo Roldán García, Teresa Cámara García, Vanesa Delgado Belmar y Rosa María Rodríguez Galán, por su ayuda, su tiempo y sus esfuerzos en hacer que todo esto haya sido posible.

En tercer lugar me gustaría agradecer a todos los investigadores del proyecto TRITIUM, gente que me ha acogido con los brazos abiertos,

que me ha ayudado en todo lo que les ha sido posible y con la que he tenido el placer de trabajar y aprender a su lado. Me gustaría agradecer en especial a Carlos Azevedo, junto al cual tuve el placer de trabajar. Gracias por todo el tiempo que invertiste en mi y en mi formación en temas tan interesantes y dispares como programación con Arduino y Rasberry Pi (llegando a realizar proyectos en común) o simulaciones con el paquete de programación Geant4 (llegando a realizar mis propias simulaciones).

En cuarto lugar me gustaría agradecer a David Calvo Díaz-Aldagalán, ingeniero del IFIC, gracias al cual pudieron llevarse a cabo los diseños de las distintas PCBs utilizadas en el proyecto TRITIUM.

Finalmente me gustaría dar las gracias a los investigadores de otros proyectos los cuales, pese a no ayudarme directamente en mi labor de investigación, si han aportado a mi trabajo debido a las sinergias existentes entre los objetivos experimentales de los proyectos:

- A los investigadores del proyecto DUNE, Anselmo Cervera, Miguel Ángel García y Justo Martín-Albo, los cuales me han ayudado con su tiempo, sus conocimientos e su instrumentación experimental a completar la caracterización de los SiPMs.
- A los ingenieros del proyecto NEXT, Vicente Álvarez, Marc Querol, Javier Rodríguez Samaniego y Sara Cárcel, con quienes he compartido laboratorio y, aun sin trabajar directamente con ellos, siempre han estado dispuestos a echarme una mano.
- A los investigadores del IFIMED, Gabriela Llosá, Ana Ros, Marina Borja Lloret, John Barrio, Rita Viegas y Jorge Roser e investigadores del proyecto ATLAS (Urmila Soldevila y Carlos Mariña) por prestarnos sus instalaciones y, en concreto, sus sistemas de control de temperatura los cuales fueron necesario para la caracterización de los SiPMs.

-
- A los investigadores del laboratorio HYMNS, Ion Ladarescu y César Domingo, quienes me ayudaron en mis primeros pasos con la electrónica PETsys además de asesorarme con las questiones que me han surgido a lo largo del camino.
 - A los investigadores del ICMOL, Henk Bolink, Alejandra Soriano y Lidón Gil Escrig, por ayudarnos con el protocolo de limpieza de las fibras centelleadoras además de permitirnos usar sus instalaciones.
 - A toda la gente de los distintos departamentos del IFIC que hay ayudado con su tiempo y sus consejos. Me gustaría agradecer especialmente la ayuda de Jose Vicente Civera, Manolo Montserrat, Jose Luis Jordan y Daniel Tchogna del departamento de mecánica, Ximo Navajas, Ximo Nadal, Carlos Martinez y Francisco Javier Sanchez del departamento de informática y Manuel Lopez, Jorge Nacher y Jose Mazorra del departamento de electrónica.
 - A mis amigos del IFIC, Pepe, Kevin, Jose Antonio, Pablo, Stefan y Victor, los cuales, aun sin haber aportado directamente a mi trabajo, compartir mis días con ellos ha sido uno de los mayores apoyos de esta aventura. No solo me llevo amigos de esta etapa, me llevo una familia.
 - A mi amigo, Galo, una amistad que empezó en el master, donde tuve el placer de compartir muchas de las duras horas de estudio, y continuó en el doctorado, donde compartimos muchos buenos momentos y siento que nos ayudamos a crecer mutuamente tanto profesional como personalmente. Amistad que, sinceramente, espero que dure para toda la vida.
 - A mi familia, quienes sin comprender exactamente en que consiste mi trabajo, me han apoyado y animado ciegamente desde el principio. Fueron, son y serán una pieza imprescindible en todas las areas de mi vida.

Finalmente me gustaría agradecer al programa INTERREG-SUDOE por financiar el proyecto TRITIUM, gracias al cual todo esto se ha podido materializar.

Abstract

Tritium is one of the most abundantly emitted radioisotopes by nuclear facilities and, specifically, by nuclear power plants. Large amounts of tritium are normally produced in the water of their cooling system, which are finally emitted to the environment. Due to the fact that large releases of tritium could be dangerous for human health and for the environment, there exist several regulations around the world which try to control this radioactive emissions in each country, like the Directive Europeen 2013/51/Euratom, which establishes the tritium limit for drinking water in Europe to 100 Bq/L, or the Environmental Protection Agency, in United States, that limits tritium in drinking water to 20 nCi/L.

Due to the low energy of electrons emitted in the tritium decay, very sensitive detectors are needed for measuring them like LSC. The issue with LSC is that it is an off-line method and the measurement process can take 2 days or more, a time too long to detect a problem in the NPP.

Detectors based on solid scintillators are a promising idea for building a tritium detector that works in quasi-real time. This type of detectors is developed so far successfully but without achieving the required sensitivity of the legal limits.

The results of the TRITIUM project are presented in this thesis. In the framework of this project a quasi-real time monitor for low tritium

activities in water have been developed. This monitor is based on a tritium detector that contains several detection cells which are read in parallel, several active vetos and a passive shielding for reducing the natural background of the natural radioactivity and a water purification system to prepare the sample before being measured. Each detection cell is made up of hundreds of scintillating fibers read out by PMTs or SiPM arrays.

The final objective of this monitor will be the radiological protection around the nuclear power plant. This monitor will provide an alarm in case of an unexpected tritium release that exceeds the legal limits established in Europe. The final idea will be to include this monitor in the early alarm system of Extremadura consisting of several detectors the objective of which is to control the impact of Nuclear Power Plants to the environment.

Keywords: Very low-energy charged particle detectors, radiation monitoring, tritium detection, scintillators, scintillating fibers and light guides, detector design and construction technologies and materials, instruments for environmental monitoring, detector modelling and simulations.

Acronyms and Symbols

Acronyms:

<i>ALARA</i>	— As low as reasonably achievable criterium
<i>APD</i>	— Avalanche photodiode
<i>BIXS</i>	— Beta induced X-ray spectrometry
<i>BWR</i>	— Boiling water reactor
<i>CCD</i>	— Charge-coupled device
<i>CNRS</i>	— Centre National de la Recherche Scientifique
<i>CSN</i>	— Consejo de Seguridad Nuclear
<i>DAQ</i>	— Data acquisition system
<i>I3N</i>	— Institute for Nanostructures, Nanomodelling and Nanofabrication.
<i>EEC</i>	— European Economical Community
<i>EPA</i>	— Environmental Protection Agency
<i>EU</i>	— European Union
<i>EURATOM</i>	— European Atomic Energy Community
<i>G – APD</i>	— Geiger avalanche photodiode
<i>GCR</i>	— Gas cooled reactor
<i>HPGe</i>	— High purity germanium detector
<i>HWR</i>	— Heavy water reactor
<i>IAEA</i>	— International Atomic Energy Agency
<i>IC</i>	— Ionization chamber
<i>ICRP</i>	— International Commission on Radiological Protection

<i>ICRU</i>	— International Commission of Radioactivity Units and Measurements
<i>ISR</i>	— International Society of Radiology
<i>LARUEX</i>	— Laboratorio de Radiactividad Ambiental of the University of Extremadura (Environmental Radioactivity Laboratory of the University of Extremadura)
<i>LED</i>	— Light-emitting diode
<i>LSC</i>	— Liquid scintillation counting
<i>LWR</i>	— Light water reactor
<i>MAPD</i>	— Micro-pixel avalanche photodiode
<i>MDA</i>	— Minimum detectable activity
<i>MPPC</i>	— Multi-pixel photon counter
<i>MRS – ADP</i>	— Metal-resistor-semiconductor avalanche photodiode
<i>NPP</i>	— Nuclear power plant
<i>PCB</i>	— Printed circuit board
<i>PHWR</i>	— Pressurized heavy water reactor
<i>PMMA</i>	— Polymethyl methacrylate
<i>PMT</i>	— Photomultiplier tube
<i>POF</i>	— Plastic optical fiber
<i>PVC</i>	— Polyvinyl chloride
<i>PWR</i>	— Pressurized water reactor
<i>RDL</i>	— Reference dose level
<i>REA</i>	— Red de Estaciones Automáticas
<i>REM</i>	— Red de Estaciones de Muestreo
<i>ROI</i>	— Region of interest
<i>SDD</i>	— Silicon drift detector
<i>SiPM</i>	— Silicon photomultiplier
<i>SSPM</i>	— Solid state photomultiplier
<i>STP</i>	— Standard temperature and pressure conditions
<i>UDL</i>	— Upper detection limit
<i>UNSCEAR</i>	— United Nations Scientific Committee on the Effects of Atomic Radiation

<i>DOE</i>	— United States Department of Energy
<i>EIA</i>	— United States Energy Information Administration
<i>EPA</i>	— United States Environmental Protection Agency
<i>WHO</i>	— World Health Organization

Symbols

A_m	— Activity measured
CE	— Collection efficiency
C_t	— Terminal capacitance of SiPM
DCF	— Dose conversion factor
δ	— Multiplication factor of a PMT dynode
ΔTV_{op}	— Temperature coefficient ($mV/^\circ C$)
E_b	— Binding energy of the electron in a specific material
ε_{det}	— Specific detector efficiency
E_e	— Electron energy
$E_\gamma = h\nu$	— Photon Energy
FF	— SiPM fill factor
F_{sci}	— Plastic scintillator active surface
GL	— Guideline level
G_{PMT}	— PMT Gain
G_{SiPM}	— SiPM Gain
η_{det}	— Intrinsic detector efficiency
HV	— High voltage
I_{DC}	— PMT dark current
I_{PMT}	— PMT Intensity
λ	— Wavelength
λ_p	— Most probable wavelength of a spectrum
mip	— Minimum ionizing particle
m_0	— Electron rest mass
NaI(Tl)	— Thallium doped Sodium Iodide

NA	— Numerical aperture
OBT	— Organically bound tritium molecule
P_{av}	— SiPM avalanche probability
PDE	— Photodetection efficiency of the SiPM
q	— Annual volume of drinking water consumed per capita
QE	— Quantum efficiency
q_e	— Electron charge
Q_β	— Energy released in decay
R_q	— SiPM Quenching resistance
S	— Specific energy loss
S_{ij}	— Single states of energy levels of electrons in a scintillator
S/cm	— Siemens per centimeter
σ	— Cross section of a radioactive process
σ^{rel}	— Relative uncertainty
σ_{sys}	— Systematic uncertainty
σ_{st}	— Statistical uncertainty
σ_t	— Total uncertainty
σ_{TM}	— Uncertainty of a tritium measurement due to the scintillating fibers
$T_{1/2}$	— Half-life time of a radioactive element
T_{ij}	— Triple states of energy levels of electrons in a scintillator
V_{BD}	— SiPM breakdown voltage
V_{bias}	— SiPM supply voltage
V_{OV}	— SiPM over voltage a SiPM

Contents

Acknowledgements	III
Abstract	VII
Nomenclature and Acronyms	IX
List of Figures	XXXI
List of Tables	XXXVI
1 Introduction	1
1.1 Tritium and Nuclear Energy	1
1.2 Tritium Properties and Radiological Hazards	8
1.3 Current Legislation	16
1.4 This Thesis	19

CONTENTS

2 Methods of Detection of Tritium In Water	21
2.1 Tritium Detection State-of-the-Art	21
2.2 The TRITIUM Project	25
3 Design Principles and Components of TRITIUM	29
3.1 Detector System Overview	29
3.2 TRITIUM Detector	31
3.2.1 Interaction of Particles with Matter	31
3.2.2 Plastic Scintillators	35
3.2.3 Light Detection in Photosensors	41
3.2.3.1 Photomultiplier Tubes (PMTs)	43
3.2.3.2 Silicon Photomultiplier Array	48
3.2.3.3 Photosensors in TRITIUM	56
3.2.4 Electronics	56
3.2.4.1 Electronic for PMTs	56
3.2.4.2 Electronics for SiPMs	60
3.3 The Water Purification System	62
3.3.1 Objectives	62
3.3.2 Design of the Water Purification System	63
3.4 The Background Rejection System	65

3.4.1	Passive Shield (Lead)	67
3.4.2	Active Shield (Cosmic Veto)	68
4	TRITIUM Monitor R&D	75
4.1	R&D for the Scintillating Fibers	75
4.1.1	Preparation of Scintillating Fibers.	76
4.1.1.1	Cleaving of Scintillating Fibers.	76
4.1.1.2	Polishing of Scintillating Fibers.	78
4.1.1.3	Cleaning of Scintillating Fibers.	87
4.1.2	Characterization of Scintillating Fibers	90
4.1.2.1	Measurement Conditions.	93
4.1.2.2	Results of the Characterization of Scintillat- ing Fibers	94
4.2	Characterization of the SiPM	102
4.3	Characterization of the Water Purification System	111
4.4	Characterization of the Cosmic Veto	113
5	TRITIUM Detector Prototypes	121
5.1	First Prototypes	122
5.1.1	TRITIUM-IFIC-0	122
5.1.2	TRITIUM-IFIC-1	127

CONTENTS

5.2 Latest TRITIUM Prototypes	132
5.2.1 TRITIUM-Aveiro	133
5.2.2 TRITIUM-IFIC-2	139
5.3 Experimental Results in Arrocampo Dam	147
5.4 Modular TRITIUM Detector	149
6 Simulations	153
6.1 Geant4 Environment	153
6.2 Simulations for the design of the TRITIUM Detector	155
6.2.1 The Tritiated Water Source	155
6.2.2 Energy Deposition and Light Output in Scintillating Fibers	158
6.2.3 Optimization of the Fiber Length	160
6.2.4 Fiber Diameter Influence on Cosmic Background	162
6.2.5 Influence of the PMMA Windows on the Tritium Signal	164
6.3 Simulations of the TRITIUM Monitor	166
6.3.1 Simulation of the TRITIUM-IFIC-2 Prototype	166
6.3.2 Lead Shield and Cosmic Veto	169
7 Present Status and Summary of the Results of the TRITIUM Project	177

8 Conclusions and Prospects	187
 Appendices	
A Electronics for the SiPM Characterization	193
B Water Purification System	197
C Preparation of Tritiated Water Sources	203
D Electronic System of TRITIUM-Aveiro prototype	205

CONTENTS

List of Figures

1.1	Annual average distribution of the radioactive dose received by the population [Thea].	2
1.2	Networks of automatic and sampling stations managed by the spanish CSN. a) Measurement locations of the REA [CSNa]. The white box is the daily average of the gamma dose and the green box is the monthly average of the gamma dose. b) Measurement locations of the REM [CSNb]. Blue dots are locations near nuclear facilities, and green dots are locations uniformly distributed throughout the country.	5
1.3	(Above) Tritium energy levels [IAE]. (Below) Graphic representation of tritium decay [Jor20].	9
1.4	Energy spectrum of tritium electrons [Lin20].	10
1.5	Tritium sampling locations around Cofrentes NPP.	13

LIST OF FIGURES

1.6 Tritium activity levels in surface water around Cofrentes NPP from January 2006 to November 2019. a) 6 km upstream. b) 1 km downstream. c) 5 km downstream. The white points are the detection limits and the green points are the measured activity when this is above the detection limit [CSNb]. The maximum level of tritium measured since January 2, 2006 is around 32 Bq/L.	14
1.7 Tritium activity levels in groundwater around Cofrentes NPP from January 2006 to November 2019 [CSNb]. a) 1 km upstream from the NPP. b) 1 km downstream from the NPP.	15
2.1 a) Arrocampo dam and Almaraz Nuclear Power Plant. b) Tagus river along Spain and Portugal.	26
3.1 Scheme of the scintillator detector.	31
3.2 Domain regions of the three most probable types of interactions of gamma rays with matter. The lines show the atomic number Z and gamma energy $h\nu$ where two interaction processes are equally likely [Kno99].	33
3.3 Jablonsky diagram [Kno99].	36
3.4 Stokes shift [Kno99].	37
3.5 Emission spectrum of BCF-12 scintillating fibers of Saint-Gobain [Sai21b].	39
3.6 Photon collection in a single clad fiber [Sai21b].	40
3.7 Scheme of a PMT [Kno99].	44

3.8	Quantum efficiency spectrum for the PMT used in TRITIUM R&D studies (R8520-406) [Ham19].	45
3.9	Hamamatsu commercial voltage divider electronic circuit with negative (up) and positive (below) supply high voltage [Ham19].	46
3.10	Electronic scheme of the voltage divider circuit used for working with PMTs without internal gain.	47
3.11	Scheme of a APD and electrical symbol used [OSI].	49
3.12	SiPM output pulses displayed on the oscilloscope, model MSO44X from Tektronix [Tek21]. Several height pulses are observed, associated to a different number of SiPM pixels fired at the same time. The persistence function of the oscilloscope is used.	50
3.13	(a) Electronic scheme of a SiPM and (b) output current of a SiPM as a function of the reverse voltage. As shown, the quenching is an essential working mechanism of SiPMs [Sen17].	51
3.14	PDE spectrum for SiPM S13360-**75 models [Ham16b]. . .	55
3.15	Electronic schemes employed for measuring with a) one PMT, b) two PMTs in coincidence and c) four PMTs in coincidence.	58
3.16	Different possibilities for time coincidence of four PMTs. Case d) shows coincident events.	59
3.17	Amplified signal and logic gate (input signals of the MCA). .	60
3.18	Different parts of PETsys system [PET].	61
3.19	a) Electronic board used in the SiPM characterization. b) Electronic scheme on which this PCB is based.	62
3.20	Scheme of the water purification system of TRITIUM. . . .	64

LIST OF FIGURES

3.21 Lead bricks.	67
3.22 Two layers for the lead bricks of the shield.	68
3.23 a) Scheme of the aluminium structure of the shield. b) The lead shield partially mounted.	69
3.24 Cosmic veto and Tritium-IFIC-2 prototype inside the aluminium mechanical structure developed at IFIC.	70
3.25 Hard cosmic events detected with the cosmic veto of TRITIUM: a) Real coincidence event. b) Random coincidence event.	71
3.26 Hard cosmic muon rate at different depths [Szu15].	72
3.27 Emission spectrum of the plastic scintillator from Epic-Crystals [Epi20].	72
3.28 Different layers used to wrap the cosmic veto detectors. a) Scintillator without wrapping. b) PTFE wrapping. c) Aluminium wrapping. c) d) Black tape wrapping.	73
4.1 Results of using commercial techniques for cleaving the scintillating fibers a) Fiber end deformation b) Fiber end cracks. Pictures taken with a microscope PB 4161 from EUROMEX.	77
4.2 Plastic fiber cleaver developed in TRITIUM project.	78
4.3 Fiber end after cleaving process using the home-made cleaver. Pictures taken with the microscope PB 4161 from EUROMEX.	79
4.4 Manual polishing method implemented by Thorlabs.	80

4.5	Result of the polishing process. a) Fiber end after cleaving b) Fiber end after cleaving and manual polishing with Thorlabs technique. Pictures taken with the microscope PB 4161 from EUROMEX.	81
4.6	Polishing machine developed for TRITIUM.	82
4.7	Components of the fiber polishing machine. a) Polishing table. b) Fiber with ballast metal piece. c) Horizontal screws and PMMA plate. d) A movement switch with its cables inserted inside its holding piece.	83
4.8	Electronic system of Polishing machine.	85
4.9	Setup used to quantify the improvement of the light collection of the fibers and their transmision to the PMTs due to the polishing process. This setup was placed inside a light-tight box for the measurements.	86
4.10	Background energy spectra recorded with polished and unpolished fibers.	86
4.11	Energy spectra recorded with polished and unpolished fibers. a) ^{60}Co source. b) ^{90}Sr source.	88
4.12	Schematic representation of the wetting properties of a flat surface (gray) in contact with a drop of liquid (blue). The wetting property is characterized by the angle formed between the surface of both objects. The smaller angle, the better wetting property of the material. [San]	89
4.13	Measured background energy spectra before and after cleaning.	90
4.14	Energy spectra obtained before and after the cleaning for a radioactive source. a) ^{137}Cs . b) ^{90}Sr	91

LIST OF FIGURES

4.15 Setup used for fiber characterization.	92
4.16 Emission spectrum mesured for the 435-03 LED from Roithner LaserTechnik GmbH.	93
4.17 PMT photocurrent as a function of the first dynode voltage with the dark current subtracted. Error bars are smaller than dot size.	94
4.18 Rate of photons measured by the PMT as a function of the LED current. a) Response of the PMT in the intensity range of tritium events. b) Response of the PMT in the range 0 – 2500 photons/ns. Error bars are smaller than the dot size.	95
4.19 Rate of photons reaching the PMT for uncladded fibers. Er- ror bars are smaller than the dot size.	97
4.20 Photon rate reaching the PMT for ten different fibers. a) Single clad fibers. b) Multiclad fibers. Error bars are smaller than the dot size.	98
4.21 Average photon rate versus LED current for 10 samples of dif- ferent fiber types (uncladded, singleclad and multiclad fibers). Error bars are smaller than the dot size.	100
4.22 I-V curves measured for the S13360-1375 SiPM model from Hamamatsu. a) Forward bias. b) Reverse bias. The meas- urements were taken at $T = 25^\circ\text{C}$ and $H = 45\%$	103
4.23 Above) Trigger signal (green) and SiPM output pulses (yel- low). Below) SPS spectrum obtained by integrating and his- tograming the SiPM output pulses. This measurement was done at $T = 25^\circ\text{C}$, $V_{bias} = 53.98$ and $H = 60\%$	105

4.24 a) Fit of the SPS spectrum to Gaussian functions. b) Charge as a function of the number of pixels fired. Error bars are within point size. Data taken at $T = 25^\circ\text{C}$, $V_{bias} = 53.98$ V and of $H = 45\%$.	106
4.25 SiPM gain versus a) Temperature. b) Bias voltage.	108
4.26 SiPM gain as a function of the temperature after implementation of the gain stabilization method.	110
4.27 Test points used for the cosmic veto mapping.	114
4.28 Energy spectra measured with the ^{137}Cs radioactive source with and without wrapping the veto.	115
4.29 Bidimensional graph of the counting rate (mapping) measured for two different cosmic vetos using a ^{60}Co source.	116
4.30 Counting rate of two cosmic vetos in coincidence a) as a function of PMT HV for three different thresholds and b) as a function of threshold for three different high voltages.	118
4.31 Energy spectrum measured with the cosmic veto.	119
4.32 a) Energy spectra of the cosmic veto for several separations of the scintillators. b) Fit to a second degree polynomial of the cosmic ray rate versus the separation of the veto scintillators.	120
5.1 a) Metallic piece of the fiber bundle. b) Bundle of 35 fibers of 20 cm length used in TRITIUM-IFIC-0.	123
5.2 TRITIUM-IFIC-0 prototype.	124
5.3 a) Fiber bundle in a PMMA vessel. b) Illumination test of the bundle to visualize the light loss due to fiber curvature..	125

LIST OF FIGURES

5.4	Energy spectra measured with TRITIUM-IFIC-0 prototype. a) Signal and background energy spectra. b) Tritium energy spectrum.	126
5.5	PTFE structure used to arrange the fibers of TRITIUM- IFIC-1 prototype in a matrix of 8×8	128
5.6	Pictures of the TRITIUM-IFIC-1 PTFE vessel.	129
5.7	A picture of the TRITIUM-IFIC-1 prototype. The photo- sensor lodging is shown.	130
5.8	Energy spectra measured with TRITIUM-IFIC-1. a) Signal and background energy spectra. b) Tritium energy spectrum.	131
5.9	TRITIUM-Aveiro prototype. A and B are the PVC structure, C is the PMT, D is the PTFE vessel, E is the 3D printer piece and F is the electronics.	133
5.10	PTFE vessel and fiber bundle used in TRITIUM-Aveiro pro- totype.	134
5.11	Background rate of the TRITIUM-Aveiro prototype. A) Without shielding. B) With a lead shield of 2.5 mm thickness. C) With two lead shields of 2.5 mm thickness each one [Aze22].	136
5.12	Background and tritium liquid source (29.8 kBq/L) with the TRITIUM-Aveiro prototype [Aze22]. a) Counts per minut measured as a function of time. b) Distribution of the ac- quired data.	137
5.13	Background and tritium liquid source counting rates meas- ured with TRITIUM-Aveiro [Aze22]	138

5.14 (A) TRITIUM-IFIC-2 prototype, (B) water inlet/outlet, (C) PETsys flat wires, (D) the metallic structure and (E) active veto.	139
5.15 a) TRITIUM-IFIC-2 PTFE vessel. b) TRITIUM-IFIC-2 PTFE vessel with two PVC caps that provide a light-tight environ- ment for the SiPM arrays.	140
5.16 Light transmission spectrum of a 5 mm thick PMMA plate, measured at ICMOL.	141
5.17 Graphical User Interface of PETsys.	142
5.18 Energy spectra measured with TRITIUM-IFIC-2. a) Signal and background energy spectra. b) Tritium energy spectrum.	143
5.19 a) Single photon distribution of TRITIUM-IFIC-2 PMTs. b) Tritium energy spectrum measured with TRITIUM-IFIC-2 versus number of photons detected per event.	145
5.20 Signal and background rates for a long time measurement. .	146
5.21 MDA as a function of the number of TRITIUM-IFIC-2 mod- ules read out in parallel for an integration time of 10 min (blue line) and 1 h (black line). The dotted red line corres- ponds to 100 Bq/L.	147
5.22 Background measured with the TRITIUM-Aveiro prototype in the Arrocampo site [Aze22].	148
5.23 A schematic design of the TRITIUM detector.	150
5.24 A TRITIUM monitor design based on the TRITIUM-IFIC-2 prototype.	151

LIST OF FIGURES

6.1 Energy distribution of a) simulated tritium decays b) Initial energy of tritium decays that reach the scintillating fibers (red histogram) compared to all simulated tritium events (blue histogram) [Aze20].	156
6.2 a) Cross section of a simulated scintillating fiber (yellow) and the tritium source (green) with various tritium decays (red dots) b) Distribution of the radial distance between the position where the tritium decays take place and the surface of the scintillating fiber [Aze20]. A zoom of low energy events is shown in the inset.	157
6.3 Distribution of the initial energy of tritium events that reach the scintillating fibers (blue histogram) and the energy deposited in them (red histogram) [Aze20].	159
6.4 Energy distributions of photons produced in the scintillating fiber, without the Birk's coefficient (red histogram) and with the Birk's coefficient $k_B = 0.126 \text{ mm/MeV}$ (blue histogram)[Aze20].	160
6.5 Number of photons produced versus the energy deposited in the scintillating fibers when a) $k_B = 0$ b) $k_B = 0.126 \text{ mm/MeV}$ [Aze20].	161
6.6 Number of photons produced in a fiber per tritium event for all tritium electrons that reach the fiber (blue histogram) and for only tritium electrons producing photons detected in coincidence by photosensors (red histogram) [Aze20].	162
6.7 Simulated counting statistics normalized to the active area in 1 h bins during a week for 1 m (dashed lines) and 20 cm (solid lines) and 0.5 kBq/L (blue lines) and 2.5 kBq/L (red lines) activities [Aze20].	163

6.8 Comparison of the energy deposition by cosmic rays in scintillating fibers of 1 mm and 2 mm diameter.	164
6.9 Distribution of photons reaching the PMMA windows. The red histogram corresponds to the photons guided by fibers and the blue histogram to photons guided through water [Aze20].	165
6.10 Distribution of the scintillating fibers in the simulations of the TRITIUM-IFIC-2 prototype.	166
6.11 Simulation of the inner part of the TRITIUM-IFIC-2 prototype. PMTs (black), optical grease (blue), PMMA windows (white), tritiated water (green) and scintillating fibers (yellow).	167
6.12 Tritium electron detected in the simulated TRITIUM-IFIC-2 prototype. The path of the optical photons is represented by green lines and the position in which they are absorbed is represented by red and blue dots for absorption in water or PMT, respectively.	168
6.13 Photons detected by both PMTs per tritium event in the simulated TRITIUM-IFIC-2 prototype.	169
6.14 a) TRITIUM-IFIC-2 simulated statistics with an integration time of 10 min during three months (13248 bins for each activity). b) Distribution of counting statics versus activities.	170
6.15 Simulated statistics distributions obtained with a TRITIUM-IFIC-2 prototype for several tritium activity and three different integration times: a)10 min (13248 bins), b) 30 min (4416 bins) and c) 60 min (2208 bins).	171

LIST OF FIGURES

6.16 Simulated statistic distribution for an integration time of 10 min (13248 time bins), several tritium activities and different number of TRITIUM-IFIC-2 modules a) 1, b) 5 and c) 10	172
6.17 a) Resolution of TRITIUM-IFIC-2 versus tritium activity for different integration time using 1 TRITIUM-IFIC 2 module. b) Resolution of TRITIUM-IFIC-2 versus tritium activity for different number of modules and 10 min integration time.	173
6.18 Total cosmic ray events detected by TRITIUM-IFIC-2 from 10^5 generated cosmic events, which are misidentified as tritium events in three different shielding configurations. Bin 1 corresponds to a no background rejection system. Bin 2 corresponds to the passive shield and bin 3 corresponds to both lead shield and cosmic veto.	175
A.1 The three PCBs used for SiPM characterization a) The PCB 1 used to connect up to 8 SiPMs inside the black box. b) The PCB 2 used to sum and amplify the output signals of the SiPMs. c) The PCB 3 used to rearrange the input and output signals of the system. d) The LED emission spectrum.	195
B.1 Scheme of the water purification system.	198
B.2 Different stages of filtration of the water purification system. a) The gross filtering stage. b) The fine filtering stage. c) The super-fine filtering stage.	198
B.3 a) Doble phase reverse osmosis stage. b) Containers used to gather the output water of the water purification system.	199

LIST OF FIGURES

B.4 Siemens PLC displays for the remote control of the water purification system.	200
B.5 Picture of the water purification system.	201
B.6 Raw, reject and pure water obtained with the water purification system.	201
D.1 a) The electronic scheme of the PCB designed to power the PMTs of Aveiro prototype b) The graphical user interface developed to control the prototype.	206
D.2 Electronic scheme that process and analyze the signal of the TRITIUM-Aveiro prototype.	207
D.3 Graphical user interface used to manage the counter system.	208
D.4 a) Tritium event accepted as veto has not detected it. b) Background event rejected because veto has fired.	209

LIST OF FIGURES

List of Tables

1.1	Annual average distribution of the effective dose received by the population due to natural radioactivity [Theb, Con].	2
1.2	Emission of tritium per year from different types of nuclear reactors: Pressurized Water Reactor (PWR), Boiling Water Reactor (BWR), Heavy Water Reactor (HWR) and Gas-Cooled Reactor (GCR) [Hou18]. .	7
1.3	Penetration depth of decay electrons of mean (5.7 keV) and maximum (18.6 keV) energies in different media (tritium gas, air at STP and water) [Bla91]. .	11
1.4	Most common nuclear reactions of artificial tritium production [Hou18]. .	11
1.5	Legal limit of tritium in drinking water (GL) established in several countries. .	19
2.1	State-of-the-art tritium detection techniques. This table shows the measured quantity, the minimum detectable activity (MDA) and the sample form for four different techniques, liquid scintillator counting (LSC), ionization chamber (IC), calorimetry and beta induced X-ray spectrometry (BIXS).	22

LIST OF TABLES

2.2	Results of scintillator detectors developed for experiments for tritiated water detection. This table shows for the quoted studies the efficiency of the detector (ε_{det}), its active surface (F_{sci}), its specific efficiency, defined as efficiency normalized to active surface ($\eta_{det} = \varepsilon_{det}/F_{sci}$), and MDA.	24
3.1	Critical angles associated to different interfaces between polystyrene ($n_0 = 1.6$) and other materials.	41
3.2	Properties of BCF-12 scintillating fibers from Saint-Gobain Inc. [Sai21b].	42
3.3	Characteristics of SiPM S13360-1375 and S13360-6075 from Hamamatsu Photonics [Ham16b].	54
3.4	Classification of natural radioactive series [The96, Eva95]. The information displayed for each radioactive series is, the name of the series, the primary and final element, and the half-life of the primary element.	66
3.5	Properties of the plastic scintillator from Epic-Crystals [Epi20].	71
4.1	Mean, standard deviation and relative standard deviation due to fiber positioning in the setup of the photon rate that reach the PMT for 0.1 mA LED intensity.	97
4.2	Photons rate versus LED intensity for the different type of fibers.	99
4.3	Relative standard deviation of the photon rate σ_{sys}^{rel} (%) versus LED intensity for the different fiber types.	99
4.4	Measured relative standard deviations σ_{sys}^{rel} , $\sigma_{sys-pos}^{rel}$ and σ_{sys-SF}^{rel} .100	100

4.5	Average photon rate versus LED intensity for 10 different samples of 10 cm length for uncladded, single clad and multiclad fibers.	101
4.6	Average collection efficiency CE_{10} for different types of scintillating fibers.	102
4.7	Chemical components measured in the raw water sample. . . .	112
4.8	Conductivity of different samples of water.	113
4.9	Tritium activity measured for different samples of both raw and purified water.	113
5.1	Rates obtained from the TRITIUM-IFIC-0 prototype.	125
5.2	Counting rates obtained with TRITIUM-IFIC-1.	129
5.3	Counting rates measured by TRITIUM-IFIC-2.	142
5.4	Mean value \bar{N} and standard deviation $\sigma_{\bar{N}}$ of fourteen background measurements. N_D and L_C obtained from the Currie criterium.	146
6.1	Tritium activity difference that can be visually resolved for different integration times and different number of TRITIUM-IFIC-2 modules.	170

LIST OF TABLES

Chapter 1

Introduction

1.1 Tritium and Nuclear Energy

Radioactivity is the process by which an unstable atomic nucleus decays through the emission of particles. This process is present in the Universe since the Big Bang. The formation of the Earth from the remains of supernova explosions explains why the different layers that make up the Earth contain radioactive elements.

Humanity has always been exposed to ionizing radiation, both from the Earth's crust radioactivity and cosmic rays (external natural irradiation). The human body also contains radioactive elements such as ^{3}H , ^{14}C and ^{40}K , introduced into it through food, water ingestion and air inhalation (internal natural irradiation).

As it can be seen in Figure 1.1, most of the radioactive dose received by the population is due to both internal and external natural radioactivity, the effective dose¹ of which is estimated to be 2.42 mSv/yr as

¹The effective dose is the radioactive dose absorbed by the population, weighted by

1.1. TRITIUM AND NUCLEAR ENERGY

shown in Table 1.1.

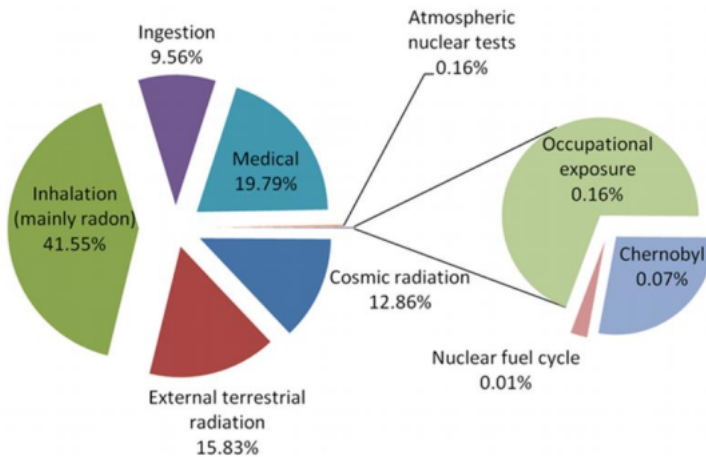


Figure 1.1 – Annual average distribution of the radioactive dose received by the population [Thea].

Radiation source	Eff. dose (mSv/yr)	Typical range (mSv/yr)
Cosmic (external)	0.39	0.3 – 1.0
Terrestrial (external)	0.48	0.3 – 0.6
Inhalation (internal)	1.26	0.2 – 10
Ingestion(internal)	0.29	0.2 – 0.8
Total	2.42	1 – 12.4

Table 1.1: Annual average distribution of the effective dose received by the population due to natural radioactivity [Theb, Con].

Since the discovery of radioactivity by Henri Becquerel in 1896, lots of nuclear-based technologies were developed and applied to various fields such as Energy, Chemistry, Biology, Technology, Medicine, Industry, etc. Due to nuclear applications, a number of anthropogenic radioactive sources have emerged in society, resulting in radioactive elements released into the environment. It can be noticed in Figure 1.1 that the most important part

the radiosensitivity of each organ or tissue.

of the dose received by the population from artificial sources comes from medical practice. The growth of knowledge and the development of measurement techniques of radioactivity have provided evidence of the harmful effects of radioactivity in living organisms. This lead to the necessity of controlling the radiation exposed to the population keeping it under safe limits. To accomplish that purpose, several organizations were created to propose recommendations for radiological protection to the different state organisms and governments at the international level. The main ones are:

1. The International Commission of Radiological Units and Measurements (ICRU) [Intb] was created during the first International Conference of Radiology, held in London in 1925, to define concepts and units, necessary to quantify the negative effects of radioactivity.
2. The International Commission on Radiological Protection (ICRP) [Inta] was created in 1928 by the International Society of Radiology (ISR) [Intc]. The ICRP aims to make recommendations and to provide guidance on different aspects of protection against radioactivity. The ICRP does not have the legal capacity to enforce its recommendations, but these are widely included in the legislation of most countries.
3. The United Nations Scientific Committee on the Effects of Atomic Radiation (UNSCEAR) [Theb] was created in 1955 with the goal of estimating and reporting the levels and effects of ionizing radiation on the population and the environment. These estimates are taken into account by governments worldwide to establish their safety standards.
4. The International Atomic Energy Agency (IAEA) [Thea] was created in 1957 to promote the peaceful use of nuclear energy and to avoid its use for military purposes such as nuclear weapons. Although established independently from the United Nations through its own international treaty, the IAEA reports regularly to both the United Nations and the Security Council.

1.1. TRITIUM AND NUCLEAR ENERGY

5. The European Atomic Energy Community (EURATOM), created in 1957, is an international organization ruled by the EURATOM treaty. Its objective is to coordinate research programs for the peaceful use of nuclear energy and the sharing of knowledge, infrastructure and funding of nuclear energy.
6. The Nuclear Safety Council (CSN) [Con] of Spain, created in 1980, is the authority in Spain for nuclear safety and radiation protection and has the objective of protecting employees, the general population and the environment from the harmful effects of ionizing radiation from anthropogenic origin. For this goal, the CSN ensures that nuclear and radioactive facilities are operated safely and establishes the preventive and corrective measures to be applied in radiological emergencies. The CSN manages two detectors networks to control the levels of radioactivity in the environment and to assess the impact of radioactive facilities:
 - (a) The network of automatic stations REA (Red de Estaciones Automáticas) [CSNa]. The REA consists of several gamma detectors, distributed as indicated in Figure 1.2a, that measure the radioactive dose in real time. The REA is employed for real-time detection of radiological issues to enable taking prompt safety measures.
 - (b) The network of sampling stations REM (Red de Estaciones de Muestreo) [CSNb]. The REM consists of a collection of points, shown in Figure 1.2b, from which samples are taken and measured in a laboratory. About twenty laboratories integrate this network. The objective of the REM is to characterize the concentration and evolution of radioisotopes present in the radioactive background of Spain and to quantify the impact of radioactive facilities on the environment.

The goal of the TRITIUM project is to develop a monitor capable

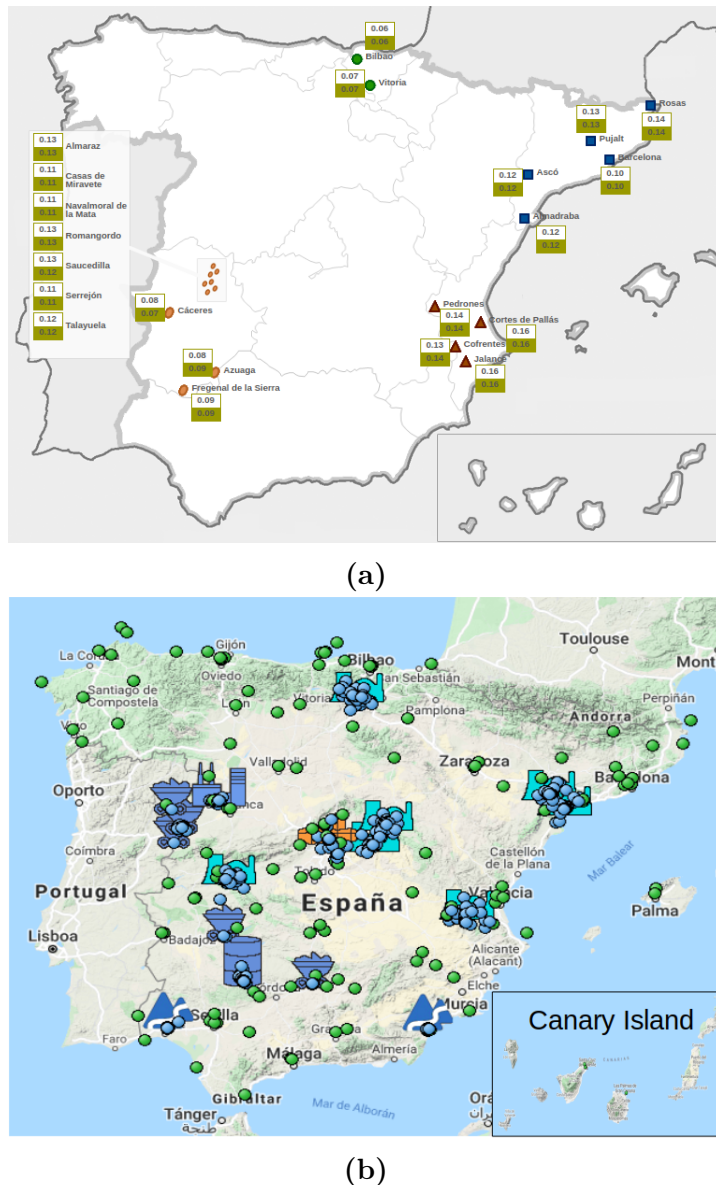


Figure 1.2 – Networks of automatic and sampling stations managed by the Spanish CSN. a) Measurement locations of the REA [CSNa]. The white box is the daily average of the gamma dose and the green box is the monthly average of the gamma dose. b) Measurement locations of the REM [CSNb]. Blue dots are locations near nuclear facilities, and green dots are locations uniformly distributed throughout the country.

1.1. TRITIUM AND NUCLEAR ENERGY

of automatically measuring low levels of tritium in water in quasi-real time². This monitor is intended to be finally included in the REA.

Tritium is one of the radioactive isotopes routinely measured in REM tests. Tritium is detected through the low-energy electrons produced in its beta decay, mainly using the Liquid Scintillation Counter Technique (LSC). Due to the limitations of the current tritium detection techniques, described in section 2.1, the TRITIUM project was recently proposed with the objective of building a tritium detector based on scintillating fibers in contact with the water sample. The photons produced in these scintillating fibers are read out by photosensors, either photomultiplier tubes (PMTs) or silicon photomultipliers (SiPMs).

The TRITIUM collaboration is an international consortium of 6 institutions from 3 European countries: Portugal, France and Spain. The final emplacement of the TRITIUM monitor is a site close to the Arrocampo dam (Extremadura, Spain), the water of which is used for the cooling system of the Almaraz nuclear power plant (NPP), located 4 km upstream from the Arrocampo dam.

The monitor will be used to ensure that the tritium levels of the Arrocampo dam water are below the legal limit of 100 Bq/L specified in the EURATOM Directive 2013/59/Euratom [Eur14]. In addition, this will confirm the correct operation of the Almaraz NPP, since an increase of tritium activity released could indicate a malfunctioning of the reactor.

Tritium is one of the most abundantly produced radioisotope in a NPP, as it was verified in the United States Department of Energy (DOE) [Ber98b, Ber98a], in several research facilities in China [Hou18] and in places close to them (ground, surface and waste water).

Tritium is produced in the nuclear reactor cooling water system of

²Quasi-real time is an approximation of real-time measurements. It means a relatively small time, like ten minutes.

NPP by neutron capture of deuterium existing in the heavy water (D_2O), semi-heavy water (HDO) or deuterium created by neutron capture in light water (H_2O). All these processes have a large probability of happening due to the huge neutron flux, of the order of $10^{14} \text{ n cm}^{-2}\text{s}^{-1}$ in the nuclear reactor [?]. Tritium is finally released partially or totally into the environment in a quantity that depends on the reactor type, as shown in Table 1.2. The most common form in which tritium is released into the environment is HTO [Hou18].

Reactor type	Gaseous discharge (GBq/y)	Liquid discharge (GBq/y)
PWR	$3.70 \cdot 10^3$	$2.59 \cdot 10^4$
BWR	$1.85 \cdot 10^3$	$3.70 \cdot 10^3$
HWR	$7.40 \cdot 10^5$	$1.85 \cdot 10^5$
GCR	$7.40 \cdot 10^3$	$1.11 \cdot 10^4$

Table 1.2: Emission of tritium per year from different types of nuclear reactors: Pressurized Water Reactor (PWR), Boiling Water Reactor (BWR), Heavy Water Reactor (HWR) and Gas-Cooled Reactor (GCR) [Hou18].

NPPs are operational for more than 60 years and, nowadays, they are essential for providing a large part of the electric power used all over the world (more than 20% in Spain [Red19] and more than 10% in the world [Int14]). Although the Spanish government is planning to progressively shut all NPPs down, there are other countries like China [Eur16] or United States [Noe19] that promote their use. NPPs are a profitable investment since they are one of the cheapest source of energy production. Their energy production rate is stable as does not depend on meteorological parameters. Moreover, NPPs do not emit greenhouse gases. Although there are alternative energy sources which are being developed quickly (photovoltaic, wind, tidal energy, etc.), as well as other concepts of energy production and saving (local production, energy efficiency, smart cities, etc.), they are currently not enough to cover the population needs. However, NPPs have some important drawbacks such as contamination of fresh water from uranium

1.2. TRITIUM PROPERTIES AND RADIOLOGICAL HAZARDS

mining, nuclear waste, nuclear proliferation and risk of radioactive contamination from accidents as happened in the past: Chernobyl, Fukushima and Three Mile Island [Wor20]. In any case, world nuclear energy production is most likely not going to be stopped in the next decade. In fact, the United States Energy Information Administration (EIA) expects a future increase of nuclear energy production [Cap20]. Therefore, safety is not a negotiable aspect and there must be a development in the safeguards, like alarm systems, that warn us of any malfunction of a NPP.

The objective of the TRITIUM project is to ensure that the level of tritium in water is below the Spanish legal limit. This monitor could be used in many different places with radioactive facilities like the future fusion power plants³, nuclear research facilities⁴ or tracking the pathway of tritium discharges to ground water [Saw00].

1.2 Tritium Properties and Radiological Hazards

Tritium is the only radioactive isotope of hydrogen present in the environment. Tritium was produced artificially for the first time in 1934 in neutron capture on deuterium by Ernest Rutherford, Mark Oliphant and Paul Harteck [Oli34] and was isolated in 1939 by Luis Walter Alvarez and Robert Cornog [Alv39], who discovered that tritium is radioactive.

Tritium is a radioactive element with a half-life time of $T_{1/2} = 12.32$ years. It has one proton and two neutrons and decays exclusively through β radiation to the ground state of the ^3_2He isotope of helium, which is a stable nuclei, through the process,

³The International Thermonuclear Experimental Reactor, ITER, will need up to several tens of kilograms of tritium to function, which corresponds to various TBq of activity.

⁴Tritium is one of the main emission from nuclear research facilities [Fer19, Env].



Figure 1.3 – (Above) Tritium energy levels [IAE]. (Below) Graphic representation of tritium decay [Jor20].



In Figure 1.3, the scheme of tritium energy levels is shown. In this decay it is not possible to detect the neutrino because of its extremely weak interaction with matter ($\sigma \approx 10^{-44} \text{ cm}^2$) [Val07] and, since ${}^3\text{He}$ has a much larger mass than electrons and neutrinos, the energy carried by the daughter nucleus is very small. Therefore, the detection of tritium is only feasible through its decay electron.

The energy released in the tritium decay is $Q_\beta = 18.6 \text{ keV}$, shared between the decay products. Therefore, the energy spectrum of the decay electrons is a continuum with a maximum value of 18.6 keV, as shown in Figure 1.4. This energy spectrum has an average of 5.7 keV and the most likely energy is around 4.5 keV. Tritium is the radioactive isotope with the lowest energy released in β decay [Dep16]. Consequently, the β particle emitted has a very short mean free path, given in Table 1.3. This short mean free path is a major issue in tritium detection, as the electron detection requires a highly sensitive detector. Tritium electrons have a low penetration in the human body and they are easily stopped by clothes

1.2. TRITIUM PROPERTIES AND RADIOLOGICAL HAZARDS

or laboratory gloves, resulting in a low radiological hazard from external exposure. Nevertheless, the danger of tritium increases when it is ingested or inhaled since it binds and undergoes the same chemical reactions as hydrogen.

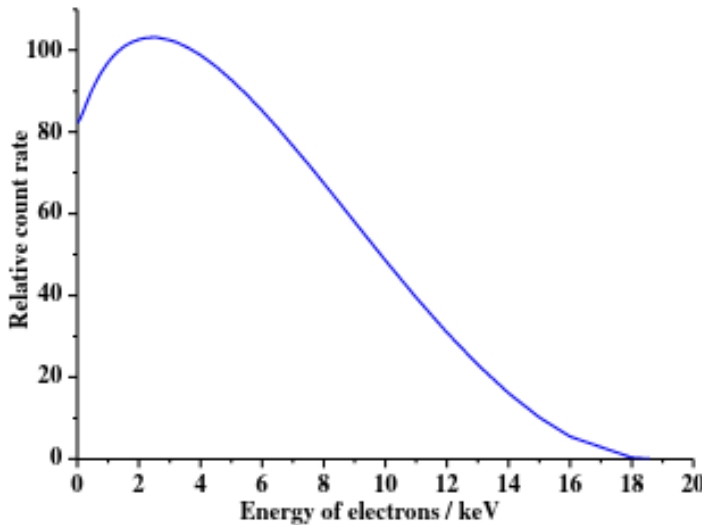


Figure 1.4 – Energy spectrum of tritium electrons [Lin20].

Tritium is naturally produced in the environment through the interaction of cosmic rays with elements of the upper atmosphere like nitrogen $^{14}\text{N}(\text{n}, ^3\text{H})^{12}\text{C}$ [Dep16] and oxygen $^{16}\text{O}(\text{n}, ^3\text{H})^{14}\text{N}$ [Hai14]. Around 99% of cosmogenic tritium forms water (HTO) and reaches the Earth's surface as rain with an estimated production rate of $4 \cdot 10^6$ Ci/yr ($1.48 \cdot 10^8$ GBq/yr), producing a tritium concentration of 0.6–1.2 Bq/L in precipitation [Hou18, Dep16].

Tritium can be produced artificially in the environment from different anthropogenic sources [Hou18, Dep16]. There is a large amount of tritium which was produced in military nuclear explosions between 1945 and 1975, with an estimated total production of $8 \cdot 10^9$ Ci ($2.96 \cdot 10^{11}$ GBq), a part of which remains to the date. In these nuclear explosions, tritium was

	Penetration Depth	
Energy	5.7 keV	18.6 keV
Material		
${}^3_1\text{H}_2$	0.26 cm	3.2 cm
Air	0.036 cm	0.45 cm
Water, soft tissue (solid matter with a density of $1 \text{ g} \cdot \text{cm}^{-3}$)	0.42 μm	5.2 μm

Table 1.3: Penetration depth of decay electrons of mean (5.7 keV) and maximum (18.6 keV) energies in different media (tritium gas, air at STP and water) [Bla91].

produced mainly from the nuclear reactions ${}^{14}\text{N}(\text{n}, {}^3\text{H}) {}^{12}\text{C}$ and ${}^2\text{H}(\text{n}, \gamma) {}^3\text{H}$. Tritium is produced by commercial producers of radioluminescent and neutron generator devices ($1 \cdot 10^6 \text{ Ci/yr}$), nuclear power and defense industries (around $2 \cdot 10^6 \text{ Ci/yr}$) and several research facilities and nuclear reactors for energy production ($2 \cdot 10^6 \text{ Ci/GWyr}$). The production cross sections of the relevant processes are shown in Table 1.4.

Source	Origin	Nuclear reaction	Cross section (b)
${}^2_1\text{H}$	Water coolant	${}^2_1\text{H}(\text{n}, \gamma) {}^3_1\text{H}$	$5.2 \cdot 10^{-4}$
${}^3_2\text{He}$	Helium coolant	${}^3_2\text{He}(\text{n}, \text{p}) {}^2_1\text{H}$	5330
${}^6_3\text{Li}$	Moderator	${}^6_3\text{Li}(\text{n}, \alpha) {}^3_1\text{H}$	940
${}^{10}_5\text{B}$	Moderator, control rods	${}^{10}_5\text{B}(\text{n}, 2\alpha) {}^3_1\text{H}$	3835

Table 1.4: Most common nuclear reactions of artificial tritium production [Hou18].

Tritium levels in water of the environment, excluding the current anthropogenic radioactive sources, are between 1 and 4 Bq/L, larger than expected from cosmogenic background levels (0.6 – 1.2 Bq/L) [Cal12]. This is attributed to nuclear weapon tests. Tritium levels in rivers around a NPP

1.2. TRITIUM PROPERTIES AND RADIOLOGICAL HAZARDS

are between 1 and 10 Bq/L and even between 20 and 50 Bq/L at the water discharge site of NPPs [Cal12], where the produced tritium is partially or totally released into the environment, mainly in HTO form.

The effect of NPPs on tritium levels in the environment can be observed in the REM data, for example for the case of Cofrentes NPP. The tritium level is measured in three different places along the Jucar river, marked on the map shown in Figure 1.5. P1 is located on the river 6 km upstream from the NPP, and P2 and P3 are located 1 and 5 km downstream, respectively. The level of tritium measured in these three locations is shown as a function of time in Figures 1.6a, 1.6b and 1.6c respectively. In these figures, the detection limit and the measured activity are plotted with white and green dots, respectively. The measured activity is only displayed when it is larger than the corresponding detection limit. The tritium level in the river is larger near the discharge of the NPP and decreases 4 km downstream, as can be seen from these data. Two additional measurements of the tritium level in groundwater are included, points S1 and S2 on the map in Figure 1.5, located 1 km upstream and downstream from the NPP, respectively. Both tritium levels are shown in Figures 1.7a and 1.7b, respectively, where it can be observed that they are below the detection limit. It is important to note that, although environmental tritium level is affected by the NPP in the case of Cofrentes, these levels are below the maximum allowed limit. The maximum level of tritium measured since January 2, 2006 is around 32 Bq/L, below the limit of 100 Bq/L recommended by the Euratom 2013 directive.

Tritium can be absorbed in our body by inhalation and ingestion. Tritium is present in three different chemical forms, gaseous tritium (mainly HT), tritiated water (mainly HTO) and organically bound tritium (OBT):

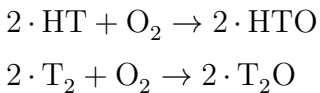
1. Gaseous tritium, usually found mixed in the air, is the least harmful form since less than a $(3 - 5) \cdot 10^{-3} \%$ is absorbed by the human body, which is negligible [Dep16]. However, gaseous tritium can be



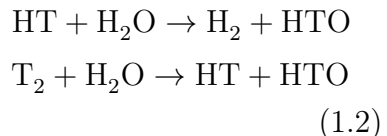
Figure 1.5 – Tritium sampling locations around Cofrentes NPP.

transformed into tritiated water, more harmful from the radiological point of view [Dep16], through the oxidation and exchange reactions by

Oxidation :



Exchange



2. Tritiated water, called tissue free water tritium, TFWT, is found in drinking water and food. This type of tritium molecule has a large impact since the 99% of it is absorbed [Dep16]. The biological life-time of tritiated water corresponds to the water cycle in the body, around 9.5 days ($\pm 50\%$), during which tritium remains in our body [Dep16, Cal12, Mas21, Lee18]. As in the case of water, the biological life-time of tritiated water depends on various external parameters such as temperature, humidity, drinking habits, etc. and can be reduced by the use of diuretics [Dep16].

1.2. TRITIUM PROPERTIES AND RADIOLOGICAL HAZARDS

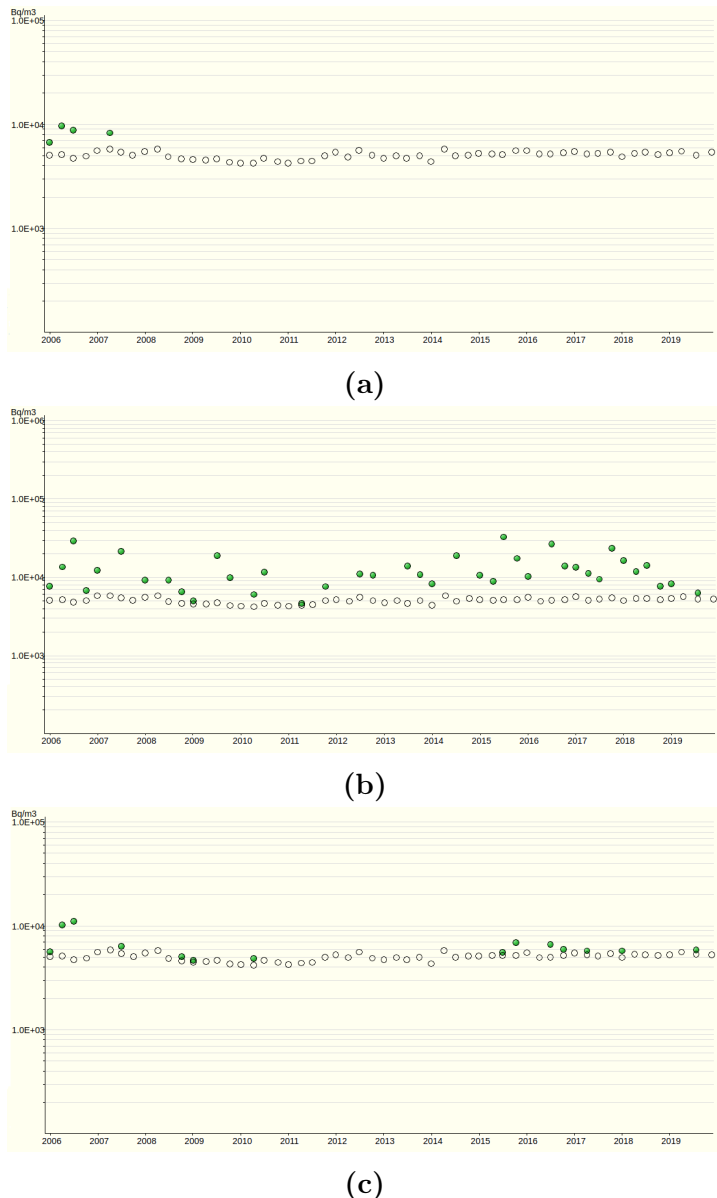


Figure 1.6 – Tritium activity levels in surface water around Cofrentes NPP from January 2006 to November 2019. a) 6 km upstream. b) 1 km downstream. c) 5 km downstream. The white points are the detection limits and the green points are the measured activity when this is above the detection limit [CSNb]. The maximum level of tritium measured since January 2, 2006 is around 32 Bq/L.

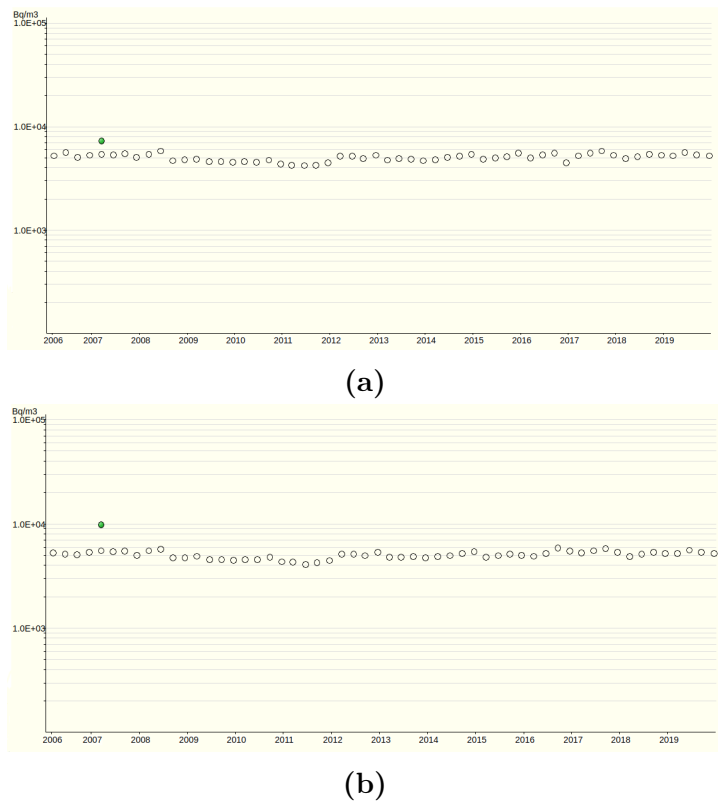


Figure 1.7 – Tritium activity levels in groundwater around Cofrentes NPP from January 2006 to November 2019 [CSNb]. a) 1 km upstream from the NPP. b) 1 km downstream from the NPP.

1.3. CURRENT LEGISLATION

3. Organically bound tritium (OBT), normally found in food, forms a covalent bond with carbon molecules in organs. This form corresponds to 5 – 10 % of tritium absorbed in the body. Although OBT is less absorbed in the body than tritiated water, it can be more dangerous since it has a longer biological life time, that varies from twenty to more than fifty days [Mar72, Lee18], depending on the type of bond that tritium forms, either OBT exchange (e-OBT), an unstable bond that can be eliminated by metabolic processes, or tightly OBT (t-OBT), a stable bond that cannot be eliminated by metabolic processes [Cal12, Mas21, PF81, Mar72].

Tritium can cause the same effects than X-rays or γ rays, such as DNA mutations or cell death. In the worst cases, tritium can produce the loss of the functionality of the organ or the development of tumors. In fact, the consequences of tritium radiation may be worse than similar doses of γ radiation since its biological efficiency⁵ is two or three times higher [Str93].

In summary, tritium is a naturally occurring radioactive element. It affects health of living organisms if these are excessively or chronically exposed to tritium. Because of that, several countries have developed a legislation to manage the release of tritium into the environment and to ensure that tritium levels are safe for living organisms.

1.3 Current Legislation

Due to the radiological risk of tritium, the current legislation limits the release of tritium into the environment, ensuring that the levels are below a safe value for public health.

⁵The biological efficiency is used to quantify the damage produced in the living cells due to an external radiation.

The guidelines to limit the radioactive elements in drinking water for many countries are based on the radiation protection methodology developed by the ICRP [ICR91] and the recommendations from WHO [WHO17]. The objective of the international radiation methodology is to protect people and the environment from the negative effects of ionizing radiations but allowing beneficial activities that involve a reasonable radiation exposure. This is based on three main points, which are:

1. The justification: The benefit from radiological exposure must outweigh the detriment to health that it causes.
2. The ALARA principle ("As Low As Reasonably Achievable"): The radiological exposure must be kept as low as possible considering social and economic factors.
3. The dose limitation: Limit that must never be exceeded.

While the ICRP recommends a maximum dose of 1 mSv/yr, excluding the natural background and medical interventions, the WHO is more conservative, recommending a maximum dose of 0.1 mSv/yr, which corresponds to less than 5% of the annual dose due to background radiation, 2.42 mSv/year. The guideline reference level of each radionuclide in drinking water, GL, is usually calculated from these recommendations as,

$$GL(\text{Bq/L}) = \frac{RDL}{DCF \cdot q} \quad (1.3)$$

where RDL is the reference dose level in Sv/yr, DCF is the dose conversion factor (the value provided by ICRP for tritium is $1.8 \cdot 10^{-11}$ Sv/Bq [ICR96]) and q is an estimation of the annual volume of drinking water consumed by a person (normally assumed two liters per day, 730 L/yr). The GL calculated for tritium in drinking water according to the ICRP and WHO recommendations is 76 103 Bq/L and 7 610 Bq/L respectively. This means that tritiated water with activities below these values is considered not

1.3. CURRENT LEGISLATION

harmful for health. Based on these recommendations, the national organizations develop their own legislation limits of exposure to radionuclides. In Spain, the responsible organization for this commitment is the CSN. Most of the countries in the world implement the RDL of 0.1 mSv/yr recommended by the WHO. The legal limit for tritium in drinking water in this case is 7 610 Bq/L but it is often approximated in different ways. Some countries like Switzerland [Dep17] or some organizations like the WHO [WHO17] take this value as 10 000 Bq/L. Others like some territories of Canada, such as Ontario and Québec, truncate this value to the first number 7 000 Bq/L [OME94, Hyd16]. There are other countries, like Russia, which use the much more accurate approximation value of 7 700 Bq/L [Int07]. Other countries, like Australia, prefer to implement the RDL of 1 mSv/yr recommended by the ICRP, which corresponds to 76 103 Bq/L [NHM21]. Finland takes the ICRP recommendations but uses only half of this value, 0.5 mSv/yr, rounded to a legal limit of 30 000 Bq/L for tritium in drinking water [Nuc93]. There are two different exceptions to these recommendations:

1. Most of the USA states, like California, establish a RDL of 4 mrem (0.04 mSv), which corresponds to a legal limit of 20 nCi/L (740 Bq/L) [EPA06]. This value was proposed by the United States Environmental Protection Agency (EPA) as a result of an analysis carried out on the available data [EPA01].
2. Most of the EU countries, such as France, Germany or Spain, consider a GL of 100 Bq/L, which is one of the most restrictive limit in the world [Ré18, Fed06, CSN13]. This value arises from the consideration that tritium is an indicator of the presence of other radionuclides more dangerous than tritium. These limits are fixed by the EURATOM Council Directive [Eur13].

All limits mentioned in this section are summarized in table 1.5.

Country/Agency	GL (Bq/L)
ICRP	76 103
WHO	10 000
Switzerland	10 000
Canada	7 000
Russia	7 700
Australia	76 103
Finland	30 000
United States	740
European Union	100

Table 1.5: Legal limit of tritium in drinking water (GL) established in several countries.

1.4 This Thesis

The objective of this thesis is to design, build and commission an automatic station for real-time monitoring of low tritium activities in water. This is mainly focused on the development and optimization of the TRITIUM prototypes and the active veto. This thesis is divided into eight chapters structured as follows:

1. **Chapter 1** provides a brief introduction to tritium detection, reports some important properties of tritium, and discusses the current legislation that limits tritium levels for human consumption in many countries around the world.
2. **Chapter 2** describes the state-of-the-art of tritium detection and introduces the TRITIUM project.
3. **Chapter 3** outlines the different parts of the TRITIUM monitor, which are the water purification system, the background rejection system (consisting of a lead shield and a active veto) and the tritium detector.

1.4. THIS THESIS

4. **Chapter 4** reports the calibrations of the different parts of the TRITIUM monitor and describes the developments aimed at improving the efficiency of tritium detection.
5. **Chapter 5** details the geometrical configuration of the different prototypes built in the TRITIUM project and the measurements taken with them.
6. **Chapter 6** details the Monte Carlo simulations performed in the TRITIUM project and shows the results obtained.
7. **Chapter 7** summarizes and discusses the most important results achieved by the TRITIUM collaboration.
8. **Chapter 8** Summarize the main results of this PhD work and discusses the future of the TRITIUM project.

Chapter 2

Methods of Detection of Tritium In Water

2.1 Tritium Detection State-of-the-Art

Measurement of tritium activity is one of the routine environmental controls that are carried out in the vicinity of nuclear research facilities and nuclear power plants during their energy production lifetime. This measurement is carried out with different available technologies according to the state of the art of tritium detection. The most employed techniques are summarized in Table 2.1.

Nowadays, the most used technique for measuring tritium in water is liquid scintillator counting (LSC). This technique consists of mixing a liquid sample (some milliliters for environmental measurements or less for higher activities) with liquid scintillator. This mixture is usually made in a ratio of 50:50 but it depends on the detection system and on the activity of the samples [AH99, Hof92a]. In this technique, the β particles emitted from the sample excite the molecular energy levels of the liquid scintillator

2.1. TRITIUM DETECTION STATE-OF-THE-ART

	LSC	IC	Calorimetry	BIXS
Measured quantity	Scintillation photons	Ionization current	Heat	X-rays
MDA	\sim Bq	10 – 100 kBq	\sim GBq	\sim MBq
Sample state	Liquid	Gas, vapor	All	All

Table 2.1: State-of-the-art tritium detection techniques. This table shows the measured quantity, the minimum detectable activity (MDA) and the sample form for four different techniques, liquid scintillator counting (LSC), ionization chamber (IC), calorimetry and beta induced X-ray spectrometry (BIXS).

which promptly decays emitting several photons with a well-known energy (fluorescence), usually in the visible spectrum. Finally, these photons are detected with photosensors which convert the optical signal into a measurable electrical charge. The liquid scintillator technique has a very good detection sensitivity for low activity levels of tritiated water (< 1 Bq/L) [Pal07] but has the disadvantages of long measurement time (up to 2 days) and production of chemical waste, since liquid scintillators contain toluene which is toxic. In addition, the LSC technique requires special staff for sampling, chain of custody and laboratory analysis which require economic and time resources. In order to overcome these difficulties, efforts were made to build a tritium monitor based on LSC which have not achieved a low enough MDA [Sig94].

The ionization chamber technique (IC) consists of a gas chamber filled with gas (sample), which contains electrodes that collect the ionization current produced by the β radiation in the gas. This is a simple and fast system, but it has a high MDA (> 10 kBq) and requires samples in a state of gas or steam [Khe02, Che13]. The IC technique also requires sample conditioning, chain of custody and laboratory analysis.

The calorimetry method is based on the measurement of the heat generated in the detection medium (normally platinum) [Ale11, BD13]. The disadvantages of this technique are its high MDA (of the order of a GBq) and the requirement of a long measurement time (2 days or more).

The Beta Induced X-ray Spectrometry (BIXS) is based on the measurement of the bremsstrahlung radiation produced by the tritium decay electrons, by a NaI(Tl) crystal coupled to a PMT [Mat07, Mat08] or silicon drift detector (SDD) [Nie15]. The limitation with this technique is its high MDA (of the order of MBq).

There are additional methods for tritium detection, although they are less employed or less developed, each one with its own advantages and limitations. For example, the avalanche photodiode (APD) cannot be used in contact with water [Sha97], the mass spectrometry needs to store the sample during several months [JB10] and the cavity ring spectroscopy requires a special optical configuration that is not possible outside a laboratory [Bra15].

All the above techniques are offline methods that need a long time for sample collection, shipment to a laboratory and activity measurement. Therefore, they cannot be used for in-situ monitoring of tritium in water. The liquid scintillation technique is the only one with a MDA smaller than the requirement of 100 Bq/L of tritium in water established by the EURATOM directive.

The purpose of the TRITIUM project is to develop an alternative method, based on solid scintillators, that allows to accomplish the requirements of in-situ monitoring of levels as low as 100 Bq/L in quasi-real time. There are several studies with solid scintillators so far:

1. The study by M. Muramatsu, A. Koyano and N. Tokunaga in 1967 used a scintillator plate read out by two PMTs in coincidence [Mur67].

2.1. TRITIUM DETECTION STATE-OF-THE-ART

2. The study by A. A. Moghissi, H. L. Kelley, C. R. Phillips and J. E. Regnier in 1969 used one hundred plastic fibers coated with anthracene powder and read out by two PMTs in coincidence [Mog69].
3. The study by R. V. Osborne in 1969 used sixty stacked scintillator plates read out by two PMTs in coincidence [Osb70].
4. The study by A. N. Singh, M. Ratnakaran and K. G. Vohra in 1985 used a scintillator with several holes read out by PMTs in electronic coincidence [Sin85, Rat00].
5. The study by K. J. Hofstetter and H. T. Wilson in 1991 tested different shapes of scintillator plastics like several sizes of beads, fibers, etc. The best result obtained for solid plastic scintillators was a tritium detection efficiency, ε_{det} , of the order of $10^{-3}(\text{Ls}^{-1}\text{kBq}^{-1})$ [Hof92a, Hof92b].

Reference	$\varepsilon_{det} \times 10^{-3}$ $\text{L kBq}^{-1}\text{s}^{-1}$	F_{sci} cm^2	$\eta_{det} \times 10^{-6}$ $\text{L kBq}^{-1}\text{s cm}^{-2}$	MDA kBq L^{-1}
[Mur67]	0.39	123	3.13	370
[Mog69]	4.50	> 424	< 10.6	37
[Osb70]	12	3000	4	37
[Sin85]	41	3000	13.7	< 37
[Hof92a]	2.22	~ 100	< 22.2	25

Table 2.2: Results of scintillator detectors developed for experiments for tritiated water detection. This table shows for the quoted studies the efficiency of the detector (ε_{det}), its active surface (F_{sci}), its specific efficiency, defined as efficiency normalized to active surface ($\eta_{det} = \varepsilon_{det}/F_{sci}$), and MDA.

The results of those studies are summarized in Table 2.2. As the active surface of the plastic scintillator (F_{sci}) varies largely with the detector type, the specific detector efficiency (η_{det}), which is the intrinsic efficiency normalized to its active surface, is used to compare the results. Finally,

the MDA in those studies are of the order of a few tens of kBq/L. The development of a detector with a much lower MDA is thus essential to comply with the EURATOM directive of 100 Bq/L of tritium in water for human consumption.

2.2 The TRITIUM Project

As a conclusion of section 2.1, the current techniques cannot be used for tritium monitoring in quasi-real time since they have either a high MDA or they work in off-line mode. To overcome these limitations, the TRITIUM project [Tri], with the title of "Design, construction and commissioning of automatic stations for quasi-real time monitoring of low radioactive levels of tritium in water", was proposed. The TRITIUM collaboration is an international consortium of six institutions from three European countries: The I3N¹, in Portugal, the University of Bordeaux and the Centre National de la Recherche Scientifique (CNRS, Section Aquitaine-Limousin), in France and the University of Extremadura, the Junta de Extremadura and the University of Valencia, in Spain.

This project was funded by the Interreg Sudoe program of the European Economic Community in the 2016 call, with reference number SOE1/P4/EO214. The purpose of this project is the development of an automatic station for in-water tritium monitoring, in situ and in quasi-real time. The tritium detector consists of a bundle of scintillating fibers in contact with the water sample which detect the tritium decay electrons. These fibers are read out with photosensors (PMTs or SiPM). The specific efficiency obtained by Moghissi et al. for scintillating fibers is sufficiently high to justify our choice of scintillating fibers as a detection medium. Additional elements are used to improve the tritium detection sensitivity such

¹Institute for Nanostructures, Nanomodelling and Nanofabrication, University of Aveiro.

2.2. THE TRITIUM PROJECT



Figure 2.1 – a) Arrocampo dam and Almaraz Nuclear Power Plant. b) Tagus river along Spain and Portugal.

as a water purification system, which prepares the water sample before introducing it in the detector for tritium measurement, and a cosmic veto and a passive shielding, which reduce the natural radioactive background of the tritium detector. Several electronic modules which control the different parts of the monitor, analyze the tritium measurement and send an alarm if the configured limit (100 Bq/L) is exceeded.

A crucial problem is to distinguish tritium signals from the background because tritium events have low energy (\sim keV) and fall in an energy range of the spectrum where background events are significant. To reduce the background of TRITIUM monitor, coincidence techniques are employed.

The TRITIUM monitor will be installed in the Arrocampo dam, Almaraz (Spain), displayed in Figure 2.1, where the Almaraz NPP releases the water from its secondary cooling circuit. This NPP has two nuclear reactors of PWR type. Arrocampo dam is located near the Tagus river, shown in Figure 2.1b, which is the longest river in Spain, with a length of 1007 km. This river, shown in Figure 2.1a, rises in Aragon (Spain) and flows into the Atlantic Ocean through Lisbon (Portugal). The water of this river is used for agriculture and drinking water by both Spanish and Portuguese people. For this reason, an international cooperation is necessary in order to control and maintain the quality of the Tagus river water.

Each institution of the TRITIUM collaboration is dedicated to the development of a different part of this project:

1. The University of Extremadura group has developed and installed the water purification system to produce water with very low conductivity, $\sigma \approx 10 \mu\text{S}/\text{cm}$ (two orders of magnitude less than raw water, $1000 \mu\text{S}/\text{cm}$). This purification process is very important for two reasons. On the one hand, for maintaining the TRITIUM detector pristine, which is critical for its long-term functionality. On the other hand, to reduce the natural background since several natural radioactive isotopes present in this water (except tritium), such as ^{40}K and natural radioactive series, are removed. This system is described in section 3.3.
2. The French group has developed the passive shielding for the detector. This shielding is made of lead with low intrinsic activity in order to reduce the external natural background of the system. This shielding is presented in section 3.4.1.
3. The Aveiro and Valencia groups have collaborated for designing, developing and building four different prototypes of the TRITIUM detector and active vetos for reducing cosmic events. These prototypes and vetos are described in chapter 5 and section 3.4.2, respectively. These groups have also carried out simulations of the detector, which are reported in chapter 6.

The important characteristics required for the TRITIUM detector are:

1. *Compactness.* This is an important requirement because in the place where the detector is planned to be installed there is little space. Compactness also allows portability and cost reduction.

2.2. THE TRITIUM PROJECT

2. *Modularity.* The modularity of the TRITIUM detector is important for flexible geometrical configuration and for improving its tritium detection sensitivity. Modularity also facilitates construction and maintenance.
3. *Thin active volume and large active area.* The mean free path of β particle from tritium decay is very short. Thus, a thin detector active volume is needed. In practice, an active thickness beyond the mean free path of the tritium electrons only contributes to background. In addition, as reported in section 2.1, the efficiency of this type of detector scales with the active area, so it is crucial to design a detector with the largest possible active area.
4. *High detection efficiency for tritium.* As the tritium activities to be measured are very low, the loss of tritium events strongly affects the accuracy of measurements.
5. *High specificity to tritium.* The monitor must be able to distinguish tritium signals from other radioactive decays in the sample.
6. *Quasi-real time response.* It is crucial that the system operates in quasi-real time (1 h or less) in order to detect any anomalous tritium release as fast as possible.
7. *Ruggedness.* The final goal of the project is to install an automatic system working during a number of years requiring only occasional intervention of specialized operators. Therefore, a rugged monitor is required.

In order to measure in quasi-real time, it is needed to work *in situ*, that is, in the same place where the water sample is taken. Working *in situ* has some advantages such as: 1) Cheap running cost, since sampling process, chain of custody, etc. are eliminated. 2) Quasi-real time measurements. 3) Safe monitoring since personal dose is reduced. 4) Changes in activity can be detected quickly.

Chapter 3

Design Principles and Components of TRITIUM

3.1 Detector System Overview

The objective of the TRITIUM project is the design, development, construction and commissioning of an automatic station for real-time monitoring of low levels of tritium in water. To achieve this aim, the TRITIUM collaboration has developed a monitor consisting of several parts, listed below:

1. The TRITIUM detector, described in chapter 5, is based on several modules read out in parallel. Each module consists of hundreds of plastic scintillating fibers, which are in contact with the water sample measured, read out by two coincident photosensors. The photosensors considered are photomultiplier tubes (PMT) and silicon photomultipliers (SiPM) (section 3.2).
2. The water purification system (section 3.3) that prepares for measurement the water sample, taken from the Arrocampo dam. This system

3.1. DETECTOR SYSTEM OVERVIEW

removes all the organic particles dissolved and all the particles with a diameter greater than $1 \mu\text{m}$ without affecting the tritium content of the sample. This system is important for two reasons: First, because the mean free path of tritium in water is very short, 5 to $6 \mu\text{m}$, hence it is essential to avoid organic and mineral depositions onto the fibers surface since this would prevent the tritium decay electrons from reaching the fibers. Second, minerals dissolved in water may contain radioactive isotopes like ^{40}K , which would increase the background. As the activity limit to be measured is low (down to 100 Bq/L), background reduction is crucial.

3. The background rejection system (section 3.4) has two different parts. The first one is a passive shield, consisting of a lead castle inside which the TRITIUM detector is located. This castle is employed to suppress the background from natural radioactivity and cosmic rays with energies up to 200 MeV. The second part is an active veto, consisting of two plastic scintillating plates located inside the passive shield, above and below the tritium detector, which are read out by photosensors. The goal of this active veto is to suppress the remaining high energy events ($> 200 \text{ MeV}$) from cosmic rays that cross the passive shield and contribute to the background. The technique employed to suppress their contribution consists in reading the tritium detector in anti-coincidence with the active veto.
4. A readout electronic system which allows the acquisition and processing of the data, in order to provide an alarm signal in case the tritium level measurement within a short interval of time exceeds the required limit of 100 Bq/L.

The TRITIUM system is planned to be part of the network of automatic stations, REA.

3.2 TRITIUM Detector

As discussed in section 2.1, the TRITIUM monitor consists of a chain of three main elements, plastic scintillating fibers, that produce scintillating photons in response to a tritium electron decay, the photosensor, that detects the photons produced in the scintillator and produces an electronic pulse than gives information on the detected photons, and the electronic system, which processes and analyzes the electronic pulses provided by the photosensor. A scheme of a scintillation detector setup is shown in Figure 3.1.

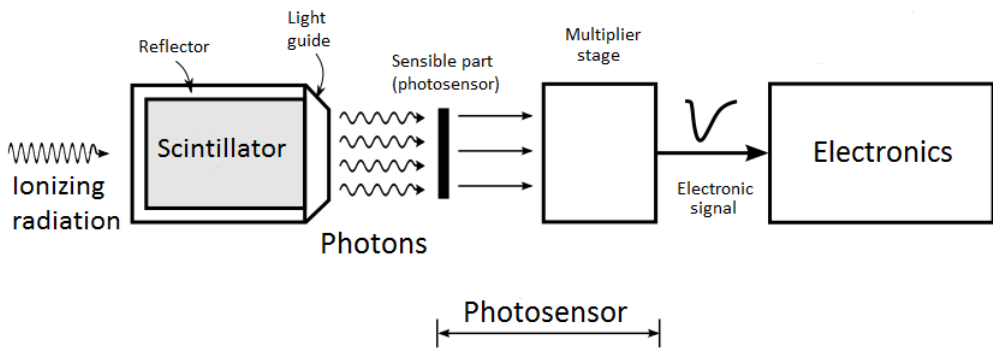


Figure 3.1 – Scheme of the scintillator detector.

3.2.1 Interaction of Fast Electrons and Photons with Matter

The interaction of particles with matter is described in this section, focusing on the particles and energy range relevant for this thesis, electrons (0 – 18 keV), photons in the visible range (approx. 380 – 750 nm) and γ rays from the background and high energy cosmic rays.

Electrons have charge, so their interaction with matter is mainly

3.2. TRITIUM DETECTOR

through the orbital atomic electrons by the Coulomb force. The electron trajectory is much more tortuous than that of heavier particles because of its small mass. Furthermore, these electrons lose a significant amount of energy in each collision. The specific energy loss, defined as $S = -\frac{dE}{dx}$, gives the energy loss of the particle per unit of path length. In the case of electrons, the total energy loss has two main contributions, the collisions (elastic and inelastic) and the radiative processes (bremsstrahlung), which are roughly proportional [Kno99, Leo94]:

$$\frac{dE}{dx} \approx \left(\frac{dE}{dx} \right)_c + \left(\frac{dE}{dx} \right)_{br}; \quad \frac{\left(\frac{dE}{dx} \right)_{br}}{\left(\frac{dE}{dx} \right)_c} \approx \frac{EZ}{700} \quad (3.1)$$

where E is the energy of the electron in MeV and Z is the atomic number of the absorbing material. Due to this energy loss, electrons penetrate a material to a depth where they have lost their kinetic energy. This distance, known as range, is quoted for tritium electrons in Table 1.3.

The material chosen for the detection of tritium decay electrons is organic plastic since, due to its low density, the backscattering process is reduced. It has been chosen in the form of fibers in order to increase the active area and, therefore, the efficiency of the detector.

As photons do not have charge, their possible interactions with matter are photoelectric effect, Compton effect, coherent scattering and pair production. The probability of each process, displayed in Figure 3.2, depends on the energy of the photon, $E_\gamma = h\nu$, and on the atomic number of the material, Z . The optical photons have a wavelength between 400 and 700 nm, that corresponds to energies of the order of the eV. Therefore, pair production does not play any role for optical photons since this requires a photon energy of at least 1.022 MeV.

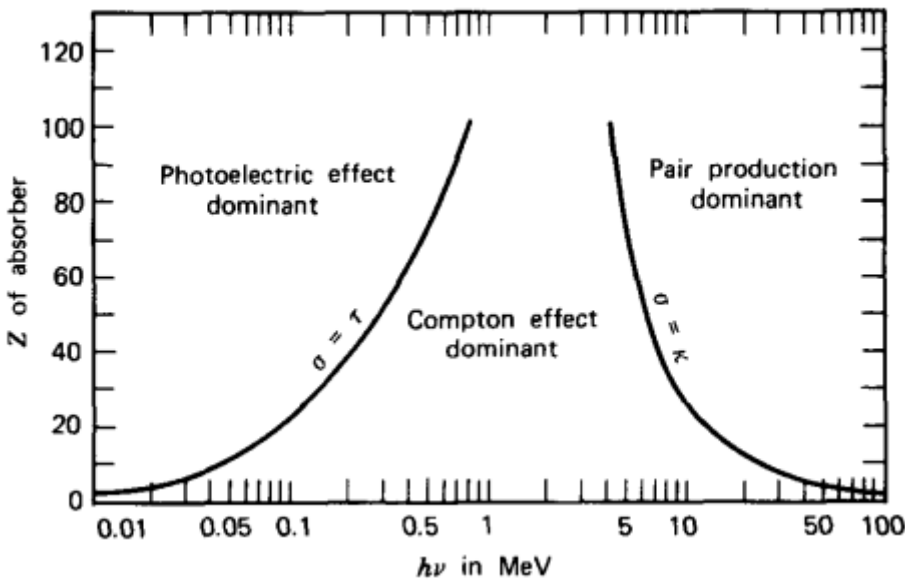


Figure 3.2 – Domain regions of the three most probable types of interactions of gamma rays with matter. The lines show the atomic number Z and gamma energy $h\nu$ where two interaction processes are equally likely [Kno99].

The photoelectric effect occurs when a photon interacts with an orbital electron in the material, losing all its energy. This energy is absorbed by an electron that is ejected from the atom (ionization). The energy of the resulting electron, E_e , is [Kno99, Leo94]:

$$E_e = E_\gamma - E_b \quad (3.2)$$

where E_b is the binding energy of the electron in this material. The probability of this effect depends on the number of available electrons in matter through the atomic number Z , and the energy of the electron according to the expression [Kno99]:

$$(Pr)_{Ph-eff} \approx \frac{Z^n}{E_\gamma^{3.5}} \quad (3.3)$$

3.2. TRITIUM DETECTOR

Thus, the photoelectric effect is most probable for elements with high atomic number. This is the reason why this type of elements are the best shields against gamma radiation and why the passive shield of TRITIUM monitor consists of lead bricks (section 3.4.1).

The Compton effect occurs when a photon interacts with an orbital electron of the material, transferring part of its energy to the electron, which is scattered at an angle θ with respect to the direction of the incident photon. If the electron binding energy is neglected, the energy transferred to it, E_e , is given by [Kno99, Leo94]:

$$E_e = \frac{\frac{E_\gamma^2}{m_0 c^2} (1 - \cos\theta)}{1 + \frac{E_\gamma^2}{m_0 c^2} (1 - \cos\theta)} \quad (3.4)$$

where m_0 is the rest mass of the electron and c is the speed of the light in vacuum. The probability of the Compton effect is proportional to the atomic number, Z , and decreases with the energy of the photon. As it can be seen in Figure 3.2, for photon energies in the visible spectrum (of the order of eV), the Compton effect is only likely for very light materials ($Z < 4$). For heavier materials the photoelectric effect is dominant.

In the coherent scattering, the atom is neither excited nor ionized and the photon conserves its energy in the collision. Coherent scattering is probable for photons with low energies and materials with high atomic numbers.

Finally, in the pair production process, the photon is converted into an electron and a positron.



As can be seen in Figure 3.2, this is the dominant interaction process for

high energy photons, which are the photons produced by cosmic rays that can affect the TRITIUM detector.

3.2.2 Plastic Scintillators

Scintillators are materials widely employed for radiation detection in nuclear physics. Scintillators convert kinetic energy of the incoming particles into light which can be detected and quantified. Light emission is produced due to the photon de-excitation of atoms of fluorescent molecules in the material.

Light production is linear with energy for a wide energy range of incoming particles. Scintillators should have good optical properties, such as being transparent to the wavelength of their own emission and having a refractive index close to that of photosensor windows in order to optimize optical coupling and light transmission. Photon emission in scintillators is a statistical process that follows a Poisson distribution.

Scintillators can be organic or inorganic. Inorganic scintillators normally have a high atomic number and density, so their light output is high. For these reasons they are suitable for gamma-ray spectroscopy. Organic scintillators are generally fast and they are used for charged particles and neutron detection. This section is focussed on organic scintillators since they are the ones used in the TRITIUM detector. Organic scintillators are based on fluorescent molecules dissolved in a base solvent, usually aromatic hydrocarbons as $C_{18}H_{14}$, $C_{24}H_{22}N_2O$ or $C_{15}H_{11}NO$ with an average atomic number between 3.5 and 5. The fluorescent molecules of organic scintillators have a π -electron structure. The energy levels of their electrons are commonly illustrated with a Jablonsky diagram, shown in Figure 3.3. This diagram shows the fundamental singlet states, S_{0i} , the excited singlet states, S_{jk} , and the excited triplet states, T_{lm} . The energy difference between S_1 and S_0 states is around 3 to 4 eV, which corresponds to the

3.2. TRITIUM DETECTOR

visible photon emission. As shown in the figure, each energy state is split into close sublevels separated around 0.15 eV. This fine energy structure is due to excitations of molecular vibrational modes tagged by the second index of the energy states. As the energy levels and sublevels have an energy larger than the thermal energy, 0.025 eV, electrons are in the ground state S_{00} at STP. When a particle deposits its kinetic energy in a scintillator, the valence electrons are excited very fast ($\tau \approx 1 \text{ ps}$) to higher singlet energy states and are quickly de-excited to the first singlet excited state, S_{10} , through non-radiative processes known as internal conversion. These electrons can de-excite to the fundamental singlet state, S_{00} , through three different physical mechanisms:

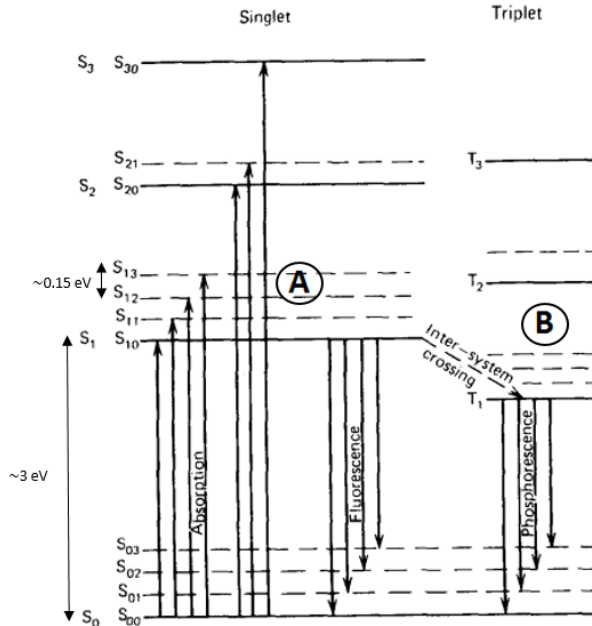


Figure 3.3 – Jablonsky diagram [Kno99].

- Prompt fluorescence (process A in Figure 3.3), where the electron in the S_{10} level is de-excited to a sublevel of the ground state S_{0i} , emitting a photon. This process happens immediately after the excitation of the scintillator molecules (of the order of nanoseconds after

excitation). Each scintillator has a characteristic emission spectrum. Organic scintillators are practically transparent to their own fluorescence emission because scintillating photons have less energy than the excitation energy. This effect is called Stokes shift and it is represented in Figure 3.4. The intensity of the fluorescence emission in an organic scintillator versus time is the combination of two exponential functions, one associated with the lifetime of the level τ (of the order of nanoseconds), and the other associated with the energy level population τ_1 (of the order of picoseconds) [Kno99],

$$I = I_0 (e^{-t/\tau} - e^{-t/\tau_1}) \quad (3.6)$$

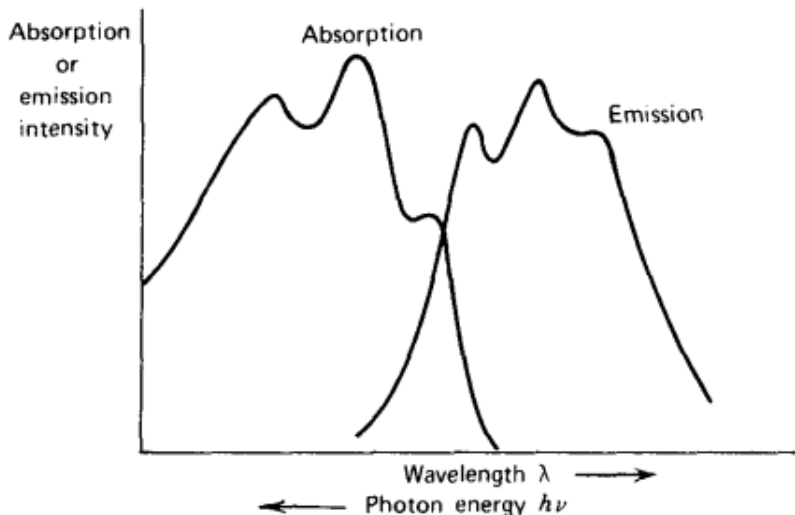


Figure 3.4 – Stokes shift [Kno99].

2. Phosphorescence, where the electron that is in the first singlet excited state crosses to a triplet excited state (process B in Figure 3.3). Such a transition process is called "intersystem crossing". The triplet state is a metastable state with a longer lifetime than fluorescence, of the order of milliseconds after scintillator excitation.

3.2. TRITIUM DETECTOR

3. Delayed fluorescence, which occurs when an electron is in a triplet excited state but its transition to the ground state is forbidden. In this case, the electron interacts with another electron in a similar state, falling to the first singlet state and quickly de-exciting to the ground state,



This emission has the same emission spectrum as the prompt fluorescence, but with a longer lifetime.

As the prompt fluorescence light produces the scintillator signal, the detector design should optimize its collection and detection and reduce other possible physical mechanisms like phosphorescence or delayed fluorescence. One of the most important parameters that characterizes the scintillator is the scintillation yield, defined as the number of photons emitted per unit of absorbed energy. This yield depends on the type of particle and on other mechanisms that do not produce prompt fluorescence light, like phosphorescence, delayed fluorescence, and non radiative processes like internal conversion. The scintillator yield is normally quoted by the manufacturer for mips¹.

Plastic scintillators are easy to machine to any desired shape. The chosen shape for TRITIUM detector is the fiber, specifically, commercial fibers BCF-12 from Saint-Gobain Crystals Inc [Sai21b]. This type of fiber was chosen as the result of a comparative study [Sol17] among some of the best-known commercial manufacturers. The BCF-12 fibers consist of a scintillating polystyrene core with the possibility of being covered by polymethylmethacrylate (PMMA) claddings.

When a particle deposits all or part of its kinetic energy in a scin-

¹A mip or minimum ionizing particle is a particle that has a speed at which the ionization produced is minimal.

tillating fiber, photons are produced in the fiber core as a result of the fluorescence process. The number of photons produced depends on the scintillating efficiency and its value is around 2.4% for the BCF-12 fibers, which means that a scintillation yield of about 8000 photons per MeV is produced for a mip. For instance, for tritium electrons of 18.6 keV, these fibers emit at least 149 photons, as electrons of these energies are not mips. The emission spectrum of the fibers employed in this work is shown in Figure 3.5.

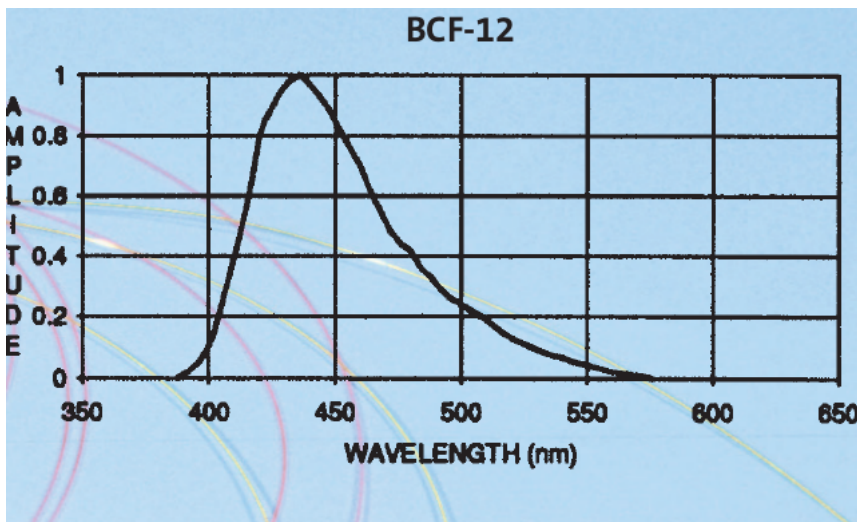


Figure 3.5 – Emission spectrum of BCF-12 scintillating fibers of Saint-Gobain [Sai21b].

The scintillation light is guided to the sensitive part of the photo-sensor. A single photon produces a signal with a probability called quantum efficiency. Photons are guided in fibers according to the Snell's law [Bor19]. The guiding mechanism is determined by the interface between the core and the surrounding material. When a photon hits this interface, it is refracted (and therefore lost) following the Snell equation [Bor19],

$$n_0 \sin\theta_0 = n_1 \sin\theta_1 \quad (3.8)$$

3.2. TRITIUM DETECTOR

where θ_0 is the incident angle formed by the photon and the normal to the surface of the first medium with refractive index n_0 , and θ_1 is the refraction angle formed by the photon and the normal to the second medium with refractive index n_1 . If the surrounding material has a lower refractive index than the core of the fiber, as it is the case with scintillating fibers, there exist a critical angle, θ_c , beyond which photons will be totally reflected ($\theta_1 = 90^\circ$) and therefore kept within the fiber as illustrated in Figure 3.6,

$$\theta_c = \arcsin \left(\frac{n_1}{n_0} \right) \quad (3.9)$$

The trapping efficiency or photon collection efficiency is defined as the efficiency of the scintillator to guide photons. For BCF-12 fibers with optical clad this efficiency is between 3.4% and 7% per meter of fiber (depending on the emission point, it is minimum on the fiber axis and maximum near the core-clad interface). In Figure 3.6, the light collection in a fiber is illustrated.

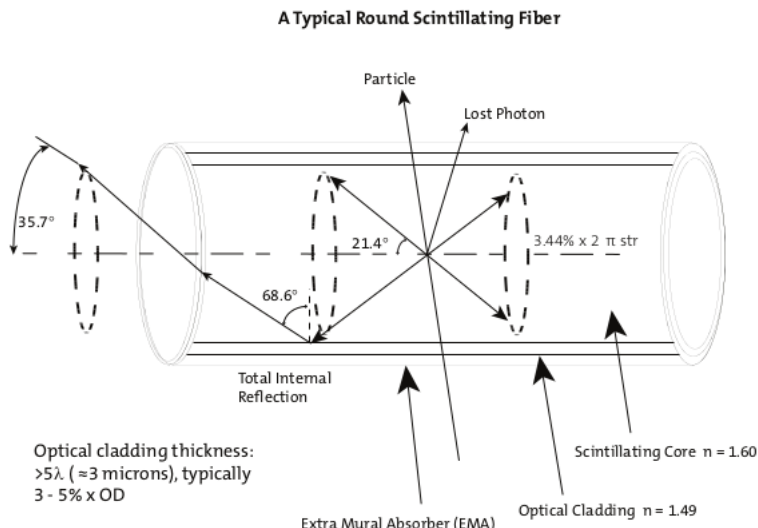


Figure 3.6 – Photon collection in a single clad fiber [Sai21b].

The cladding material has a higher refractive index than air and water. Therefore, it increases the critical angle and reduces the light collection. However, it is useful for protecting the core surface from dirt and aggressive external agents that would reduce the light collection. Three different cases are shown in Table 3.1, where the cladding effect is illustrated. As can be seen, the critical angle for uncladded fibers surrounded by water

Material	Refractive index	critical angle (°)
Air	1	38.68
Water	1.33	56.23
Cladding of PMMA	1.49	68.63

Table 3.1: Critical angles associated to different interfaces between polystyrene ($n_0 = 1.6$) and other materials.

or air is smaller than for cladded fibers, which implies a larger trapping efficiency. However, in practice, it is difficult to achieve a perfect air-core or water-core interface, and this affects light collection. As commercial claddings are thicker (30 μm) than the mean free path of tritium decay electrons in water (around 5 μm), cladded fibers are not an option for the TRITIUM detector. Hence, special attention is needed for achieving a good enough water-core interface. To achieve this goal a special method was developed in the ICMOL laboratory² for preparing fibers for tritium detection, described in section 4.1.1. The relevant parameters of the scintillating fibers used for the TRITIUM detector are given in Table 3.2.

3.2.3 Light Detection in Photosensors

The scintillating photons created in the core of the fiber and directed to its ends are detected by photosensors. Photosensors have a sensitive part

²ICMOL, *Instituto de Ciencia Molecular*, is a research institute located in the *Parc Científic* of the University of Valencia.

3.2. TRITIUM DETECTOR

Property	Value
Core material	Polystyrene
Core refractive index	1.60
Density (g/cm ³)	1.05
Cladding material	Acrylic (PMMA)
Cladding refractive index	1.49
Cladding thickness	3% Ø
Numerical aperture	0.58
Trapping efficiency	3.4% to 7%
# of H atoms per cc (core)	$4.82 \cdot 10^{22}$
# of C atoms per cc (core)	$4.85 \cdot 10^{22}$
# of electrons per cc (core)	$3.4 \cdot 10^{23}$
Radiation length (cm)	42
Emission peak (nm)	435 (blue)
Decay time (ns)	3.2
1/e Attenuation length (m)	2.7
Scintillator yield (# γ /MeV)	~ 8000
Operating Temperature	-20°C to 50°C

Table 3.2: Properties of BCF-12 scintillating fibers from Saint-Gobain Inc. [Sai21b].

that is optimized to detect photons in a range of energy (usually in the visible range) with a certain probability, called quantum efficiency. The photosensors produce an electronic signal that carries information about the detected photons such as their number, detection time, etc. There are many available photosensors that rely on various physical processes, such as photomultiplier tubes (PMTs), silicon photomultipliers (SiPM) or Charge-coupled devices (CCD).

The optimization of the efficiency of a scintillation detector is essential. To do so, the emission spectrum of the scintillator (Figure 3.5 for the fibers used) must match as much as possible the detection efficiency spectrum of the photosensor. The efficiency of a detector is proportional to the product of the emission and the detection efficiency spectra and is largest when both spectra match.

The requirements imposed on the photosensor of the TRITIUM detector are fast response, high gain and high photodetection efficiency. Two different proposals for the TRITIUM detector are investigated, SiPMs and PMTs. Both meet these requirements since they are very fast (of the order of ns), have high gain (of the order of 10^6) and have a high photodetection efficiency (around 50% for SiPMs and 30% for PMTs). Each proposal has its own advantages. SiPMs are more robust and need a lower supply voltage (of the order of 50 V) than PMTs (of the order of 1000 V). Furthermore, due to this difference in the supply voltage, SiPMs have smaller cost per channel than PMTs. However, PMTs, which are the conventional choice, have lower dark count rate than SiPMs and a much lower dependence of gain with temperature.

3.2.3.1 Photomultiplier Tubes (PMTs)

Photomultiplier tubes are employed as photosensors in nuclear physics since decades. They detect the scintillating photons that reach its sensitive part,

3.2. TRITIUM DETECTOR

the photocathode, and produce an electronic signal, large enough to be easily measured. In Figure 3.7 a schematic drawing of a PMT is given. The PMTs consists of a vacuum tube that has a glass window through which photons can penetrate. The electrons created in the photocathode travel in vacuum. The signal production has two phases:

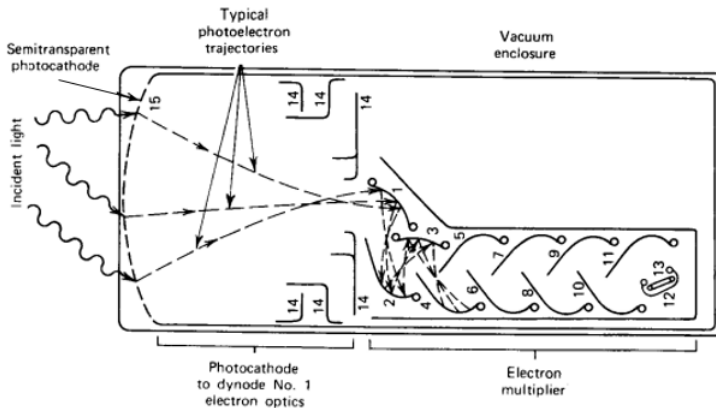


Figure 3.7 – Scheme of a PMT [Kno99].

1. In the photocathode, photons are converted into photoelectrons through the photoelectric effect. The photocathode consists of a thin layer of material, of the order of nanometers, deposited on the inner surface of the PMT window. The material of the photocathode is chosen to optimize the probability of producing photoelectric effect with the scintillating photons. The PMTs used in different R&D setups of the TRITIUM experiment in the University of Valencia are the model R8520-406 from Hamamatsu [Ham19] and the material of their photocathode is Bialkali³.

The response of the PMT has a strong dependence on the energy of the photon. The quantum efficiency (QE) spectrum, shown in Figure 3.8 for the PMTs mentioned above, is defined as the ratio of the number

³The bialkali material is based on the elements $^{121}_{51}\text{Sb}$, $^{85}_{37}\text{Rb}$ and $^{132}_{55}\text{Cs}$

of photoelectrons produced at the photocathode of the PMT and the number of photons reaching it.

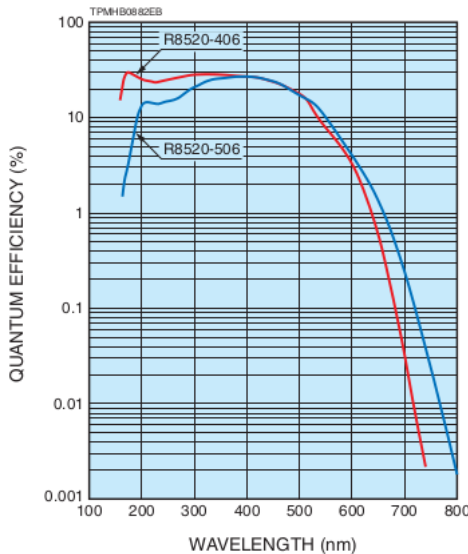


Figure 3.8 – Quantum efficiency spectrum for the PMT used in TRITIUM R&D studies (R8520-406) [Ham19].

The maximum value of the PMT quantum efficiency is usually between 20% and 30% [Kno99] (slightly less than 30% for the PMTs used in this thesis). The emission spectrum of the scintillating fibers used, Figure 3.5, matches the quantum efficiency spectrum of the PMTs used, Figure 3.8, and the positions of both peaks are very close, 435 nm and 420 nm for fibers and PMT respectively. Because of that, the intrinsic efficiency of the TRITIUM detector is maximized.

2. As the number of photoelectrons produced in the photocatode is very small, an electron multiplication stage is employed to obtain an electronic signal of sufficient size to be processed by the electronic system. The amplification stage is based on three elements, focusing electrodes, dynodes and anode, which are metallic plates with a shape and position designed to optimize the collection and multiplication of

3.2. TRITIUM DETECTOR

electrons. A high voltage (HV) is applied to the PMT which is distributed between all these elements, including the photocathode, with the help of a voltage divider circuit. A positive HV, grounded in the photocathode, is convenient for measuring PMT currents, and a negative HV, grounded in the anode, gives a faster response. The electronic scheme of the voltage divider circuit of Hamamatsu is shown in Figure 3.9.

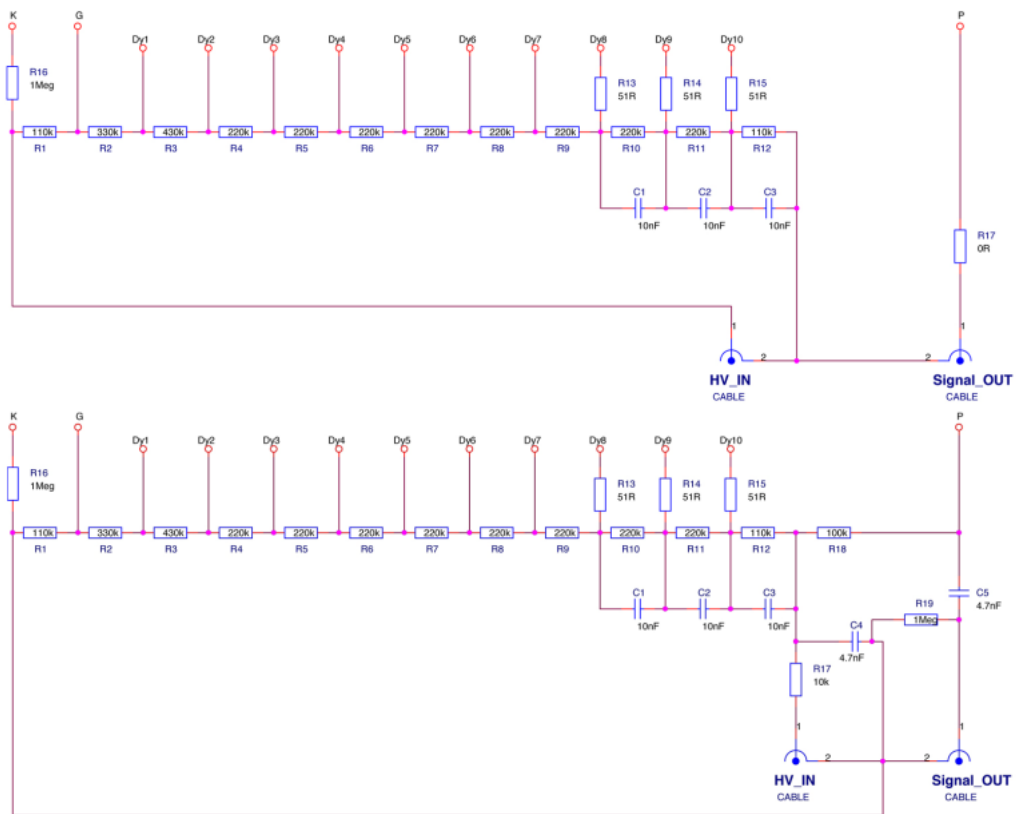


Figure 3.9 – Hamamatsu commercial voltage divider electronic circuit with negative (up) and positive (below) supply high voltage [Ham19].

Focusing electrodes guide the photoelectrons to the first dynode. They have a collection efficiency (CE) defined as the ratio of the number of photoelectrons reaching the first dynode and leaving the photocath-

ode. The value of the CE depends on the voltage between photocathode and the first dynode and reaches a 100% at voltages above 100 V. The dynodes produce the electron multiplication. A voltage difference between adjacent dynodes accelerates the electrons and produce their multiplication. The multiplication factor of each dynode, δ , is usually around 5 and depends on the HV. If all dynodes have the same gain, the overall gain of a PMT with N dynodes is given by [Kno99]:

$$G_{PMT} = CE \cdot \delta^N \quad (3.10)$$

and is of the order of 10^6 , strongly dependent on the applied HV.

The multiplication stage adds an uncertainty to the measurement. Working without gain allows us to count the number of photons that reach the PMT. This can be done by short-circuiting all the dynodes and the anode and collecting the signal directly from the first dynode. This voltage divider circuit, shown in Figure 3.10, was used for fiber characterization.

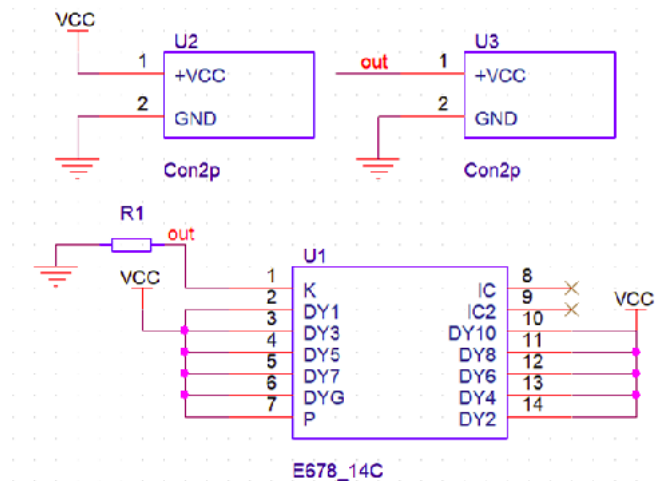


Figure 3.10 – Electronic scheme of the voltage divider circuit used for working with PMTs without internal gain.

3.2. TRITIUM DETECTOR

The output pulse of a PMT has a width of the order of tens of nanoseconds. The multiplication process can be described as a Poisson statistical process. For each electron in the first dynode, G_{PMT} new electrons are created with a variance of $\sqrt{G_{PMT}}$.

The output signal of a PMT is linear with the number of photons that reach its sensitive part up to a saturation limit, after which the linearity is lost. This limit depends on the PMT characteristics. The photocathode may emit electrons in absence of any light. This signal, called dark current, I_{DC} , can arise due to thermoionic emission. For the PMTs employed in this work, this value is around 2 nA according to their data sheet.

3.2.3.2 Silicon Photomultiplier Array

The Silicon Photomultiplier (SiPM), also called Multi-Pixel Photon Counter (MPPC), is a kind of photosensor based on silicon, developed in the last two decades. SiPMs are replacing progressively conventional PMTs in many experiments and applications. They have outstanding photon counting capabilities at the single photon level with higher photodetection efficiency than PMTs and they have a similar gain. SiPMs have, in addition, several advantages as insensitiveness to magnetic fields, low operating voltage, compactness and ruggedness. The only drawback with respect to PMTs is their high dark count rate (between 100 kHz and 1 MHz).

SiPMs are formed by a matrix of Avalanche Photodiodes (APDs) connected in parallel and operating in Geiger mode. APDs, shown in Figure 3.11, are based on p-n junctions.

The voltage at which a SiPM starts operating in Geiger mode is called the breakdown voltage, V_{BD} . At voltages lower than V_{BD} SiPMs work in proportional mode in which the signal of each APD is proportional to the energy deposited. The measurement of the V_{BD} , described in section

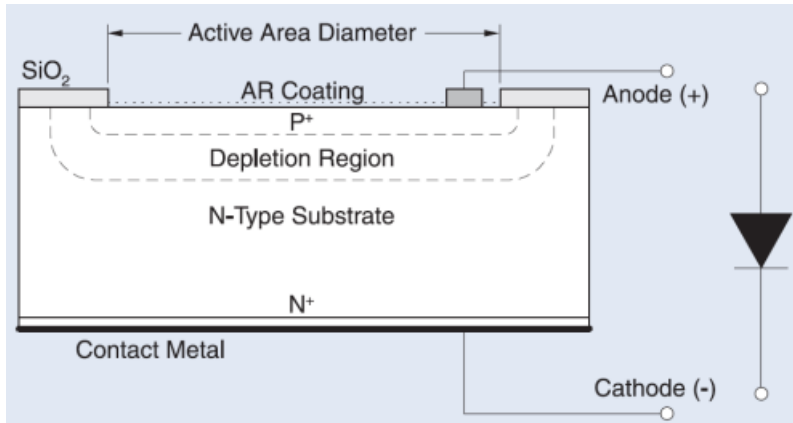


Figure 3.11 – Scheme of a APD and electrical symbol used [OSI].

4.2, is important to characterize a SiPM, since its properties, as the gain, depend on the overvoltage, V_{OV} , that is the SiPM bias voltage above V_{BD} ,

$$V_{OV} = V_{bias} - V_{BD} \quad (3.11)$$

These APDs, called pixels when they are part of a SiPM, are connected in parallel to give the SiPM output signal. If the photon flux is low enough, each SiPM pixel detects at most one photon. All pixels produce a similar output signal, regardless of the energy deposited. Therefore, the charge of the output signal when n pixels are simultaneously fired is n times the charge of a single pixel, illustrated in Figure 3.12. Hence, the number of detected photons is proportional to the integrated output signal. Once the SiPM is calibrated, the energy of tritium events can be determined. If the photon flux is high (typically several thousands of photons per event) more than one photon impinge simultaneously on the same pixel, producing the signal corresponding to a single photon. This effect, known as saturation, produces a loss of linearity of the output signal. However, this effect is negligible for the TRITIUM detector since tritium electrons produce few photons.

3.2. TRITIUM DETECTOR

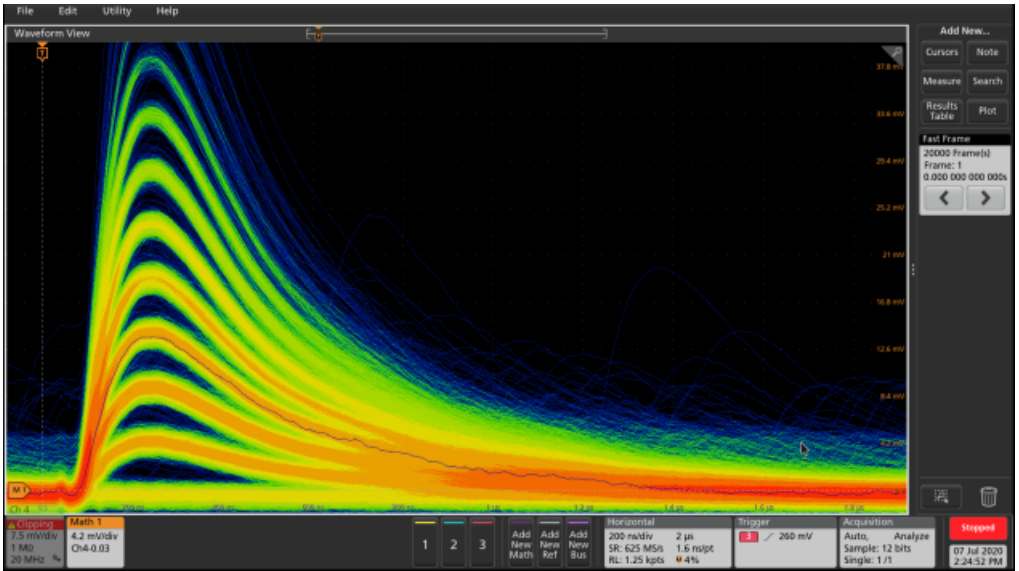


Figure 3.12 – SiPM output pulses displayed on the oscilloscope, model MSO44X from Tektronix [Tek21]. Several height pulses are observed, associated to a different number of SiPM pixels fired at the same time. The persistence function of the oscilloscope is used.

Different sizes of the SiPM pixel are available⁴. For a given SiPM active area, a small pixel size allows a high dynamic range at the cost of reducing the photon detection efficiency (PDE). As tritium electrons produce few photons, the SiPMs chosen have a large pixel size ($75\ \mu\text{m}$) since we are well within the dynamic range.

A SiPM can be modeled as an electrical circuit, shown in Figure 3.13a. The depletion zone is represented by a capacitance, C_d . When a photon impinges on the pixel, the capacitor is discharged, creating an electronic pulse. Each pixel of a SiPM has a quenching resistance⁵ in series R_q that limits the avalanche current produced when this pixel is fired. When the discharge is produced, a current flows through the resistance, reducing

⁴Pixel sizes for commercial SiPMs are 25, 50 and $75\mu\text{m}$ [Ham16a, Ham16c, Ham16d]

⁵The tipical value of this quenching resistance for commercial SiPMs is around $500\ \text{k}\Omega$

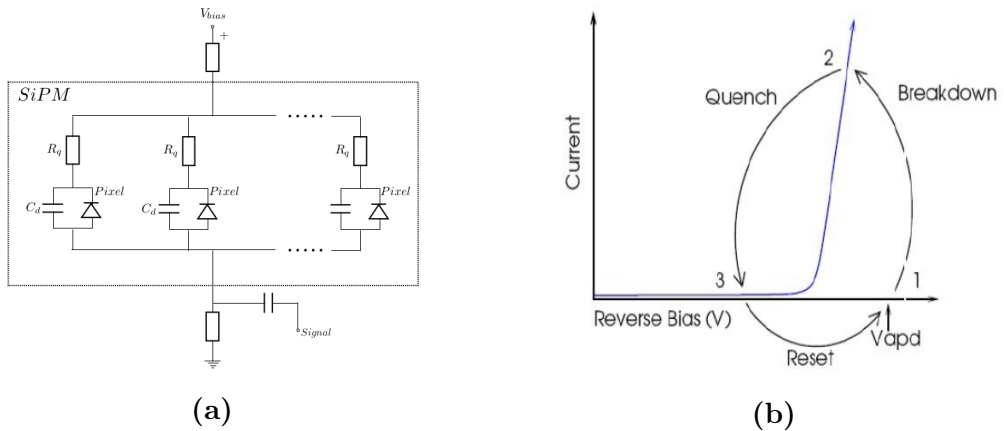


Figure 3.13 – (a) Electronic scheme of a SiPM and (b) output current of a SiPM as a function of the reverse voltage. As shown, the quenching is an essential working mechanism of SiPMs [Sen17].

the reverse voltage seen by the diode below the breakdown voltage. Then, the current through the diode vanishes and the bias voltage is reset. This behaviour is schematically shown in Figure 3.13b. The voltage after photon detection is characteristic of a RC circuit, described by the equation:

$$V(t) = V_{bias} \left(1 - e^{-t/\tau}\right) \quad (3.12)$$

where τ is the recovery time constant of the system, given by $\tau = C_d \cdot R_q$. In section 4.2 the capacitance C_d and the quenching resistance R_q are measured to obtain the recovery time constant extrapolated from both.

The SiPM gain (typically of the order of 10^6) is defined as the number of e-h pairs produced when a pixel is fired. This can be measured from the SiPM single photon spectrum (SPS), which is the spectrum obtained when the SiPM output signal is integrated. The measurement of the SPS and the calculation of the gain is presented in section 4.2. It has to be taken into account that the SiPM gain is highly dependent on temperature,

3.2. TRITIUM DETECTOR

which cannot be controlled to less than 1°C in the final location of the TRITIUM monitor. Therefore, a gain stabilization method was implemented to compensate for temperature changes. This method is detailed in section 4.2.

An important parameter for SiPMs is the photon detection efficiency (PDE), defined as the probability of recording the electrical pulse produced by a photon that hits the SiPM. The PDE of a SiPM depends on three different parameters: the fill factor (FF), which is the ratio between the active area of the SiPM and its total area, the quantum efficiency (QE), which is the probability of producing a photoelectron when a photon hits the SiPM and the probability, P_{av} , that an avalanche is produced. Thus,

$$PDE = FF \times QE \times P_{av} \quad (3.13)$$

Likewise PMTs, SiPMs may produce dark current that depends on temperature. The dark current signal is identical to that of a single photon, so it cannot be discriminated. Therefore, it is essential to determine the magnitude of the dark current in the TRITIUM detector.

Avalanche electrons in a pixel can emit secondary optical photons⁶. These optical photons can reach other pixels, producing new avalanches. This effect, called optical cross-talk, produces photoelectrons that add to those truly induced by incident photons, and hence leads to an overestimation of the number of photons detected. The probability of producing an optical crosstalk event depends on the number of electrons produced in the avalanche (gain) and, therefore, on temperature and overvoltage. This probability is typically less than 10% at the overvoltage recommended at 25°C by the manufacturer.

⁶Around 20 secondary optical photons are emitted in each pixel for gains of the order of 10^6 [Spi97]

Due to imperfections existing in the cristal lattice of a SiPM, called traps, an electron of an avalanche can be captured and released after a characteristic time, τ_a . If this characteristic time is longer than the pixel recovery time, typically 3τ , this electron can trigger a new avalanche which will be seen as a new event. These events, called afterpulses, are often emitted around $1 \mu\text{s}$ after the incident photon pulses. The afterpulse probability was not measured since it is not relevant for the TRITIUM detector because SiPM are read out in coincidence within 10 ns time. The afterpulse probability is thus negligible since it happens about $1 \mu\text{s}$ after the SiPM output pulse.

The initial SiPM candidate for the TRITIUM detector and the one which was characterized in this thesis is the model S13360-1375 from Hamamatsu Photonics [Ham16b], which properties are given in Table 3.3. This model was mainly chosen due to its large pixel size, $75 \mu\text{m}$, which implies high PDE and gain. This SiPM model was later replaced by the model S13360-6075 from Hamamatsu Photonics [Ham16d], the properties of which are also listed in Table 3.3. The only difference between this model and the first is its larger active area ($6 \times 6 \text{ mm}^2$) that allows to read more scintillating fibers but at the price of a higher dark count rate (typically 2 Mcps).

The parameters quoted in Table 3.3, are typical values provided by the manufacturer. They can vary from one SiPM to another of the same model. Thus, it is necessary to measure them. Some of these measurements are reported in section 4.2. This SiPM was also chosen because, as it can be observed in Figure 3.14, its maximum PDE is reached at $\lambda_{p,SiPM} = 450 \text{ nm}$, which is very close to the peak of the emission spectrum of the scintillating fibers used, $\lambda_{p,fiber} = 435 \text{ nm}$.

Although the TRITIUM detector uses SiPM arrays, the characterization was carried out at the level of a single SiPM to mesure the SiPM parameters and to test the gain control method.

3.2. TRITIUM DETECTOR

Parameter	S13360-1375	S13360-6075
Series	S13360	S13360
Model	1375	16075
Pixel Pitch (μm)	75	75
Effective photosensitive area (mm^2)	1.3×1.3	6.0×6.0
Number of pixels	285	6400
Fill factor	82%	82%
Refractive index of windows material	1.55	1.55
Operating temperature range ($^\circ\text{C}$)	$[-20, 60]$	$[-20, 60]$
Spectral response range, λ (nm)	[320, 900]	[320, 900]
Peak sensitivity wavelength, λ_p (nm)	450	450
PDE (%)	50	50
Dark counts, Typical/Maximum (kcps)	90/270	2000/6000
Terminal capacitance, C_t (pF)	60	1280
Gain	$4 \cdot 10^6$	$4 \cdot 10^6$
V_{BD} (V)	50.97	53
Cross talk probability(%)	7	7
Temperature coefficient (mV/ $^\circ\text{C}$)	54	54

Table 3.3: Characteristics of SiPM S13360-1375 and S13360-6075 from Hamamatsu Photonics [Ham16b].

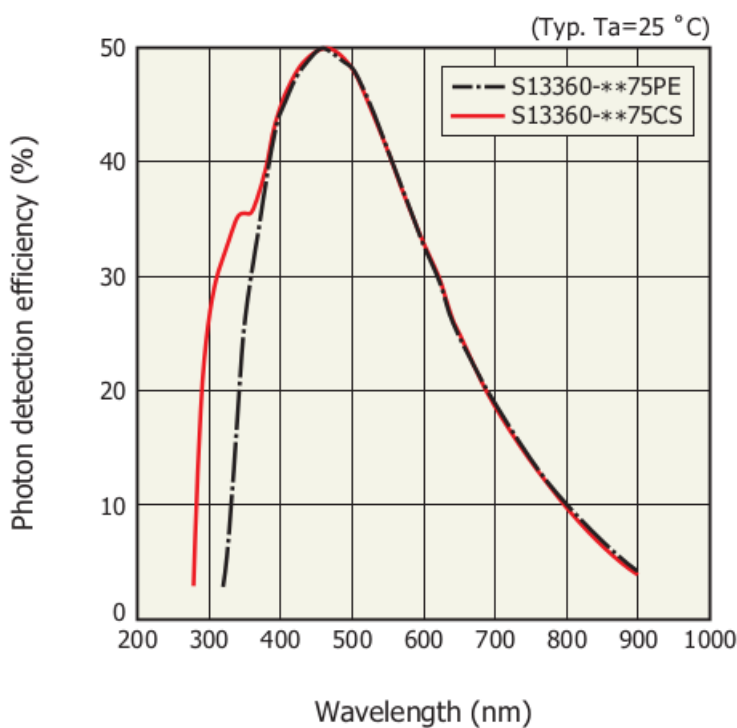


Figure 3.14 – PDE spectrum for SiPM S13360-**75 models [Ham16b].

3.2. TRITIUM DETECTOR

3.2.3.3 Photosensors in TRITIUM

Two different types of photosensors are proposed for the TRITIUM monitor, PMTs and SiPM arrays. Each type of photosensor has advantages and disadvantages and must be tested to determine the most suitable option. PMTs are used in the TRITIUM prototypes developed by the Aveiro experimental group while SiPM arrays are used in the TRITIUM prototypes developed at IFIC.

The IFIC group has chosen SiPM arrays as photosensors for their advantages over PMTs, which are compactness and robustness, necessary to work during several years without supervision, larger efficiency for detection of photons in the visible range and more economical price of both photosensors and electronics.

3.2.4 Electronics

In this section, the PETsys electronics for SiPM arrays and the electronics for single SiPM and PMT characterization are described. For the final TRITIUM prototype there are two different proposals for the DAQ system: the PETsys system and an specific electronic system developed by Aveiro group to read the TRITIUM monitor with PMTs. This electronics is described in Appendix D.

3.2.4.1 Electronics for PMTs

PMTs are used in the TRITIUM experiment for two main objectives. On the one hand, to determine the amount of incident photons that reach the PMT photocathode and, on the other hand, to measure the energy spectrum of tritium events in the laboratory prototypes.

To determine the amount of photons reaching the photocathode, the PMT should work without gain which is a source of uncertainty. For this, the bias circuit shown in Figure 3.10 was employed. As electrons are not multiplied, the output current of the photosensor is very small (currents in the nanoampere range). This output current was read out by a Keithley 6487 Picoammeter/Voltage Source [Keia].

The energy of the events was measured using PMTs biased with the voltage divider shown in Figure 3.9. A scheme of the electronics for different number of PMTs employed is shown in Figures 3.15a, 3.15b and 3.15c.

The PMTs were powered by a TC 952 High Voltage Supply from Tennelec [SAS] and a HV Power Supply N 1130-4 from Wenzel Elektronik [Wen]. The PMT output signals were split by an analog FAN IN-OUT model 740 from Philips Scintific [Phi] to feed the amplification and time coincidence lines. The amplification line consists of a preamplifier, model 9326 FAST PREAMP from ORTEC [ORTd], which gives an output signal with a height proportional to the charge of the input pulse and of an amplifier, model 575A or 671 from ORTEC [ORTb, ORTc], which produces a Gaussian shaped output signal. An example of the 575A module output signal is shown in Figure 3.17, green color.

The time coincidence line consists of the following branches,

1. A constant fraction discriminator, either module CF8000 from ORTEC [ORTe] or model 84 from CAEN [CAE91], which produces a logic signal of -1.2 V height and of 240 ns width when a given threshold is exceeded.
2. In the case of two or four PMTs, a coincidence module, either model 465 from LeCroy [LeC] or Coincidence Type N6234 from CERN-NP [CERa], used to generate an output signal of -1.4 V height and of 20 ns width when both inputs are in time coincidence.

3.2. TRITIUM DETECTOR

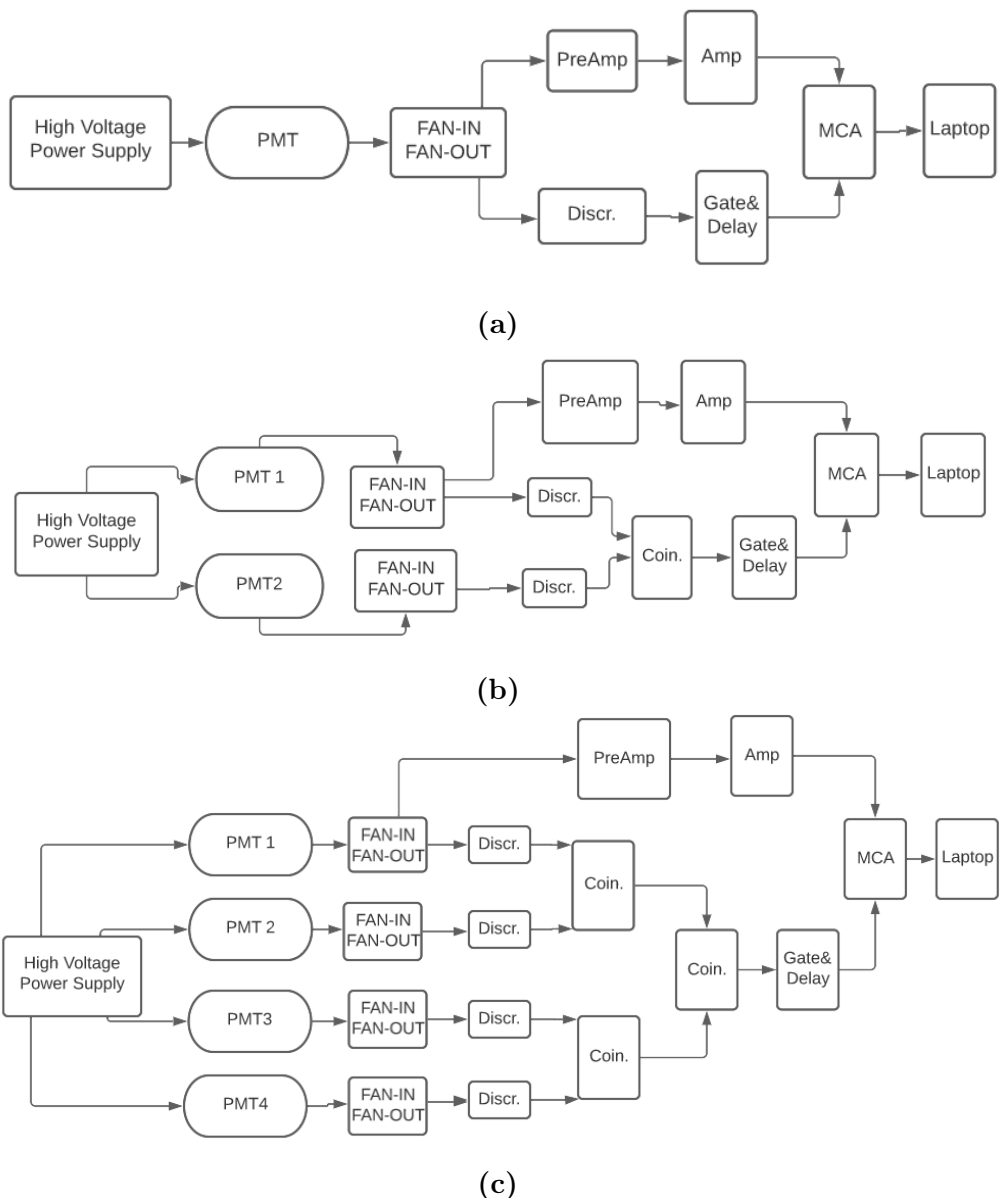


Figure 3.15 – Electronic schemes employed for measuring with a) one PMT, b) two PMTs in coincidence and c) four PMTs in coincidence.

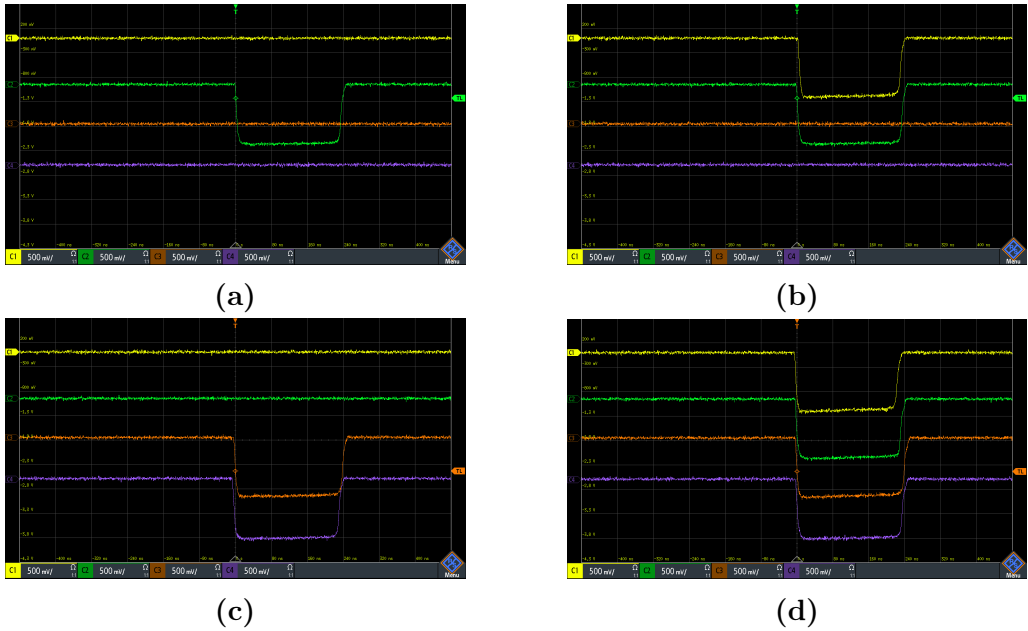


Figure 3.16 – Different possibilities for time coincidence of four PMTs. Case d) shows coincident events.

3. In the case of four PMTs, an additional coincidence stage. In Figure 3.16, time coincidences of 4 PMTs are shown. Case d) shows coincident events.
4. A Gate and Delay Generator, model 416A from ORTEC [ORTa], which produces a positive logic signal 8 V height and $2 \mu\text{s}$ width. This module delays the time windows until they overlap with the energy signal as shown in Figure 3.17.

The energy signal and the coincidence signal, shown in Figure 3.17, are recorded by the MCA, model 8000D from AMPTEK [Amp].

3.2. TRITIUM DETECTOR



Figure 3.17 – Amplified signal and logic gate (input signals of the MCA).

3.2.4.2 Electronics for SiPMs

The TRITIUM SiPMs are Hamamatsu SiPM arrays of 4×4 , model S13361-6050 [Ham16e]. The electronics chosen to acquire and analyze the output signals of these SiPM arrays is PETsys [PET], displayed in Figure 3.18. PETsys is a commercial readout system designed for Hamamatsu SiPM arrays which includes QDCs⁷ and TDCs⁸, providing time and energy digitization of up to 1024 SiPM channels.

TRITIUM is a modular detector which sensitivity could be improved by adding more modules and, therefore, its readout electronics should be scalable. This requirement is fulfilled by PETsys since it has an additional module, called Clock and Trigger, with which up to 16 different PETsys basic boards can be read out in parallel. This gives to PETsys a capacity of reading up to 256 SiPM arrays.

⁷charge-to-digital converter

⁸time-to-digital converter



Figure 3.18 – Different parts of PETsys system [PET].

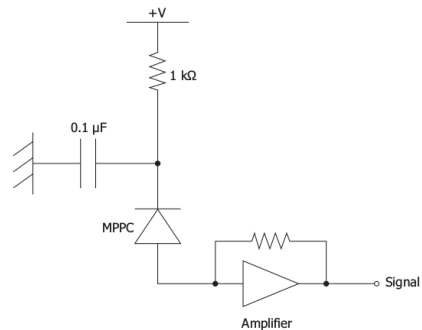
The PETsys software is based on C++ and Python scripts that drive the main tasks required, such as time coincidence options between SiPM arrays or energy discrimination. This software is open source, giving the possibility to modify the current scripts or to develop others with additional functions. PETsys has a time resolution better than 30 ps which is one of the best time resolution of commercial systems available. Its price is around 10 $e/\text{channel}$, which is cheaper than similar electronic systems. The PETsys system has the ability to monitor the temperature of the SiPM arrays and ASICS. In PETsys, the stabilization method of the SiPM gain, reported in section 4.2, can be implemented.

Some characterization measurements were carried out using the PETsys system to verify that the system works properly but the SiPM characterization was carried out at the level of a single channel (individual SiPM). The reason is that the output information of PETsys is already

3.3. THE WATER PURIFICATION SYSTEM



(a)



(b)

Figure 3.19 – a) Electronic board used in the SiPM characterization. **b)** Electronic scheme on which this PCB is based.

integrated and digitized, so it does not allow SiPM to be calibrated. Therefore, to characterize a SiPM, a PCB shown in Figure 3.19 was designed to bias the SiPM and to amplify its output signal.

This PCB was powered at ± 6 V using a ISOTECH IPS-4303 voltage source [ISO] and the SiPM was biased by a KETHLEY 6517B electrometer [Keib]. The output signal was connected to a LeCroy WaveRunner 625Zi oscilloscope [Tel17] that recorded the data which were subsequently analyzed using ROOT.

3.3 The Water Purification System

3.3.1 Objectives

The water samples to be measured by the TRITIUM detector are taken directly from the Tagus river, in a site 4 km downstream from the water discharge of Almaraz NPP. These samples contain minerals, organic depos-

its, and living matter, which should be removed for the following reasons:

1. The mean free path of tritium electrons in water is around $5 \mu\text{m}$ and even less in solid materials. If the analyzed water contains particles that may deposit on the fibers, a layer of dirt could be formed, preventing tritium decay electrons from reaching the fibers and reducing drastically the tritium detection efficiency. Therefore, the detector must be kept pristine.
2. The tritium monitor does not have any spectrometric capability that could be used to distinguish tritium from other radioactive elements present in water.

The water purification system was designed to remove organic matter and mineral particles with a size over $1 \mu\text{m}$ without modifying the tritium level in water.

3.3.2 Design of the Water Purification System

The requirements of the water purification system are:

1. A high degree of purification of the water sample extracted from the dam, reducing its conductivity by approximately two orders of magnitude (from $1000 \mu\text{S}/\text{cm}$ to $10 \mu\text{S}/\text{cm}$).
2. Low maintenance cost and manpower.
3. Remote management of the system.

The LARUEX laboratory has designed and built the water purification system, which scheme is shown in Figure 3.20.

3.3. THE WATER PURIFICATION SYSTEM

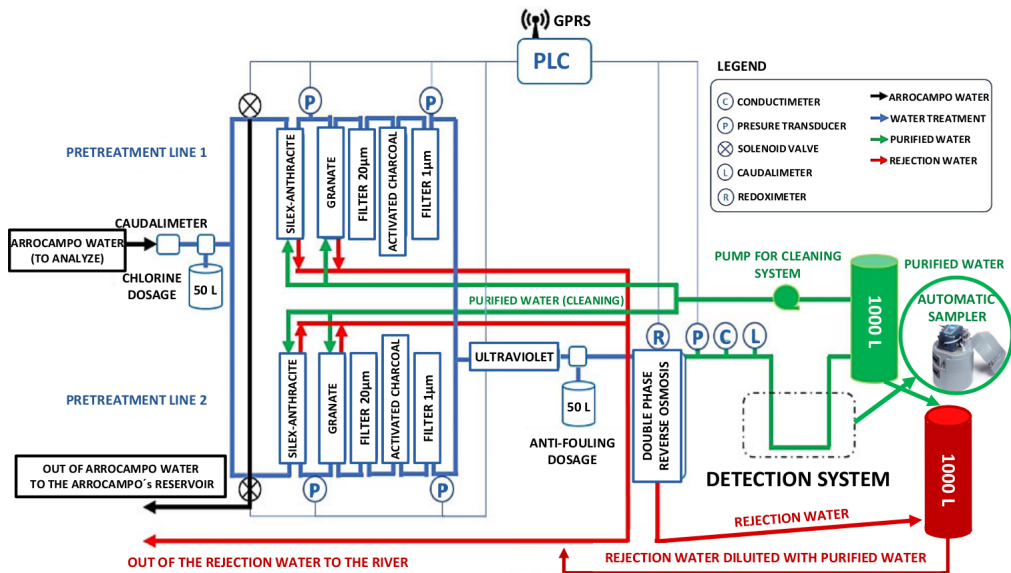


Figure 3.20 – Scheme of the water purification system of TRITIUM.

This system is installed in the Arrocampo site and consists of four different stages:

1. The raw water from the Tagus river passes through two different filters, the first made of silex-anthracite and the second of garnet, with which a rough filtering is made (the largest particles are eliminated). This system has two identical parallel lines and implements a self-cleaning function by injecting purified water in the opposite direction.
2. The outlet water from the first stage, called fine filtration stage, passes through a $20 \mu\text{m}$ filter (formed by a synthetic mesh) and activated charcoal filters (one per line) that remove chlorine and iron particles present in the water.
3. The outlet water from second stage goes into a super-fine filtering stage consisting of a $1 \mu\text{m}$ filter, made of a dense polypropylene mesh and of UV lamps. The filter removes all the particles with the diameter

larger than $1 \mu\text{m}$ and the UV lamps sterilize the water, eliminating bacteria and microscopic life.

4. Finally, the water is introduced into the last stage that consists of a double-phase reverse osmosis which reduces the conductivity of the water to about $10 \mu\text{S}/\text{cm}$.

As a result of the purification process, besides the pure water that is introduced into the TRITIUM detector, a rejection water is produced, which contains the particles removed from the sample. The water purification system is able to process up to $0.850 \text{ m}^3/\text{h}$ with a single operating line or $1.480 \text{ m}^3/\text{h}$ with both lines.

The software used for remote controlling the water purification system is the Siemens Programmable Logic Controller (Siemens PLC), that gives information such as the state of the valves, the reading of pressure probes and the amount of ultrapure water production in real time. The appendix B contains several pictures of different parts of this system.

3.4 The Background Rejection System

The aim of the background rejection system is to reduce the radioactive and cosmic background that affects the TRITIUM monitor. The TRITIUM project follows the ALARA principle for the tritium activity measurement, that is, to measure a tritium activity "as low as reasonably achievable". The detection limit of tritium activity is set by the uncertainty of the background measured by the TRITIUM detector, since tritium activities below this uncertainty cannot be resolved. Therefore, the background must be reduced as much as possible. The total uncertainty is given by the rms of the statistical σ_{st} and systematic uncertainties σ_{sys} . Because of the Poissonian nature of the process, the statistical uncertainty is given by the square root of the

3.4. THE BACKGROUND REJECTION SYSTEM

total activity A_m which can be reduced by minimizing the background.

$$\sigma_T^2 = \sigma_{st}^2 + \sigma_{sys}^2; \quad \sigma_{st,bac} = \sqrt{A_{m,bac}} \quad (3.14)$$

The background rejection system of the TRITIUM monitor suppresses the background of the TRITIUM detector, reducing the total uncertainty.

The background of TRITIUM has two different sources. On the one hand, the radioactive elements present in the Earth crust, mainly ^{40}K and elements from the four natural radioactive series, listed in Table 3.4. On the other hand, the cosmic ray radiation. The primary cosmic radiation, of extra-terrestrial origin, is composed of high-energy particles, mainly protons and α particles, which interact with the Earth's atmosphere and generate a shower mainly composed by muons, electrons, photons and neutrons. Cosmic radiation depends on several parameters like the longitude, latitude, and the solar activity cycle. The spatial distribution of cosmic rays, mainly muons, follows a $\cos^2(\theta)$ distribution with the zenith angle, θ .

Mass Num.	Series	Primary	Half life (y)	Final
4n	Thorium	^{232}Th	$1.41 \cdot 10^{10}$	^{208}Pb
4n+1	Neptunium	^{237}Np	$2.14 \cdot 10^6$	^{209}Pb
4n+2	Uranium-Radium	^{238}U	$4.51 \cdot 10^9$	^{206}Pb
4n+3	Uranium-Actinium	^{235}U	$7.18 \cdot 10^8$	^{204}Pb

Table 3.4: Classification of natural radioactive series [The96, Eva95]. The information displayed for each radioactive series is, the name of the series, the primary and final element, and the half-life of the primary element.

Two different techniques are employed for background suppression:

1. The soft background component, with energy below 200 MeV, is stopped by a lead castle, described in section 3.4.1.
2. The hard background component, with energy greater than 200 MeV,

is harder to stop and the technique employed is the use of a cosmic veto in anti-coincidence with the TRITIUM detector, reported in section 3.4.2.

3.4.1 Passive Shield (Lead)

The soft background component is suppressed by a lead shield inside which the TRITIUM detector is placed. This lead shield is efficient for suppressing particles with energies below 200 MeV, that originate from the Earth's natural radioactivity and the soft component of cosmic radiation. This lead shield consists of 158 low intrinsic radioactivity lead bricks of 25 mm thickness. The bricks are chevron shaped, as shown in Figure 3.21, specially designed for a perfect fit and easy assembly. As can be seen in Figures 3.22a and 3.22b, these lead bricks are arranged in two layers with a total thickness of 50 mm.



Figure 3.21 – Lead bricks.

An aluminium structure capable of supporting the total weight of 2.4 tons of lead bricks, shown in Figure 3.23, was designed by the Mechanical Engineering Department of the CENBG.

The internal room of the lead shield is divided into two parts, as indicated in Figure 3.23. The larger one has internal dimensions of $90.5 \times 41 \times 51$ cm³ and is used to place the TRITIUM detector. The smaller one,

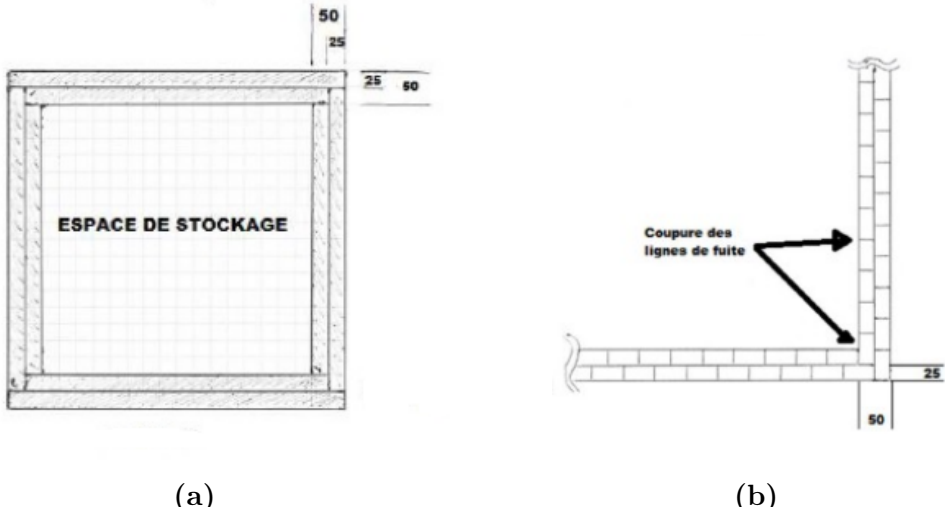


Figure 3.22 – Two layers for the lead bricks of the shield.

of dimensions of $33 \times 41 \times 51 \text{ cm}^3$, contains the DAQ system of the detector. The external dimensions of the lead shield are $148 \times 60 \times 70 \text{ cm}^3$ and its total weight is 2.5 tons.

3.4.2 Active Shield (Cosmic Veto)

As hard radiation cannot be stopped by a moderate lead thickness, cosmic vetos are employed, which consist of two complementary detectors in coincidence that reject events simultaneously detected in both of them. As shown in Figure 3.24, the two complementary detectors are placed one above and the other below the TRITIUM detector. The distance between both detectors is 34.2 cm, just enough to enclose the TRITIUM IFIC prototype.

A hard cosmic event crossing simultaneously both cosmic detectors is sketched in figure 3.25a. Each cosmic detector has two photosensors, so the electronic configuration given in Figure 3.15c is used to make time coincidence. The TRITIUM detector is read out in anti-coincidence with the

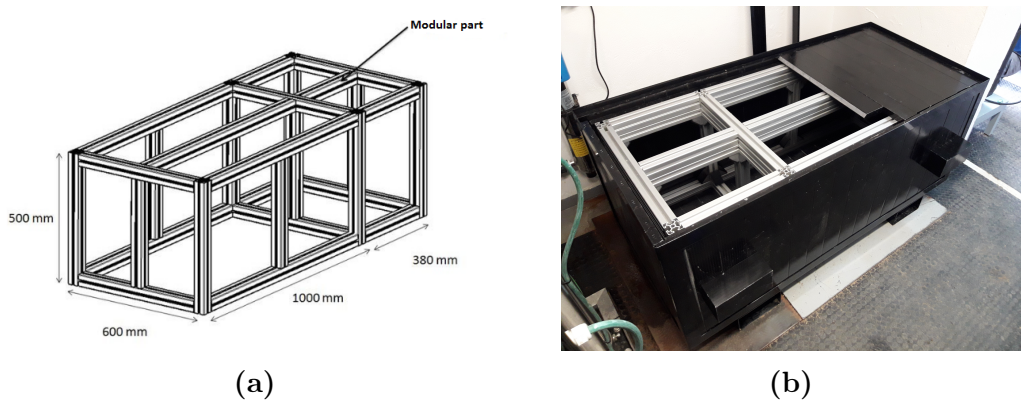


Figure 3.23 – a) Scheme of the aluminium structure of the shield. b) The lead shield partially mounted.

cosmic veto to reject the hard cosmic events from the tritium measurements. The expected hard cosmic rate at sea level for muons is $7 \times 10^{-3} \text{ cm}^{-2}\text{s}^{-1}\text{sr}^{-1}$ [Zyl20, Sag12], as shown in Figure 3.26. As time coincidences are triggered by logic gates of about 10 ns, the probability of recording two different hard cosmic events in coincidence is negligible.

The vetos are made of a plastic scintillator plates from Epic-Crystal [Epi20] which properties are given in Table 3.5 and its energy emission spectrum is displayed in Figure 3.27. The energy spectrum has a peak very close to that of the scintillating fibers used, so the same photosensors are used. The dimensions of the scintillator plates are $45 \times 17 \text{ cm}^2$ with a thickness of 1 cm. They are wrapped by three different layers, PTFE sheet, aluminium leaf and black tape, as shown in Figure 3.28. These layers prevent external photons from reaching the plastic scintillator and photons generated by the scintillator from escaping before reaching the photosensor. Two $2.5 \times 2.5 \text{ cm}^2$ windows are made on the wrapping for coupling the photosensors.

The solid angle subtended by each veto plate on the other is $\omega = 0.5434 \text{ sr}$ and the area is 765 cm^2 . Considering the expected hard cosmic

3.4. THE BACKGROUND REJECTION SYSTEM

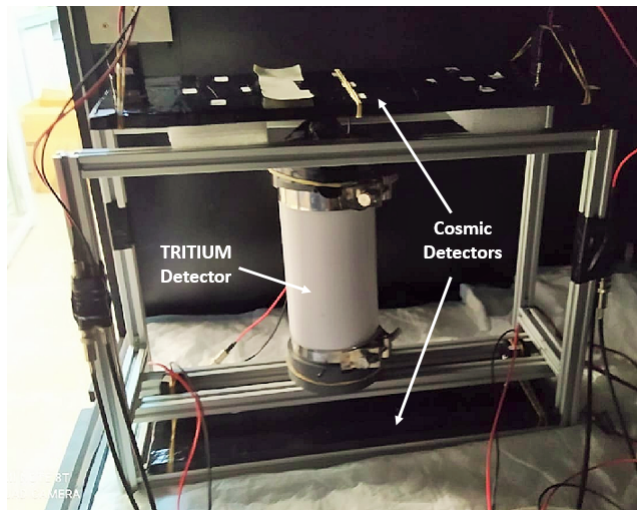


Figure 3.24 – Cosmic veto and Tritium-IFIC-2 prototype inside the aluminium mechanical structure developed at IFIC.

rate of $7 \times 10^{-3} \text{ cm}^{-2}\text{s}^{-1}\text{sr}^{-1}$ at sea level the expected hard cosmic ray rate measured is 2.909 Hz, which is used in section 4.4 to determine the efficiency of the veto.

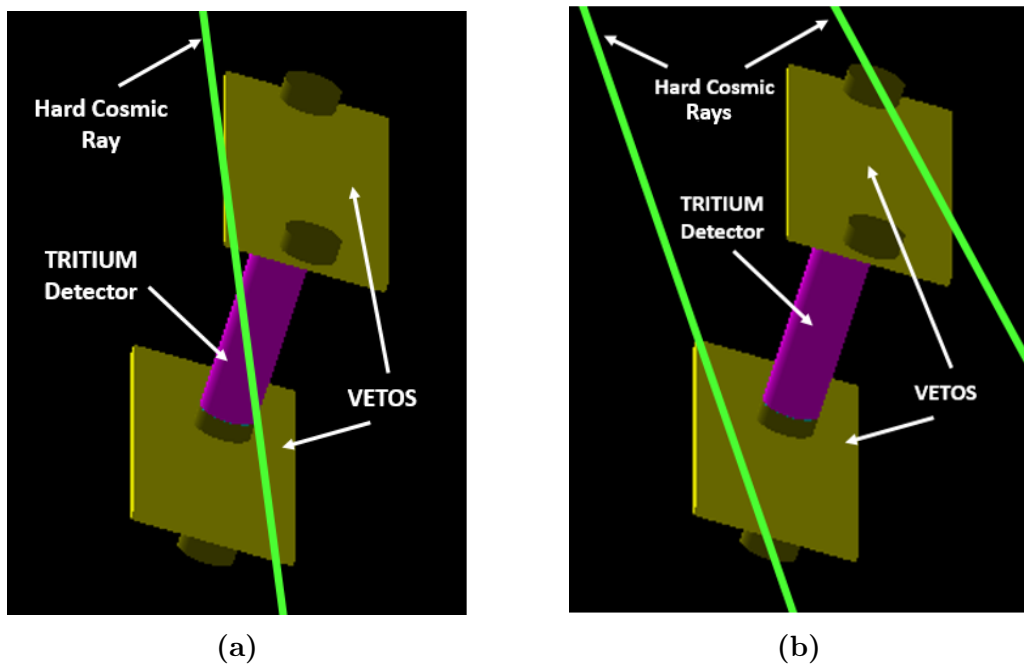


Figure 3.25 – Hard cosmic events detected with the cosmic veto of TRIUM: a) Real coincidence event. b) Random coincidence event.

Property	Value
Base material	Polystyrene
Growth method	Polymeric
Density (g/cm ³)	1.05
Refractive index	1.58
Soften temperature (°C)	75-80
Light output (anthracene)	50-60%
H/C ratio	1.1
Emission peak (nm)	415 (blue)
Decay Time (ns)	2.4
Hygroscopic	No

Table 3.5: Properties of the plastic scintillator from Epic-Crystals [Epi20].

3.4. THE BACKGROUND REJECTION SYSTEM

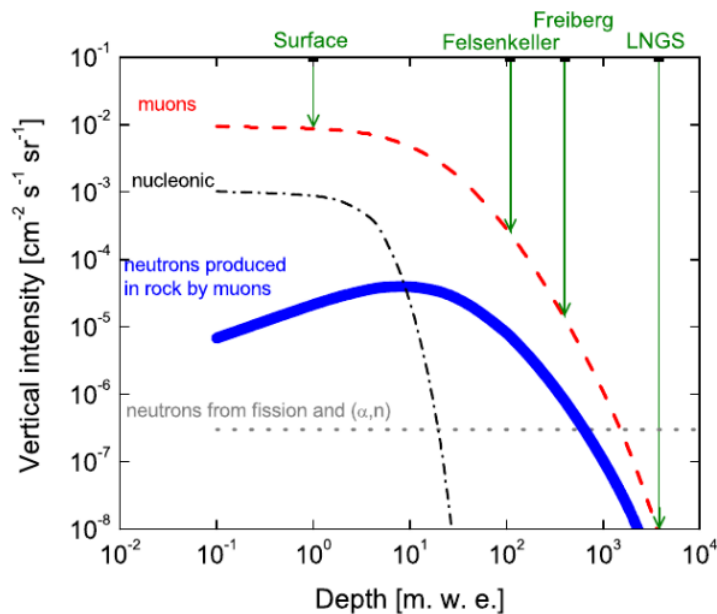


Figure 3.26 – Hard cosmic muon rate at different depths [Szu15].

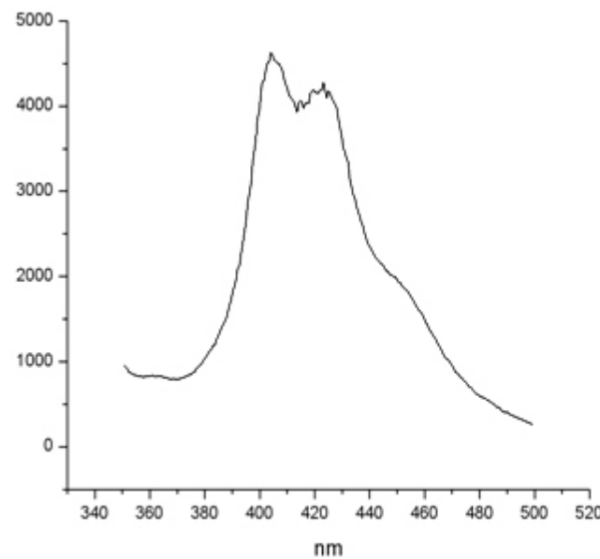


Figure 3.27 – Emission spectrum of the plastic scintillator from Epic-Crystals [Epi20].

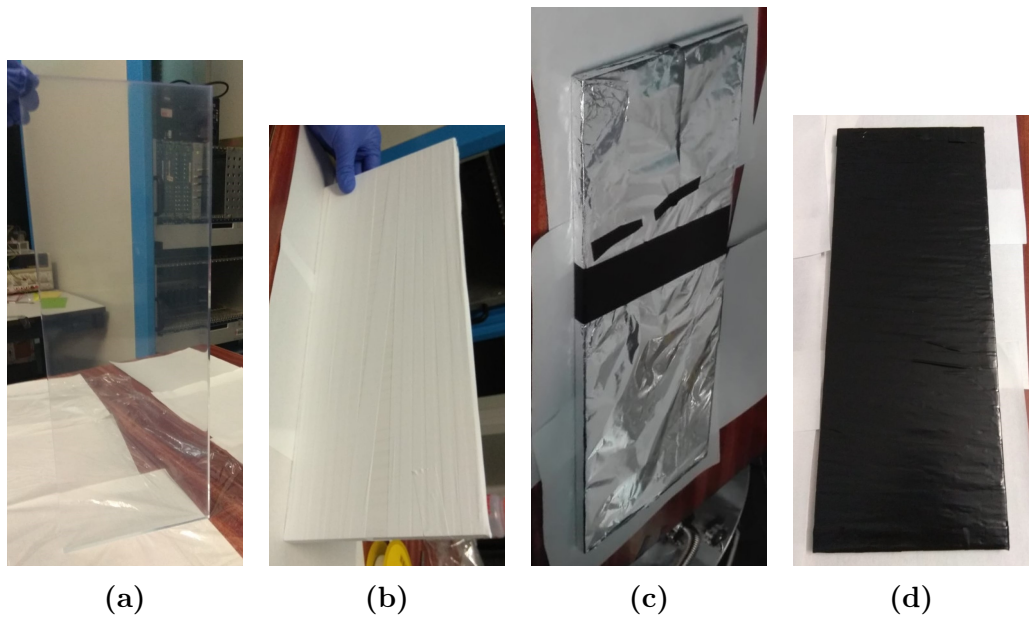


Figure 3.28 – Different layers used to wrap the cosmic veto detectors. a) Scintillator without wrapping. b) PTFE wrapping. c) Aluminium wrapping. d) Black tape wrapping.

3.4. THE BACKGROUND REJECTION SYSTEM

Chapter 4

TRITIUM Monitor R&D

The characterization of the different parts of the TRITIUM monitor, including scintillating fibers, SiPMs, the water purification system and the background rejection system, are described in this chapter. This characterization is crucial to understand the behaviour of the different parts and the measurement results. Furthermore, several developments were made to improve parameters of the TRITIUM monitor components to enhance its sensitivity to low levels of tritium in water.

4.1 R&D for the Scintillating Fibers

Measurements of the plastic scintillating fiber parameters relevant for tritium detection, such as collection efficiency and systematic uncertainty of the measured tritium activity are reported in this section. The TRITIUM detector is composed of thousands of scintillating fibers which have to be prepared. Various mechanical and electronic devices were developed to prepare a large number of fibers simultaneously.

4.1.1 Preparation of Scintillating Fibers.

The preparation of scintillating fibers consists in cleaving, polishing and cleaning. A surface-conditioning of the scintillating fibers was implemented to improve their photon collection efficiency. These methods are described in the following subsections.

4.1.1.1 Cleaving of Scintillating Fibers.

The first step in the TRITIUM design was to choose the fiber length and the fiber diameter (1 or 2 mm) for which the signal of tritium events is optimized. For a given active area, the longer the fibers, the smaller the number of photosensors needed. However, in long fibers photons are reflected on their boundaries many times before reaching the photosensors, which may produce a deterioration in the tritium signal. To determine the optimal fiber length, several simulations, described in section 6.2.3, were carried out using Geant4 [GEA]. It was concluded that the optimal fiber length for measuring tritium in water is around 20 cm, which is the fiber length used in the TRITIUM prototypes developed at IFIC and for most of the characterization studies carried out in this thesis. As the manufacturer [Saia] delivers 1 m long fibers, an effective cleaving technique had to be developed with stringent requirements on the cleaving quality, since this greatly affects the transmission of photons and, consequently, the detection efficiency of the TRITIUM detector. The cleaving must be done perpendicular to the fiber axis and with small uncertainty in the cleaving position to enable optimal coupling of the fiber to the photosensor. It is also important that the fiber integrity be preserved, without cracks or deformations that may contribute to photon loss.

Cleaving plastic fibers is a current challenge. There are many different techniques such as milling, laser cleaving, focused-ion-beam, blade cleaving, etc. The blade cleaving technique was chosen because of its mech-

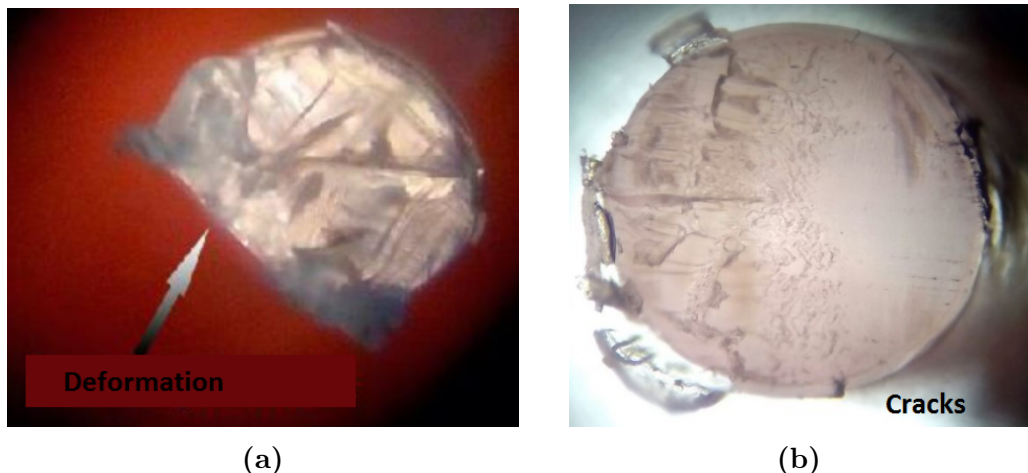


Figure 4.1 – Results of using commercial techniques for cleaving the scintillating fibers a) Fiber end deformation b) Fiber end cracks. Pictures taken with a microscope PB 4161 from EUROMEX.

anical simplicity and because, unlike other techniques, it preserves the integrity of plastic fibers. Many commercial devices based on blade cleaving, such as the one provided by Thorlabs with a diamond tipped blade [Tho06], or guillotines designed for industrial fiber optics [Ind], were tested in an comprehensive study with unsuccessful results [Sol17]. As it can be seen in Figure 4.1, commercial techniques produce deformations, cracks and imperfections so they do not yield results with the quality standard required for the detector. Because commercial devices are not suitable for polymer fibers, a cleaving device, shown in Figure 4.2, was designed and built at IFIC laboratory. This device consists of an aluminium plate endowed with fourteen grooves to accommodate the fibers. A thin razor blade attached to a mobile piece is used to cleave the fibers. The perpendicular cleave, which is one of the requirements, can be ensured since the moving piece to which the blade is attached is placed perpendicular to the fiber axis. The blade used is a typical commercial razor blade, of 0.1 mm thickness, which is the thickness that gave the best results. The blade was positioned with a 5° inclination with respect to the horizontal axis since it was found in

4.1. R&D FOR THE SCINTILLATING FIBERS

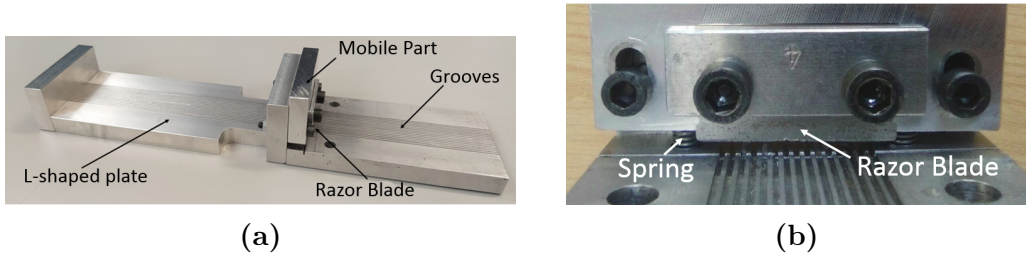


Figure 4.2 – Plastic fiber cleaver developed in TRITIUM project.

several studies that this helps to obtain a less aggressive and cleaner cleave [SR15, Law06]. As it can be seen in Figure 4.3, the integrity of the fiber is preserved and no deformation is observed. However, it can be noticed some tears on the clad, but it is reported in section 4.1.2.2 that these tears affect negligibly the photon collection.

An additional parameter that could affect the cleaving quality of the fiber ends is the temperature of both fiber and blade. A study was carried out in which both were subject to different temperatures, from room temperature to 110°C. No significant conclusions were obtained [Sol17]. Thus, the cleaving process was carried out at room temperature to make the cleaving process easier.

A second L-shaped aluminium plate with grooves was attached to the first one (see Figure 4.2) to set accurately the length of the fibers to 200 mm, with an uncertainty of ± 1 mm.

4.1.1.2 Polishing of Scintillating Fibers.

As can be seen in Figure 4.3, a slightly darkened zone at the bottom of the fiber is observed. This is an unavoidable effect of the cleaving process on plastic fibers, which produces unpolished end-surfaces. To polish the end-surfaces, a method implemented by Thorlabs was applied [Tho06].



Figure 4.3 – Fiber end after cleaving process using the home-made cleaver. Pictures taken with the microscope PB 4161 from EUROMEX.

Manual Polishing Method.

The Thorlabs polishing method consists in rubbing the fibers ends with five different polishing papers made of aluminium oxyde grains with a decreasing grain size ($30 \mu\text{m}$, $20 \mu\text{m}$, $12 \mu\text{m}$, $5 \mu\text{m}$ and $0.3 \mu\text{m}$). To polish the fiber, this is placed into a polishing connector, shown in Figure 4.4, and a shape of an 8 must be outlined on each polishing papers during 2 minutes (approximately 120 movements).

The result obtained after polishing is shown in Figure 4.5b, where it can be noticed that the darkened zone has completely disappeared and the fiber end is uniform, which favors optimal coupling and transmision of photons of the scintillating fibers to the photodetectors.

Automatic Polishing Machine.

4.1. R&D FOR THE SCINTILLATING FIBERS

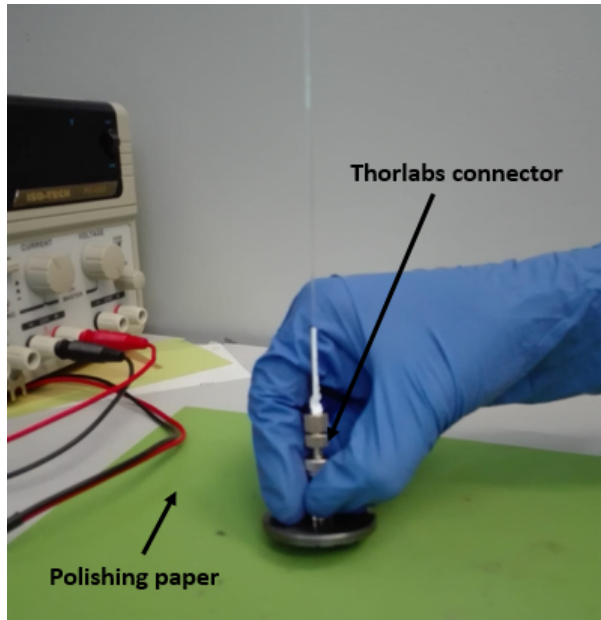


Figure 4.4 – Manual polishing method implemented by Thorlabs.

The main drawback of the manual polishing method is that it takes more than 10 minutes to polish a fiber. This implies an unaffordable time to polish the thousands of fibers needed for the TRITIUM detector (see section 5.4). For this reason, an automated polishing process was developed within this thesis work.

A machine was designed and built in the laboratory for automatically polishing up to one hundred plastic scintillating fibers at the same time. This machine is easily scalable to larger number of fibers. This automatic polishing machine, displayed in Figure 4.6, consists of two main parts:

1. A polishing table, shown in Figure 4.7a, where the fibers are polished. This is composed of two parts, a static part, to which the fibers are attached, and a movable part on bottom of the previous one, where the polishing papers are fixed. It was decided to move the polishing paper instead of the fibers to avoid damaging them.

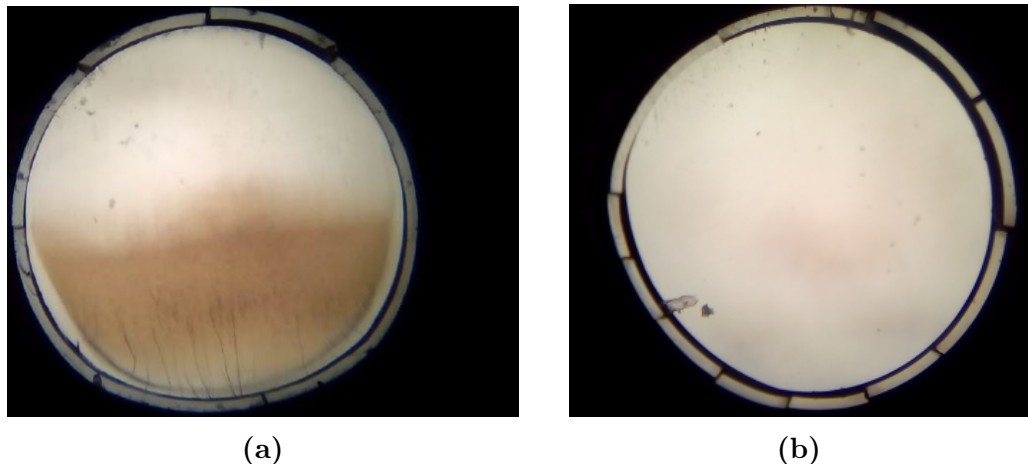


Figure 4.5 – Result of the polishing process. a) Fiber end after cleaving b) Fiber end after cleaving and manual polishing with Thorlabs technique. Pictures taken with the microscope PB 4161 from EUROMEX.

The static part that holds the fibers, shown in Figure 4.7a, consists of a plastic piece locked to the system by four vertical screws. There are two nuts on each screw used to set the relative height and the inclination of fibers relative to the polishing paper. This piece contains one hundred holes in which a hundred fibers are lodged.

As the fibers are too light (0.16 g) to make the necessary pressure on the polishing paper by gravity, a plastic belt and a piece of metal of about 1.5 g weight were attached to the individual fibers, as shown in Figure 4.7b, to increase their contact pressure, in a similar way as with manual polishing connectors.

The movable part of the polishing table consists of a flat PMMA plate of $18 \times 18 \text{ cm}^2$ to which the polishing paper is attached. This part is locked to a structure [IGU] that contains two horizontal screws, perpendicular to each other, which allow a movement in the horizontal plane, as shown in Figure 4.7c.

The polishing system contains several high accuracy switches, model DB1 6A250, shown in Figures 4.7a, 4.7c and 4.7d, which are used to



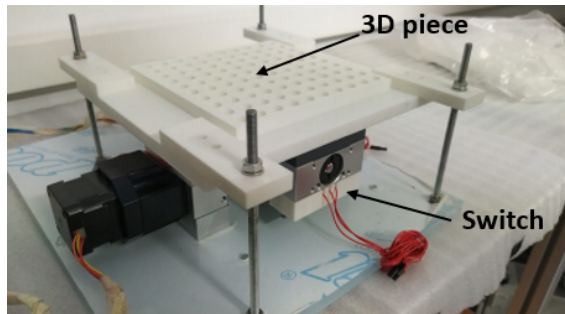
Figure 4.6 – Polishing machine developed for TRITIUM.

find the origin of coordinates when the system is reinitiated and to stop the movable part when the end of the path is reached.

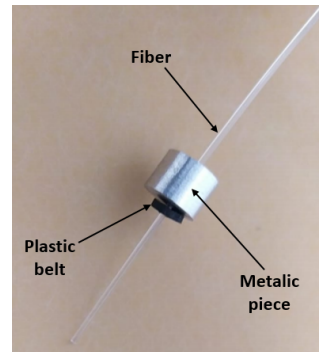
2. An Arduino-based electronics, shown in Figure 4.8, that controls the movement of the polishing paper. It consists of two stepper motors controlled by an Arduino UNO [ARD] that uses a CNC shield [OSO17].

The stepper motor is a type of DC motor in which a full rotation is divided into a number of steps that define the stepping angle. The stepper motors used for the polishing machine are model NEMA ST4209S1404-A [Nan06], with bipolar voltage of 2.77 V_{DC} , 1.33 A maximum current and a stepping angle of 0.9° (400 steps/rev). They can be operated with a position sensor for feedback control. These stepper motors are used to move the horizontal screws on which the PMMA plate that holds the polishing paper is attached.

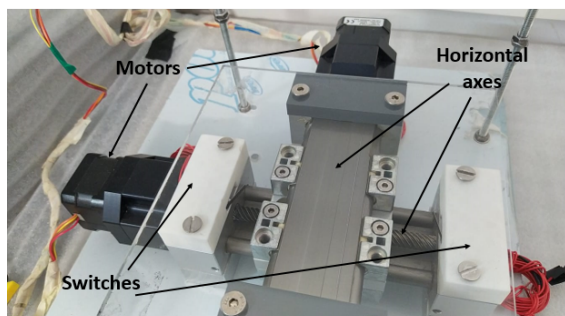
Two drivers are connected to the CNC shield, which limit the current



(a)



(b)



(c)



(d)

Figure 4.7 – Components of the fiber polishing machine. a) Polishing table. b) Fiber with ballast metal piece. c) Horizontal screws and PMMA plate. d) A movement switch with its cables inserted inside its holding piece.

4.1. R&D FOR THE SCINTILLATING FIBERS

supplied to the motors. Choosing the right drivers is crucial because overpowering the motors could damage them, while underpowering them would induce an inadequate stepping. Several drivers were successively tested: the driver Pololu A4988 (35 V, 2 A and 16 steps) [All11], the driver DRV8825 (45 V, 2.5 A and 32 steps) [Tex14] and the TMC2208 (35 V, 2.5 A and 256 steps, with more microstepping modes, which result in a more accurate and smooth movement) [Int19]. The last driver includes a StealthChop function that allows the driver to operate in silence mode for low motor velocities. The TMC2208 driver is the one used for the control of the stepper motors since it produce the most accurate and smooth movement. A cooling system, shown in Figure 4.8, was needed to ensure the correct operation of the polishing system. This consists of a copper heat sink in contact with both controllers and a fan, which prevents heat accumulation inside the electronics box. The cooling power can be improved by a PELTIER cell.

The polishing machine is controlled by a Raspberry Pi computer board [Ras] using the Universal G-code Sender software, a graphical interface based on the GRBL package [GRB]. In this software, there are several pre-programmed functions, such as "HOME" that finds the system origin of coordinates when it is turned on. The GRBL software loads the file containing the G-code that defines the 120 movements required for polishing.

Experimental Test.

The improvement of the light transmission of scintillating fibers due to the polishing process was tested with twenty uncladded scintillating fibers of 15 cm length. These fibers were arranged in a bundle that was coupled to two PMTs and read out in coincidence, as shown in Figure 4.9.

This experiment was carried out inside a light-tight box, to avoid external light. The spectra produced by background radiation before and

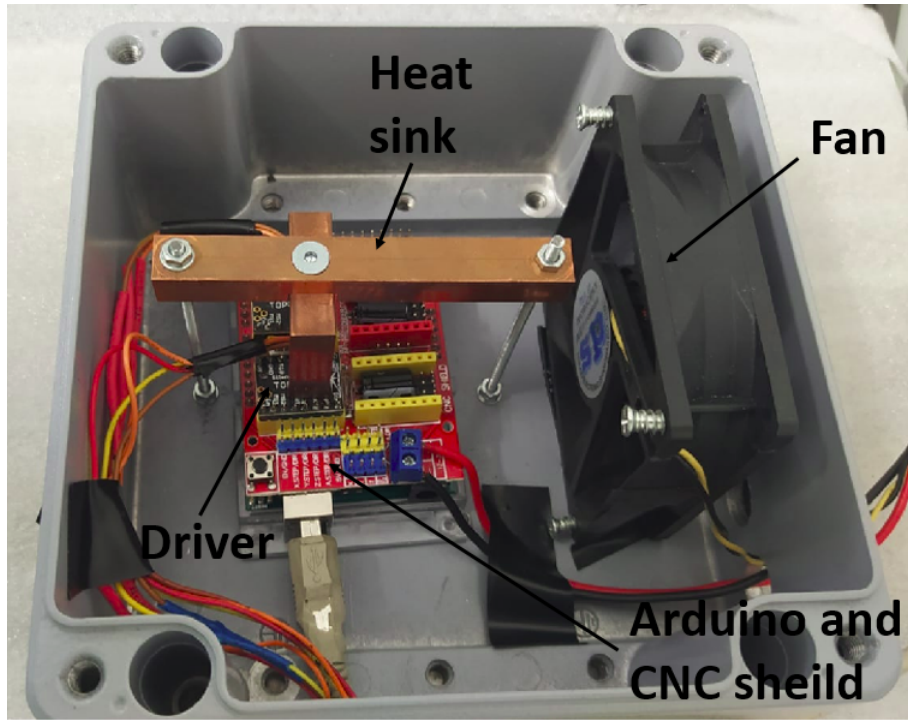


Figure 4.8 – Electronic system of Polishing machine.

after the polishing process are displayed in Figure 4.10. As it can be seen in this figure, the energy spectrum after applying the polishing process is shifted to the right, which means that the detected events have more energy than before the polishing process, more photons per event reach the PMTs. The improvement of the photon collection efficiency of the scintillating fibers is quantified by a parameter F defined as,

$$F = \frac{A_P}{A_{NP}} \quad (4.1)$$

where A_P and A_{NP} are the integrals of the energy spectra measured after and before the polishing process, respectively. The polishing results in a factor 2.2 improvement in light collection.

The test was repeated with two radioactive sources, an encapsu-

4.1. R&D FOR THE SCINTILLATING FIBERS

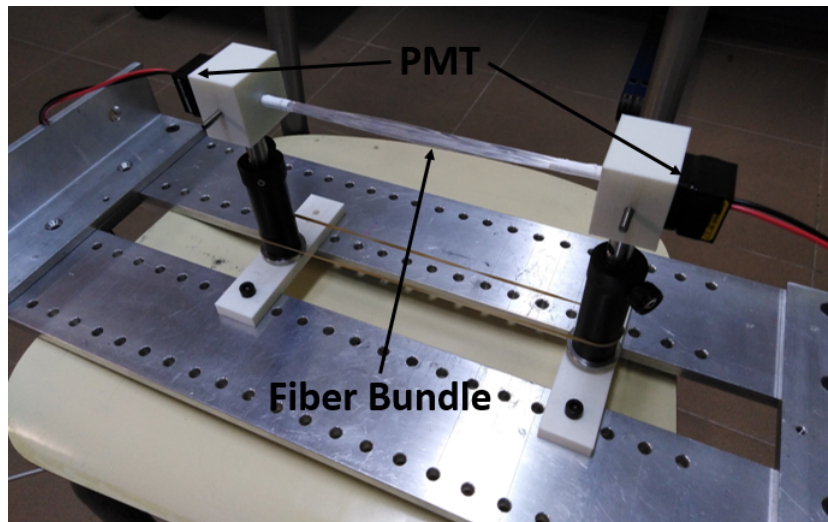


Figure 4.9 – Setup used to quantify the improvement of the light collection of the fibers and their transmission to the PMTs due to the polishing process. This setup was placed inside a light-tight box for the measurements.

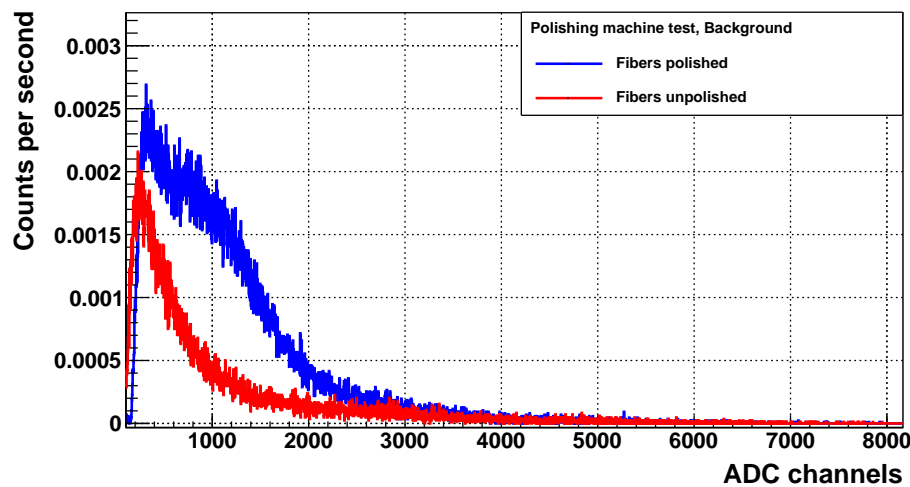


Figure 4.10 – Background energy spectra recorded with polished and unpolished fibers.

lated ^{60}Co source of 715 Bq activity and a ^{90}Sr source of 17.8 kBq activity. The radioactive sources were placed next to the center of the fiber bundle (at 7.5 cm from each PMT). The energy spectra recorded for both radioactive sources are shown in Figure 4.11. It can be noticed that both energy spectra are shifted to the right after polishing, obtaining an improvement of a factor 1.7 and 2 with respect to the spectra before polishing for the ^{60}Co and ^{90}Sr sources, respectively.

In summary, the photon collection efficiency of the fibers was significantly improved by polishing (mainly due to the improvement of the interface between fibers and PMTs). As the expected number of photons per tritium event is quite low (less than 20, as demonstrated by both simulations and measurements), it is crucial to achieve a high light collection.

4.1.1.3 Cleaning of Scintillating Fibers.

As it was demonstrated in subsection 4.1.2, the quality of the interface between the core of uncladded fibers and the environment (tritiated water in the case of TRITIUM detector) affects conspicuously the photon collection efficiency. To improve the quality of the interface, a fiber cleaning process was implemented, aiming to remove particles deposited on the fibers, such as dust and grease. Through this cleaning process, the wetting property of the fibers is improved, as illustrated in Figure 4.12. The contact angle between fibers and water is decreased, preventing air molecules from attaching to the fibers and producing a uniform contact between fibers and water. This cleaning process was developed and carried out in the clean room of IC-MOL. Three different beakers were used, the first filled with alkaline soap, the second with pure water (conductivity of the order of $10 \mu\text{S}/\text{cm}$) and the third with isopropanol. The fibers were manually rubbed with alkaline soap during 5 minutes, afterwards introduced into the first beaker which was placed in an ultrasonic bath at 17 kHz frequency during 3 minutes. Subsequently, the fibers were cleaned with a constant flow of water during

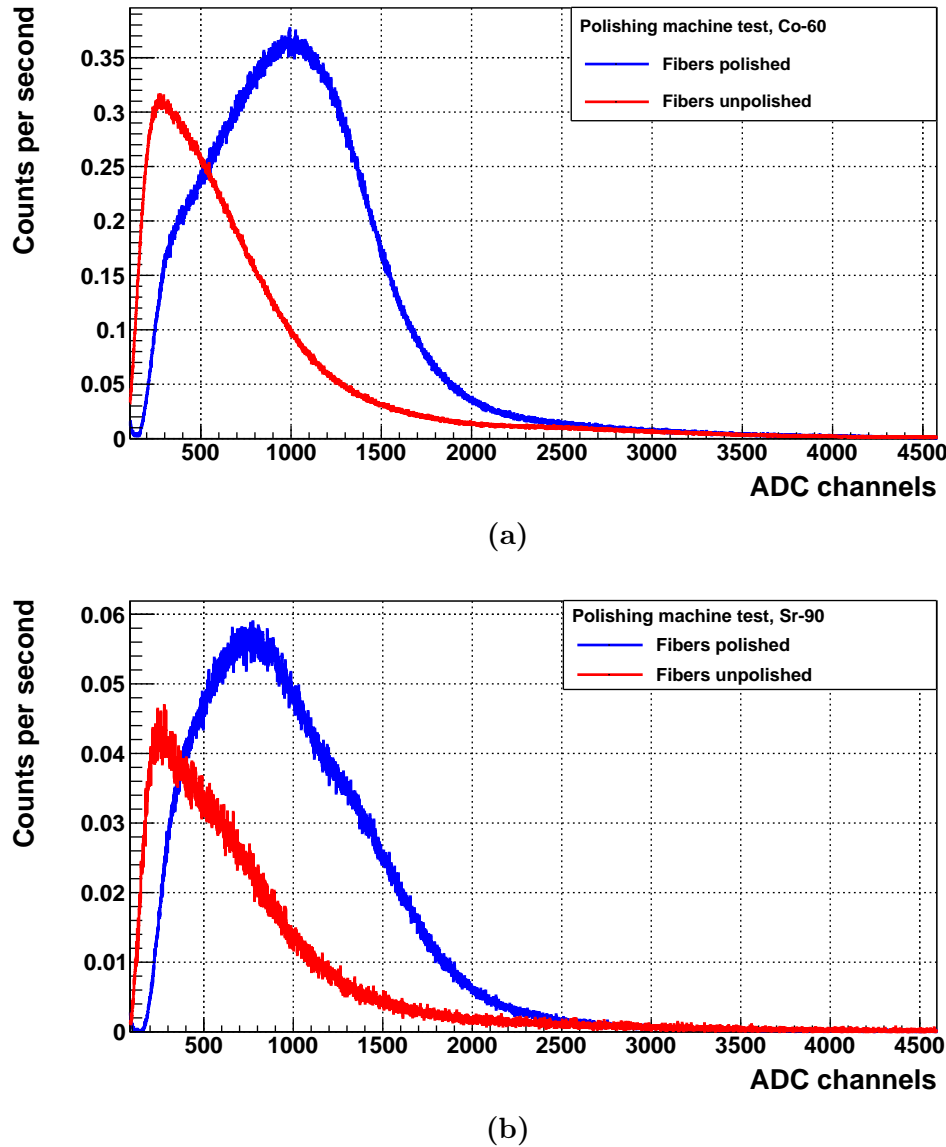


Figure 4.11 – Energy spectra recorded with polished and unpolished fibers.
a) ^{60}Co source. b) ^{90}Sr source.

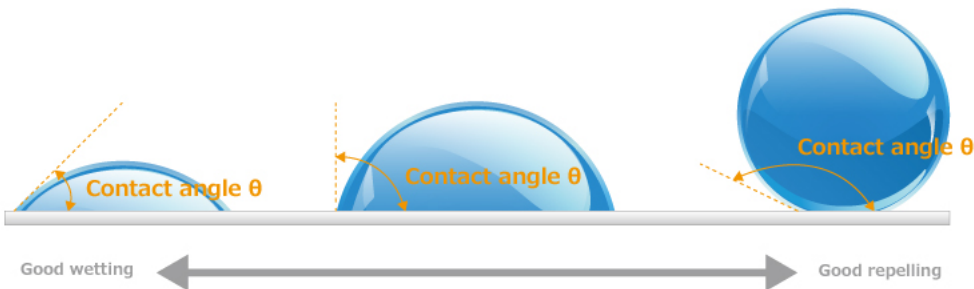


Figure 4.12 – Schematic representation of the wetting properties of a flat surface (gray) in contact with a drop of liquid (blue). The wetting property is characterized by the angle formed between the surface of both objects. The smaller angle, the better wetting property of the material. [San]

5 minutes and they were placed in the second beaker for ultrasonic bath during 3 minutes and next placed in the third beaker for ultrasonic bath during 3 minutes. Finally, the fibers were dried with a flow of gaseous N₂ and kept in clean conditions until their introduction into the detector vessel. The improvement of the light collection of the scintillating fibers after this cleaning process was determined by measuring the energy spectra of a bundle of twenty uncladded fibers of 15 cm length before and after undergoing this cleaning process. The setup used for this measurements is described in Figure 4.9. The energy spectra were measured for the background and for a ⁹⁰Sr and ¹³⁷Cs radioactive sources, shown in Figures 4.13 and 4.14, respectively. A shift of the spectra to higher energies was observed for the clean fibers with respect to the spectra of fibers without cleaning. The equation 4.1 was used to quantify the improvement achieved by the cleaning process. Although no improvement in the number of detected events was observed for the background measurement, an improvement of photon collection efficiency of a factor of 1.26 and 1.35 was obtained for the ⁹⁰Sr and ¹³⁷Cs sources, respectively.

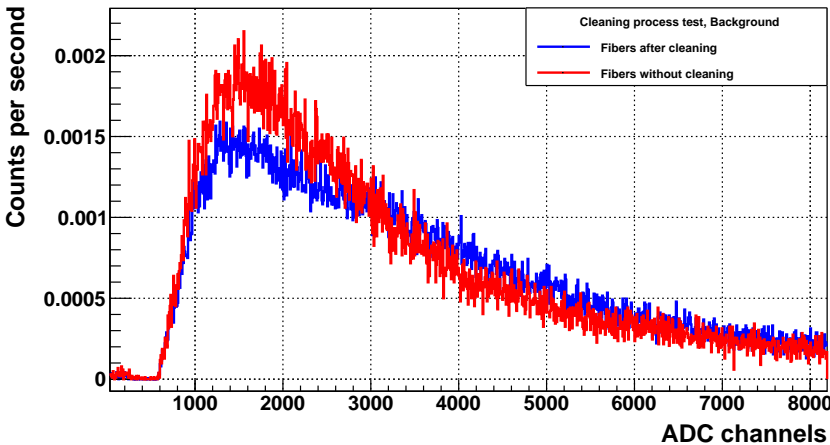
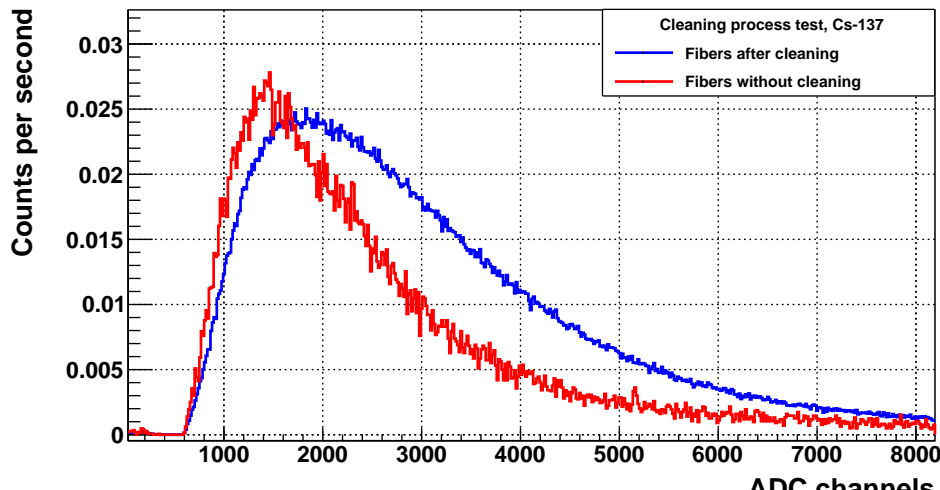


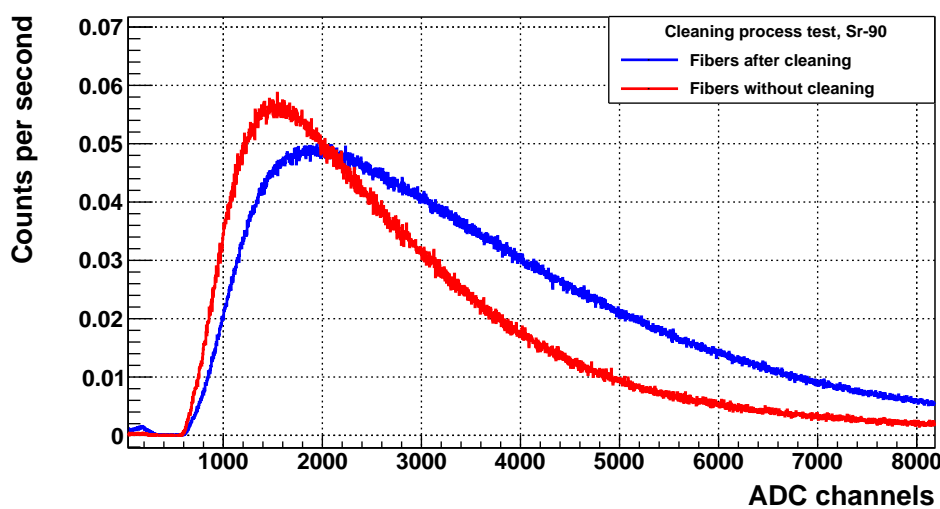
Figure 4.13 – Measured background energy spectra before and after cleaning.

4.1.2 Characterization of Scintillating Fibers

In this section, the characterization of unclad BCF-12 fibers from Saint-Gobain, selected for the TRITIUM monitor, is described. These fibers are compared to single clad and multiclad BCF-12 fibers with the same external diameter to quantify the influence of the clad on their photon collection efficiency. Commercial clads are too thick ($30\ \mu\text{m}$ for 1 mm fiber diameter) for tritium measurements but a sufficiently thin clad could be obtained by vapor deposition if needed. The difference between these three types of fibers is that unclad fibers consist of a polystyrene core with a refractive index of 1.60, whereas single clad and multiclad fibers have a PMMA clad of $30\ \mu\text{m}$ thickness and a refractive index of 1.49. Multiclad fibers have, in addition, a second fluor-acrylic clad of $10\ \mu\text{m}$ thickness and a refractive index of 1.42. The characterization was carried out for individual scintillating fibers and consisted in a comparative study of the fiber photon collection. The setup used, shown in Figure 4.15, consists of an optical board on which a LED and a PMT were placed in front of each other. A LED (LED435-03 from Roithner LaserTechnik GmbH [Roi10]), with an emission spectrum



(a)



(b)

Figure 4.14 – Energy spectra obtained before and after the cleaning for a radioactive source. a) ^{137}Cs . b) ^{90}Sr .

4.1. R&D FOR THE SCINTILLATING FIBERS

similar to that of the scintillating fibers, was used. The emission spectrum of the LED, given in Figure 4.16, was measured using a spectrometer and fitted to a Gaussian function. The LED emission peak is at 434 nm with a σ of 8 nm. The LED was fed in current mode with a sourcemeter. A calibrated Hamamatsu R8520-06SEL PMT with $QE = 29.76\%$ quantum efficiency at $\lambda = 430$ nm was employed. A 20 cm long fiber was placed

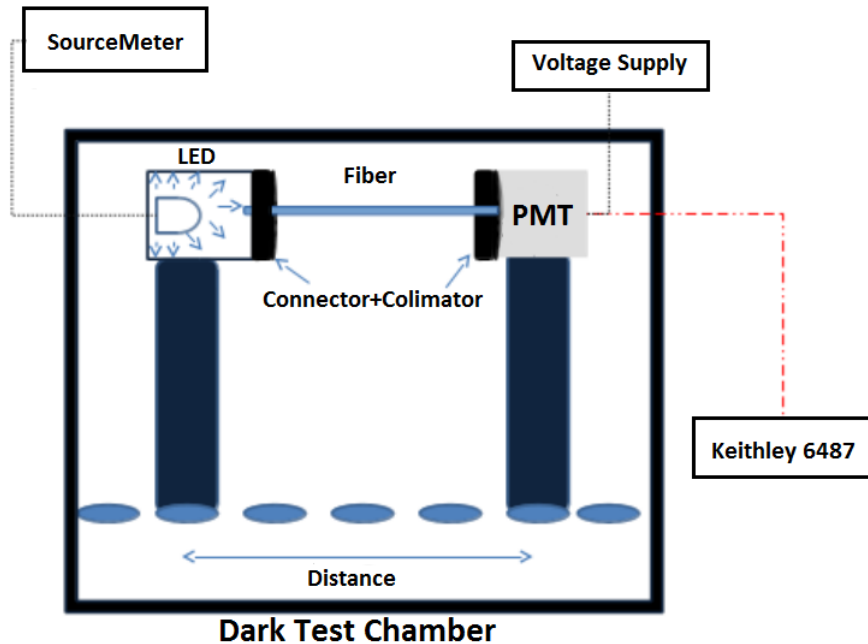


Figure 4.15 – Setup used for fiber characterization.

between the LED and the PMT, optically coupled to their end-surfaces by optical grease [Saib]. Two collimators were used to ensure that only photons emitted from the LED were detected by the PMT. Two FH-ST connectors from RoHS [] were used to fasten the fiber to the system. To determine the photon collection efficiency, the rate of photons reaching the active area of the PMT was measured for the different type of fibers. The photon rate R_γ

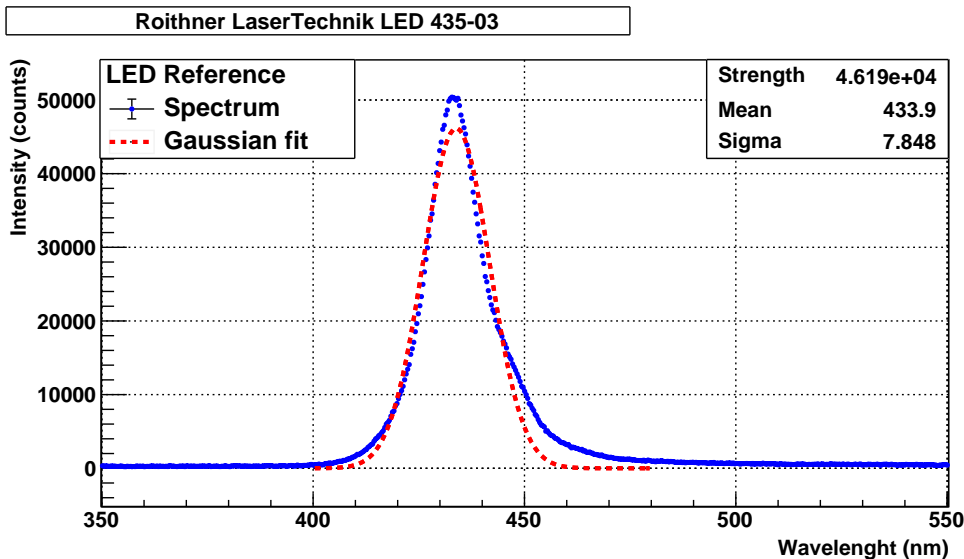


Figure 4.16 – Emission spectrum measured for the 435-03 LED from Roithner LaserTechnik GmbH.

reaching the photocathode was calculated from,

$$R_\gamma = \frac{(I_{PMT} - I_{DC})}{q_e \cdot QE \cdot CE} \quad (4.2)$$

where I_{PMT} is the output current of the PMT, I_{DC} is the dark current, CE is the photoelectron collection efficiency and q_e is the electron charge.

4.1.2.1 Measurement Conditions.

The experimental setup was placed in a light-tight box. The light-tightness of the box was carefully checked. To select the optimal PMT HV, the photocurrent as a function of the first dynode voltage was measured. The PMT HV was taken as the voltage at the beginning of the plateau (250 V) shown in Figure 4.17. At this HV the CE is equal to 1 and no secondary electrons are produced. This plot was measured between 0 and 800 V without fibers,

4.1. R&D FOR THE SCINTILLATING FIBERS

first with the LED off (PMT dark current) and then with the LED current at 1 mA. The number of photons detected by the PMT (difference between both spectra) is plotted in Figure 4.17.

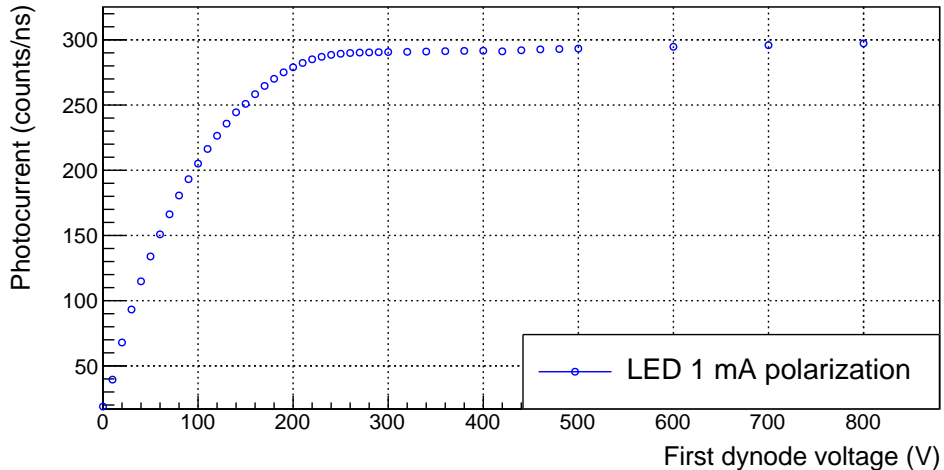


Figure 4.17 – PMT photocurrent as a function of the first dynode voltage with the dark current subtracted. Error bars are smaller than dot size.

The linear response of the PMT (in absence of fibers) was verified both, for a few photons/ns, which is the expected number of photons for tritium events, and up to ~ 2500 photons/ns, employed for fiber characterization. The results in the low and high illumination cases are plotted in Figure 4.18, in which no saturation of the PMT response is observed.

4.1.2.2 Results of the Characterization of Scintillating Fibers

Cleaving and polishing add a systematic dispersion σ_{sys-SF} to the intrinsic fiber response. In addition, the position of the connectors that lock the fiber to the experimental setup of Figure 4.15 produces an additional systematic uncertainty $\sigma_{sys-pos}$. Since both uncertainties are independent, the total

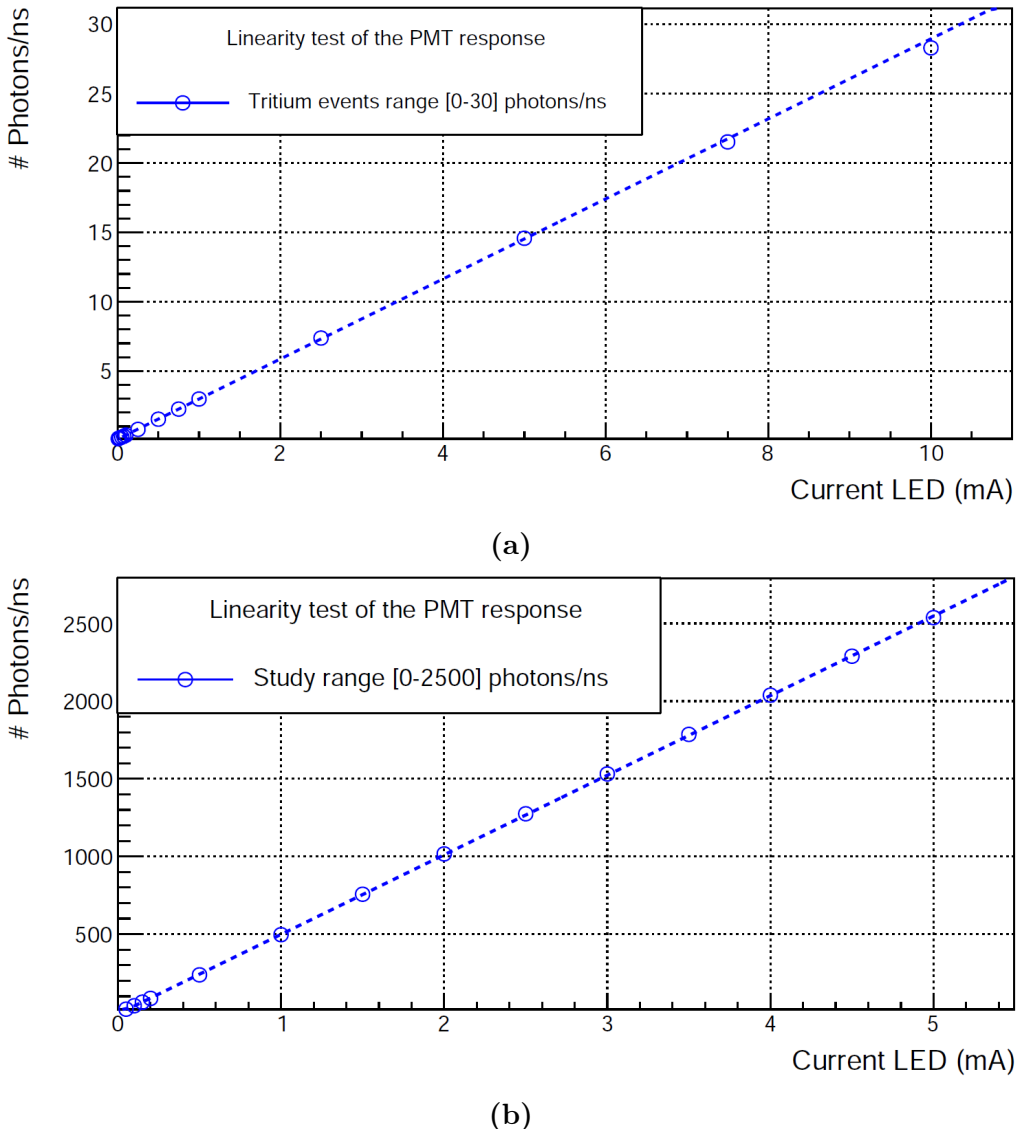


Figure 4.18 – Rate of photons measured by the PMT as a function of the LED current. a) Response of the PMT in the intensity range of tritium events. b) Response of the PMT in the range 0 – 2500 photons/ns. Error bars are smaller than the dot size.

4.1. R&D FOR THE SCINTILLATING FIBERS

systematic uncertainty is given by,

$$\sigma_{sys} = \sqrt{\sigma_{sys-SF}^2 + \sigma_{sys-pos}^2} \quad (4.3)$$

The uncertainty due to fiber positioning $\sigma_{sys-pos}$ was measured to extract σ_{sys-SF} from the total systematic uncertainty. Two different experiments were designed, the first giving only the systematic uncertainty $\sigma_{sys-pos}$, and the second the total uncertainty. Thus, σ_{sys-SF} is given by,

$$\sigma_{sys-SF} = \sqrt{\sigma_{sys}^2 - \sigma_{sys-pos}^2} \quad (4.4)$$

The test designed to measure $\sigma_{sys-pos}$ consisted in preparing one conditioned fiber of each type (uncladded, single clad and multiclaid), all of 1 mm diameter and 20 cm length. Each fiber was locked to the setup, and the PMT photocurrent was measured for the LED fed at 1 mA. These measurements were repeated ten times for each fiber, removing and inserting the fiber each time. The mean \bar{x} , the standard deviation and the relative standard deviation $\sigma_{sys-pos}^{rel}$ of the PMT photocurrent for each fiber type are shown in Table 4.1. The relative standard deviation is defined as

$$\sigma_{sys-pos}^{rel} = \frac{\sigma_{sys-pos}}{\bar{x}} \quad (4.5)$$

As it can be noticed, larger photon rates are obtained for single clad and multiclaid fibers than for uncladded fibers. The reason could be that the interface between the core and the clad of the fiber is more uniform for single clad and multiclaid fibers than for uncladded fibers, for which the interface is air. External conditions as dirt may produce significant interface fluctuations. The statistical error of these measurements is three orders of magnitude smaller than the systematic uncertainties $\sigma_{sys-pos}$.

To determine the total systematic uncertainty σ_{sys} , ten different samples of each fiber type were prepared and each fiber was measured as described above. These measurements were done for increasing LED emis-

Fiber type	Photon rate (ns^{-1})	$\sigma_{sys-pos}$ (ns^{-1})	$\sigma_{sys-pos}^{rel}$ (%)
Uncladded	524.09 ± 0.01	17.7	3.4
Single Clad	1071.70 ± 0.01	9.1	0.9
Multiclad	949.93 ± 0.03	9.9	1

Table 4.1: Mean, standard deviation and relative standard deviation due to fiber positioning in the setup of the photon rate that reach the PMT for 0.1 mA LED intensity.

sion intensities, corresponding to 0.05, 0.1, 0.15 and 0.2 mA LED current. The results for uncladded fibers are plotted in Figure 4.19, where it can be seen that, although each fiber shows a linear trend with increasing LED intensity, a dispersion of the fiber response is clearly observed. Similar results were obtained for single clad and multiclad fibers, displayed in figures 4.20a and 4.20b, respectively.

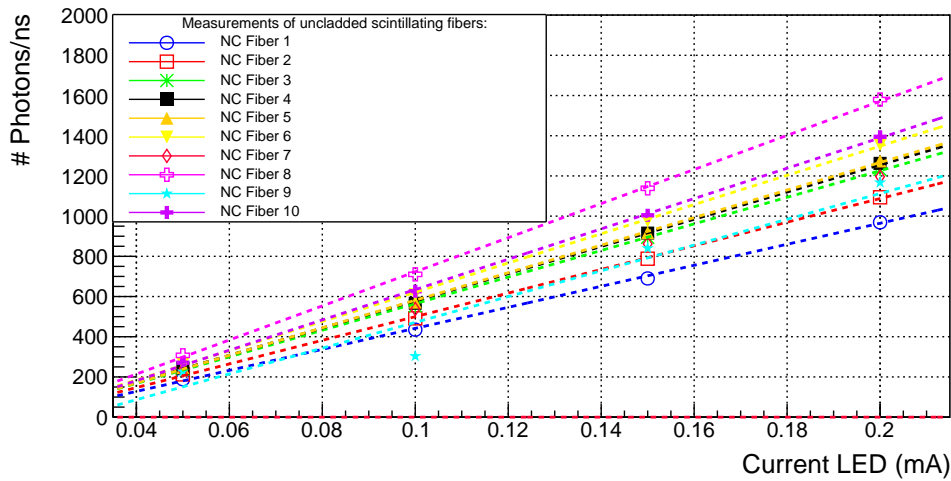


Figure 4.19 – Rate of photons reaching the PMT for uncladded fibers. Error bars are smaller than the dot size.

The average of the photon rate and the relative standard deviation

4.1. R&D FOR THE SCINTILLATING FIBERS

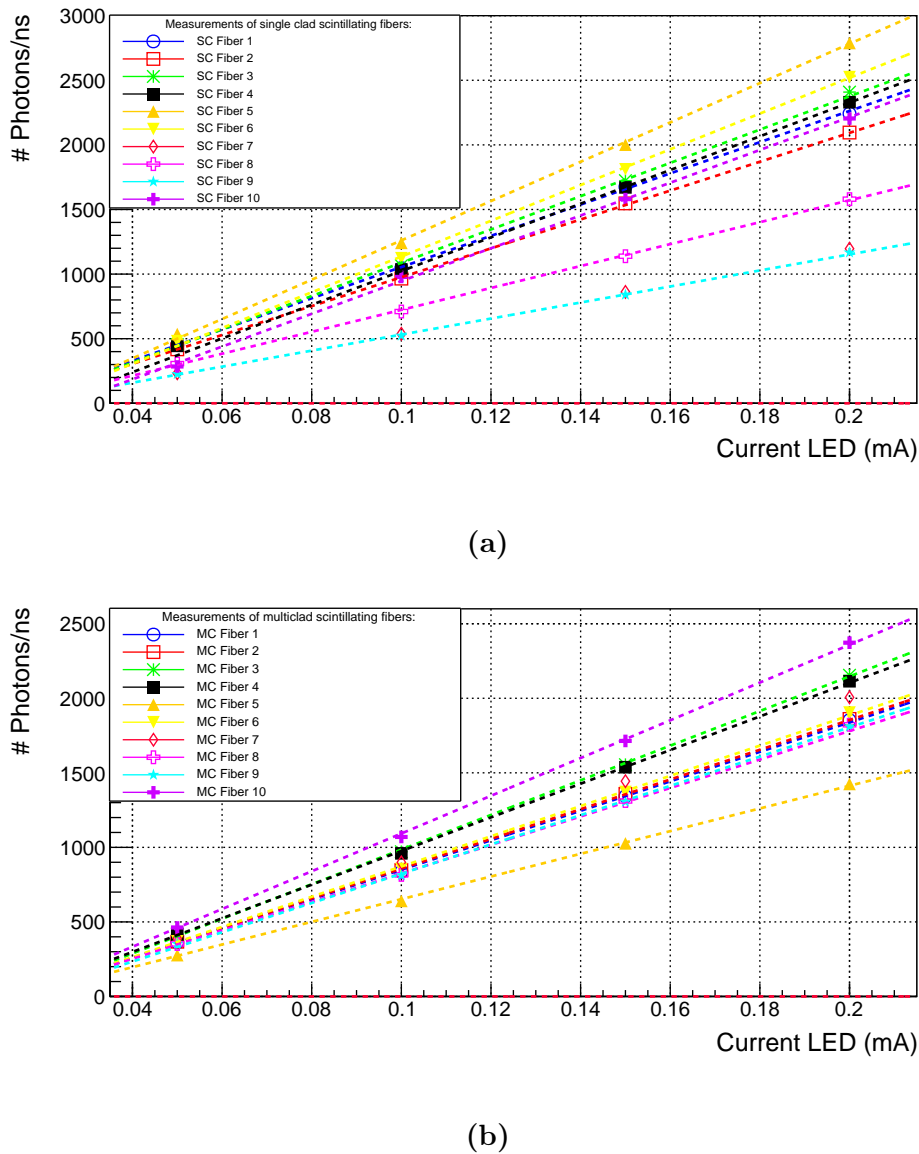


Figure 4.20 – Photon rate reaching the PMT for ten different fibers. a) Single clad fibers. b) Multiclad fibers. Error bars are smaller than the dot size.

versus LED intensity for each type of fiber are given in Tables 4.2 and 4.3 respectively, and are plotted in Figure 4.21. As it can be noticed in Figures 4.19 and 4.20, the fiber response is quite linear with current. Single clad and multiclad fibers give larger signals than uncladded fibers (a factor two in the case of single clad), which indicates that the clad has a significant effect on the fiber collection efficiency. It can also be observed in Table 4.3 that the relative standard deviation σ_{sys}^{rel} does not vary with the LED intensity. The largest uncertainty was found for single clad fibers, despite of their higher light collection. This is most probably due to the cleaving process that produces cracks in the clad, as observed in Figure 4.3. This damage seems to be reduced for multi-clad fibers, probably due to their larger mechanical resistance.

Intensity (mA)		Photon rate (10 ns^{-1})		
Fiber type		Uncladded	Single clad	MultiClad
0.05		24.5 ± 1.1	38 ± 3	37.7 ± 1.5
0.1		57 ± 3	92 ± 7	87 ± 4
0.15		92 ± 4	149 ± 12	140 ± 6
0.2		127 ± 6	205 ± 17	193 ± 8

Table 4.2: Photons rate versus LED intensity for the different type of fibers.

Intensity (mA)		$\sigma_{sys}^{rel}(\%)$		
Fiber type		Uncladded	Single clad	MultiClad
0.05		4.4	8.7	4
0.1		4.6	8	4
0.15		4.3	8.1	4
0.2		4.4	8.1	3.9
Mean		4.4	8.2	4

Table 4.3: Relative standard deviation of the photon rate $\sigma_{sys}^{rel}(\%)$ versus LED intensity for the different fiber types.

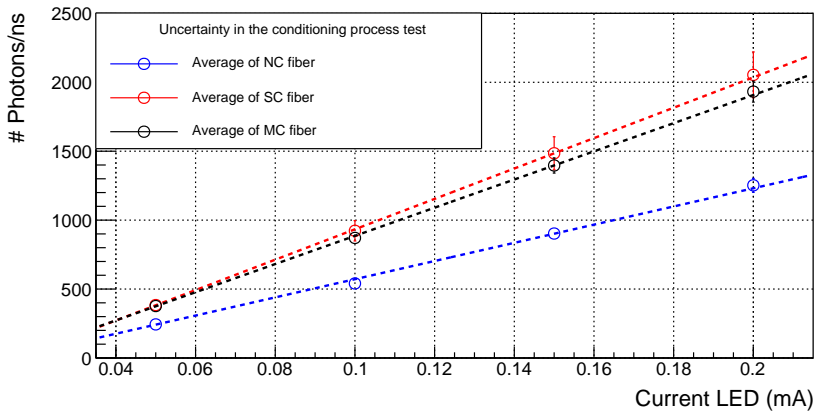


Figure 4.21 – Average photon rate versus LED current for 10 samples of different fiber types (uncladded, singleclad and multiclad fibers). Error bars are smaller than the dot size.

The average of σ_{sys}^{rel} , $\sigma_{sys-pos}^{rel}$ and σ_{sys-SF}^{rel} are given in Table 4.4. The smallest relative standard deviation was found for uncladded fibers, which means that the damage occurs mainly in the fiber clad, as illustrated in Figure 4.5 where cracks in the clad due to the cleaving process can be seen. It was checked under microscope that this damage only occurs at the end of the fiber. Also, the largest relative standard deviation is obtained for single clad fibers, which indicates that a second clad increases the tolerance of the fiber to conditioning.

Fiber type	σ_{sys}^{rel} (%)	$\sigma_{sys-pos}^{rel}$ (%)	σ_{sys-SF}^{rel} (%)
Uncladded	4.4	3.4	2.9
Single Clad	8.2	0.9	8.1
Multiclad	4	1	3.8

Table 4.4: Measured relative standard deviations σ_{sys}^{rel} , $\sigma_{sys-pos}^{rel}$ and σ_{sys-SF}^{rel} .

In summary, the relative statistical deviation due to fiber conditioning was quantified for the different fiber types. It was found that a fiber

clad improves the photon collection efficiency but at the cost of worsening its standard deviation. Larger uncertainties (a factor two) in the light collection were observed in single clad fibers compared to multiclads and unclad ones. This may be due to the damage in the clad produced during the cleaving process of these fibers.

The absolute photon collection efficiency of 10 cm scintillating fibers CE_{10} was measured for each type of fiber. Ten different fibers of 10 cm length for each fiber type were prepared and the photon rates were measured and summarized in Table 4.5. CE_{10} was calculated by comparing the collected photon rate to that for a fiber length of 20 cm.

$$CE_{10} = \frac{R_{ph}(20 \text{ cm})}{R_{ph}(10 \text{ cm})} = e^{-10/L} = 96\% \quad (4.6)$$

where $L = 270$ cm is the attenuation length provided by the manufacturer. Considering an exponential attenuation of the photon rate N_{ph} with length [Leo94],

$$N_{ph}(x) = N_{ph}(x_0) \times e^{-(x-x_0)/L} \quad (4.7)$$

The absolute collection efficiency obtained was somewhat smaller than the obtained from the attenuation length for all the scintillating fiber types.

Fiber type	Photon rate (10^2 ns^{-1})		
	Uncladded	Single clad	MultiClad
0.05	3.2 ± 0.6	5.5 ± 0.7	4.8 ± 0.8
0.1	7.4 ± 1.4	12.7 ± 1.6	11.1 ± 1.9
0.15	11.8 ± 2.3	19.8 ± 2.3	18 ± 3
0.2	16 ± 3	25.1 ± 2.1	23 ± 4

Table 4.5: Average photon rate versus LED intensity for 10 different samples of 10 cm length for uncladded, single clad and multiclads fibers.

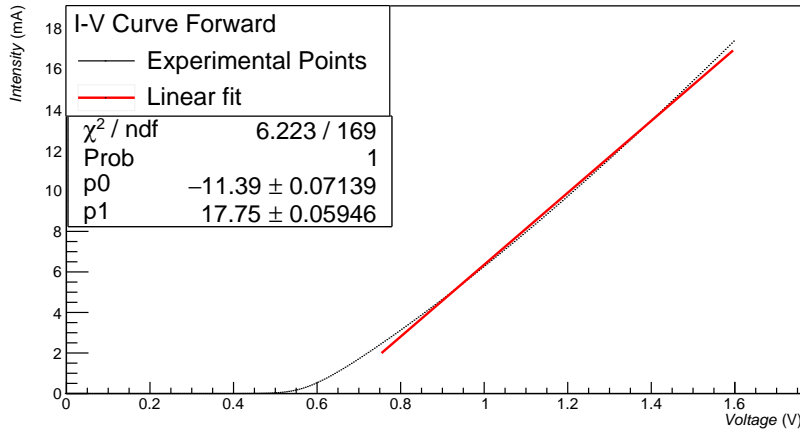
Fiber type	CE_{10} (%)
Uncladded	76 ± 8
Single clad	78 ± 6
Multiclad	83 ± 7

Table 4.6: Average collection efficiency CE_{10} for different types of scintillating fibers.

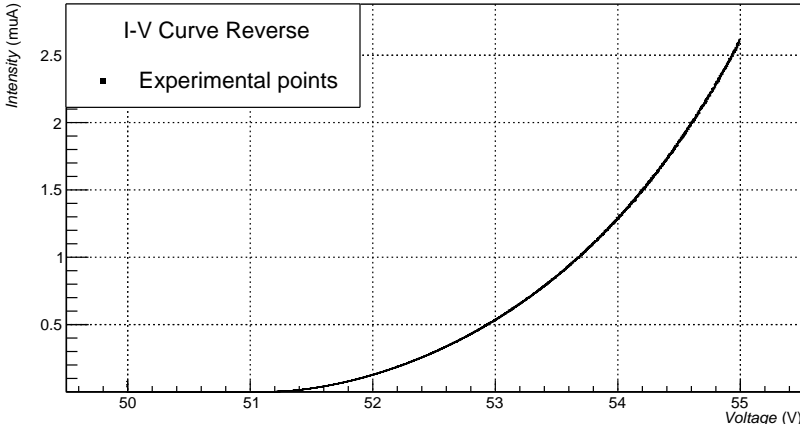
4.2 Characterization of SiPM

The characterization of the most relevant parameters of the SiPM S13360-1375 from Hamamatsu, which was the first choice for the TRITIUM monitor photosensor, is described in this section. The most relevant SiPM parameters are breakdown voltage V_{BD} , SiPM gain, the gain dependence on operating voltage and temperature $G_{SiPM}(V_{bias}, T)$ and temperature coefficient ΔTV_{op} . Additional parameters were measured to verify the accuracy of the characterization such as the quenching resistance R_q , the pixel capacitance C_d , and the terminal capacitance C_t . The afterpulse probability was not measured since, as reported in seccion 3.1, it is negligible when time coincidence windows of 10 ns are employed. The SiPM characterization was carried out inside of a climatic chamber, model CCM 81 from DYCOMETAL [DYC]. This climatic chamber allows to control both temperature and humidity with a precision of 0.1°C and 0.1%, respectively. In addition, this chamber works as a Faraday cage. A special black blanket [Thob] screened the SiPM from external light.

The quenching resistance and the breakdown voltage were measured from the output current of the SiPM as a function of its forward and reverse bias voltage, respectively. The output current of the SiPM was measured by a Keithley 6487 Picoammeter/Voltage Source [Keia]. The LabView sofware was used to take the data. The current-voltage curves are shown in Figure 4.22. As can be seen, when the SiPM is forward biased (Figure



(a)



(b)

Figure 4.22 – I-V curves measured for the S13360-1375 SiPM model from Hamamatsu. a) Forward bias. b) Reverse bias. The measurements were taken at $T = 25^\circ\text{C}$ and $H = 45\%$.

4.2. CHARACTERIZATION OF THE SiPM

4.22a) there is no output current until a potential drop of $V_0 = 0.5$ V is reached. When the current starts to flow, the intensity is linear with the applied voltage. The equivalent resistance R_{eq} was determined from,

$$I = \frac{1}{R_{eq}}V; \quad \frac{1}{R_{eq}} = \sum_{i=1}^N \frac{1}{R_q} = \frac{N}{R_q} \quad (4.8)$$

and R_q is the pixel quenching resistance. A value of $R_q = 360.56 \pm 0.07$ k Ω was obtained from a linear fit to the data, which is in agreement with the typical values given by Hamamatsu. The breakdown voltage V_{BD} was obtained from the reverse bias voltage plot (Figure 4.22b). V_{BD} is the point at which the SiPM begins to operate in avalanche mode for reverse bias. V_{BD} is calculated from the maximum of the function

$$f = \frac{1}{I} \frac{dI}{dV} \quad (4.9)$$

The value obtained $V_{BD} = 51.02$ V is in agreement with the value provided by Hamamatsu, given in Table 3.3.

To measure the SiPM gain G_{SiPM} , the electronic board described in section 3.1 with an amplification factor of $F_{amp} = 170$ was employed. An incoherent light source, LED435-03 [Roi10], described in section 4.1, was used to illuminate the SiPM with low enough light intensity. The SiPM output signal shows various well-defined pulse heights, shown in Figure 4.23, corresponding to the number of pixels simultaneously fired. The single photon spectrum SPS is displayed in Figure 4.23. This spectrum was obtained by integrating and histogramming the SiPM output pulses within a time window wide enough to contain the whole charge of the pulse. The time window used in these measurements was $t_w = 500$ ns. The light source provides a trigger signal for the measurement, represented in green line in Figure 4.23. The well-separated peaks in the SPS spectrum correspond to the charge produced by a different number of pixels fired. The first peak in the spectrum is the pedestal, which is the charge measured when no pixel is

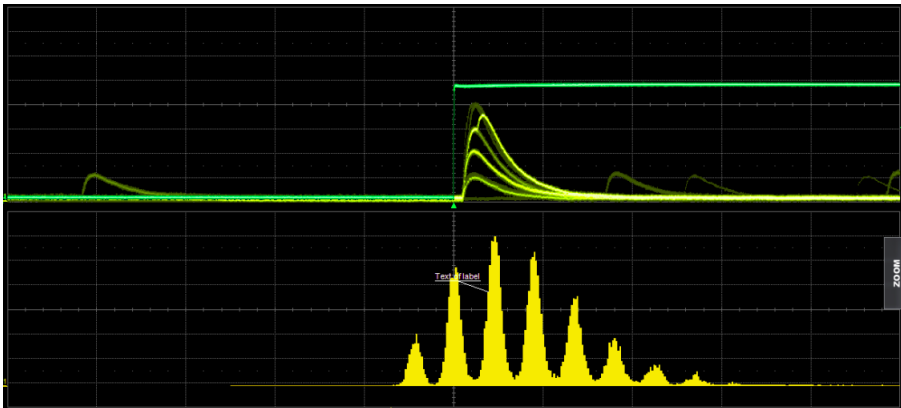


Figure 4.23 – Above) Trigger signal (green) and SiPM output pulses (yellow). Below) SPS spectrum obtained by integrating and histogramming the SiPM output pulses. This measurement was done at $T = 25^{\circ}\text{C}$, $V_{bias} = 53.98$ and $H = 60\%$.

fired. This peak is caused by the electronic noise of the system. The second peak corresponds to one fired pixel and so on. The SiPM gain G_{SiPM} can be obtained from the SPS spectrum from the equation,

$$G = \frac{\overline{\Delta Q}}{e F_{amp}} \quad (4.10)$$

where e is the electron charge and $\overline{\Delta Q}$ is the average peak distance in the SPS spectrum, corresponding to the charge released by a fired pixel. To obtain the value of $\overline{\Delta Q}$, a macro was written in ROOT [CERb]. This macro extracts the background (the pedestal subtracted output signals when the SiPM is not illuminated), which is crucial in some cases like high temperatures or high bias voltages since background can hide peaks. After subtracting the background, this macro finds all peaks in the SPS spectrum and fits each one to a Gaussian function, as shown in Figure 4.24a. The charge produced by multiple fired pixels is obtained from the centroid of the peaks. The charge fitted versus the number of fired pixels is shown in Figure 4.24b. Up to 10 simultaneously fired pixels were obtained with

4.2. CHARACTERIZATION OF THE SIPM

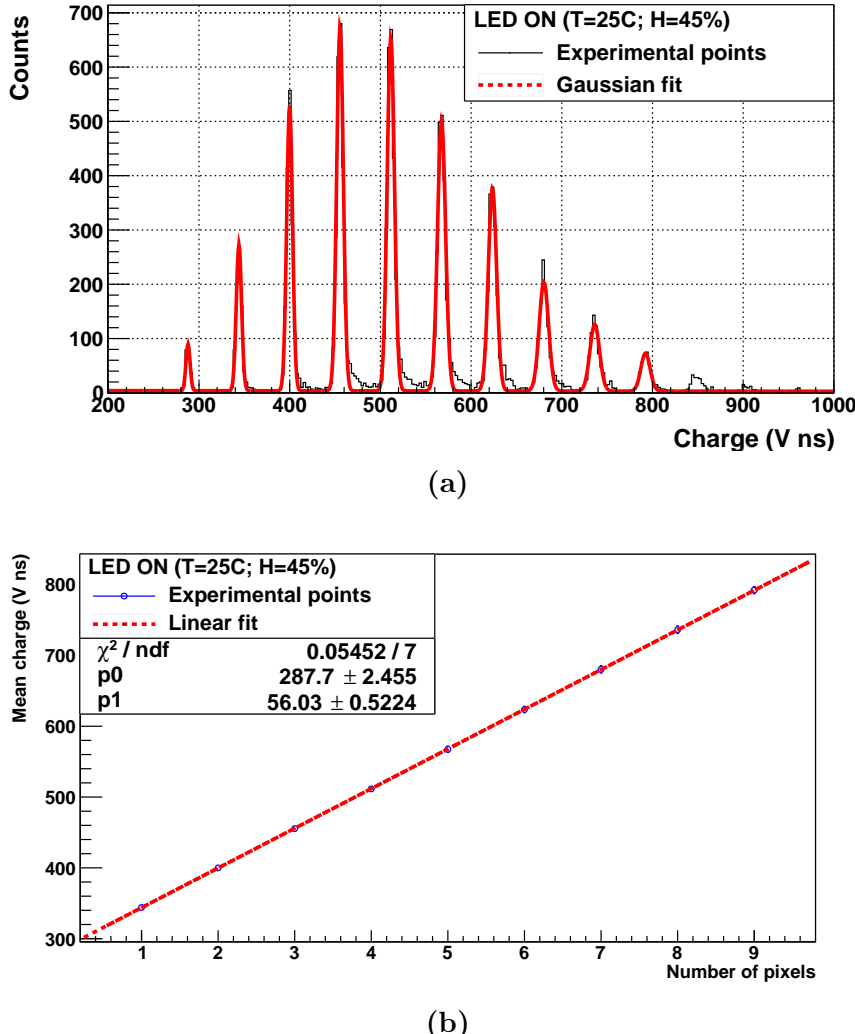


Figure 4.24 – a) Fit of the SPS spectrum to Gaussian functions. **b)** Charge as a function of the number of pixels fired. Error bars are within point size. Data taken at $T = 25^\circ\text{C}$, $V_{bias} = 53.98$ V and of $H = 45\%$.

a relative uncertainty of the charge measurement of less than 2%. The slope of the straight line in Figure 4.24b corresponds to $\overline{\Delta Q}$. For the case studied, which corresponds to a temperature of 25°C and a bias voltage of 53.96 V (overvoltage of 3 V), the value obtained for the SiPM gain is $G_{SiPM} = (4.11 \pm 0.04) \cdot 10^6$, very close to the data sheet value, given in Table 3.3.

A method for SiPM gain stabilization against temperature changes was implemented. This is necessary for the TRITIUM project since the temperature in the final location of the tritium detector cannot be controlled with the sufficient accuracy to avoid significant variations of the SiPM gain. This method consists in compensating variations of the SiPM gain caused by temperature changes, by controlled modification of the bias voltage. For this task, the dependence of the SiPM gain with the temperature and bias voltage was measured. The SiPM gain was measured from 15°C to 41°C in steps of 2°C, which is expected to be the temperature range in the final detector location. The bias voltage was $V_{bias} = V_{BD} + 3$. The SiPM gain was measured at several overvoltages from 1 V to 5 V in steps of 0.2 V. The temperature was $T = 25^\circ\text{C}$. Both measurements are shown in Figure 4.25. An excellent linear behaviour is obtained for both cases. From a linear fit, It is obtained,

$$\begin{aligned} G_{SiPM} &= a \cdot T + b; & G_{SiPM} &= c \cdot V_{bias} + d \\ a &= (-82.5 \pm 1.6) \cdot 10^3; & c &= (137.7 \pm 1.5) \cdot 10^4 \\ b &= (618 \pm 5) \cdot 10^4; & d &= (-762 \pm 8) \cdot 10^5 \end{aligned}$$

The breakdown voltage V_{BD} and the terminal capacitance C_t can be obtained from the linear fit of the SiPM gain versus the bias voltage V_{bias} ,

$$G_{SiPM} = \frac{Q_{pixel}}{e} = C_d \frac{V_{bias} - V_{BD}}{e} = c \cdot V_{bias} + d \quad (4.11)$$

where C_d is the pixel capacitance. From the linear fit of Figure 4.25b,

4.2. CHARACTERIZATION OF THE SiPM

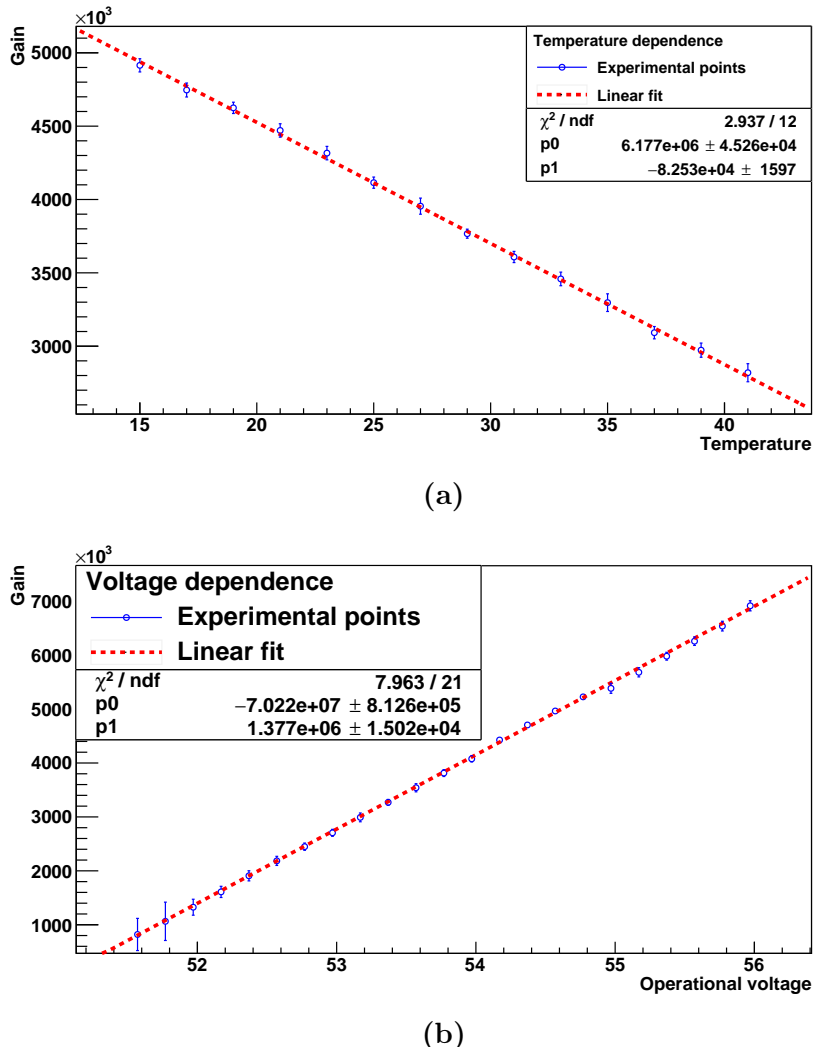


Figure 4.25 – SiPM gain versus a) Temperature. b) Bias voltage.

$V_{BD} = 51 \pm 0.6$ V and $C_d = 220.6 \pm 2.4$ fF are obtained. The terminal capacitance of the SiPM is calculated as $C_t = N_p \cdot C_d = 62.9 \pm 0.7$ pF, where N_p is the SiPM number of pixels. Both breakdown voltage and terminal capacitance are in agreement with the values given in Table 3.3. Finally, the bias voltage needed to compensate for the variation of the SiPM gain due to temperature changes is obtained from the derivatives of the linear relations,

$$G_{SiPM} = a \cdot T + b \longrightarrow \frac{\partial G_{SiPM}}{\partial T} = a$$

$$G_{SiPM} = c \cdot V_{bias} + d \longrightarrow \frac{\partial G_{SiPM}}{\partial V_{bias}} = c$$

The total variation of the SiPM gain produced by the variation of both V_{bias} and T , must cancel,

$$dG_{SiPM,tot} = \frac{\partial G_{SiPM}}{\partial T}dT + \frac{\partial G_{SiPM}}{\partial V_{bias}}dV_{bias} = a \cdot dT + c \cdot dV_{bias} = 0$$

$$dV_{bias} = -\frac{a}{c}dT = -edT$$

where the parameter

$$e = \Delta TV_{op} = 59.9 \pm 1.3 \text{ mV/}^\circ\text{C}$$

agrees with the temperature coefficient provided in the data sheet, given in Table 3.3. Converting the differentials in finite increments,

$$\int_{V_i}^{V_f} dV_{bias} = -e \int_{T_i}^{T_f} dT \longrightarrow \Delta V_{bias} = -e \Delta T \quad (4.12)$$

gives the variation of the voltage ΔV_{bias} that keeps constant the SiPM gain for a variation in temperature, ΔT . To determine the bias voltage V_{bias} to be applied as a function of the temperature T a reference value is needed. The reference considered is $V_{ref} = V_{BD} + 3$ V = 53.98 V and $T_i = T_{ref} = 25^\circ\text{C}$,

4.2. CHARACTERIZATION OF THE SiPM

at which the measured gain is $4.2 \cdot 10^6$. Thus, we get,

$$(V_{bias} - V_{ref}) = -e(T - T_{ref})$$

$$V_{bias}(\text{V}) = 55.48 - 59.93 \cdot 10^{-3} \cdot T(\text{°C}) \quad (4.13)$$

To test the gain stabilization, the temperature was varied from 21°C to 29°C and the bias voltage was modified according to the equation 4.13. The value of the SiPM gain obtained as a function of the temperature is shown in Figure 4.26. The red dotted line indicates the reference SiPM

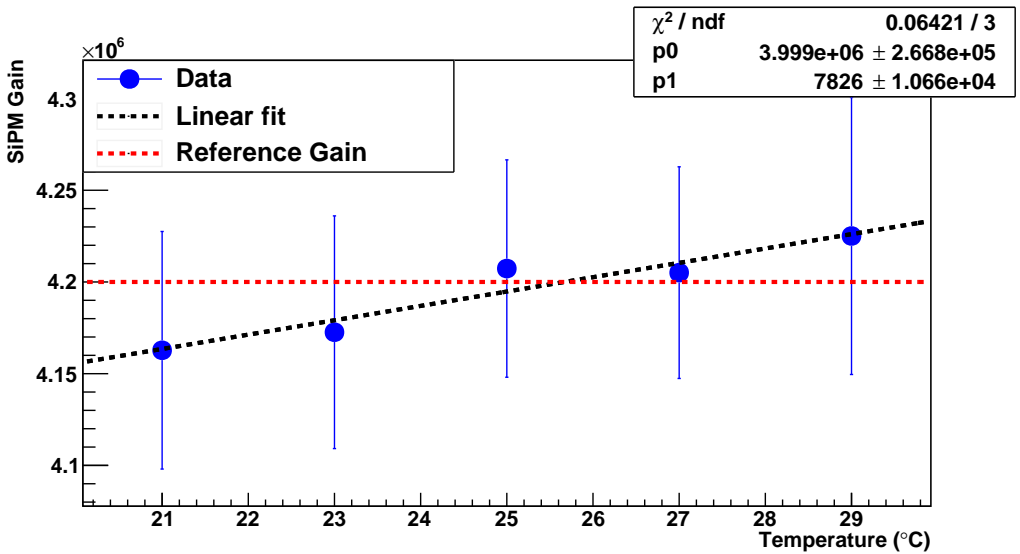


Figure 4.26 – SiPM gain as a function of the temperature after implementation of the gain stabilization method.

gain. As it can be seen, the gain variation with temperature is reduced to $0.25\% \text{ }^{\circ}\text{C}^{-1}$ which is negligible. Furthermore, all measured points are compatible with the initially value measured for the SiPM gain. Therefore, this method stabilizes the gain of the SiPM against temperature variations.

4.3 Characterization of the Water Purification System

The characterization of the water purification system is described in this section. This system guarantees that the quality of the water sample fulfills the requirements of the TRITIUM detector. These requirements are:

1. A low water conductivity, around $10 \mu\text{S}/\text{cm}$, to avoid that particles in the water be deposited on the fibers, which would drastically reduces the detector efficiency.
2. The radioactive elements (other than tritium) in the water sample should be removed to avoid background.
3. The tritium activity of the sample should not be affected by the water purification process.

To verify that these requirements are fulfilled, a characterization of the water sample for both raw and purified water was done. This characterization consisted in measuring the water sample conductivity, the activity of the different radioactive elements present in the sample, the turbidity and the chemical components of the water sample. The sample of raw water is taken at a depth of two meters in the river and 40 meters distance from the TRITIUM monitor site towards the NPP. The chemical composition of the water, shown in Table 4.7, was measured by a physico-chemical analysis before the purification process. The water sample contains a number of components that must be removed to prevent their deposition on the scintillating fibers of the detector.

The water turbidity¹ was measured using the Hanna Hi 9829 port-

¹The turbidity of water is the loss of transparency due to dissolved particles, normally measured in Nephelometric Units of Turbidity, NTU, as the intensity of scattered light at 90 degrees.

4.3. CHARACTERIZATION OF THE WATER PURIFICATION SYSTEM

Chemical components	Concentration (mg/L)
CO_3H^-	154
Mg^{++}	46
Ca^{++}	105
NO_3^-	16
Cl^-	196
NO_2^-	0.03
K^+	11
Na^+	173
SO_4^-	217
Dry Residue	1029

Table 4.7: Chemical components measured in the raw water sample.

able multiparameter system from Hanna Instruments [Han], obtaining a value of 29 NTU, much higher than the limit of 5 NTU for drinking water recommended by the WHO. The water conductivity was also measured for raw, pure and reject water using the same instrument. The results are shown in Table 4.8. As it can be seen in the first column, the raw water has a high conductivity due to its content of ions. It can be noticed in the second column of the table that the conductivity of pure water was reduced by almost two orders of magnitude, to values close to $10 \mu\text{S}/\text{cm}$. In the third column, it can be remarked that the reject water conductivity is higher than that of raw water because this water contains the ions removed from the purified water.

The gamma radioactive elements present in both raw and purified water were identified and their activities measured by a HPGe detector. A gamma analysis was carried out to determine the emitters with long enough lifetime to be measured. The radioactive isotopes found in the raw water with measurable activities were ^{40}K and ^{226}Ra which were not detected in the purified water.

The tritium activity was measured by liquid scintillation counting

Conductivity ($\mu\text{S}/\text{cm}$)			
Date	Raw	Pure	Reject
1/8/18	970	11.85	1442
7/8/18	958	11.8	1632
14/8/18	966	12.04	1725
22/8/18	980	12.54	1702
28/8/18	987	9.9	1692
5/9/18	1009	12.02	1645

Table 4.8: Conductivity of different samples of water.

(LSC) to check if it was modified by the purification process. The raw water was filtered at 0.45 microns to remove any particles that could cause extinction of the scintillation signal. Table 4.9 shows the tritium activity measured for different water samples before and after purification. As seen in the table, tritium activity is not affected by the purification process.

Activity (Bq/L)		
Date	Raw	Pure
7/8/18	24 ± 3	26 ± 4
11/12/19	13.2 ± 2.1	13.9 ± 2.2
15/01/20	31 ± 4	30 ± 4

Table 4.9: Tritium activity measured for different samples of both raw and purified water.

4.4 Characterization of the Cosmic Veto

The characterization of the cosmic active shield (cosmic veto), which was carried out using PMTs as photosensors, is reported in this section. The quality of the veto wrapping was checked. The configuration of the elec-

4.4. CHARACTERIZATION OF THE COSMIC VETO

tronics used was the one given in Figure 3.15b. The surface of the veto was divided in 9 parts, depicted in Figure 4.27, on which a gamma source was placed for this test. Two different tests were carried out:

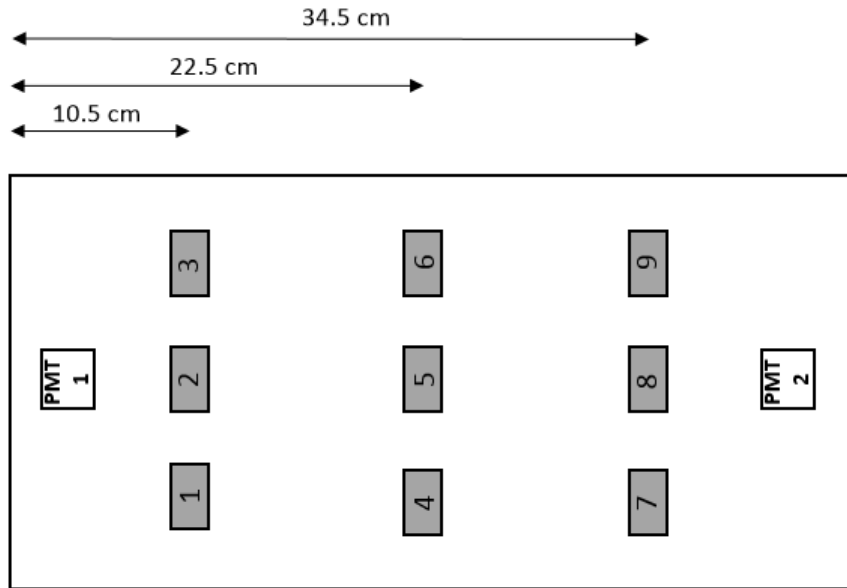


Figure 4.27 – Test points used for the cosmic veto mapping.

1. To quantify the improvement of the veto signal due to wrapping, a ^{137}Cs source was placed at point 2 before wrapping and an energy spectrum was measured. The measurement was repeated after wrapping. The spectra obtained are displayed in Figure 4.28.

The spectrum of the wrapped veto is shifted about a factor two to higher energies, which means that more photons per event are collected. No improvement was obtained on the number of events detected, only on the photon collection efficiency.

2. The spatial uniformity of the signal of the wrapped veto was evaluated. A mapping of the veto response to a ^{60}Co source placed successively on each test point was done for two different veto modules and the

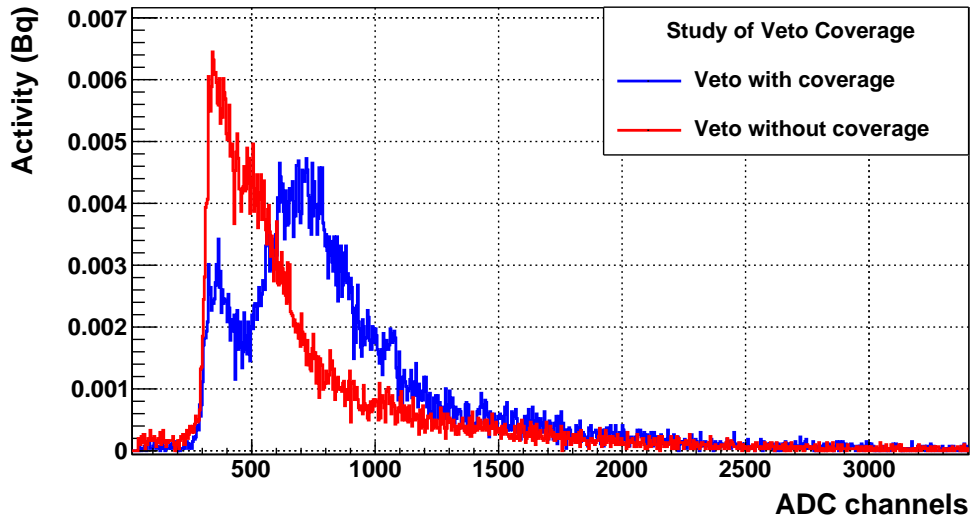


Figure 4.28 – Energy spectra measured with the ^{137}Cs radioactive source with and without wrapping the veto.

energy spectra obtained were integrated. The counting rates obtained are plotted in Figure 4.29. It can be observed that the veto signal has a uniform response on its whole surface, giving a fairly similar counting rate at all the points.

In a second test, two cosmic vetos were studied in coincidence. The electronic configuration of Figure 3.15c was employed. The output signal of the coincidence module was connected to a 1145 CAEN Quad Scaler And Preset Counter-Timer module [CAE]. The goal of this test was to find the PMT high voltage and the threshold discrimination for which the detection of cosmic rays is optimized. The test consisted in finding the PMT high voltage plateau on which the veto efficiency is constant and the discriminator threshold plateau on which no loss of cosmic events is produced. The counting rate was measured versus the PMT high voltage at three different thresholds (60 mV, 100 mV and 200 mV) and versus the threshold at three different PMT high voltages (700 V, 730 V and 780 V). The counting rate

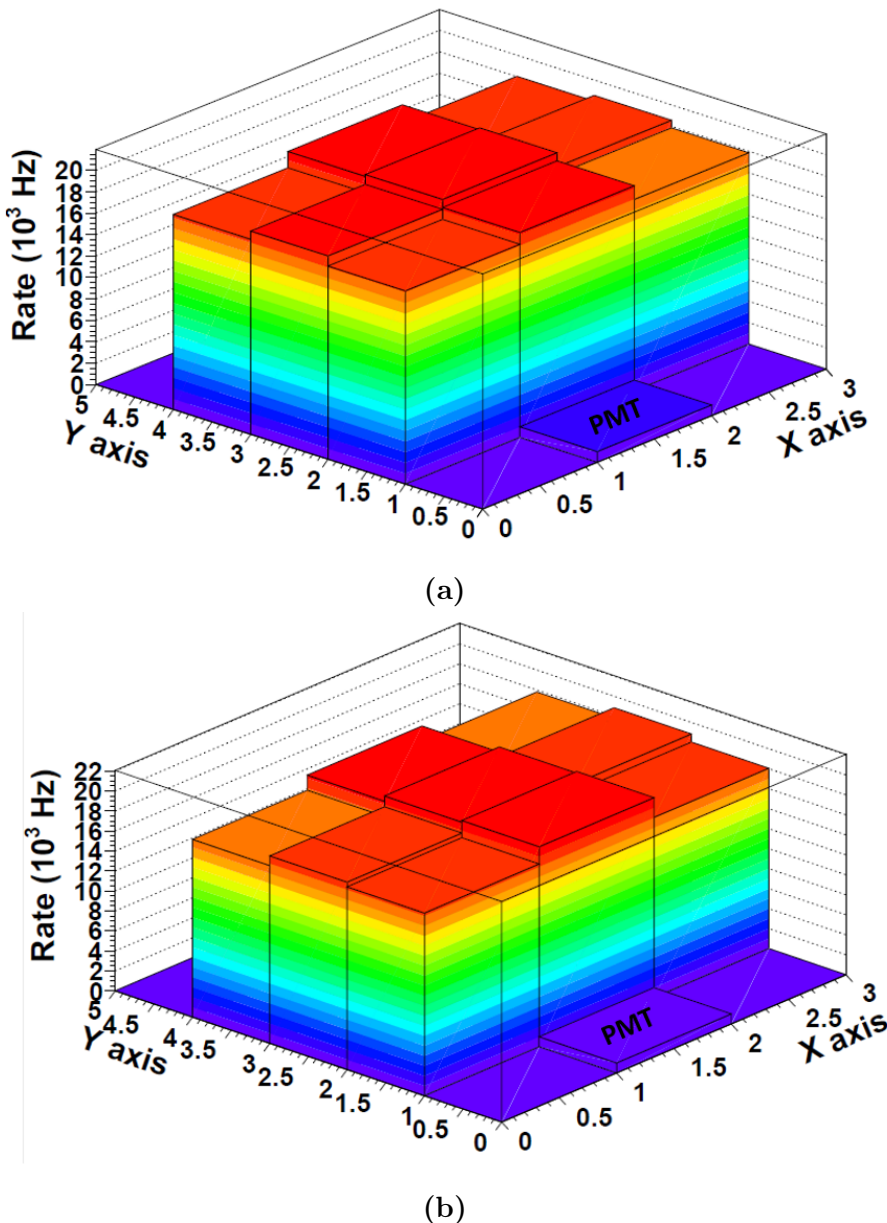
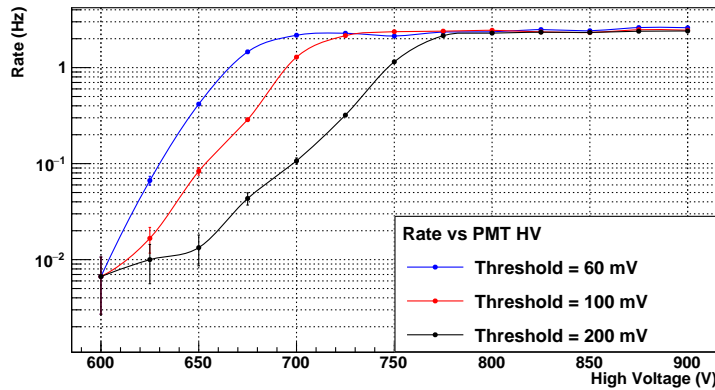


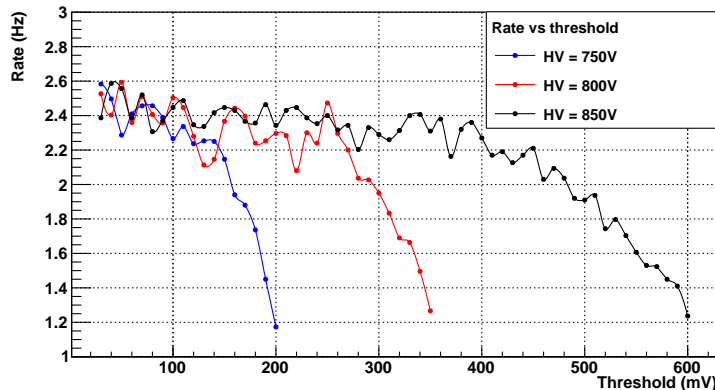
Figure 4.29 – Bidimensional graph of the counting rate (mapping) measured for two different cosmic vetos using a ^{60}Co source.

was measured in a time window of 300 s. The results are plotted in Figure 4.30. The PMT high voltage chosen was 800 V since it is on the plateau for the three threshold settings and the threshold chosen was 200 mV which is on the plateau for the selected high voltage.

The energy spectrum of cosmic rays was measured using the electronics of Figure 3.15c. A plot of this spectrum is shown in Figure 4.31. As expected, this energy spectrum fits well to a Landau function. The cosmic ray rate determined from the area of this spectrum is 2.5 event/s. The expected cosmic rate calculated in section 3.4.2 is 2.9 event/s. Thus, the efficiency of the active veto is 85%, which is a usual value of the efficiency of plastic detectors for mips. Finally, the detected cosmic ray rate versus the separation distance between the two cosmic vetos was measured. The spectra are shown in Figure 4.32a. The counting rate decreases with the distance but the spectrum shape and peak position remain unchanged. The integrated spectrum as a function of distance was fitted to a second degree polynomial. The fit is shown in Figure 4.32b and allows us to estimate the cosmic ray rate for a given veto separation.



(a)



(b)

Figure 4.30 – Counting rate of two cosmic vetos in coincidence a) as a function of PMT HV for three different thresholds and b) as a function of threshold for three different high voltages.

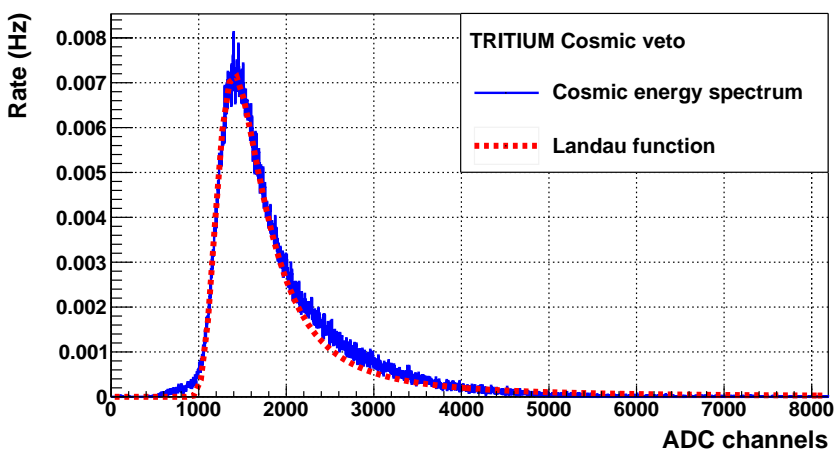


Figure 4.31 – Energy spectrum measured with the cosmic veto.

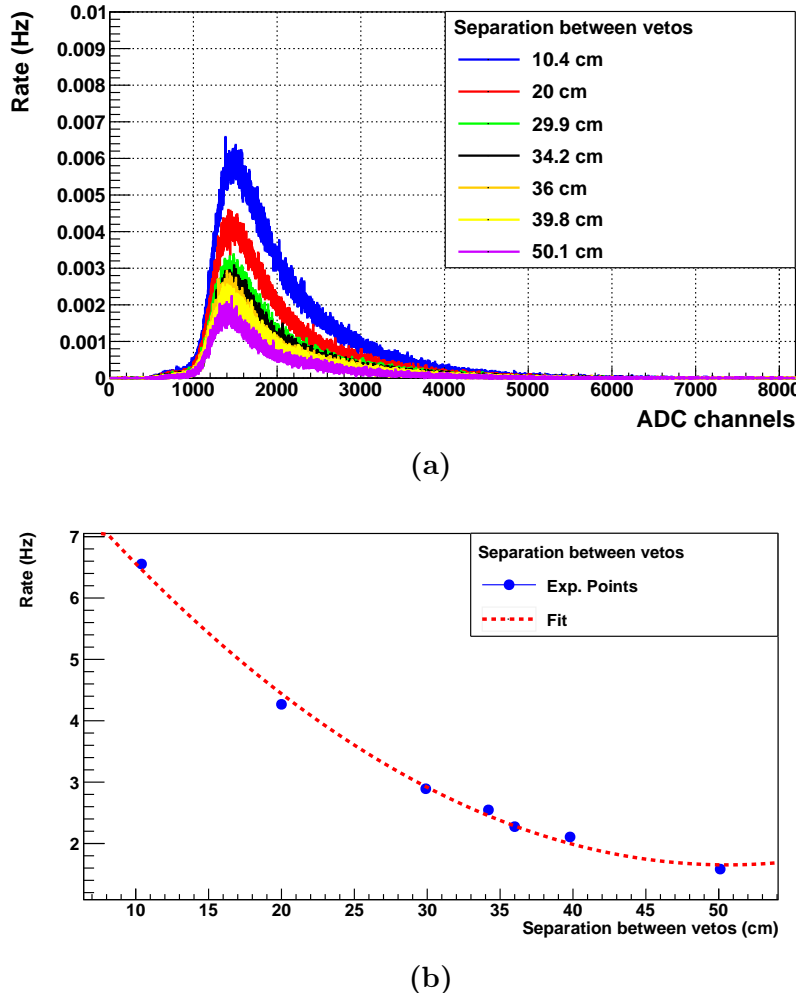


Figure 4.32 – a) Energy spectra of the cosmic veto for several separations of the scintillators. b) Fit to a second degree polynomial of the cosmic ray rate versus the separation of the veto scintillators.

Chapter 5

TRITIUM Detector Prototypes

The different prototypes developed in the framework of the TRITIUM project and their characterization are described in this chapter. They are named TRITIUM-IFIC-0, TRITIUM-IFIC-1, TRITIUM-Aveiro and TRITIUM-IFIC-2, listed in chronological order of their construction. The first two prototypes, TRITIUM-IFIC-0 and TRITIUM-IFIC-1, are preliminary prototypes used to learn about in-water tritium detection and to define the monitor design. The prototypes TRITIUM-Aveiro and TRITIUM-IFIC-2 have an optimized design based on the lessons learned from the former prototypes. Each prototype was filled with tritiated water following a specific method. Several water tightness and filling tests were carried out for each prototype. The measurements obtained by the different prototypes in the laboratories and at the Arrocampo dam are discussed in this chapter. At the end of the chapter, the final monitor design of the TRITIUM detector is described.

5.1 First IFIC prototypes

The preliminary prototypes, TRITIUM-IFIC-0 and TRITIUM-IFIC-1, were designed and built at the IFIC workshop. They are a small-scale proof of concept of the final TRITIUM detector module. They allowed us to learn about in-water tritium detection, to identify design problems and to implement improvements for the final monitor.

5.1.1 TRITIUM-IFIC-0

TRITIUM-IFIC-0 was the first prototype developed in the TRITIUM project to check the feasibility of the technology proposed by TRITIUM, that is, to employ plastic scintillating fibers to detect tritium in water with good sensitivity. As liquid radioactive sources were involved, a special attention was paid to radiation safety in the design.

TRITIUM-IFIC-0 consists of a bundle of 35 fibers of 20 cm length, which were cleaved and polished with the techniques reported in section 4.1. This bundle is attached to the vessel by means of metallic pieces located at its ends, as shown in Figure 5.1. The PVC¹ vessel, shown in Figure 5.2, was designed in a U-shape to improve radiological safety. However, this shape was not appropriate, as we learned afterwards. A frame of methacrylate and steel, shown in Figure 5.2, was designed and built to hold the prototype. Two calibrated Hamamatsu R8520-06SEL PMTs [Ham19] were optically coupled to the fiber bundle by optical grease [Saib]. The voltage divider circuit employed is shown in Figure 3.9. The high voltage was set to -800 V, at which the gains are $1.26 \cdot 10^6$ and $1.01 \cdot 10^6$, and the quantum efficiencies are 29.76% and 28.66% at $\lambda = 430$ nm, respectively. The two PMTs were read out in coincidence by the electronics shown in Figure 3.15b.

¹Polyvinyl Chloride, PVC

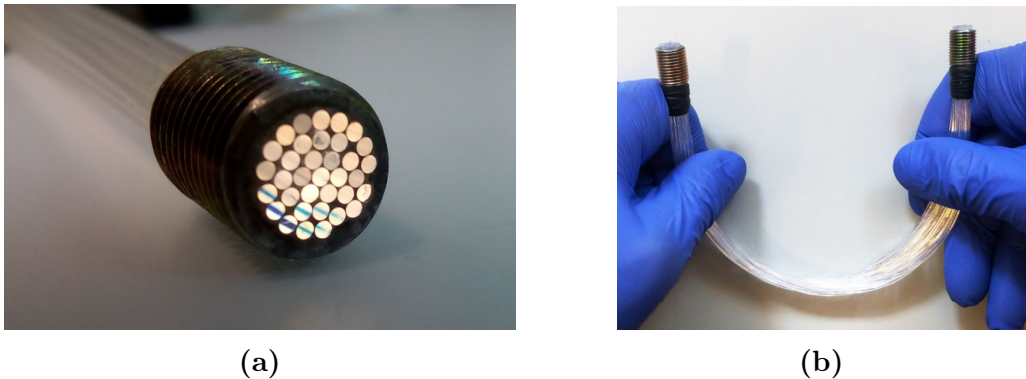


Figure 5.1 – a) Metallic piece of the fiber bundle. b) Bundle of 35 fibers of 20 cm length used in TRITIUM-IFIC-0.

Two identical prototypes were built. The first prototype, called “TRITIUM-IFIC-0 Background”, was filled with pure water (39 mL, uncertainty of 0.05%) and was used to measure the background whereas the second prototype, called “TRITIUM-IFIC-0 Signal”, was filled with a radioactive liquid source of tritiated water of a specific activity of 99.696 kBq/L (uncertainty of 2.24%) as reported in the appendix C. This second prototype was employed to measure the total signal (tritium + background). The tritium signal was determined by subtracting the background from the total signal. The number of time coincident events was too weak. The loss of photons was caused by several reasons, such as an excessive curvature of the fiber bundle due to the U-shape of the PVC vessel. Most of the photons escaped from the fibers due to both the shape of the bundle and the poor quality of the tritiated water-fiber interface (the implementation of the cleaning process described in section 4.1 was motivated by this result).

A transparent glass vessel similar to the TRITIUM-IFIC-0 prototype vessel, shown in Figure 5.3a, was built to study the effect of the fiber bundle curvature. The LED described in section 4.1 was used to verify the reduction in photon collection efficiency of the fiber bundle due to its curvature. As can be seen in Figure 5.3b, most of the photons introduced

5.1. FIRST PROTOTYPES

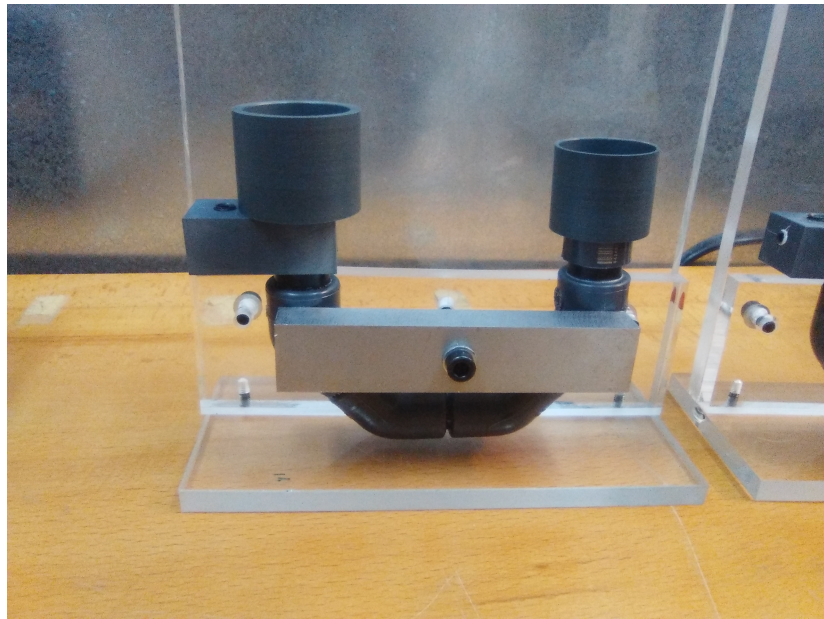


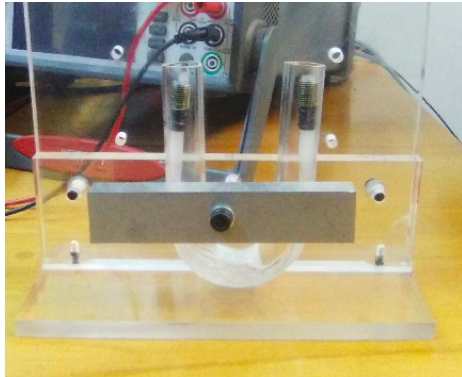
Figure 5.2 – TRITIUM-IFIC-0 prototype.

from one side of the bundle do not reach the other side due to the fiber curvature. This test shows essential to keep a straight fiber arrangement in the design of the next prototypes. A second point is that the fiber bundle employed was too compact and water may not be able to flow around the fibers. In the TRITIUM-IFIC-1 prototype the fibers were sufficiently spaced by using a PTFE matrix.

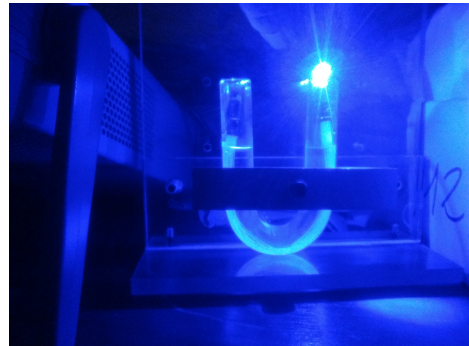
Data with TRITIUM-IFIC-0 were taken with a single PMT. The energy spectra measured for both the signal and background prototypes are shown in Figure 5.4a. The difference between signal and background, shown in Figure 5.4b, corresponds to the energy spectrum of tritium. The counting rate obtained for the three spectra are given in Table 5.1.

The tritium detection efficiency obtained for this prototype is

$$\eta = (2.1 \pm 0.9) \cdot 10^{-3} \text{ L kBq}^{-1}\text{s}^{-1}$$



(a)



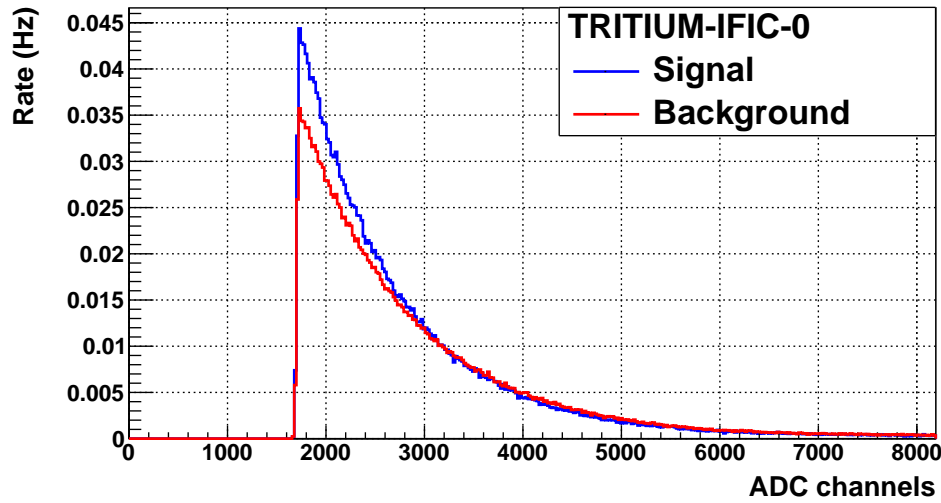
(b)

Figure 5.3 – a) Fiber bundle in a PMMA vessel. b) Illumination test of the bundle to visualize the light loss due to fiber curvature.

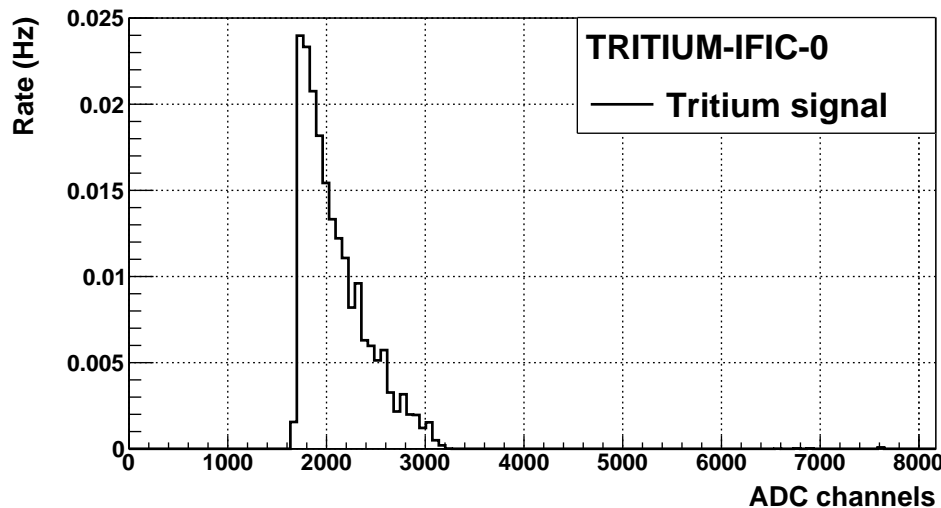
Spectrum	Rate (Hz)
Signal	2.27 ± 0.06
Background	2.06 ± 0.06
Tritium	0.21 ± 0.09

Table 5.1: Rates obtained from the TRITIUM-IFIC-0 prototype.

5.1. FIRST PROTOTYPES



(a) .



(b)

Figure 5.4 – Energy spectra measured with TRITIUM-IFIC-0 prototype.
a) Signal and background energy spectra. b) Tritium energy spectrum.

, was calculated as the ratio of the tritium counting rate to the specific activity of the tritium liquid source. As reported in section 2.1, the tritium detection efficiency scales with the active area of the scintillator used. Therefore, to compare the efficiency with other detectors in the literature and with other prototypes developed in the TRITIUM project, the specific efficiency S of this prototype is calculated by normalizing to the scintillator area,

$$S = (9.6 \pm 3.9) \cdot 10^{-6} \text{ L kBq}^{-1}\text{s}^{-1}\text{cm}^{-2}$$

As can be seen in Table 2.2, the specific efficiency is somewhat larger than that obtained by Muramatsu [Mur67], $S = 3.13 \cdot 10^{-6} \text{ L kBq}^{-1}\text{s}^{-1}\text{cm}^{-2}$, and similar to that obtained by Moghissi [Mog69], $S = 10.6 \cdot 10^{-6} \text{ L kBq}^{-1}\text{s}^{-1}\text{cm}^{-2}$. These efficiencies are too low to achieve the objective of measuring activities of the order of 100 Bq/L.

5.1.2 TRITIUM-IFIC-1

TRITIUM-IFIC-1 was designed to correct the issues found in TRITIUM-IFIC-0. The main improvements were:

1. The fiber bundle was arranged straight to optimize the photon collection efficiency of the fibers. In addition, a PTFE matrix was used to maintain a distance of 1 mm between fibers.
2. A special fiber cleaning method, described in section 4.1, was applied to the fibers to improve the quality of the interface between fibers and tritiated water. This method produces a better wetting property of the fibers, which improves their photon collection efficiency.
3. A PTFE vessel was used to improve the collection of photons inside the prototype. Indeed, PTFE has a reflectivity close to 100% at the fiber scintillating wavelengths. Thus, the photons that escape from

5.1. FIRST PROTOTYPES

fibers and hit the vessel walls are reflected back into the scintillating fibers.

The TRITIUM-IFIC-1 prototype consists of 64 straight scintillating fibers of 20 cm length, arranged in an 8×8 PTFE squared matrix, as shown in Figure 5.5. This structure is placed within a cylindrical PTFE

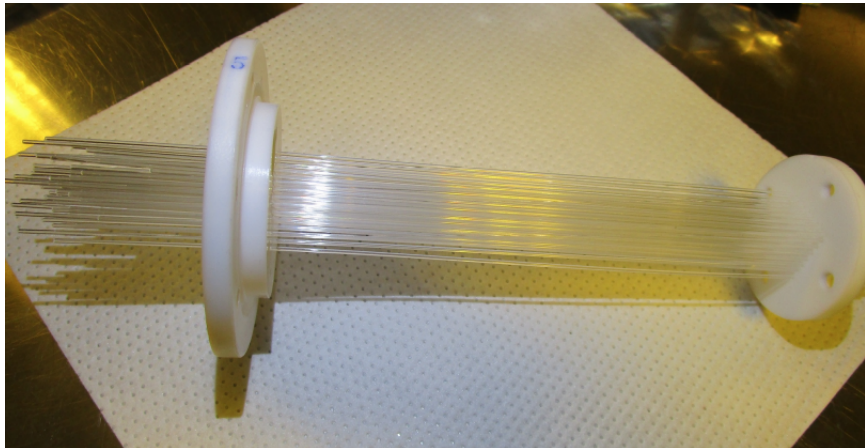


Figure 5.5 – PTFE structure used to arrange the fibers of TRITIUM-IFIC-1 prototype in a matrix of 8×8 .

vessel of 48 mm diameter and 200 mm length, shown in Figure 5.6. The cleaning process described in section 4.1 was applied to the fibers to achieve a better tritiated water-fiber interface. A PVC piece was used to couple a photosensor to the prototype and to prevent external light, as shown in Figure 5.7.

The prototype was instrumented with a PMT model R8520-06SEL, from Hamamatsu Photonics [Ham19], coupled directly to the fiber bundle by optical grease [Saib]. The quantum efficiency of this PMT is 28.66% at $\lambda = 430$ nm. The PMT high voltage was -800 V. The DAQ was the same as for TRITIUM-IFIC-0. In a first measurement, this prototype was filled with pure water (118 mL, uncertainty of 0.05%) and several background

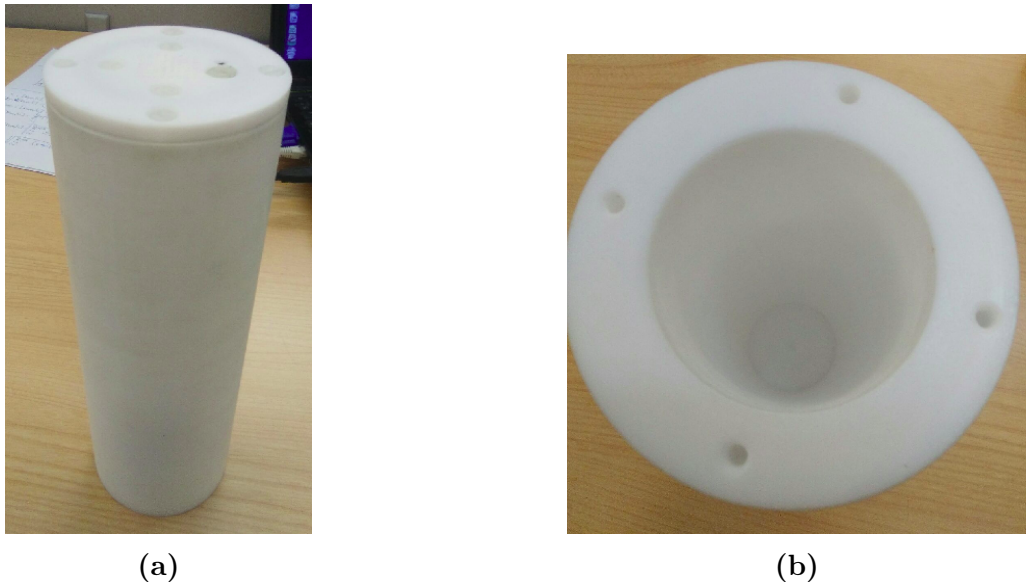


Figure 5.6 – Pictures of the TRITIUM-IFIC-1 PTFE vessel.

measurements were taken during a week. Subsequently, it was emptied and refilled with 118 mL (uncertainty of 0.05%) tritiated water of 99.696 kBq/L activity. The measured signal and background energy spectra are shown in Figure 5.8a. The tritium spectrum is shown in Figure 5.8b. The rates obtained from the integration of the spectra are given in Table 5.2.

Spectrum	Rate (Hz)
Signal	7.82 ± 0.11
Background	3.99 ± 0.08
Tritium	3.83 ± 0.13

Table 5.2: Counting rates obtained with TRITIUM-IFIC-1.

The tritium detection efficiency obtained for TRITIUM-IFIC-1 is

$$\eta = (3.84 \pm 0.16) \cdot 10^{-2} \text{ L kBq}^{-1}\text{s}^{-1}$$

5.1. FIRST PROTOTYPES

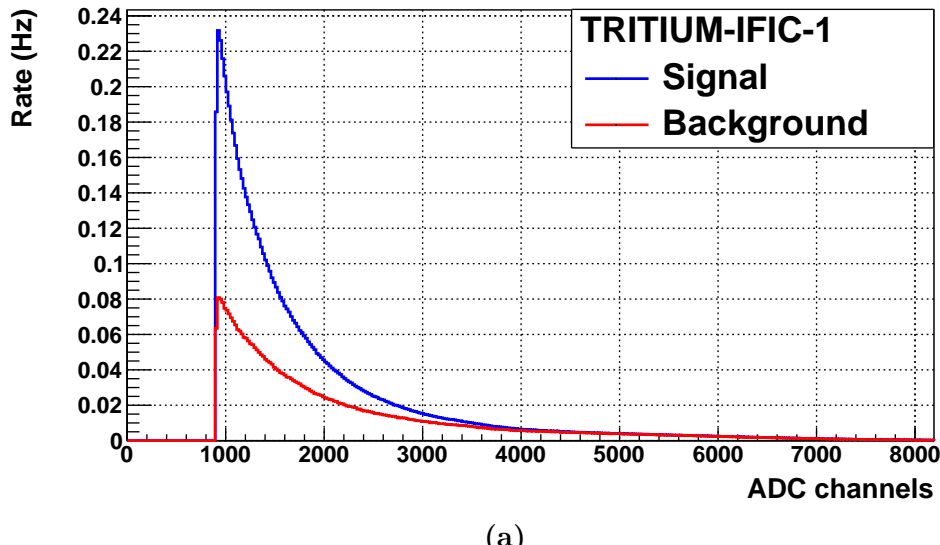


Figure 5.7 – A picture of the TRITIUM-IFIC-1 prototype. The photo-sensor lodging is shown.

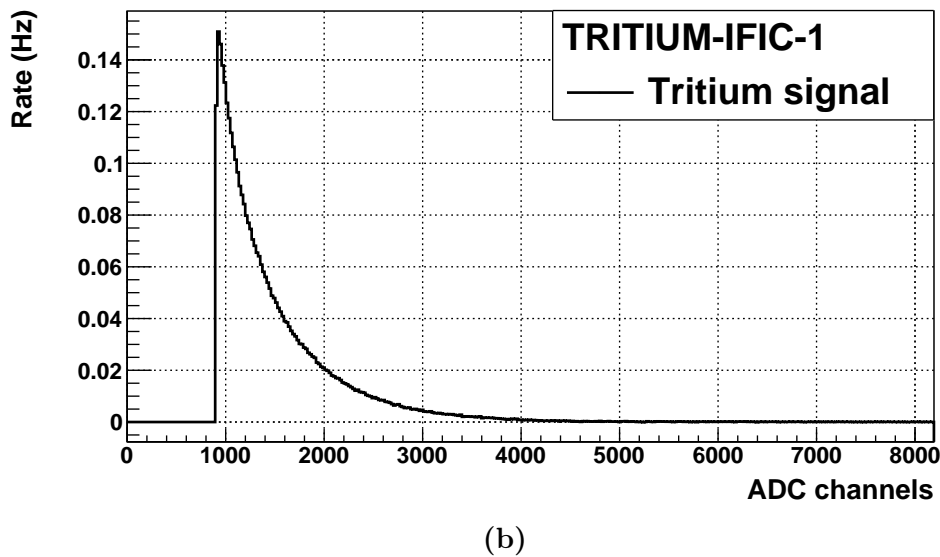
. The specific efficiency obtained is

$$S = (9.6 \pm 0.4) \cdot 10^{-5} \text{ L kBq}^{-1}\text{s}^{-1}\text{cm}^{-2}$$

which is a factor ten better than that of TRITIUM-IFIC-0. Furthermore, compared to the scintillating detectors for tritium in water given in table 2.2, the efficiency of this prototype is very close to the best result obtained by Singh [Sin85, Rat00], $\eta = 4,1 \cdot 10^{-2} \text{ L kBq}^{-1}\text{s}^{-1}$, and the specific efficiency, which is the most relevant parameter for comparison, is almost 5 times larger than that obtained by Hofstetter [Hof92a, Hof92b], $S < 22.2 \cdot 10^{-6} \text{ L kBq}^{-1}\text{s}^{-1}\text{cm}^{-2}$.



(a)



(b)

Figure 5.8 – Energy spectra measured with TRITIUM-IFIC-1. a) Signal and background energy spectra. b) Tritium energy spectrum.

5.2 Latest TRITIUM Prototypes

TRITIUM-Aveiro and TRITIUM-IFIC-2 have a different design than the previous prototypes that allows the reading of a large number of straight fibers with two photosensors operating in coincidence. Furthermore, the activity of the radioactive liquid source employed was much lower than for the first prototypes to investigate the MDA. The main differences between TRITIUM-Aveiro and TRITIUM-IFIC-2 are:

1. The diameter of the scintillating fibers, 2 mm for TRITIUM-Aveiro and 1 mm for TRITIUM-IFIC-2. The use of a larger diameter may facilitate the flow of water around the fibers, reducing issues related to surface tension and ensuring that the entire active volume of the fibers participates in tritium detection. In addition, a large radius increases the rigidity of the fibers, improving their robustness. However, the larger the radius the smaller the signal-to-background ratio. The detector active volume for 2 mm fibers is smaller than for 1 mm fibers for the same filling volume. Also, the internal volume of the fibers unreachable by tritium decay electrons, which contributes to background, is larger for 2 mm fibers.
2. The whole surface-conditioning method consisting in cleaving, polishing and cleaning methods is applied to the scintillating fibers of TRITIUM-IFIC-2. However, only the cleaving method is applied to the scintillating fibers of TRITIUM-Aveiro.
3. TRITIUM-Aveiro uses PMTs as photosensors. Although most of the development of TRITIUM-IFIC-2 was made with PMTs, it is intended to employ SiPM arrays that provides a larger photodetection efficiency than PMTs for a similar price. In addition, no high voltage is needed for SiPMs, which reduces the price of both prototype and electronics.
4. TRITIUM-Aveiro uses a home-made PCB-based electronics which is

cheaper than PETsys. However, the PETsys system is quite stable and meets the TRITIUM monitor scalability requirement without any additional development.

The development and operation of these two prototypes aim at defining the best design for the final TRITIUM monitor.

5.2.1 TRITIUM-Aveiro

TRITIUM-Aveiro is a proposal for the final TRITIUM detector module. This prototype, shown in Figure 5.9, was designed and built in the University of Aveiro. It consists of a PTFE vessel, shown in Figure 5.10, with an internal cylindrical hole of 43 mm diameter and 18 cm length. This

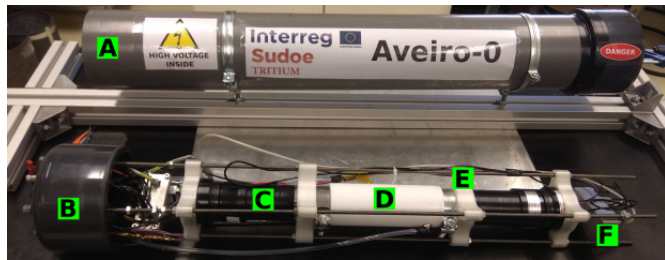


Figure 5.9 – TRITIUM-Aveiro prototype. A and B are the PVC structure, C is the PMT, D is the PTFE vessel, E is the 3D printer piece and F is the electronics.

vessel contains 360 BCF-10 uncladded scintillating fibers of 180 mm length from Saint-Gobain [Sai21b], which are similar to the BCF-12 fibers except the diameter and the attenuation length (2.2 m for BCF-10 and 2.7 m for BCF-12). The scintillating fibers are stacked within the PTFE vessel in the maximum number that allows water to flow around them. These fibers were cleaved with the device described in section 4.1, but they were neither polished nor cleaned because the automatic polishing machine was not yet

5.2. LATEST TRITIUM PROTOTYPES



Figure 5.10 – PTFE vessel and fiber bundle used in TRITIUM-Aveiro prototype.

developed and it was not feasible to polish 360 fibers by hand. The PTFE vessel is totally closed and a water inlet and outlet were installed to allow a constant water flux through it. Two PMMA 10 mm thick windows located at both ends of the fiber bundle are used to read out the fibers. Two clamps are used to make a tight junction of the PTFE walls and the PMMA windows. PMMA was chosen for its optical properties, especially its transmission coefficient which is larger than 95% at the scintillating fiber wavelength. Two R2154-02 2" PMTs from Hamamatsu [Ham10], shown in Figure 5.9), are used to read out this prototype in coincidence. The PMT quantum efficiency is 26% at $\lambda = 430$ nm and the HV was set at -1500 V. The PMTs are optically coupled to the PMMA windows through optical grease [Saib]. The Aveiro prototype and its electronics were arranged in a structure composed of several clamps and four stainless-steel screws locked to an external PVC structure. This structure protects the prototype from physical damage and provides a light-tight operation environment. Only one

prototype was built, which was designed to be installed in the Arrocampo dam. Two graphical interfaces were developed to control the PMT power supply and the data adquisition, respectively.

Measurements to characterize the detector were carried out in the I3N and LARUEX laboratories. The prototype was in first place filled with pure water to measure the background and next with a radioactive liquid tritium solution of 30 kBq/L activity, which was used to measure the prototype efficiency and MDA. The volume of pure water and tritium solution used in TRITIUM-Aveiro prototype was 58 mL.

To quantify the background attenuation by a lead shield, measurements without shielding and with 2.5 mm and 5 mm lead shields were carried out at I3N. A background reduction by factors about 2 and 4 was obtained by the 2.5 mm and 5 mm lead shields, respectively, as shown in Figure 5.11.

The prototype was installed in the LARUEX laboratory in order to be tested with tritiated water. The background was measured during 4 days with the prototype filled with pure water and shielded by 5 cm lead. The events were grouped in 1 minute time bins and the data were fitted to a Gaussian function as shown in Figure 5.12. An average rate of 540 min^{-1} with a standard deviation of $\sigma_{Nb} = 23 \text{ min}^{-1}$ was obtained. To calculate the MDA, the detection limit concepts developed by Lloyd A. Currie [Kno10] were applied. The minimum number of net counts with a probability of a false-negative less than 5% is given by,

$$N_D = 4.65 \cdot \sigma_{Nb} + 2.71 = 111 \text{ min}^{-1} \quad (5.1)$$

which corresponds to a critical level of

$$L_C = 2.33 \cdot \sigma_{Nb} = 53 \text{ min}^{-1}$$

L_C and N_D are calculateed after background subtraction. Therefore, the

5.2. LATEST TRITIUM PROTOTYPES

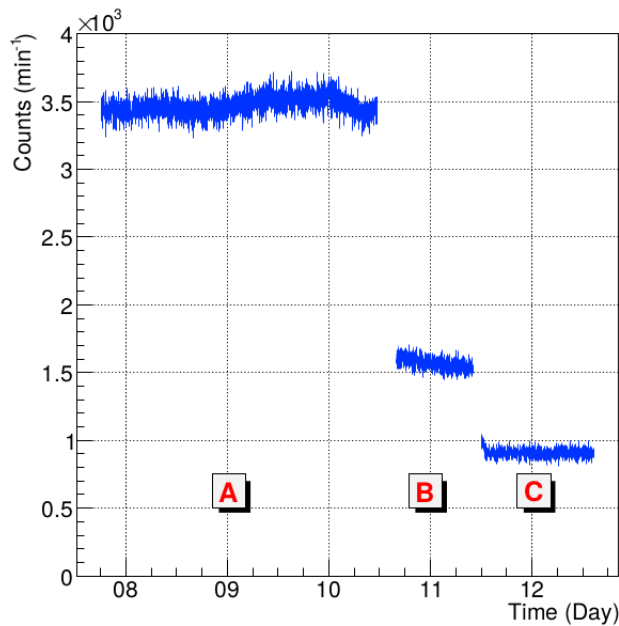


Figure 5.11 – Background rate of the TRITIUM-Aveiro prototype. A) Without shielding. B) With a lead shield of 2.5 mm thickness. C) With two lead shields of 2.5 mm thickness each one [Aze22].

critical level L'_C and the minimum count rate distinct from the background N'_D are

$$L'_C = 540 + 53 = 593 \text{ min}^{-1}$$

and

$$N'_D = 540 + 111 = 651 \text{ min}^{-1}$$

To find the MDA, tritiated water was slowly added so that the tritium water activity increased continuously till reaching the N'_D value. A rate of $(656 \pm 26) \text{ min}^{-1}$ was obtained that corresponds to a $\text{MDA} = (29.8 \pm 3.6) \text{ kBq/L}$ measured with a Quantulus LSC.

The tritium detection efficiency was calculated from the ratio of the net tritium rate measured, $(1.9 \pm 0.6) \text{ sec}^{-1}$, and the activity of the tritium source used, 29.8 kBq/L. The tritium detection efficiency obtained

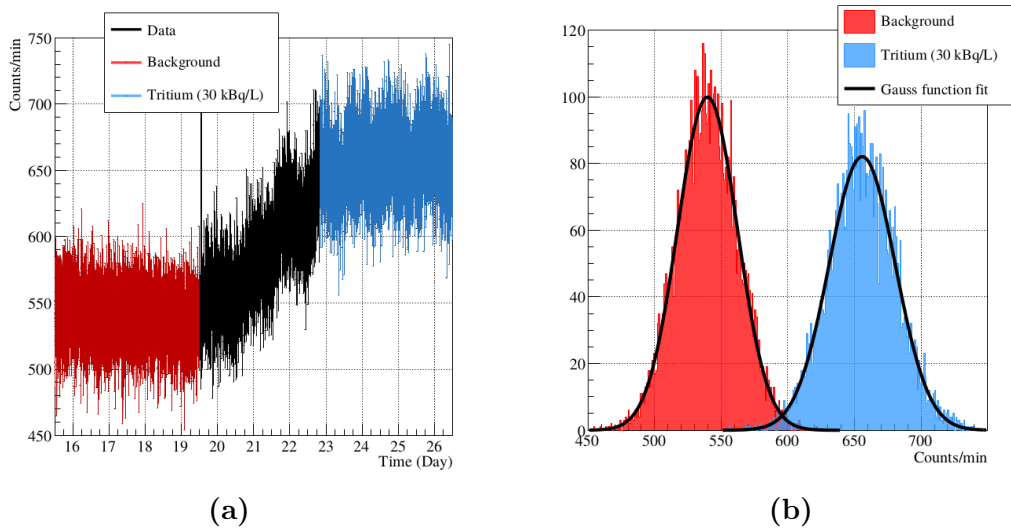


Figure 5.12 – Background and tritium liquid source (29.8 kBq/L) with the TRITIUM-Aveiro prototype [Aze22]. a) Counts per minut measured as a function of time. b) Distribution of the acquired data.

is

$$\eta = (6.5 \pm 1.9) \cdot 10^{-2} \text{ L kBq}^{-1}\text{s}^{-1}$$

and the specific efficiency is

$$S = (1.6 \pm 0.5) \cdot 10^{-5} \text{ L kBq}^{-1}\text{s}^{-1}\text{cm}^{-2}$$

Comparing to the specific efficiency obtained with scintillating detectors in the literature (Table 2.2), the specific efficiency of TRITIUM-Aveiro is close to the largest value $S < 2.22 \text{ LkBq}^{-1}\text{s}^{-1}\text{cm}^{-2}$ [Hof92a, Hof92b]. TRITIUM-Aveiro has a lower specific efficiency than TRITIUM-IFIC-1, which could be attributed to the absent of polishing and cleaning of the fibers of this prototype. The efficiency uncertainty obtained is larger than for the first TRITIUM prototypes because of the shorter measurement time (1 minute instead of several hours). As the MDA depends directly on the background uncertainty, longer measurements are needed. The data for an integrated time of 60 min is shown in Figure 5.13. The mean and the uncertainty of

5.2. LATEST TRITIUM PROTOTYPES

the measured background data are $3.186 \cdot 10^4 \text{ h}^{-1}$ and 225 h^{-1} respectively. From the equation 5.1, values of $L_C = 524 \text{ h}^{-1}$ and $N_D = 1048.96 \text{ h}^{-1}$ are obtained. Assuming linearity between the activity and the counting rate, $N'_D = 3.872 \cdot 10^4 \text{ h}^{-1}$ corresponds to MDA=(3.6 ± 0.1) kBq/L. A daily oscillation is clearly observed in Figure 5.13, indicating that the measurements are affected by external light. This oscillation begins on the 19th day when the water closed-circuit pump was installed, so it is likely that the light tightness of the system was affected. This prototype was finally installed in

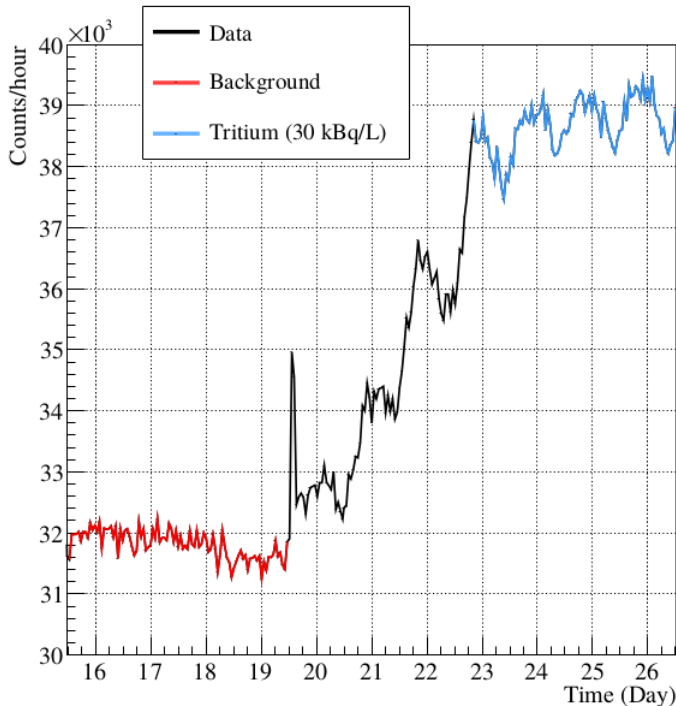


Figure 5.13 – Background and tritium liquid source counting rates measured with TRITIUM-Aveiro [Aze22] .

the Arrocampo dam to test its functionality and to begin with the tritium level monitoring reported in section 5.3.

5.2.2 TRITIUM-IFIC-2

The last prototype developed was TRITIUM-IFIC-2, shown in Figure 5.14. This prototype, built in the IFIC workshop, consists of a cylindrical PTFE vessel similar to the Aveiro prototype, shown in Figure 5.15. The internal length and diameter of the PTFE vessel were 210 mm and 36 mm respectively. This prototype contains 800 uncladded BCF-12 scintillating fibers of 200 mm length and 1 mm diameter. This number of fibers is larger than in the Aveiro prototype and is contained in a smaller volume. Fibers were cleaved, polished and cleaned with the conditioning processes described in section 4.1. These scintillating fibers were tightly stacked but allowing water to flow around them. Two 5 mm thick PMMA windows allow to read the scintillation light out in a similar way as in Tritium-Aveiro. This thickness

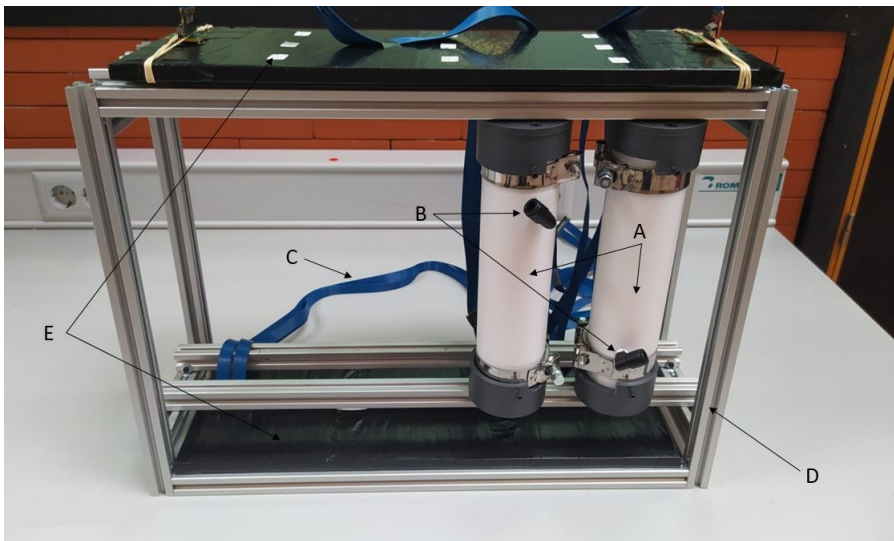


Figure 5.14 – (A) TRITIUM-IFIC-2 prototype, (B) water inlet/outlet, (C) PETsys flat wires, (D) the metallic structure and (E) active veto.

is enough to seal the vessel since the detector works at very low water pressure. PMMA was chosen for its optical properties, especially its transmission coefficient plotted in Figure 5.16 which was measured at ICMOL. This

5.2. LATEST TRITIUM PROTOTYPES



(a)



(b)

Figure 5.15 – a) TRITIUM-IFIC-2 PTFE vessel. b) TRITIUM-IFIC-2 PTFE vessel with two PVC caps that provide a light-tight environment for the SiPM arrays.

transmission coefficient is approximately 95% at the working wavelength (435 nm). Two clamps keep the prototype sealed as in TRITIUM-Aveiro. A water inlet/outlet was implemented in the PTFE vessel to allow a con-

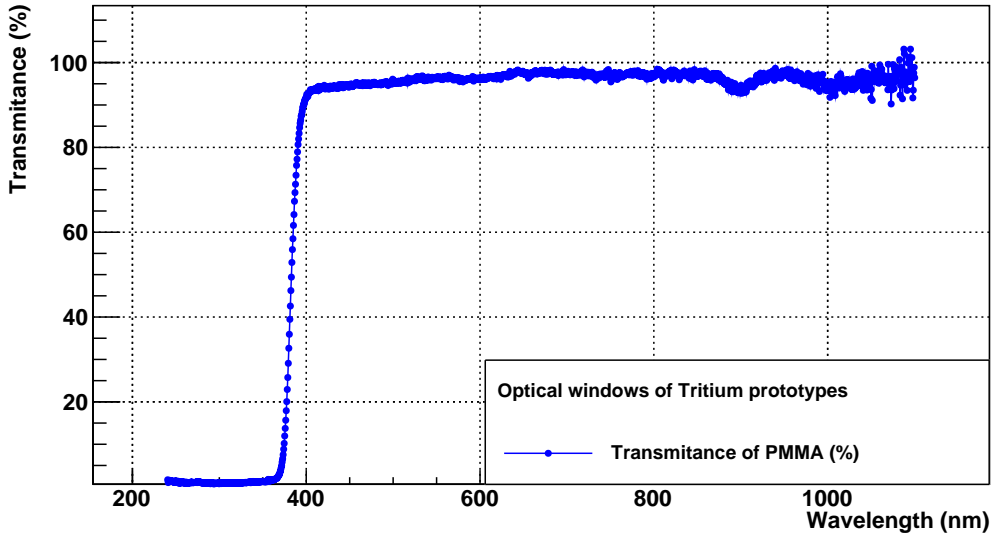


Figure 5.16 – Light transmission spectrum of a 5 mm thick PMMA plate, measured at ICMOL.

stant water flow as in TRITIUM-Aveiro.

In the laboratory measurements, two R8520-460 Hamamatsu PMTs [Ham19] were used. Measurements with SiPM arrays controlled by PETsys were also performed. PETsys has a graphical user interface that allows to remote control the different input and output options such as SiPM arrays bias voltage, thresholds, etc., via a computer terminal. A picture of the GUI is shown in Figure 5.17.

An aluminium structure was built to accommodate up to 10 TRITIUM-IFIC-2 modules and two cosmic vetos, shown in Figure 5.14. The available space inside the lead shield in Arrocampo site could lodge up to 5 structures. This means that the final TRITIUM monitor could be composed of

5.2. LATEST TRITIUM PROTOTYPES

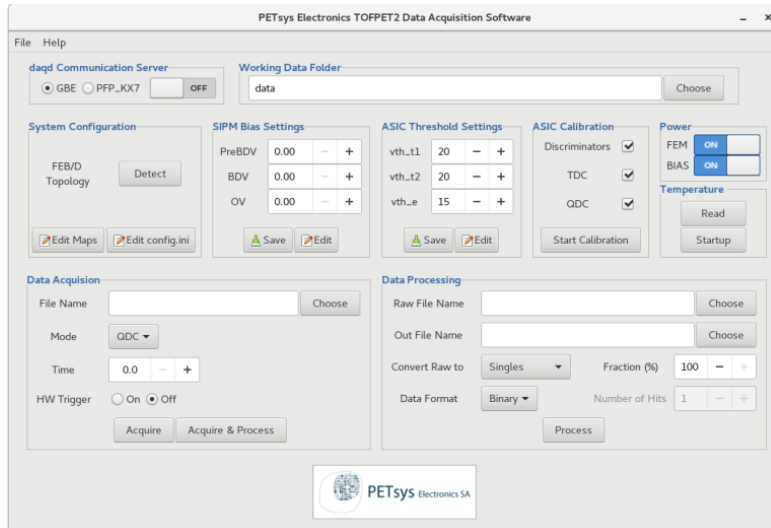


Figure 5.17 – Graphical User Interface of PETsys.

up to 50 TRITIUM-IFIC-2 modules and 5 different cosmic vetos.

Two identical TRITIUM-IFIC-2 prototypes were built. One was filled with pure water and the second with a tritium liquid source to measuring the background and the signal, respectively. The water volume in both cases was 82 mL (uncertainty of 0.05%). The activity of the tritium source employed was 10 kBq/L (uncertainty of 2.24%). The signal and background energy spectra are shown in Figure 5.18. The energy spectrum of tritium was obtained by subtracting the background from the signal spectrum. The rates obtained from these three spectra are given in Table 5.3.

Spectrum	Rate (Hz)
Signal	19.05 ± 0.18
Background	11.54 ± 0.14
Tritium	7.11 ± 0.23

Table 5.3: Counting rates measured by TRITIUM-IFIC-2.

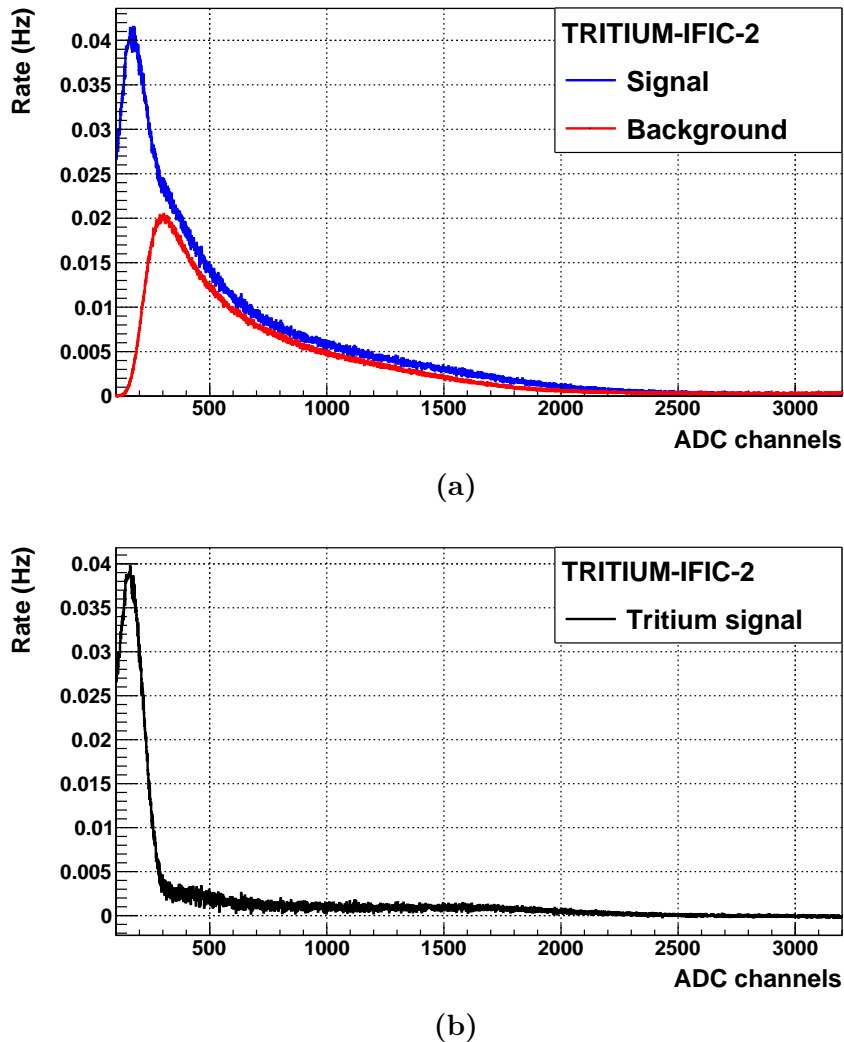


Figure 5.18 – Energy spectra measured with TRITIUM-IFIC-2. a) Signal and background energy spectra. b) Tritium energy spectrum.

5.2. LATEST TRITIUM PROTOTYPES

The tritium detection efficiency obtained for this prototype is

$$\eta = (7.11 \pm 0.28) \cdot 10^{-1} \text{ L kBq}^{-1}\text{s}^{-1}$$

This efficiency is larger than those reported in the literature (Table 2.2). This is an expected result since the active area of this prototype is the largest. The specific efficiency is

$$S = (14.1 \pm 0.6) \cdot 10^{-5} \text{ L kBq}^{-1}\text{s}^{-1}\text{cm}^{-2}$$

which is the largest reported for tritium detection.

A detector calibration in units of photons detected per event can be obtained from the single-photon distribution of the PMTs, which are fitted to a Gaussian function as shown in Figure 5.19a. As can be seen, the mean and uncertainty of the single photon signal are around 172 and 66 ADC channels, respectively, for one PMT and 173 and 57 ADC channels, respectively, for the other. The tritium signal given in number of photons detected per event, shown in Figure 5.19b, is obtained as the ratio of the tritium energy spectrum to the single-photon distribution mean. A maximum of 15 photons are measured per tritium event, which is in agreement with the results of the simulations described in Chapter 6.

A monitoring of the signal and background prototypes was carried out during several months. The rates measured are shown in Figure 5.20. No quenching of the signal with time was observed, which indicates the detector efficiency remained stable during about 6 months.

To calculate the MDA, the background was binned in 10 min and 60 min intervals. The mean values and standard deviation of these measurements are shown in the Table 5.4. The N_D and the L_C obtained from the Currie criterium (equation 5.1) are given in Table 5.4. The N'_D referred to the detector signal before background subtraction are 6019 and 34706 for an integration time of 10 min and 60 min, respectively. The MDA of tritium

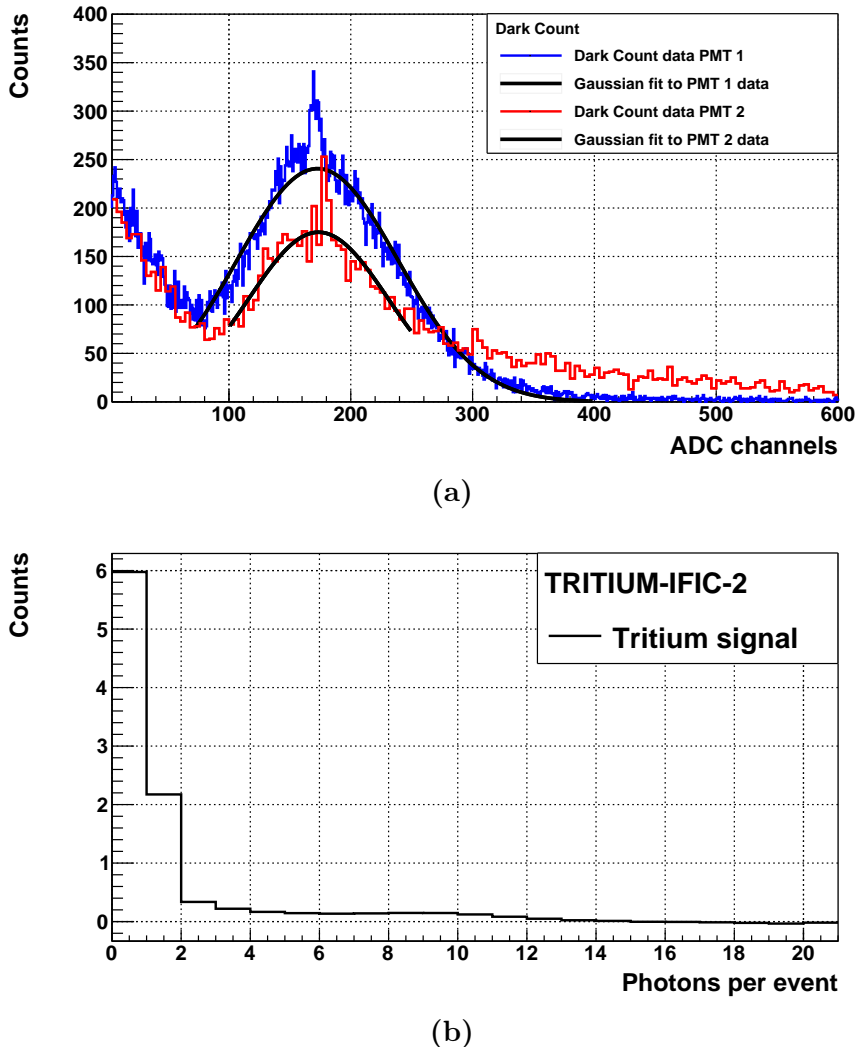


Figure 5.19 – a) Single photon distribution of TRITIUM-IFIC-2 PMTs. b) Tritium energy spectrum measured with TRITIUM-IFIC-2 versus number of photons detected per event.

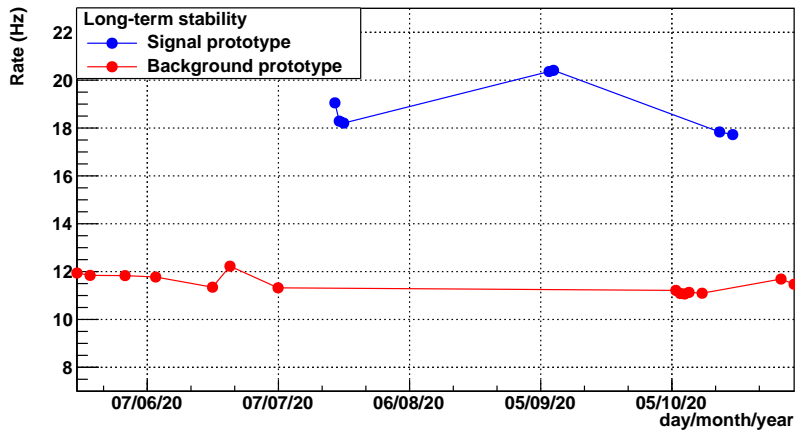


Figure 5.20 – Signal and background rates for a long time measurement.

Time (min.)	\bar{N}	$\sigma_{\bar{N}}$	L_C	N_D
10	5635	82	191	384
60	33969	158	368	737

Table 5.4: Mean value \bar{N} and standard deviation $\sigma_{\bar{N}}$ of fourteen background measurements. N_D and L_C obtained from the Currie criterium.

is obtained from N'_D by associating the mean value of the background to a null tritium activity and the mean value of the signal to a tritium activity of 10 kBq/L, assuming that counting rate scales linearly with activity. This results in a MDA of 677 Bq/L and 218 Bq/L for an integration time of 10 min and 60 min, respectively. In addition, it has to be taken into account that one of the most important properties of the TRITIUM detector is its scalability, which means that results can be improved by increasing the number of modules. The MDA of the TRITIUM monitor is expected to be reduced by the square root of the number of modules, according to equation 5.1. The plot of the MDA versus the number of modules is shown in Figure 5.21, where it can be seen that the goal of the TRITIUM project of measuring 100 Bq/L in quasi-real time is achieved with 45 TRITIUM-

IFIC-2 modules read out in parallel with an integration time of 10 min or 5 TRITIUM-IFIC-2 modules with an integration time of 1 h, which is the cheaper and more realistic option.

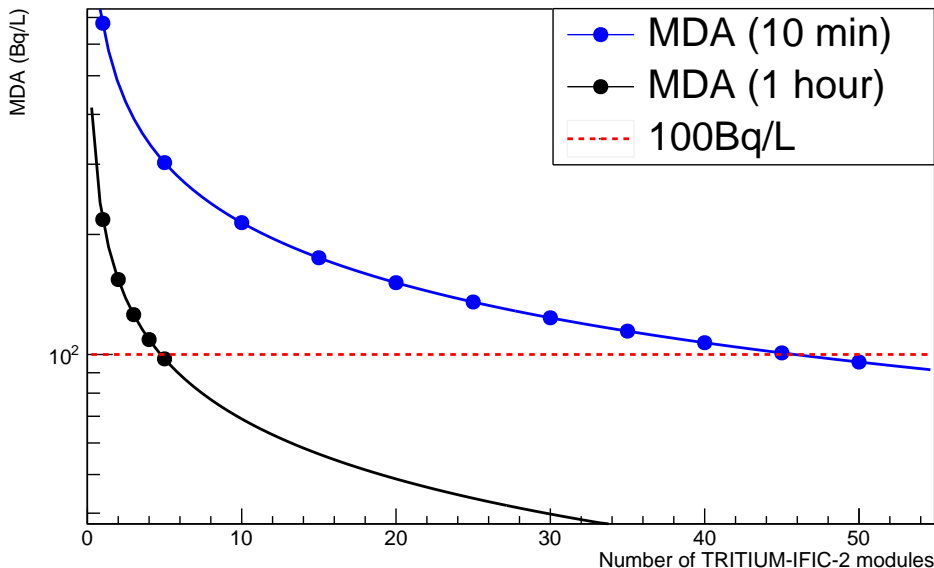


Figure 5.21 – MDA as a function of the number of TRITIUM-IFIC-2 modules read out in parallel for an integration time of 10 min (blue line) and 1 h (black line). The dotted red line corresponds to 100 Bq/L.

5.3 Results from Measurements at Arrocampo Dam

The measurements obtained with the TRITIUM-Aveiro prototype in the Arrocampo dam are reported in this section. This prototype recorded data during more than four months (27/03/2019 to 18/08/2019). The data acquired during this time are plotted in Figure 5.22, for bins of 60 minutes. The data look stable during the measuring period. An average rate of

5.3. EXPERIMENTAL RESULTS IN ARROCAMPO DAM

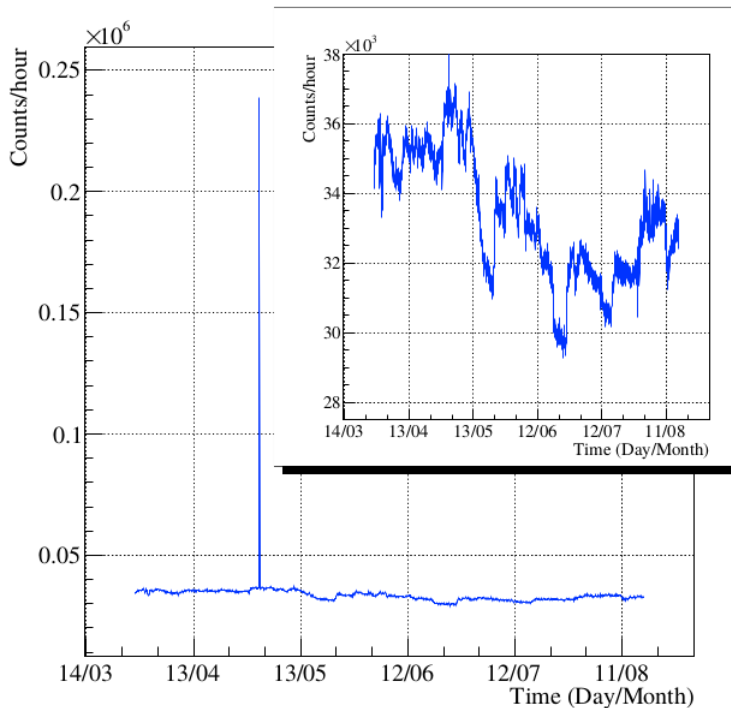


Figure 5.22 – Background measured with the TRITIUM-Aveiro prototype in the Arrocampo site [Aze22].

9.3 s^{-1} was obtained. A narrow peak is observed on May 2 caused by the removal of part of the lead shield top for an intervention in the prototype. The data are magnified in the inset of the figure. The MDA measured in Arrocampo dam for a 60 minute integration time is 6 times larger than in the laboratory measurements (section 5.2.1). This may be due to the electric noise introduced by the pumps of the water purification system and the instability observed in the electronic boards.

5.4 Modular TRITIUM Detector

The proposal of the final TRITIUM monitor is presented in this section. A schematic design is shown in Figure 5.23. This proposal consists of a number of TRITIUM modules read out in parallel. The design of the modules will be made according to the results obtained from the prototypes. These monitor is shielded from the environmental radioactivity by three different techniques:

1. An external lead shield that stops the environmental radioactivity and soft cosmic rays (particles with energies below 200 MeV).
2. Several active vetos which are placed below and above the TRITIUM detector. These active vetos are read out in anticoincidence to mitigate high energy background, mainly cosmic ray particles with energies above 200 MeV.
3. A water purification system which eliminates radioactive elements present in the water samples measured by the TRITIUM monitor.

The water purification system, the lead shield and a TRITIUM-Aveiro prototype are currently in operation at the Arrocampo site. Furthermore, two additional TRITIUM-Aveiro prototypes and four active vetos currently under construction will be installed in parallel with this prototype. The electronics of the TRITIUM-Aveiro prototype is based on a RaspberryPi and cannot read more than one module due to hardware limitation. A FPGA-based counter board will replace this electronics.

Three TRITIUM-IFIC-2 prototypes and two active veto are already built and will be installed at Arrocampo as soon as possible. At present, lateral cosmic vetos for the TRITIUM-IFIC-2 modules are not foreseen since the influence of side cosmic rays is expected to be small ($\propto \cos^2(\theta)$), but they can be included in the future if necessary.

5.4. MODULAR TRITIUM DETECTOR

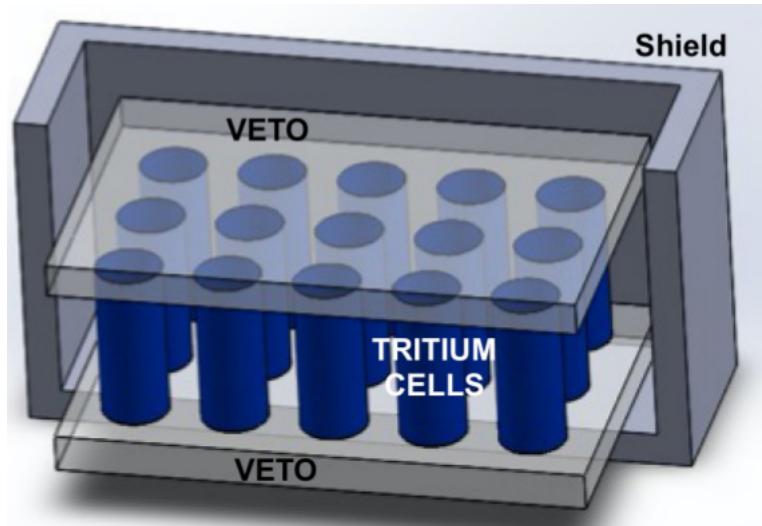


Figure 5.23 – A schematic design of the TRITIUM detector.

One of the most important aspects of the TRITIUM monitor is its modular design, which allows scalability to reach the required sensitivity of 100 Bq/L. It means that if this target sensitivity is not achieved with three modules, it can be obtained by installing additional modules. The only scalability restriction is the available space which is set by the lead shield and the cabin in which the setup is installed. In the currently available space, five different structures as the one shown in Figure 5.24 can be placed, each containing 10 modules and two active veto. If 50 TRITIUM modules are installed, the sensitivity of the TRITIUM monitor could be improved by a factor of around $\sqrt{50}$ with respect to the sensitivity of a single module.

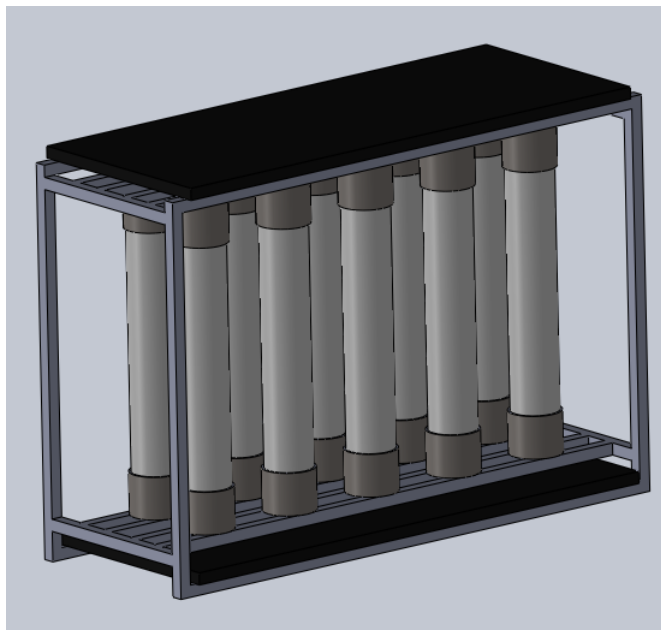


Figure 5.24 – A TRITIUM monitor design based on the TRITIUM-IFIC-2 prototype.

5.4. MODULAR TRITIUM DETECTOR

Chapter 6

Simulations

The Monte Carlo simulations performed in the TRITIUM project are described in this chapter. They were carried out to optimize the design of the TRITIUM detector, to understand its behaviour and to investigate its limitations. This chapter is divided into two different sections. The first section contains the results of simulations done to improve the design of the TRITIUM detector, while the second section describes the simulation results of a full TRITIUM monitor composed of several TRITIUM-IFIC-2 modules read out in anticoincidence mode with an active cosmic veto. Furthermore, several tests were carried out to check the different simulated steps such as the simulated tritium source and the energy deposition and the production of photons in the fibers. The simulation environment employed is Geant4 [GEA, Ago03].

6.1 Geant4 Environment

Geant4 is a software toolkit for the simulation of the passage of particles through matter developed at CERN, based on object-oriented technology

6.1. GEANT4 ENVIRONMENT

implemented in the C ++ programming language. Geant4 allows the definition of the different aspects of the simulation process such as detector geometry, materials, particles, physical processes of particle and matter interactions, response of sensitive detectors, generation, storage and analysis of event data and visualization.

Geant4 simulates particle-by-particle physics. This means that the tritium events are generated one by one, generating energy, momentum, position, etc. The propagation of each tritium decay electron and its interaction with the scintillator is simulated, and optical photons are created. The propagation of these optical photons are also simulated one by one and the simulation ends when all the created optical photons have been absorbed by either the sensitive detector or other materials present in the simulation. The physics list used for these simulations is G4EmLivermorePhysics, which is specially designed to work with low energy particles. This list includes the most important electromagnetic processes at low energies such as bremsstrahlung, Coulomb scattering, atomic radiation and other related effects. The materials included in these simulations were water (the tritiated water source), PMMA (the optical windows of the prototype), polystyrene (the scintillating fibers), PTFE (the prototype vessel), silicone (the optical grease), silicate glass (windows of the PMTs) and bialkali (the photocathode material of the PMT). The properties of water, PTFE and polystyrene were taken from the Geant4 NIST database and the other materials were built by specifying their atomic composition. The following optical properties not included in the data base were added:

1. The refraction index, the light attenuation coefficient obtained from ref. [Bui94] and the tritium decay electron spectrum uniformly distributed in the volume obtained from ref. [Mer15] for water.
2. The spectra of refractive index, light attenuation, photon emission, scintillation yield and decay time coefficient obtained from the data sheet [Sai21b] for polystyrene.

3. The quantum efficiency spectrum for the photocathode material of the PMTs [Ham19]. A refraction index of 1.46 for optical grease [Saib].
4. The optical data for PMMA windows, PTFE and silicate glass from ref. [Arg11].

6.2 Simulations for the design of the TRITIUM Detector

Several simulations were performed during the design of the TRITIUM detector to quantify the influence of some parameters as the diameter and the length of the scintillating fibers to optimize tritium detection. As the tritium electrons have a very short mean free path, the shape of the simulated tritium source was optimized to reduce computing time.

6.2.1 The Tritiated Water Source

The mean free path of tritium electrons in water is only around $5 \mu\text{m}$, so most electrons emitted in tritiated water do not reach the scintillating fibers. These electrons do not provide useful information and only consume computing resources. To optimize the simulation, the dimensions of the simulated tritium source were set to maximize the number of tritium events reaching the scintillating fibers. It was checked that the energy distribution of the simulated tritium events, shown in figure 6.1a, agrees with the input spectrum. The distribution of the initial energy of tritium electrons capable of penetrating a fiber and depositing energy, shown in Figure 6.1b, is shifted to high energies and has a peak centred at 10 keV.

A 20 cm long and 2 mm diameter scintillating fiber surrounded by a tritiated water source of the same length and 0.5 mm thickness (100

6.2. SIMULATIONS FOR THE DESIGN OF THE TRITIUM DETECTOR

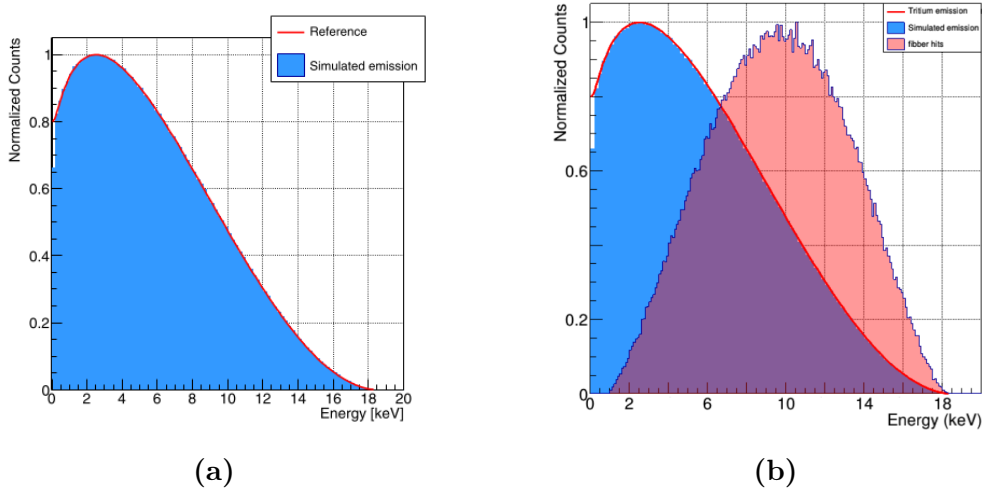


Figure 6.1 – Energy distribution of a) simulated tritium decays b) Initial energy of tritium decays that reach the scintillating fibers (red histogram) compared to all simulated tritium events (blue histogram) [Aze20].

times greater than the mean free path of tritium electrons) were simulated. Only the energy deposition of tritium electrons in the fiber was registered, excluding optical processes. The goal of these simulations was to find the radial thickness of the simulated tritium source beyond which no significant amount of tritium decay electrons are detected. In Figure 6.2a, a transversal cut of the 2 mm scintillating fiber, the 0.5 mm thick tritium source surrounding the fiber and the position where the tritium decays deposit energy in the scintillating fiber are shown. Furthermore, the distribution of the radial distance between the position where tritium decays take place and the surface of the scintillating fiber is shown in figure 6.2b. The thickness of the simulated tritium source was $5 \mu\text{m}$ since 99.4% of the events that deposit energy in the fibers are produced at a shorter distance. These results are independent of the fiber diameter.

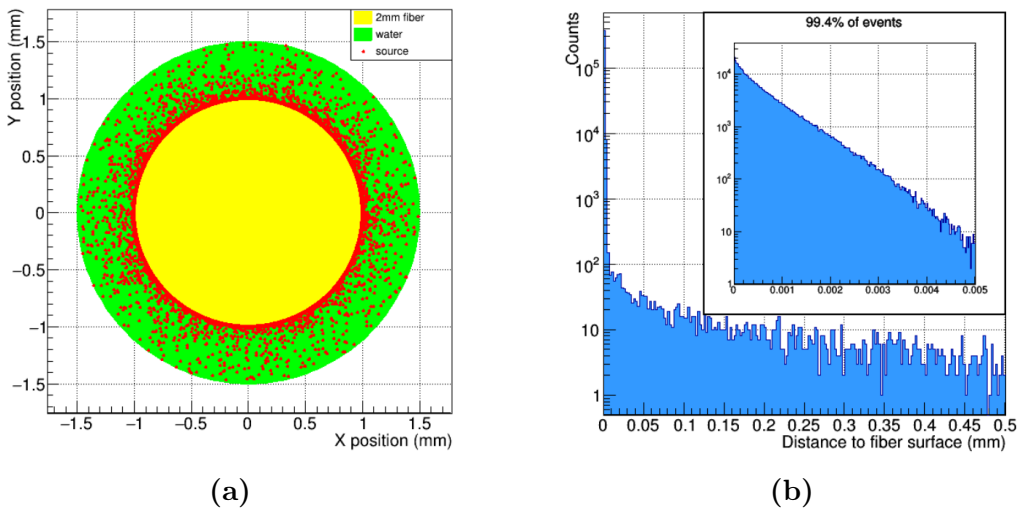


Figure 6.2 – a) Cross seccion of a simulated scintillating fiber (yellow) and the tritium source (green) with various tritium decays (red dots) b) Distribution of the radial distance between the position where the tritium decays take place and the surface of the scintillating fiber [Aze20]. A zoom of low energy events is shown in the inset.

6.2. SIMULATIONS FOR THE DESIGN OF THE TRITIUM DETECTOR

6.2.2 Energy Deposition and Light Output in Scintillating Fibers

The scintillation yield provided by the manufacturer, 8000 photons/MeV, is only valid for minimum ionizing particles (MIP). As tritium electron energies are not MIP particles, the output light generated by the scintillating fibers was studied. The emission of scintillation photons were also simulated.

When particles that are not MIP are detected in plastic scintillators, an output light quenching effect happens, which can be parametrized by the Birk's coefficient[Bir51],

$$\frac{dL}{dx} = S \frac{\frac{dE}{dx}}{1 + k_B \frac{dE}{dx}} \quad (6.1)$$

Where $\frac{dL}{dx}$ is the output light per unit of path length, $\frac{dE}{dx}$ is the energy deposited per unit of path length and S is the scintillation yield for MIPs, provided by the manufacturer. A Birk's coefficient $k_B = 0.126$ mm/MeV is typically used for scintillators based on polystyrene [Lev11]. In this section, the importance of this quenching effect and how it affects the tritium detection is discussed.

A study of the energy deposition of tritium electrons on scintillating fibers was carried out. In Figure 6.3 the initial energy of simulated tritium electrons that reach the scintillating fibers is compared to the energy deposited in them. A shift to lower energies is observed, caused by the energy loss of tritium electrons in water is observed. The cut at about 1 keV visible in both energy distributions is produced by the default energy threshold of 990 eV in the G4EmLivermorePhysics list. Figure 6.4 shows two distributions of the number of photons produced in scintillating fibers by tritium events, one in which the quenching effect is not considered ($k_B = 0$) and the other with the Birk's coefficient set to $k_B = 0.126$ mm/MeV. A dis-

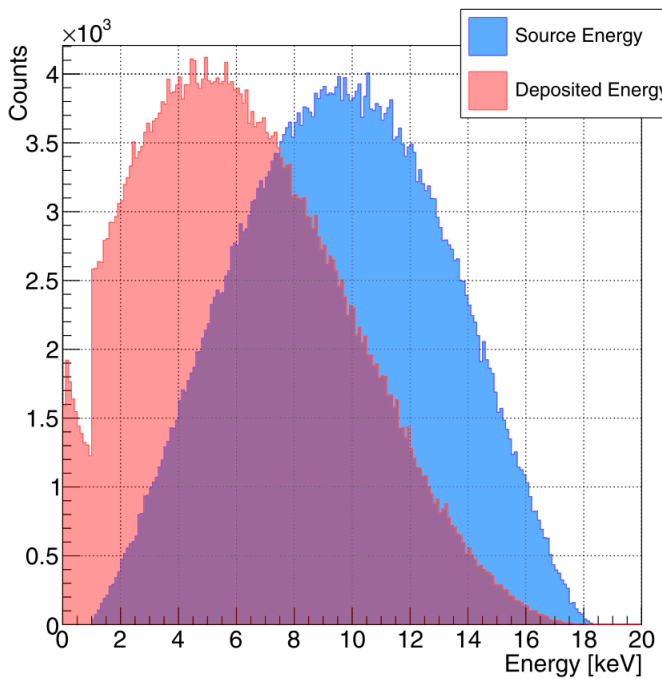


Figure 6.3 – Distribution of the initial energy of tritium events that reach the scintillating fibers (blue histogram) and the energy deposited in them (red histogram) [Aze20].

tribution with a peak close to 40 photons per tritium event and a maximum near 150 photons were obtained when the quenching effect is not considered. A significant reduction of the output light is observed when the Birk's coefficient is included, obtaining a distribution peaked at around 10 photons and a maximum of 110 photons. The quenching effect is also observed in Figure 6.5, in which the number of photons produced as a function of the energy deposited in the fibers is displayed in a two-dimensional plot. In this figure, in addition to a reduction of the number of photons produced per unit of energy deposited, a broader distribution is obtained when the Birk's coefficient is considered, indicating an increase of the fluctuations of the energy deposited.

6.2. SIMULATIONS FOR THE DESIGN OF THE TRITIUM DETECTOR

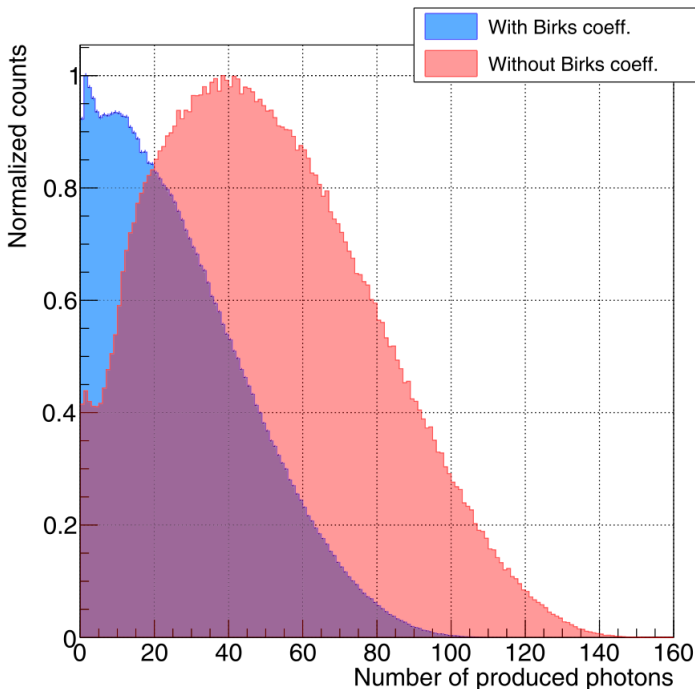


Figure 6.4 – Energy distributions of photons produced in the scintillating fiber, without the Birk's coefficient (red histogram) and with the Birk's coefficient $k_B = 0.126 \text{ mm/MeV}$ (blue histogram)[Aze20].

6.2.3 Optimization of the Fiber Length

A study to find the optimal fiber length was carried out. Two different lengths of scintillating fibers, 1 m and 20 cm, and two different tritium source activities, 0.5 kBq/L and 2.5 kBq/L, were used. Five detectors were simulated for the case of a 20 cm fiber length to have the same active area than for 1 m length. The advantage of using long fibers is their large active area for the same number of photosensors which would reduce the price of the TRITIUM monitor. However, short scintillating fibers reduce photon absorption, which increases the tritium detection efficiency per unit of active area.

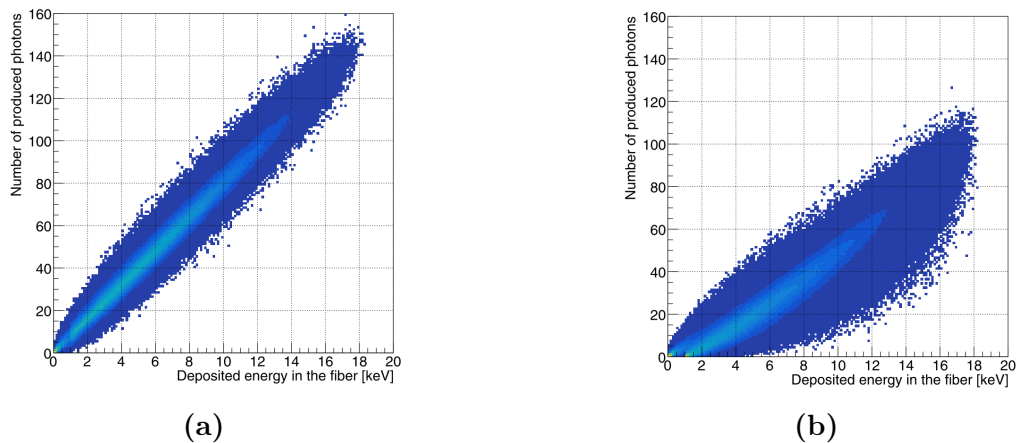


Figure 6.5 – Number of photons produced versus the energy deposited in the scintillating fibers when a) $k_B = 0$ b) $k_B = 0.126 \text{ mm/MeV}$ [Aze20].

The Tritium-Aveiro prototype, consisting of 360 scintillating fibers of 2 mm diameter, was simulated. The number of photons produced in a scintillating fiber per tritium electron for all the electrons that reach the scintillating fibers and for only those that generate photons detected in coincidence by the photosensors are plotted in Figure 6.6. Tritium events that produce a large number of photons are almost always detected but events that produce few photons are seldom detected, resulting in a peak centred at around 25 photons. The number of counts per hour during a week is shown in Figure 6.7 as a function of time for the tritium activities and fiber lengths studied. A signal 5 times larger is seen for the shorter fiber length and the two activities considered, due mainly to the lower absorption and the refraction loss of photons in shorter fibers. In addition, effects like dirt and mechanical imperfections of fiber surface not simulated increase this photon loss effect.

6.2. SIMULATIONS FOR THE DESIGN OF THE TRITIUM DETECTOR

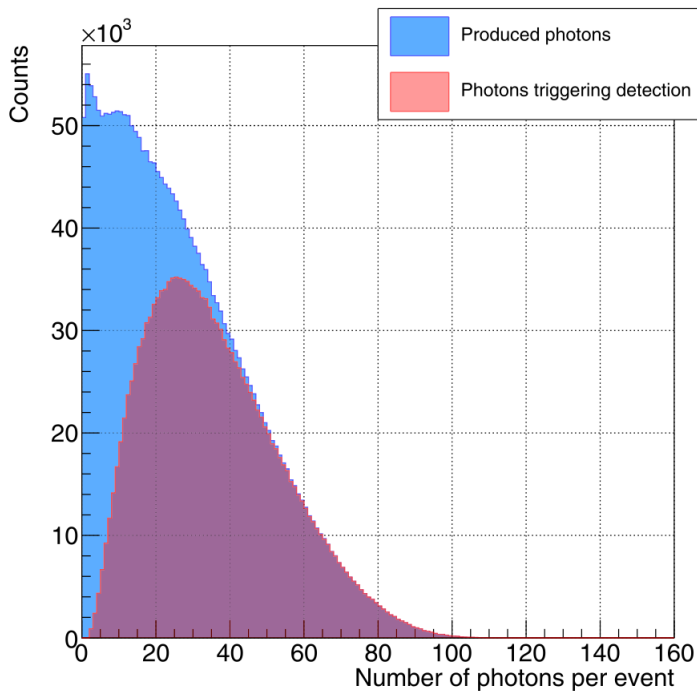


Figure 6.6 – Number of photons produced in a fiber per tritium event for all tritium electrons that reach the fiber (blue histogram) and for only tritium electrons producing photons detected in coincidence by photosensors (red histogram) [Aze20].

6.2.4 Fiber Diameter Influence on Cosmic Background

A study of the cosmic ray background as a function of the fiber diameter was carried out. Simulations of a single 20 cm length scintillating fiber of 1 mm and 2 mm were compared. The energy deposited in the scintillating fibers by cosmic rays is proportional to the active volume so, the expected cosmic ray signal is larger for 2 mm diameter fibers. The objective of this study is to simulate the background in the tritium energy range. The tritiated water source was replaced by a cosmic ray source generated by the CRY

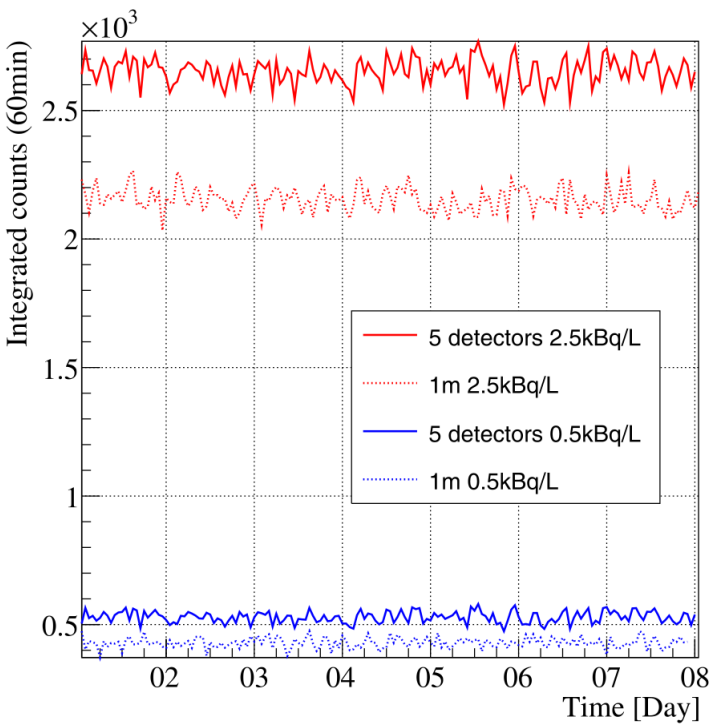


Figure 6.7 – Simulated counting statistics normalized to the active area in 1 h bins during a week for 1 m (dashed lines) and 20 cm (solid lines) and 0.5 kBq/L (blue lines) and 2.5 kBq/L (red lines) activities [Aze20].

library¹ [Plo, Hag07], a package implemented in C++. This library generates cosmic-ray showers for different particles (muons, neutrons, protons, electrons, photons and pions). The cosmic source employed is a horizontal square of $1 \times 1 \text{ m}^2$ located 35 cm over the detector with the typical distribution of cosmic particles at sea level. The distributions of energy deposited in the scintillating fibers for 1 mm and 2 mm diameters by cosmic rays are shown in Figure 6.8. As can be seen in the figure, a background about 50% smaller is obtained for 1 mm fiber diameter in the tritium energy range, which implies a smaller detector MDA.

¹CRY library, Cosmic-Ray Shower library

6.2. SIMULATIONS FOR THE DESIGN OF THE TRITIUM DETECTOR

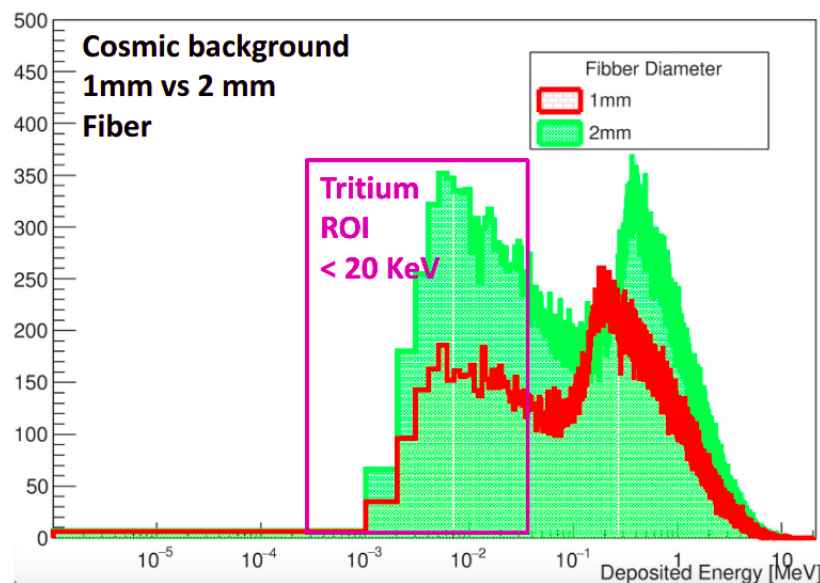


Figure 6.8 – Comparison of the energy deposition by cosmic rays in scintillating fibers of 1 mm and 2 mm diameter.

6.2.5 Influence of the PMMA Windows on the Tritium Signal

In the prototypes TRITIUM-IFIC-0 and TRITIUM-IFIC-1, the fibers were directly coupled to the photosensor, so detected photons were only those guided along the fibers. However, in TRITIUM-Aveiro and TRITIUM-IFIC-2, two PMMA windows are used which allows the transmission to the photosensors of photons propagated through water. To quantify the importance of this contribution, the TRITIUM-Aveiro prototype was simulated. The distribution of the number of photons that reach the PMMA window per tritium event is shown in Figure 6.9. Fiber-guided photons are shown in red while those travelling in water are plotted in blue. It can be seen that the tritium signal obtained from the water guided photons is as important as that obtained from the fibers. Therefore, PMMA windows improve tritium detection efficiency by around a factor 2.

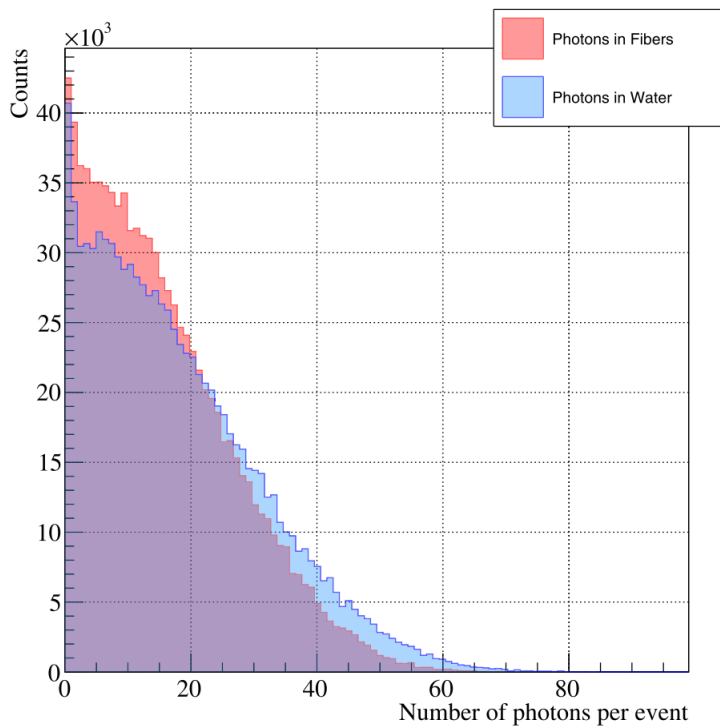


Figure 6.9 – Distribution of photons reaching the PMMA windows. The red histogram corresponds to the photons guided by fibers and the blue histogram to photons guided through water [Aze20].

6.3 Simulations of the TRITIUM Monitor

The simulations of a TRITIUM monitor consisting of several TRITIUM-IFIC-2 modules in parallel and a background rejection system are described in this section.

6.3.1 Simulation of the TRITIUM-IFIC-2 Prototype

A Tritium-IFIC-2 prototype of 800 fibers of 1 mm diameter arranged and uniformly distributed in sixteen different layers of increasing radius, as illustrated in Figure 6.10, was simulated. The source consisted of a 5 μm thick

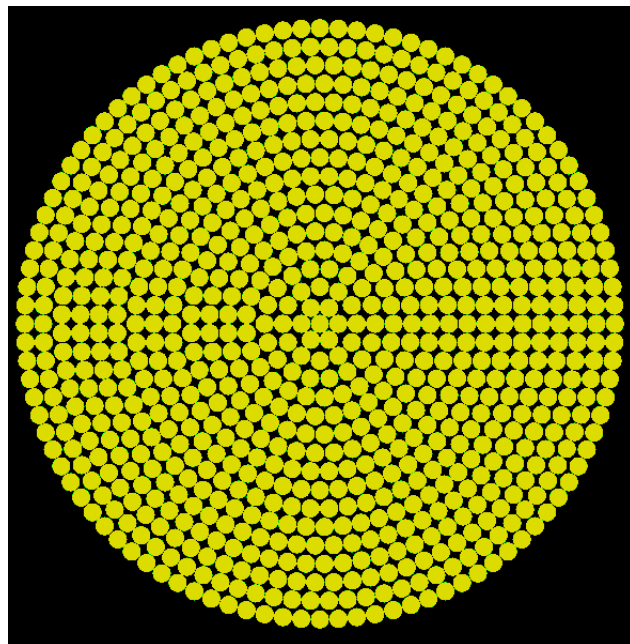


Figure 6.10 – Distribution of the scintillating fibers in the simulations of the TRITIUM-IFIC-2 prototype.

cylindrical ring of tritiated water around each fiber. Scintillating fibers were arranged within a cylindrical PTFE vessel. Two PMMA windows of 5 mm

thickness closed both ends of the vessel. A 0.5 mm layer of optical grease on each PMMA window was included. Two R8520-460 PMTs from Hamamatsu [Ham19] were simulated. The inner part of the simulated TRITIUM-IFIC-2 geometry is shown in Figure 6.11 in which the PMTs, the optical grease, the PMMA windows, the tritiated water and the scintillating fibers are shown. The PMT active area is smaller than the scintillating fibers bundle cross section. The aim of these simulations was to calculate the activity resolution

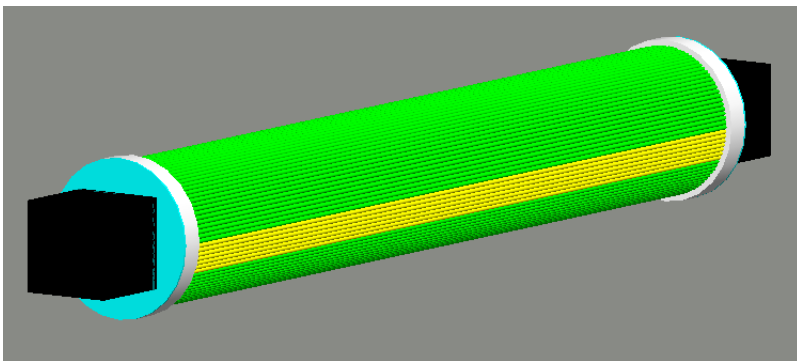


Figure 6.11 – Simulation of the inner part of the TRITIUM-IFIC-2 prototype. PMTs (black), optical grease (blue), PMMA windows (white), tritiated water (green) and scintillating fibers (yellow).

of the prototype and the improvement obtained by increasing the integration time and the number of modules read out in parallel. The detection of a tritium electron in TRITIUM-IFIC-2 is shown in Figure 6.12. The paths of the photons created in scintillating fibers are represented by green lines ending in red dots when they are absorbed in the fiber or the water and blue dots when they are absorbed in the PMTs (detected). The fiber in which the tritium electron is detected is clearly identified. Some photons go out of the fiber and are not collected. Blue dots in both PMTs indicate that photons are detected in coincidence. The distribution of the number of photons detected by photosensors per tritium event is shown in Figure 6.13. A maximum of 17 photons is obtained, which is in agreement with the distribution of photons per tritium event measured experimentally, shown in Figure 5.19. The experimental distributions are lower than the simula-

6.3. SIMULATIONS OF THE TRITIUM MONITOR

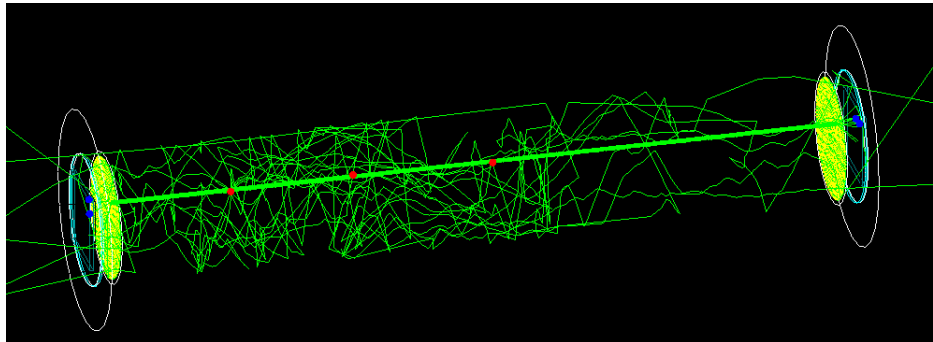


Figure 6.12 – Tritium electron detected in the simulated TRITIUM-IFIC-2 prototype. The path of the optical photons is represented by green lines and the position in which they are absorbed is represented by red and blue dots for absorption in water or PMT, respectively.

tions mainly in the range from 3 to 8 photons per event, probably due to the detector imperfections not included in the simulations.

Activities from 100 Bq/L to 5 kBq/L for three months of data taking and an integration time of 10 min were simulated. The simulation results are presented in Figure 6.14. A difference of 250 Bq/L in the activity is not distinguished due to the width of the distributions. To reduce the width, the statistics must be increased, either by increasing the integration time or the number of prototypes read out in parallel. To check the role of the integration time, distributions for integration times of 10 min, 30 min and 60 min were generated. The effect of increasing the integration time is to reduce the distribution width and to improve the activity resolution of the TRITIUM monitor as seen in Figure 6.15. Differences as low as 250 Bq/L are clearly discriminated with only one TRITIUM-IFIC-2 module and an integration time of 60 min which could still be considered a quasi-real time measurement. Similarly, these distributions are shown in Figure 6.16 for 10 min integration time and for 1, 5 and 10 modules read out in parallel. A reduction of the distribution width with increasing number of modules is clearly visible in this figure that improves the activity resolution of the detector. Differences of 250 Bq/L are clearly distinguish with an integration

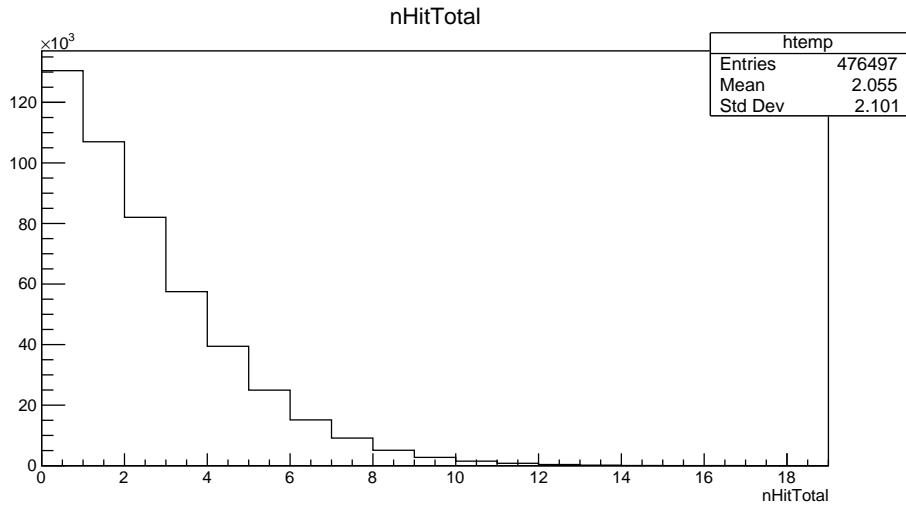


Figure 6.13 – Photons detected by both PMTs per tritium event in the simulated TRITIUM-IFIC-2 prototype.

time of 10 min and 5 TRITIUM-IFIC-2 modules. The resolution, defined as

$$\text{Resolution}(\%) = \frac{\text{FWHM}}{\text{centroid}} \cdot 100 \quad (6.2)$$

is plotted in Figure 6.17. It can be observed that the resolution improves with integration time and number of modules. The studied cases are summarized in Table 6.1. The decision adopted by the TRITIUM collaboration is to install 5 TRITIUM-IFIC-2 modules with an integration time of 1 h that provide a MDA of 100 Bq/L, as seen in Figure 5.21. With this configuration, differences of 100 Bq/L are expected to be resolved according to Table 6.1.

6.3.2 Simulation of the Lead Shield and Cosmic Veto

The lead shield and the active vetos were included in the simulation of Tritium-IFIC-2 to quantify the reduction of cosmic background detected.

6.3. SIMULATIONS OF THE TRITIUM MONITOR

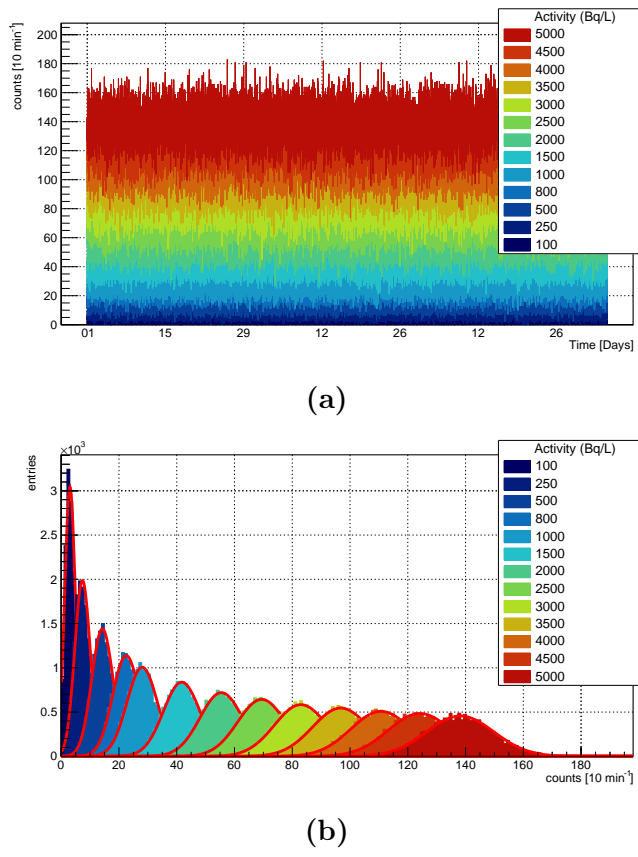


Figure 6.14 – a) TRITIUM-IFIC-2 simulated statistics with an integration time of 10 min during three months (13248 bins for each activity). b) Distribution of counting statics versus activities.

# of modules	10 min	30 min	60 min
1	< 1000 Bq/L	500 Bq/L	200 Bq/L
5	200 Bq/L	150 Bq/L	100 Bq/L
10	150 Bq/L	100 Bq/L	$\approx 50 \text{ Bq/L}$

Table 6.1: Tritium activity difference that can be visually resolved for different integration times and different number of TRITIUM-IFIC-2 modules.

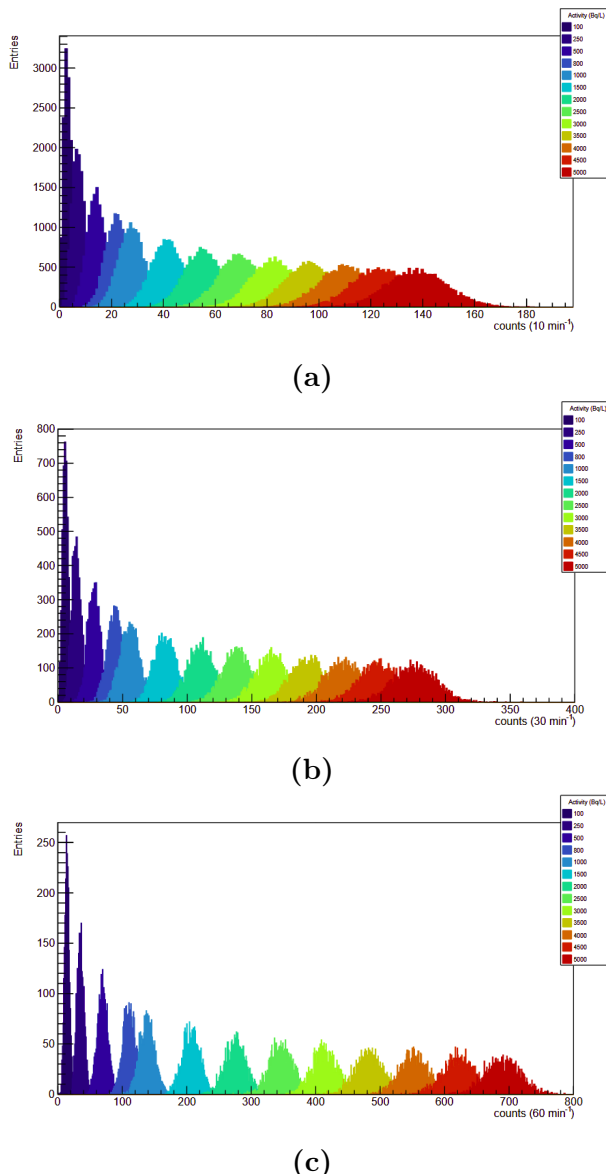


Figure 6.15 – Simulated statistics distributions obtained with a TRITIUM-IFIC-2 prototype for several tritium activity and three different integration times: a) 10 min (13248 bins), b) 30 min (4416 bins) and c) 60 min (2208 bins).

6.3. SIMULATIONS OF THE TRITIUM MONITOR

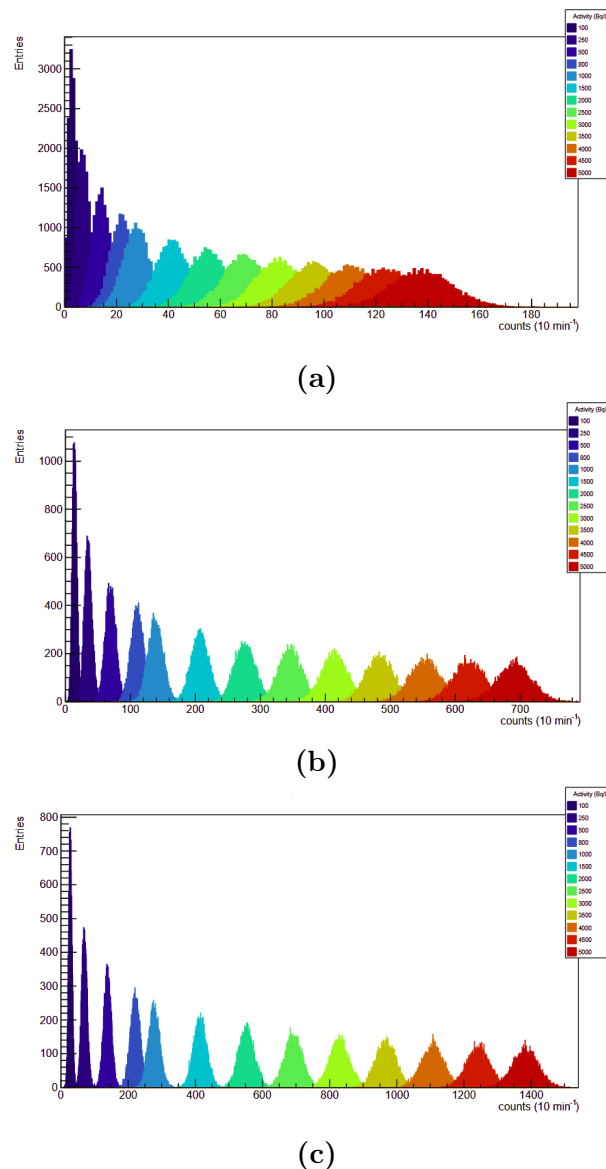
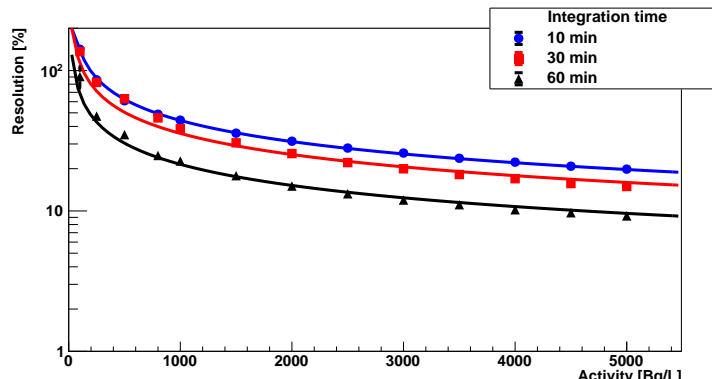
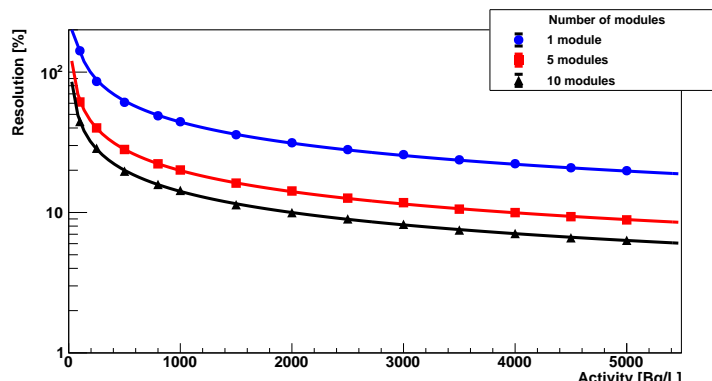


Figure 6.16 – Simulated statistic distribution for an integration time of 10 min (13248 time bins), several tritium activities and different number of TRITIUM-IFIC-2 modules a) 1, b) 5 and c) 10.



(a)



(b)

Figure 6.17 – a) Resolution of TRITIUM-IFIC-2 versus tritium activity for different integration time using 1 TRITIUM-IFIC 2 module. **b)** Resolution of TRITIUM-IFIC-2 versus tritium activity for different number of modules and 10 min integration time.

6.3. SIMULATIONS OF THE TRITIUM MONITOR

A square plane cosmic ray source of $1\text{ m} \times 1\text{ m}$ placed at a height of 70 cm was simulated with the cosmic ray generator of the CRY library. Two R8520-460 PMTs from Hamamatsu were simulated to read out each plastic scintillator, as described in section 3.4. The lead shield was simulated with the lead properties taken from the Geant4 NIST database. The dimensions of the simulated lead shield were $60 \times 60 \times 70\text{ cm}^3$, suitable for one TRITIUM-IFIC-2 prototype and an active cosmic veto but smaller than the real dimension of the lead shield at Arrocampo to optimize simulation time and computing resources. Energy distribution, position and momentum distribution were produced. Simulations with three different shielding configurations were carried out with the aim of quantifying the background rejection due to passive shield and active veto. The first simulation consisted of one TRITIUM-IFIC-2 prototype and the cosmic ray source. In the second simulation, a lead shield was added and in the third simulation, the cosmic veto was also included. The cosmic events detected by the TRITIUM-IFIC-2 prototype are shown in Figure 6.18, according to the shielding configuration. Cosmic rays detected by TRITIUM-IFIC-2 are reduced by a factor around 5.5 when a lead shield 5 cm thick is included (this is the width of the shield currently installed in Arrocampo). This reduction is caused by the suppression of the soft cosmic radiation (energy lower than 200 MeV). The natural background of the installation site was not included in this simulation, which is also mitigated by the lead shield, so the expected reduction due to the passive veto would be even better. Around 60% of the cosmic rays that penetrate the lead shield and reach TRITIUM-IFIC-2, which are mostly hard cosmic rays, are detected by the cosmic veto and, therefore, are suppressed from the background. In summary, cosmic rays that would be detected and misidentified as tritium electrons by TRITIUM-IFIC-2 are reduced by a 92.6% by means of the background rejection system and this reduction is expected to be even larger since the natural background of the site was not included in the simulations.

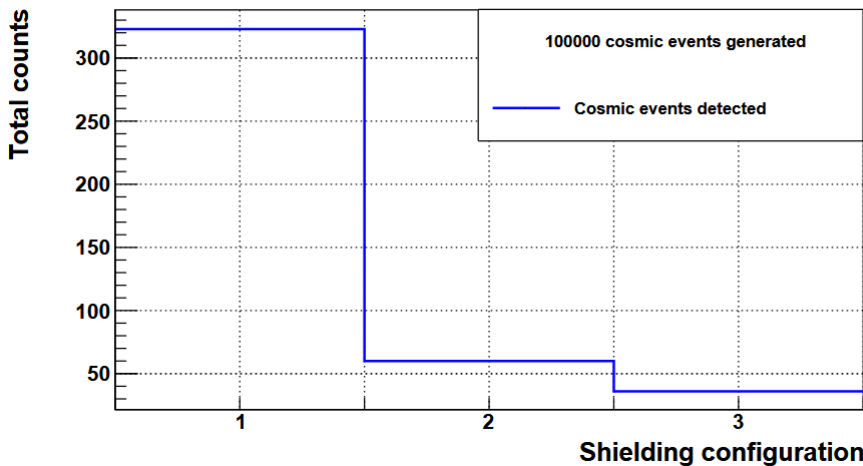


Figure 6.18 – Total cosmic ray events detected by TRITIUM-IFIC-2 from 10^5 generated cosmic events, which are misidentified as tritium events in three different shielding configurations. Bin 1 corresponds to a no background rejection system. Bin 2 corresponds to the passive shield and bin 3 corresponds to both lead shield and cosmic veto. .

Chapter 7

Present Status and Summary of the Results of the TRITIUM Project

In this chapter, the most important results obtained in this PhD thesis and in the TRITIUM project are summarized and discussed. These results were previously presented in chapters 4 to 6.

Tritium, which is a radioactive element, is one of the most abundantly produced radioisotopes in nuclear facilities such as nuclear power plants and research facilities. Due to its radiotoxicity, an excessive amount of tritium released to the environment could directly (drinking tritiated water) or indirectly (use of tritiated water for irrigation) affect human health and the environment.

The legal limit of tritium for drinking water in Europe is 100 Bq/L, which is one of the most restrictive limits in the world. This limit is established by the EURATOM Council Directive [Eur13].

The TRITIUM project was funded to investigate the feasibility of a monitor for measuring in quasi-real time low tritium activities in water. The goal of this project is to design, build, install and commission a tritium monitor that measures tritium activities as low as 100 Bq/L in 1 hour or less. The TRITIUM monitor consists of three different parts:

1. The TRITIUM detector, where tritium measurements take place. This consists of modules of hundreds of uncladded scintillating fibers read out in parallel. Various configurations for the TRITIUM module were tested, such as different diameters of the scintillating fibers (1 mm or 2 mm) and types of photosensor (PMTs or SiPM arrays).
2. The background rejection system, which is employed to suppress the radioactive background that affects the minimum detectable activity. This is based on a lead passive shield, that reduces the soft component of cosmic rays (energies below 200 MeV) and the environmental radioactive background, and an active veto that reduces the hard component of cosmic rays (energies above 200 MeV).
3. The water purification system that removes particles and minerals present in the water sample measured by the TRITIUM detector.

The results obtained by the TRITIUM collaboration are the following:

1. During the R&D activities, the TRITIUM module and the water purification and background rejection systems, were designed, built, characterized and optimized.

Regarding the detector development, the following tasks were carried out:

- (a) Simulations were performed by the TRITIUM Aveiro team using the Geant4 package to optimize tritium detection efficiency. It

was found that in 25 cm long fibers the light signal is a 23% factor larger than in 1 m long fibers.

- (b) A surface-conditioning method for scintillating fibers, which consists in cleaving, polishing and cleaning the fibers, was developed in the frame of this PhD thesis. A polishing machine, based on Arduino technology, was developed. The objective of this machine was to automate the polishing of hundreds of fibers simultaneously, a task that requires an unaffordable time for the amount of fibers needed for the TRITIUM monitor. The surface-conditioning method resulted in an increase of the light collected by the fibers, a factor of 2 due to polishing and an additional 25% due to cleaning.
- (c) A characterization of the scintillating fibers was performed in this PhD thesis. A photon collection efficiency of $76 \pm 8\%$ was obtained, smaller than stated by the manufacturer (96%). The typical deviation of the photon collection efficiency after applying the surface-conditioning method was also measured, obtaining a 3%, which is acceptable for tritium measurements.
- (d) A characterization of the S13360-1375 Hamamatsu SiPM was carried out in this PhD thesis. In this characterization, some of the most relevant parameters of the SiPM for detection of tritium, such as gain, breakdown voltage, temperature coefficient and others as the quenching resistance and the terminal capacitance, were measured and compared to the values provided by the manufacturer. The charge of the single photoelectron spectrum was measured with a resolution of 1% for each photoelectron peak and up to 10 photoelectron peaks were resolved.
- (e) Due to the strong dependence of the SiPM gain on temperature, a gain stabilization method was implemented in the temperature range of interest. This method consists in compensating the variation of the gain due to changes in the temperature by a

variation of the bias voltage. Indeed, the gain depends linearly on both temperature and voltage, increasing with voltage and decreasing with temperature. This allows us to stabilize the gain to its nominal value at 25°C by a variation of 59.9 ± 1.3 mV/°C of the bias voltage. This stabilization method was tested, obtaining variations of 0.1% in the SiPM gain in the [20 – 30]°C temperature range, which is the expected temperature range of operation. These results indicate that a stable operation of the SiPM readout can be obtained by an automatic implementation of a temperature dependent SiPM bias in the TRITIUM detector.

2. The background rejection system consists of an active veto and a passive shield. The latter consists of a lead castle of 5 cm thick walls, designed by the TRITIUM CENBG team and presently installed in the Arrocampo site.

A 5.5 reduction factor for cosmic ray events due to the lead shield was obtained by simulations performed in this PhD thesis. In addition, the background of the environmental radioactivity (which was not included in these simulations) would also be suppressed by the shield.

The active veto, built and characterized in this PhD thesis, consists of two parallel plastic scintillating plates of 1 cm thickness, separated 34.2 cm distance, that enclose the TRITIUM modules. Each scintillator plate was read out by two photosensors. The plastic scintillator plates were threefold wrapped in PTFE, aluminium and black tape layers. This wrapping improved by a factor 2 the light collection and produced a better response uniformity on the plate surface. In addition, the electronics settings that optimize the detection of hard cosmic events, such as discrimination thresholds and photosensor high voltage bias, were found. A hard cosmic rate of 2.5 events/s was measured, from which is drawn an efficiency of the cosmic veto of 85% by comparison to the cosmic ray rate at sea level. Finally, the dependence of the hard cosmic rate on the distance between the scintillating plates

was fitted to a second order polynomial, which allows us to change this distance without needing to perform a new calibration of the veto. A 60% reduction of the hard cosmic ray events due to the active veto was obtained through simulations. Therefore, a 92.7% suppression of the cosmic ray rate by the whole background rejection system was obtained from simulations. The actual cosmic ray suppression will be measured at the Arrocampo site.

3. Regarding the water purification system, a detailed analysis of the Arrocampo water was carried out. Due to the presence of the high concentrations of organic components at the site, a water purification system is needed. The TRITIUM LARUEX team designed and installed a water purification system at the Arrocampo site, consisting of several filtering stages that eliminate all organic matter and mineral particles of more than $1 \mu\text{m}$ size. Conductivities close to $10 \mu\text{S}/\text{cm}$ (two orders of magnitude less than the raw water) were achieved. Furthermore, the water tritium activity did not change after the purification process.
4. Four different detector prototypes, called TRITIUM-IFIC-0, TRITIUM-IFIC-1, TRITIUM-Aveiro and TRITIUM-IFIC-2, listed in chronological order, were developed by the TRITIUM collaboration. The first two prototypes, TRITIUM-IFIC-0 and TRITIUM-IFIC-1, (developed in this PhD thesis) were used as a proof of concept for the detection of tritium in water with scintillating fibers and to identify the different issues that affect the detection efficiency. The latest prototypes, TRITIUM-Aveiro (developed by the TRITIUM Aveiro team) and TRITIUM-IFIC-2 (developed in this PhD thesis), have slightly different designs. Small tritium activities were used to measure their tritium detection efficiency and MDA.

During the development of the first prototypes, a straight arrangement of the scintillating fibers was found crucial for tritium detection. In addition, a surface-conditioning method of scintillating fibers was

implemented, that improved the tritium detection efficiency. The use of a PTFE vessel was also found to improve the light collection due to its optical properties (reflectivity close to 95% for visible light). All these improvements were applied to the TRITIUM-IFIC-1 prototype, obtaining a factor 10 increase of the measured count rate of tritium with respect to the first prototype.

In the latest prototypes, two photosensors in time coincidence were employed to improve the MDA, since this reduces the photosensor noise. These two prototypes have a similar design but with subtle differences. One of the most important differences is the scintillating fiber diameter (2 mm for the TRITIUM-Aveiro prototype and 1 mm for the TRITIUM-IFIC-2 prototype). Fibers of 1 mm allow us to fit more of them in the same volume. This increases the total active area of the prototype (and, therefore its tritium detection efficiency) and the signal-to-background ratio (improving the MDA). Fibers of 2 mm may facilitate the water flow through the fiber bundle, which may increase the effective detection area. In addition, 2 mm fibers are stiffer which could be important for high water fluxes. It was obtained from simulations that the cosmic ray rate in the energy range of interest is a factor 2 higher for scintillating fibers of 2 mm. Additional measurements need to be done to decide the final fiber diameter. A possible way to take this decision could be to build two identical TRITIUM prototypes, one with 1 mm and the other with 2 mm fibers and compare their results.

The second important difference between the TRITIUM-Aveiro and TRITIUM-IFIC-2 prototypes is the type of photosensor proposed. TRITIUM-Aveiro uses PMTs and for TIRITIUM-IFIC-2, SiPM arrays are proposed. SiPM arrays have some advantages with respect to PMTs such as a higher photodetection efficiency, which would increase the detection efficiency of the TRITIUM detector. Furthermore, the SiPMs do not need high voltage, which implies a reduction of the TRITIUM monitor cost. However, SiPM arrays have some disadvantages

as the need to read out more channels and the need to implement a gain stabilization method due to the strong dependence of SiPMs gain on temperature.

The specific efficiency obtained with the TRITIUM-IFIC-2 prototype, $(141 \pm 6) \times 10^{-6} \text{ s}^{-1}\text{L} \text{ kBq}^{-1}\text{cm}^{-2}$, is an order of magnitud better than that obtained with the TRITIUM-Aveiro prototype, $(16 \pm 5) \times 10^{-6} \text{ s}^{-1}\text{L} \text{ kBq}^{-1}\text{cm}^{-2}$, most probably due to the surface-conditioning method applied to the fibers of the IFIC prototype. In addition, a MDA of 677 Bq/L was obtained for the TRITIUM-IFIC-2 prototype for an integration time of 10 min and 218 Bq/L for an integration time of 1 h. This is compared to a MDA of 29.8 kBq/L for an integration time of 1 min and 5 kBq/L for an integration time of 1 h for the TRITIUM-Aveiro prototype. A lower MDA allows us to discriminate smaller tritium activities from the background. An integration time of 1 h can still be considered a quasi-real time.

A summary of the state-of-the-art of the tritium detection in water is shown in Table 7.1, which includes the results obtained with the four different prototypes developed by the TRITIUM collaboration. As it can be seen in this table, the TRITIUM-IFIC-2 prototype ameliorates significantly the current state-of-the-art. A specific efficiency and a MDA almost an order of magnitud better than the results reported in the literature are obtained.

One of the most relevant properties of the TRITIUM monitor is scalability, which means that a lower MDA can be achieved by using a larger number of modules. The MDA of the TRITIUM monitor is expected to decrease with the square root of the number of modules. Therefore, as shown in Figure 5.21, a MDA of 100 Bq/L (goal of the TRITIUM project) could be achieved by using 5 TRITIUM-IFIC-2 modules and an integration time of 1 h. It has to be taken into account that the MDA reported in this PhD work was measured without the background rejection system. The TRITIUM MDA is expected

Reference	$\varepsilon_{det} \times 10^{-3}$ L kBq $^{-1}$ s $^{-1}$	F_{sci} cm 2	$\eta_{det} \times 10^{-6}$ L kBq $^{-1}$ s cm $^{-2}$	MDA kBq L $^{-1}$
[Mur67]	0.39	123	3.13	370
[Mog69]	4.50	> 424	< 10.6	37
[Osb70]	12	3000	4	37
[Sin85]	41	3000	13.7	< 37
[Hof92a]	2.22	\sim 100	< 22.2	25
T-IFIC-0†	2.1 ± 0.8	219	10 ± 4	100*
T-IFIC-1†	38.4 ± 1.6	402	96 ± 4	100*
T-Aveiro†	64 ± 19	4072	16 ± 5	5**
T-IFIC-2†	711 ± 27	5027	141 ± 6	0.22**

Table 7.1: Results of scintillator detectors developed for experiments (including the TRITIUM project) for tritiated water detection. This table shows the efficiency of the detector (ε_{det}), active surface (F_{sci}), specific efficiency ($\eta_{det} = \varepsilon_{det}/F_{sci}$, defined as efficiency normalized to active surface), and MDA.

* Specific activity measured, not MDA.

** MDA measured for 1 h integration time.

† This Thesis.

to improve when this system is included.

The stability of the tritium detection efficiency of the latest TRITIUM prototypes was monitored during six months, obtaining a stable behavior of the detector during this time with a relative standard deviation of 2.5% for the measured tritium rate.

5. Finally, simulations were carried out to determine the dependence of the tritium detection efficiency and activity resolution of the TRITIUM-IFIC-2 prototype on integration time and number of prototypes. These simulations, which agree with the experimental measurements, allow us to determine the number of modules needed in the TRITIUM monitor and the integration time to be used. With 5 modules and an integration time of 1 h a tritium activity resolution of 100 Bq/L is expected. This configuration is also the one that has an MDA of 100 Bq/L, goal of the TRITIUM project.

At present, the lead shielding, the water purification system and a TRITIUM-Aveiro module are installed in the Arrocampo site. Two additional TRITIUM-Aveiro modules and an active veto are planned to be installed as soon as possible. Moreover, three TRITIUM-IFIC-2 modules and an active veto are ready to be installed too. Their installation was delayed due to the coronavirus pandemic.

Chapter 8

Conclusions and Prospects

In this chapter, the main results and conclusions obtained in this PhD thesis are summarized and the prospects of the TRITIUM project are outlined:

1. A scalable modular monitor for measuring low activities of tritium in water is proposed. The goal of this monitor is to reach a sensitivity of 100 Bq/L of tritium activity, which is the maximum level allowed for drinking water by the EU directive. The modularity allows to reach the required sensitivity by selecting a given integration time and including the corresponding number of modules.
2. The IFIC modules of the TRITIUM monitor proposed consist of 1 mm diameter scintillating fibers read out by photosensors.
3. Three different prototypes of the TRITIUM-IFIC module in which different improvements were successively incorporated were developed.
4. A surface conditioning method for the scintillating fibers, consisting in specific rules for cleaving, polishing and cleaning the fibers was developed.

5. The conditioning method was applied to the selected 1 mm uncladded scintillating fibers from Saint-Gobain. An improvement of the photon collection efficiency of the fibers of a factor 2 due to polishing and an additional 25% due to cleaning was found.
6. Although most of the laboratory tests were carried out with PMTs as photosensors to read out the scintillating fibers, SiPM arrays are proposed by TRITIUM Valencia team for the final monitor.
7. A single SiPM, model S13360-1375 from Hamamatsu, selected for the monitor, was characterized. The most relevant parameters for tritium detection of this photosensor, such as breakdown voltage and gain, were measured.
8. As SiPM gain varies strongly with temperature, a stabilization method to maintain the gain constant with temperature was implemented. This method consisting in compensation of the gain variations with the bias voltage, was tested in the $[20 - 30]^\circ\text{C}$ temperature range of interest. Variations of the gain of the order of 0.1% were found which guarantees a stable operation of the photosensors.
9. In order to obtain the required tritium activity sensitivity a background rejection system consisting of a lead shield castle and an active plastic scintillator veto was proposed and implemented. The lead castle was designed and built by the TRITIUM CENBG group.
10. The passive background rejection system was simulated. A 5.5 reduction factor of the cosmic ray events measured by the TRITIUM-IFIC-2 prototype was obtained.
11. An active veto based on plastic scintillators read out by photosensors was designed and built.
12. A characterization of the active veto was done and the optimal parameters for detection of hard cosmic rays were found. A count rate of

2.5 events/s was measured, which gives an efficiency for cosmic ray detection of 85% by comparing the counting rate to the cosmic ray rate at sea level.

13. The active veto was simulated obtaining a suppression of the 60% of the cosmic rays that cross the lead shield and are measured by the TRITIUM-IFIC-2 prototype.
14. The total background suppression by the rejection system obtained from simulations for the TRITIUM-IFIC-2 prototype is 92.5%.
15. A specific efficiency $\eta = (141 \pm 6) \times 10^{-6} \text{ s}^{-1}\text{L}^{-1} \text{kBq}^{-1}\text{cm}^{-2}$ for the TRITIUM-IFIC-2 prototype was measured which is about an order of magnitude higher than specific efficiencies reported in the literature. The state-of-the-art of tritium detection with plastic scintillators is substantially improved.
16. The MDA obtained with the TRITIUM-IFIC-2 prototype is 680 Bq/L for 10 min integration time and 220 Bq/L for 1 h integration time.
17. Simulations of the detection resolution of TRITIUM-IFIC-2 monitor were done. A resolution of 250 Bq/L for an integration time of 30 min and three TRITIUM-IFIC-2 modules read out in parallel and 100 Bq/L for an integration time of 1 h and five modules were found.
18. The goal of the TRITIUM project of measuring 100 Bq/L in quasi-real time is expected to be reached with 5 TRITIUM-IFIC-2 prototypes read out in parallel and 1 h integration time.
19. At present, the water purification system and the lead shield are installed in the Arrocampo site, the final location of the TRITIUM monitor. A TRITIUM-Aveiro module is also installed, which was monitoring the tritium activities during several months.

CHAPTER 8. CONCLUSIONS AND PROSPECTS

20. The next step for the TRITIUM project is to install 2 additional TRITIUM-Aveiro prototypes which will be read out in parallel. In addition, an active veto for these three TRITIUM-Aveiro prototypes will be installed and read out in anticoincidence with them.
21. Three TRITIUM-IFIC-2 prototypes with the corresponding active veto are ready to be installed at Arrocampo site as soon as possible.

Appendices

Appendix A

Electronics for the SiPM Characterization

The electronic system designed to perform a complete characterization of the SiPM S13360-6075 model, which is the one proposed for the final TRI-TIUM monitor is shown in this appendix. This system consists of three different PCBs connected through HDMI connectors:

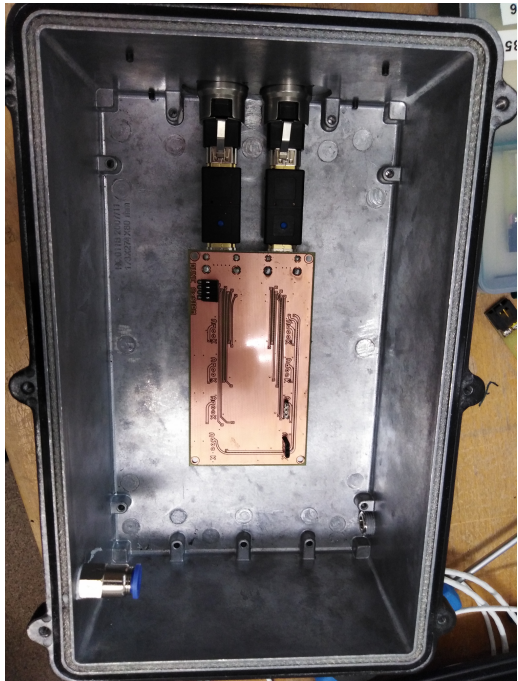
1. In the first PCB, shown in Figure A.1a, up to 8 SiPMs and one temperature sensor are connected. This PCB is placed inside a light-tight box from Thorlabs [Tho18]. This black box has a small hole of 1 mm diameter, prepared to introduce an optical fiber¹ to illuminate SiPMs with a LED, model 430L from Thorlabs [Tho18]. The spectrum of this LED, shown in Figure A.1d, was measured with a spectrometer. The emission peak of this LED is located at 436 nm with a FWHM of 19 nm. With the help of this LED, the light emission of the TRI-TIUM scintillating fibers was simulated to calibrate the SiPMs at the working wavelength.

¹The optical fiber used is BCF-98 from Saint-Gobain [Sai21a]

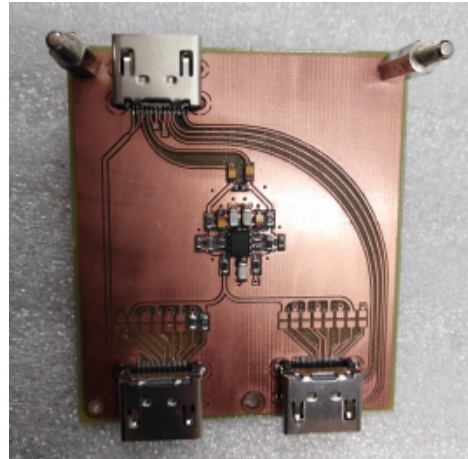
APPENDIX A. ELECTRONICS FOR THE SiPM CHARACTERIZATION

2. In the second PCB, shown in Figure A.1b, the signals of the SiPMs are summed and amplified by a factor either $G = 4187$ or $G = 10761$, depending on the input resistance of the oscilloscope, 50Ω or $1 M\Omega$ respectively. This PCB uses a differential amplifier to reduce the electronic noise of the system.
3. In the third PCB, shown in Figure A.1c, the different input and output signals are rearranged to avoid crosstalk. The input signals are the supply voltage of the SiPMs and the PCBs (± 6 V) and the output signals are the temperature sensor signal and the sum of the SiPM signals. The output signal of the third PCB is connected to an oscilloscope, model MSO44X from Tektronix [Tek21], that records the data.

APPENDIX A. ELECTRONICS FOR THE SiPM CHARACTERIZATION



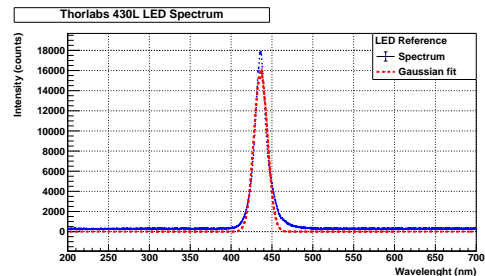
(a)



(b)



(c)



(d)

Figure A.1 – The three PCBs used for SiPM characterization a) The PCB 1 used to connect up to 8 SiPMs inside the black box. b) The PCB 2 used to sum and amplify the output signals of the SiPMs. c) The PCB 3 used to rearrange the input and output signals of the system. d) The LED emission spectrum.

APPENDIX A. ELECTRONICS FOR THE SIPM
CHARACTERIZATION

Appendix B

Water Purification System

In this appendix, several pictures of the water purification system are shown.

The scheme of the whole water purification system is shown in Figure B.1.

The gross filtering stage, made of silex-antracite and granate filters, the fine filtering stage, consisting of a $20\ \mu\text{m}$ filter and an active carbon filter, the super-fine filtering, composed of a $1\ \mu\text{m}$ filter, and the UV lamps, are shown in Figure B.2.

The double phase reverse osmosis is exhibited in Figure B.3a and the containers in which pure and reject water are gathered after treatment are displayed in Figure B.3b.

The Siemens Programmable Logic Controller (PLC), used to control the water purification system, is shown in Figure B.4.

Finally, a picture of the whole water purification system is displayed in Figure B.5.

APPENDIX B. WATER PURIFICATION SYSTEM

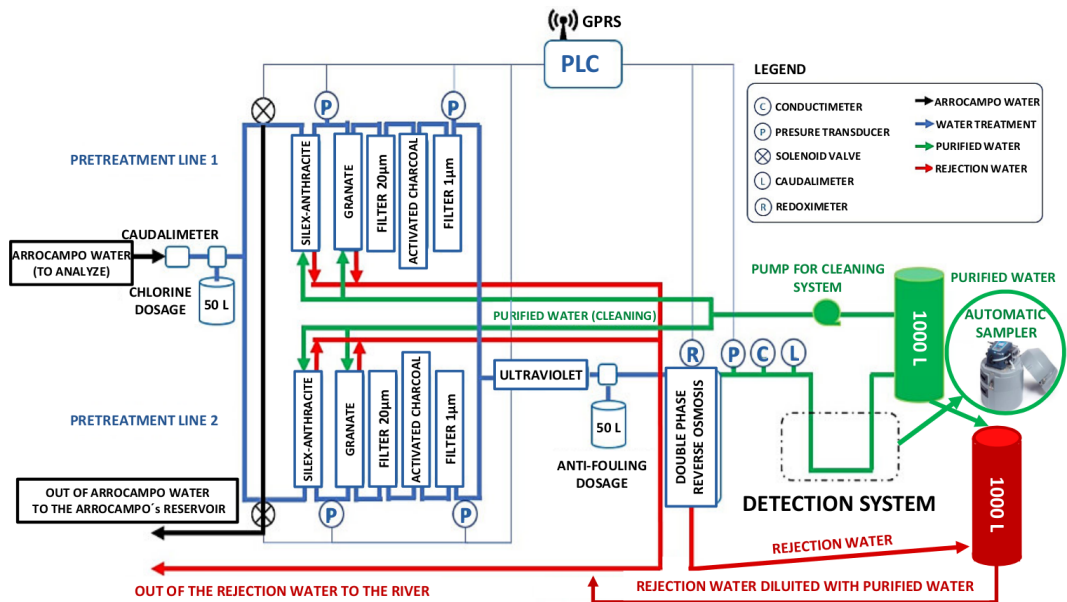


Figure B.1 – Scheme of the water purification system.

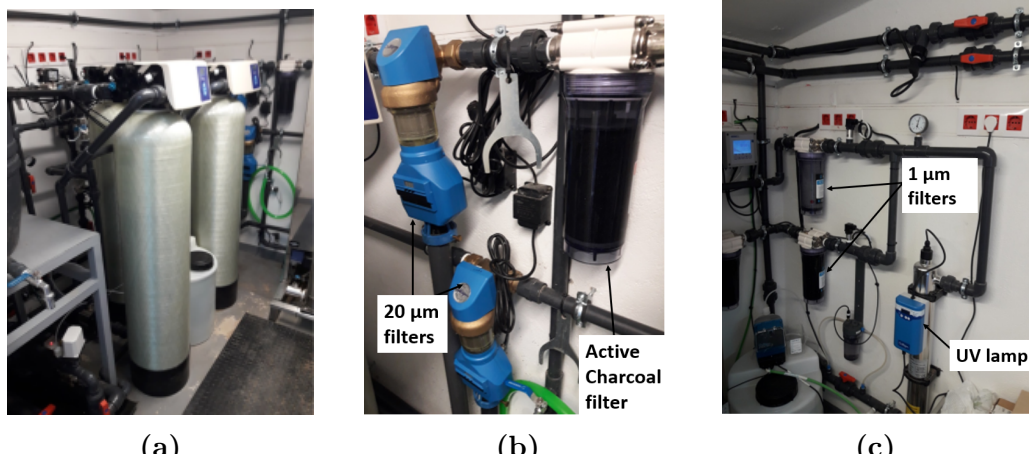


Figure B.2 – Different stages of filtration of the water purification system.
a) The gross filtering stage. b) The fine filtering stage. c) The super-fine filtering stage.

APPENDIX B. WATER PURIFICATION SYSTEM



(a)



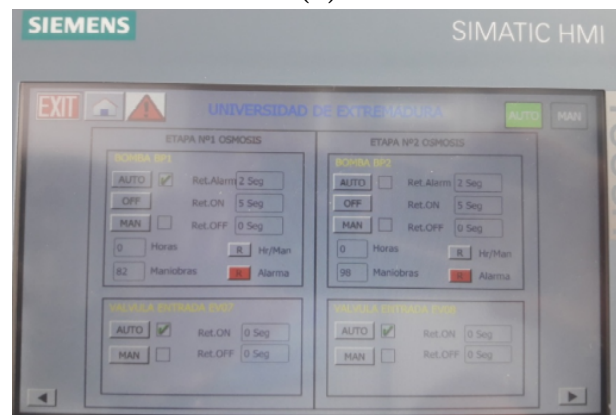
(b)

Figure B.3 – a) Doble phase reverse osmosis stage. b) Containers used to gather the output water of the water purification system.

Samples of raw, rejection and pure water are shown in Figure B.6, where the difference in the turbidity are distinguished.



(a)



(b)

Figure B.4 – Siemens PLC displays for the remote control of the water purification system.

APPENDIX B. WATER PURIFICATION SYSTEM



Figure B.5 – Picture of the water purification system.

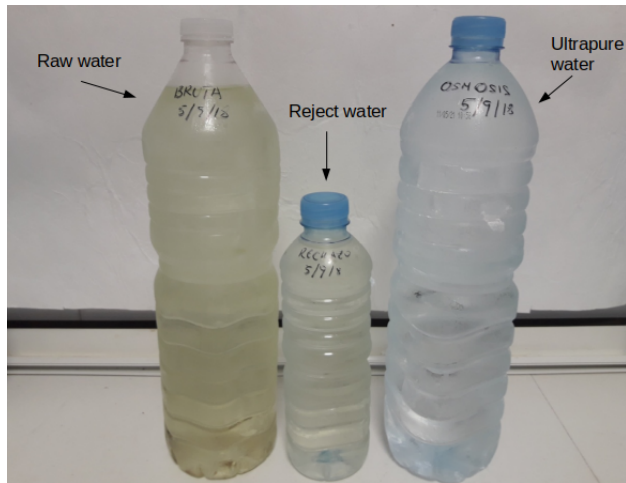


Figure B.6 – Raw, reject and pure water obtained with the water purification system.

APPENDIX B. WATER PURIFICATION SYSTEM

Appendix C

Preparation of Tritiated Water Sources

Radioactive liquid sources were prepared from 1.86 g (uncertainty of 0.05%) of tritiated water, purchased from PTB [Phy]. The activity of this tritium source was 26.8 MBq/g (uncertainty of 2.24%, reference date of 1/1/2017).

This source was dissolved in 500 mL (uncertainty of 0.05%) of hiper pure water (conductivity of 0.72 $\mu\text{S}/\text{cm}$), resulting in a solution of 500 mL of tritiated water with an activity of 100 kBq/g (uncertainty of 2.24%), that is 99.7 kBq/L (uncertainty of 2.24%).

APPENDIX C. PREPARATION OF TRITIATED WATER SOURCES

Appendix D

Electronic System of TRITIUM-Aveiro prototype

The electronic system of the TRITIUM-Aveiro prototype consists of several PCB and is divided in two parts:

1. A PCB, which electronic scheme is shown in Figure D.1, designed to power the PMTs with a negative high voltage. That consists of several high voltage power supplies, model C11152-01 from Hamamatsu Photonics [Ham15]. This PCB is controloed by a DAC¹, model MAX5500 from Maxim Integrated [Max09]. An Arduino Mega controls the DAC communication and is connected to a Raspberry Pi that runs the whole system.

A graphical interface, shown Figure D.1b, was developed to set up the different options in an easy way.

2. A electronic chain consisting of several PCBs that process and analyze the system signals, which electronic scheme is shown in Figure D.2.

¹DAC, Digital-to-analog converter

APPENDIX D. ELECTRONIC SYSTEM OF TRITIUM-AVEIRO PROTOTYPE

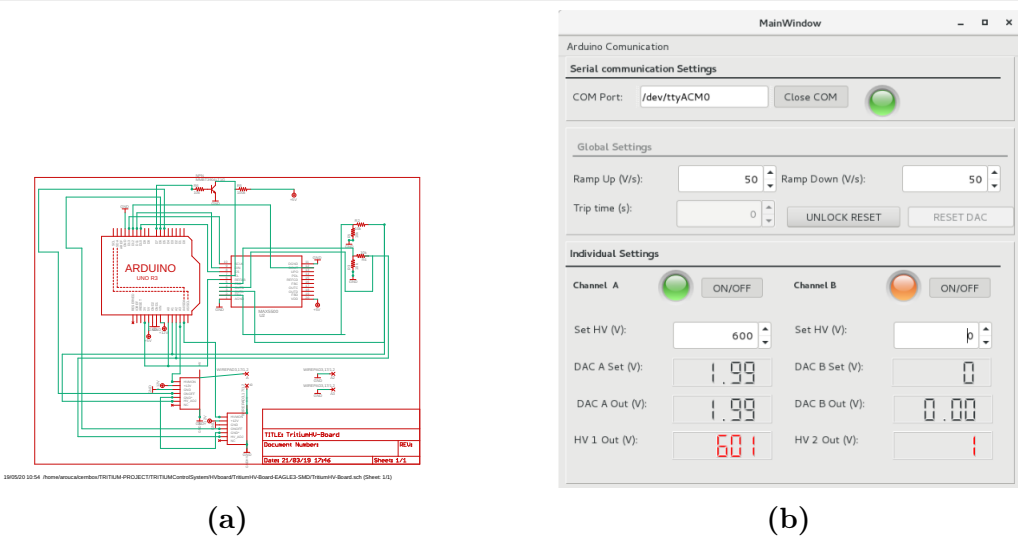


Figure D.1 – a) The electronic scheme of the PCB designed to power the PMTs of Aveiro prototype b) The graphical user interface developed to control the prototype.

This system consists of three different lines, two of them for the PMT signals of the prototype and the other for anticoincidence with an active veto.

To test this electronic chain, a plastic scintillator of $10 \times 10 \times 1 \text{ cm}^3$ dimensions was used to simulate a veto signal. Four different vetos are being built, based on a rectangular plastic scintillators from Saint-Gobain [Sai21c], of $50 \times 30 \times 2 \text{ cm}^3$ dimensions. The vetos are read out by 2" PMTs, model R2154-02 from Hamamatsu Photonics [Ham10]. The output signal of these PMTs goes into an OR stage, which output is connected to the veto line shown in Figure D.2. Thus, each veto is read in anticoincidence with the TRITIUM-Aveiro prototype.

Both lines, used to process and analyze the PMT signals of the prototypes, are equal and they are used to operate in time coincidence. Each PMT signal is introduced in a preamplifier model CR111 from CREMAT Inc. [CRE20], that shapes and pre-amplifies the signal. To

APPENDIX D. ELECTRONIC SYSTEM OF TRITIUM-AVEIRO PROTOTYPE

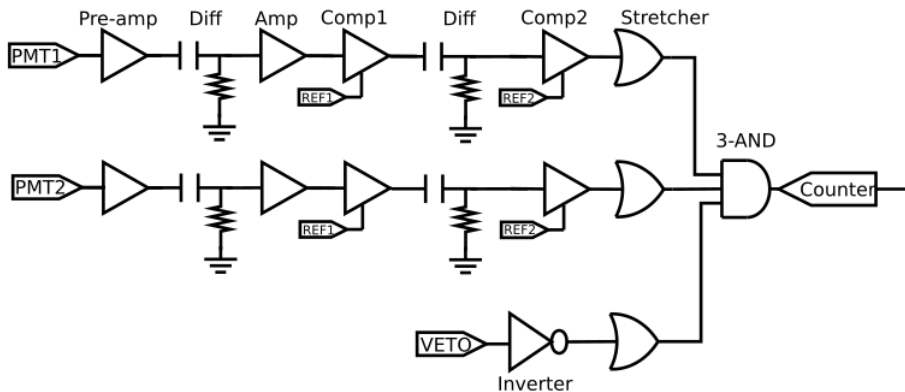


Figure D.2 – Electronic scheme that process and analyze the signal of the TRITIUM-Aveiro prototype.

reduce electronic noise and signal loss, both preamplifiers are connected as close as possible to the PMTs and they are inside aluminium boxes which act as a Faraday cage.

Each preamplifier is followed by a differentiator stage, which reduces the time width of the signal and an amplifier stage, that amplifies the signal. The amplifier is model OPA656 from Texas Instruments [Tex15].

A fast comparator, model LT111 from Linear Technology [Lin], is used to set a threshold to remove PMT signals with low amplitude (dark counts of the PMT). A MAX5500 DAC is used to configure the thresholds.

As the time width of the preamplifier output signal is too large, $200\ \mu s$, a second differentiator stage was included to reduce fake coincidences. A second comparator was added to restore a 5V square signal again.

Finally a tunable pulse stretcher based on an OR gate, model SN74AHC1 from Texas Instruments [Tex17], is used to set the time width of each signal to 100 ns. The time coincidence windows of the system is 200 ns.

The third line consists of an inverter, which gives a 5 V signal, except

APPENDIX D. ELECTRONIC SYSTEM OF TRITIUM-AVEIRO PROTOTYPE

when a cosmic particle is detected, in which case the signal is 0 V. A stretcher is used to set the signal time width to 100 ns.

The signals from the three lines are introduced into a 3-input AND gate, model SN74LVC1G11 from Texas Instruments [Tex16], that makes a logic level comparison. With this last stage a temporal coincidence of both PMT signals in anti-coincidence with the veto signal is obtained. The output signal of this stage is connected to a pulse counter.

The GPIO pins of a Raspberry Pi are used to communicate with the system and configure the threshold levels. A graphical user interface, shown in Figure D.3, was developed to set the counter system in an easy way.

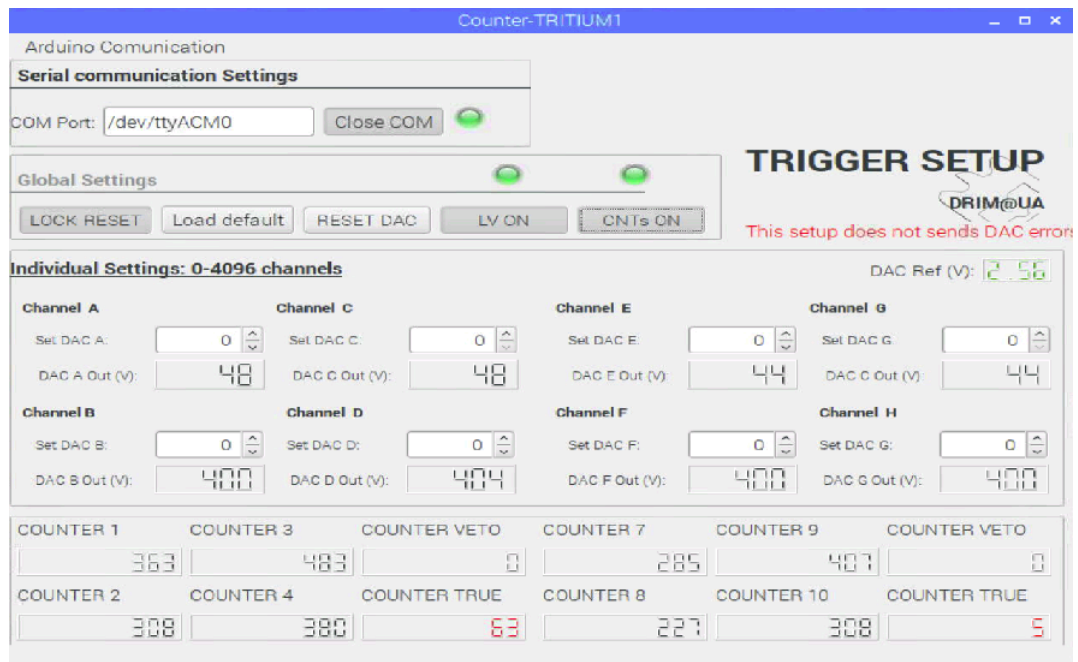


Figure D.3 – Graphical user interface used to manage the counter system.

Besides counting, this electronic system includes a voltage follower

APPENDIX D. ELECTRONIC SYSTEM OF TRITIUM-AVEIRO PROTOTYPE

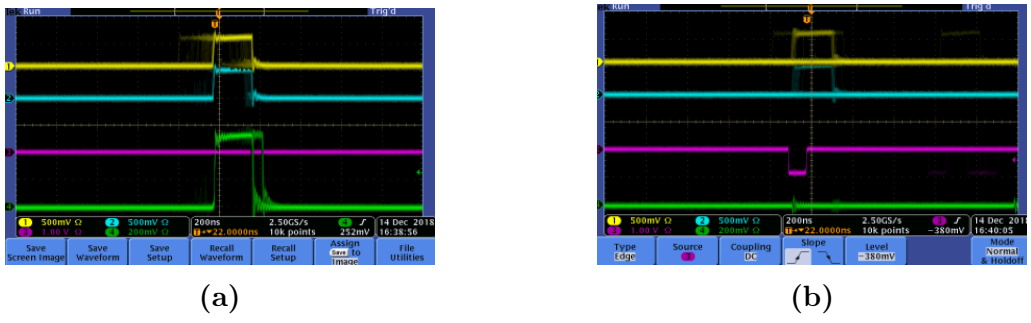


Figure D.4 – a) Tritium event accepted as veto has not detected it. **b)** Background event rejected because veto has fired.

circuit connected to the preamplifier output signal that produces an energy spectrum for each PMT.

In Figure D.4 screenshots for accepted and rejected events are displayed.

APPENDIX D. ELECTRONIC SYSTEM OF TRITIUM-AVEIRO
PROTOTYPE

Bibliography

- [Ago03] Agostinelli, S. et al., *Geant4— A Simulation Toolkit*, Nuclear Instruments and Methods in Physics Research Section A: Accelerators, Spectrometers, Detectors and Associated Equipment **506** (2003) 250–303, URL [http://dx.doi.org/10.1016/S0168-9002\(03\)01368-8](http://dx.doi.org/10.1016/S0168-9002(03)01368-8).
- [AH99] Al-Haddad, M., Fayoumi, A. and Abu-Jarad, F., *Calibration of a Liquid Scintillation Counter to Assess Tritium Levels in Various Samples*, Nuclear Instruments and Methods in Physics Research Section A: Accelerators, Spectrometers, Detectors and Associated Equipment **438** (1999) 356–361, URL [http://dx.doi.org/10.1016/S0168-9002\(99\)00272-7](http://dx.doi.org/10.1016/S0168-9002(99)00272-7).
- [Ale11] Alecu, C. G. et al., *Reachable Accuracy and Precision for Tritium Measurements by Calorimetry at TLK*, Fusion Science and Technology **60** (2011) 937–940, URL <http://dx.doi.org/10.13182/FST11-A12569>.
- [All11] Allegro MicroSystems, *Driver Pololu A4988, DMOS Microstepping Driver with Translator And Overcurrent Protection*, Allegro MicroSystems (2011).

BIBLIOGRAPHY

- [Alv39] Alvarez, W., L. and Cornog, R., *Helium and Hydrogen of Mass 3*, Phys. Rev. **56** (1939) 613–613, URL <http://dx.doi.org/10.1103/PhysRev.56.613>.
- [Amp] AmpTek, Materials Analysis Division, *MCA8000D, Pocket MCA, Digital Multichannel Analyzer*, AmpTek, Materials Analysis Division, Bedford Massachusetts, USA.
- [ARD] ARDUINO, *Arduino UNO REV3*, <https://www.arduino.cc/>.
- [Arg11] Argyriades, J. et al., *Spectral Modeling of Scintillator for the NEMO-3 and SuperNEMO Detectors*, Nuclear Instruments and Methods in Physics Research Section A: Accelerators, Spectrometers, Detectors and Associated Equipment **625** (2011) 20–28, URL <http://dx.doi.org/10.1016/j.nima.2010.09.027>.
- [Aze20] Azevedo, C. et al., *Simulation Results of a Real-Time in Water Tritium Monitor*, Nuclear Instruments and Methods in Physics Research Section A: Accelerators, Spectrometers, Detectors and Associated Equipment **982** (2020) 874–877, URL <http://dx.doi.org/10.1088/0370-1298/64/10/303>.
- [Aze22] Azevedo, C. et al., *Development of a Real-Time Tritium-in-Water Monitor* (2022), arXiv:2202.11068v1.
- [BD13] Bükk-Deme, A., Alecu, C., Kloppe, B. and Bornschein, B., *First Results With the Upgraded TLK Tritium Calorimeter IGC-V0.5*, Fusion Engineering and Design **88** (2013) 2865–2869, URL <http://dx.doi.org/10.1016/j.fusengdes.2013.05.066>.
- [Ber98a] Berthold, J. W. and Jeffers, L. A., *In-situ Tritium Beta Detector*, Technical Report AC21-96MC33128, Office of Scientific and Technical Information (OSTI.GOV), U.S. Department of Energy (1998), URL <http://dx.doi.org/10.2172/836625>.

- [Ber98b] Berthold, J. W. and Jeffers, L. A., *Phase 1 Final Report for In-Situ Tritium Beta Detector*, Technical Report AC21-96MC33128, Office of Scientific and Technical Information (OSTI.GOV), U.S. Department of Energy (1998), URL <http://dx.doi.org/10.2172/2225>.
- [Bir51] Birks, J. B., *Scintillations from Organic Crystals: Specific Fluorescence and Relative Response to Different Radiations*, Proceedings of the Physical Society. Section A **64** (1951) 874–877, URL <http://dx.doi.org/10.1088/0370-1298/64/10/303>.
- [Bla91] Blauvelt, R. K., Deaton, M. R. and Gill, J. T., *Health Physics Manual of Good Practices for Tritium Facilities*, Technical Report MLM-3719, Office of Scientific and Technical Information (OSTI.GOV), U.S. Department of Energy (1991), URL <http://dx.doi.org/10.2172/266889>.
- [Bor19] Born, Max and Wolf, Emil, *Principles of Optics: 60th Anniversary Edition*, Cambridge University Press, Cambridge, 7 edition (2019), URL <http://dx.doi.org/10.1017/9781108769914>.
- [Bra15] Bray, C., Pailloux, A. and Plumeri, S., *Tritiated Water Detection in the $2.17 \mu\text{m}$ Spectral Region by Cavity Ring Down Spectroscopy*, Nuclear Instruments and Methods in Physics Research Section A: Accelerators, Spectrometers, Detectors and Associated Equipment **789** (2015) 43–49, URL <http://dx.doi.org/10.1016/j.nima.2015.03.064>.
- [Bui94] Buiteveld, H., Hakvoort, J. H. M. and Donze, M., *Optical Properties of Pure Water*, in J. S. Jaffe (Ed.), *Ocean Optics XII, Bergen, Norway, 26 October 1994*, volume 2258, International Society for Optics and Photonics, SPIE, Honolulu, Hi, USA, 174–183, URL <http://dx.doi.org/10.1117/12.190060>.

BIBLIOGRAPHY

- [CAE] CAEN SpA, *Quad Scaler And Preset Counter-Timer, N1145*, CAEN SpA.
- [CAE91] CAEN SpA, *Model 84, 4 Channels Discriminator*, CAEN SpA (1991).
- [Cal12] Calmon, P. and Garnier-Laplace, J., *Tritium and the Environment*, <https://www.irsn.fr/EN/Research/publications-documentation/radionuclides-sheets/environment/Pages/Tritium-environment.aspx> (2012), Institut de Radioprotection et de Sureté Nucléaire (IRSN).
- [Cap20] Capuano, L., *International Energy Outlook 2013 with projections to 2050*, Center for Strategic and International Studies, U. E. Energy Information Administration, U.S. Department of Energy, Washington, DC 20585, Washington, DC 20585, United States (2020).
- [CERa] CERN Collaboration, *Coincidence Unit Type N6234*, CERN Collaboration.
- [CERb] CERN Collaboration, *ROOT: Analyzing Petabytes of Data, Scientifically*, <https://root.cern.ch/>.
- [Che13] Chen, Z., Peng, S., Meng, D., He, Y. and Wang, H., *Theoretical Study of Energy Deposition in Ionization Chambers for Tritium Measurements*, Review of Scientific Instruments **84** (2013) 650–659, URL <http://dx.doi.org/10.1063/1.4825032>.
- [Con] Consejo de Seguridad Nuclear (CSN), <https://www.csn.es/home>.
- [CRE20] CREMAT Inc., *CR 111-R2.1 Charge Sensitive Preamplifier*, CREMAT Inc., 07 (2020).
- [CSNa] CSN, *Red de Estaciones Automáticas (REA)*, <https://www.csn.es/mapa-de-valores-ambientales>.

- [CSNb] CSN, *Red de Estaciones de Muestreo (REM)*, <https://www.csn.es/kprgisweb2/index.html?lang=es>.
- [CSN13] CSN, *Regulación Nacional de Radionúclidos*, Technical report, (2013).
- [Dep16] Departament of Energy (DOE), *DOE Handbook Primer on Tritium Safe Handling Practices*, U. S. Departament of Energy Washington, D.C. 20585 (2016).
- [Dep17] Departement Federal de l'Interieur (DFI), *Ordonnance du DFI sur les Substances Etrangeres et les Composants dans les Denrees Alimentaires (817.021.23)*, The Federal Council (Swiss Government), Switzerland (2017).
- [DYC] DYCOMETAL, *Climatic Chamber Model CCK 85*, DYCOMETAL.
- [Env] Environmental Protection Division, BNL, *Why is the High Flux Beam Reactor Being Decommissioned?*, <https://www.bnl.gov/hfbr/decommission.php>.
- [EPA01] EPA, *Radionuclides Rule: A Quick Reference Guide*, Technical Report EPA 816-F-01-003, (2001).
- [EPA06] EPA, C., *Responses to Major Comments on Technical Support Document Public Health Goal For Tritium In Drinking Water*, Office of Environmental Health Hazard Assessment, OEHHA, California, USA (2006).
- [Epi20] Epic-Crystal, *Plastic Scintillator of Epic Crystal*, Epic-Crystal (2020).
- [Eur13] European Atomic Energy Community, *Laying Down Requirements for the Protection of the Health of the General Public with Regard to Radioactive Substances in Water Intended for Human Consumption*, Council directive 2013/15/euratom (2013).

BIBLIOGRAPHY

- [Eur14] European Atomic Energy Community (EUROATOM), *Council Directive 2013/59/Euratom of 5 December 2013*, <https://eur-lex.europa.eu/eli/dir/2013/59/oj> (2014).
- [Eur16] Europa Press, *China Construirá al Menos 60 Centrales Nucleares en la Próxima Década*, <https://www.europapress.es/internacional/noticia-china-construira-menos-60-centrales-nucleares-proxima.html> (2016).
- [Eva95] Evans, R. D., *The Atomic Nucleus*, McGraw-Hill, Inc., Bombay (1995), URL https://www.academia.edu/28858622/Evans_The_atomic_nucleus.
- [Fed06] Federal Office for Radiation Protection, BMU, *Environmental Radioactivity and Radiation Exposure. Annual Report*, Technical report, Bundesamt für Strahlenschutz (2006), urn:nbn:de:0221-20100331990.
- [Fer19] Fermilab, *Tritium at Fermilab*, <https://www.fnal.gov/pub/tritium/> (2019).
- [GEA] GEANT4 Collaboration, *Geant4: A Toolkit for the Simulation of the Passage of Particles Through Matter*, <https://geant4.web.cern.ch/node/1>.
- [GRB] GRBL, *GRBL Package of Arduino*, <https://github.com/grbl/grbl/wiki>.
- [Hag07] Hagmann, C., Lange, D. and Wright, D., *Cosmic-ray Shower Generator (CRY) for Monte Carlo Transport Codes*, in *2007 IEEE Nuclear Science Symposium Conference Record*, IEEE, Honolulu, Hi, USA, 1143–1146, URL <http://dx.doi.org/10.1109/NSSMIC.2007.4437209>.

- [Hai14] Haight, R., Wermer, J. and Fikani, M., *Tritium Production by Fast Neutrons on Oxygen: An Integral Experiment*, Journal of Nuclear Science and Technology **39** (2014) 1232–1235, URL <http://dx.doi.org/10.1080/00223131.2002.10875326>.
- [Ham10] Hamamatsu Photonics K.K., *Photomultiplier tube R2154-02 2*, Hamamatsu Photonics K.K., Japan (2010).
- [Ham15] Hamamatsu Photonics K.K., *High Voltage Power Supply C11152-01*, Hamamatsu Photonics K.K., Japan (2015).
- [Ham16a] Hamamatsu Photonics K.K., *MPPC Multi-Pixel Photon Counter S13360-1325*, Hamamatsu Photonics K.K., Japan (2016).
- [Ham16b] Hamamatsu Photonics K.K., *MPPC Multi-Pixel Photon Counter) S13360-1375*, Hamamatsu Photonics K.K., Japan (2016).
- [Ham16c] Hamamatsu Photonics K.K., *MPPC Multi-Pixel Photon Counter S13360-6050*, Hamamatsu Photonics K.K., Japan (2016).
- [Ham16d] Hamamatsu Photonics K.K., *MPPC Multi-Pixel Photon Counter S13360-6075*, Hamamatsu Photonics K.K., Japan (2016).
- [Ham16e] Hamamatsu Photonics K.K., *MPPC Multi-Pixel Photon Counter S13361-6050-04*, Hamamatsu Photonics K.K., Japan (2016).
- [Ham19] Hamamatsu Photonics K.K., *Photomultiplier Tube R8520-406/R8520-506*, Hamamatsu Photonics K.K., Japan (2019).
- [Han] Hanna Instruments, *Multiparamétrico con Opciones GPS, Sonda Autoregistradora, Turbidez e ISE*, Hanna Instruments.
- [Hof92a] Hofstetter, K. J. and Wilson, H. T., *Aqueous Effluent Tritium Monitor Development*, Fusion Technology **21** (1992) 446–451, URL <http://dx.doi.org/10.13182/FST92-A29786>.

BIBLIOGRAPHY

- [Hof92b] Hofstetter, K. J. and Wilson, H. T., *Continuous Tritium Effluent Water Monitor at the Savannah River Site*, Technical Report DE93002157, Office of Scientific and Technical Information (OSTI.GOV), U.S. Department of Energy (1992).
- [Hou18] Hou, X., *Tritium and ^{14}C in the Environment and Nuclear Facilities: Sources and Analytical Methods*, Journal of Nuclear Fuel Cycle and Waste Technology **16** (2018) 11–39, URL <http://dx.doi.org/10.7733/jnfcwt>.
- [Hyd16] Hydro Quebec, *Resultats du Programme de Surveillance de l'Environnement du Site de Gentilly-2*, National Library, Québec, Canada (2016).
- [IAE] IAEA, *Nuclear Data Services*, <https://www-nds.iaea.org>.
- [ICR91] ICRP, *1990 Recommendations of the International Commission on Radiological Protection*, Ann. ICRP **21** (1991), URL <https://www.icrp.org/publication.asp?id=icrp%20publication%2060>, publication 60.
- [ICR96] ICRP, *Age-Dependent Doses to Members of the Public From Intake of Radionuclides: Part 5. Compilation of Ingestion and Inhalation Dose Coefficients*, Ann. ICRP **21** **26** (1996), URL <https://www.icrp.org/publication.asp?id=ICRP%20Publication%2072>, publication 72.
- [IGU] IGUS S.L., *Carro transversal Drylin-SLW*, <https://www.igus.es/info/linear-guides-drylin-cross-slide>.
- [Ind] Industrial Fiber Optics, *POF Cutter Block*, <https://i-fiberoptics.com/tool-detail.php?id=105&cat=cutters>.
- [Inta] International Commission on Radiological Protection (ICRP), <https://www.icrp.org/>.

- [Intb] International Commission on Radiological Units and Measurements (ICRU), <https://www.icru.org/>.
- [Intc] International Society of Radiology (ISR), <https://www.isradiology.org/>.
- [Int07] International Council for Science (UCSU), World Data System, *NRB-99 Radiation Safety Norms*, World Data Centers, Russia and Ukraine (2007).
- [Int14] International Energy Agency, *Key World Energy Statistics*, <https://www.iea.org/publications/freepublications/publication/KeyWorld2014.pdf> (2014).
- [Int19] Integrated Circuits, *Driver TMC2208, Step/Dir Drivers for Two-Phase Bipolar Stepper Motors up to 2A peak- StealthChop for Quiet Movement- UART Interface Option*, Integrated Circuits (2019).
- [ISO] ISOTECH, *GPS-4303 Digital Bench Power Supply With UKAS Calibration, 4 Output*, ISOTECH.
- [JB10] Jean-Baptiste, P. et al., *³He Mass Spectrometry for Very Low-Level Measurement of Organic Tritium in Environmental Samples*, Journal of Environmental Radioactivity **101** (2010) 185–190, URL <http://dx.doi.org/10.1016/j.jenvrad.2009.10.005>.
- [Jor20] Jorge Diaz, *Tritium Decay Image*, <https://conexioncausal.wordpress.com> (2020), website: World Press.
- [Keia] Keithley Instruments, *Model 6487 Picoammeter/Voltage Source*, Keithley Instruments.
- [Keib] Keithley Instruments, *Model 6517B Electrometer User's Manual*, Keithley Instruments.

BIBLIOGRAPHY

- [Khe02] Kherani, N., *An Alternative Approach to Tritium-in-Water Monitoring*, Nuclear Instruments and Methods in Physics Research Section A: Accelerators, Spectrometers, Detectors and Associated Equipment **484** (2002) 650–659, URL [http://dx.doi.org/10.1016/S0168-9002\(01\)02008-3](http://dx.doi.org/10.1016/S0168-9002(01)02008-3).
- [Kno99] Knoll, G. F., *Radiation Detection and Measurement*, John Wiley and Sons, Inc., New York, 3 edition (1999).
- [Kno10] Knoll, G. F., *Radiation Detection and Measurement, 4th Edition*, volume 21, John Wiley & Sons, Inc. (2010), URL <https://www.wiley.com/en-sg/Radiation+Detection+and+Measurement,+4th+Edition-p-9780470131480>.
- [Law06] Law, S. et al., *Cleaving of Microstructured Polymer Optical Fibres*, Optics Communications **258** (206) 193–202, URL <http://dx.doi.org/10.1016/j.optcom.2005.08.011>.
- [LeC] LeCroy, *Model 465 Coincidence Unit*, LeCroy.
- [Lee18] Lee, J. et al., *Tissue Distribution, Excretion and Effects on Genotoxicity of Tritium Following Oral Administration to Rats*, Nuclear Engineering and Technology **51** (2018), URL <http://dx.doi.org/10.1016/j.net.2018.09.013>.
- [Leo94] Leo, W. R., *Techniques for Nuclear and Particle Physics Experiments: a How-to Approach*, Springer-Verlag Berlin Heidelberg GmbH, New York, 2 edition (1994), URL <http://dx.doi.org/10.13182/FST92-A29786>.
- [Lev11] Leverington, B. D., Anelli, M., Campana, P. and Rosellini, R., *A 1 mm Scintillating Fibre Tracker Readout by a Multi-anode Photomultiplier* (2011), URL <http://dx.doi.org/10.48550/arXiv.1106.5649>, arXiv:1106.5649v2.

- [Lin] Linear Technologies, Inc., *LT111A Voltage Comparator*, Linear Technologies, Inc.
- [Lin20] Lin, Z., *Simulation and Optimization Design of SiC-Based PN Betavoltaic Microbattery Using Tritium Source*, Crystals **10** (2020), URL <http://dx.doi.org/10.3390/cryst10020105>.
- [Mar72] Martin, J. R. and Koranda, J. J., *Biological Half-Life Studies of Tritium in Chronically Exposed Kangaroo Rats*, Radiation Research **50** (1972) 426–440, URL <http://dx.doi.org/10.2307/3573500>.
- [Mas21] Masuda, T. and Yoshioka, T., *Estimation of Radiation Dose from Ingested Tritium in Humans by Administration of Deuterium-Labelled Compounds and Food*, Scientific Reports **11** (2021) 1232–1235, URL <http://dx.doi.org/10.1038/s41598-021-82460-5>.
- [Mat07] Matsuyama, M., Torikai, Y., Hara, M. and Watanabe, K., *New Technique for Non-Destructive Measurements of Tritium in Future Fusion Reactors*, International Atomic Energy Agency (IAEA) **47** (2007) S464–S468, URL <http://dx.doi.org/10.1088/0029-5515/47/7/s09>.
- [Mat08] Matsuyama, M., *Development of a New Detection System for Monitoring High-Level Tritiated Water*, Fusion Engineering and Design **83** (2008) 1438–1441, URL <http://dx.doi.org/10.1016/j.fusengdes.2008.05.023>, proceedings of the Eight International Symposium of Fusion Nuclear Technology.
- [Max09] Maxim Integrated, *Low-Power, Quad, 12-Bit, Voltage-Output DACs with Serial Interface*, Maxim Integrated (2009).
- [Mer15] Mertens, S. et al., *Sensitivity of Next-Generation Tritium Beta-Decay Experiments for keV-Scale Sterile Neutrinos*, Journal of

BIBLIOGRAPHY

- Cosmology and Astroparticle Physics **2015** (2015) 020–020, URL <http://dx.doi.org/10.1088/1475-7516/2015/02/020>.
- [Mog69] Moghissi, A., Kelley, H., Phillips, C. and Regnier, J., *A Tritium Monitor Based on Scintillation*, Nuclear Instruments and Methods **68** (1969) 159, URL [http://dx.doi.org/10.1016/0029-554X\(69\)90705-8](http://dx.doi.org/10.1016/0029-554X(69)90705-8).
- [Mur67] Muramatsu, M., Koyano, A. and Tokunaga, N., *A Scintillation Probe for Continuous Monitoring of Tritiated Water*, Nuclear Instruments and Methods **54** (1967) 325–326, URL [http://dx.doi.org/10.1016/0029-554X\(67\)90645-3](http://dx.doi.org/10.1016/0029-554X(67)90645-3).
- [Nan06] Nanotec, *ST4209S1404-A - Stepper Motor NEMA 17*, Nanotec (2006).
- [NHM21] NHMRC, NRMMC, *Australian Drinking Water Guideilnes Paper 6. National Water Quality Managment Strategy*, National Health and Medical Research Council, National Resource Managment Ministerial Council, Commonwealth of Australia, Canberra (2021).
- [Nie15] Niemes, S., Sturm, M., Michling, R. and Bornschein, B., *High Level Tritiated Water Monitoring by Bremsstrahlung Counting Using a Silicon Drift Detector*, Fusion Science and Technology **67** (2015) 507–510, URL <http://dx.doi.org/10.13182/FST14-T66>.
- [Noe19] Noelia Lopez Redondo, *Estados Unidos Anuncia una Inversión de 35 Millones para las Centrales Nucleares*, Energy News, <https://www.energynews.es/estados-unidos-centrales-nucleares/> (2019).
- [Nuc93] Nuclear Energy Agency (NEA), *Radiation and Nuclear Safety Authority. Radioactivity of Household Water*, , Erweko Paintuote, Helsinki, Finland (1993).

- [Oli34] Oliphant, M. L., Harteck, P. and Rutherford, E., *Transmutation Effects observed with Heavy Hydrogen*, The Royal Society Publishing **133** (1934) 23–28, URL <http://dx.doi.org/10.1098/rspa.1934.0077>.
- [OME94] OME, *Ontario Drinking Water Objectives*, Ontario Ministry of Environment, Toronto, Ontario (1994).
- [ORTa] ORTEC, A., *Model 416A Gate and Delay Generator*, ORTEC, AMETEK, South Illinois Ave., Oak Ridge, USA.
- [ORTb] ORTEC, A., *Model 575A Amplifier*, ORTEC, AMETEK, South Illinois Ave., Oak Ridge, USA.
- [ORTc] ORTEC, A., *Model 671 Spectroscopy Amplifier*, ORTEC, AMETEK, South Illinois Ave., Oak Ridge, USA.
- [ORTd] ORTEC, A., *Model 9326 FastPreamplifier*, ORTEC, AMETEK, South Illinois Ave., Oak Ridge, USA.
- [ORTe] ORTEC, A., *Model CF8000 Octal Constant-Fraction Discriminator*, ORTEC, AMETEK, South Illinois Ave., Oak Ridge, USA.
- [Osb70] Osborne, R., *Detector for Tritium in Water*, Nuclear Instruments and Methods **77** (1970) 170–172, URL [http://dx.doi.org/10.1016/0029-554X\(70\)90596-3](http://dx.doi.org/10.1016/0029-554X(70)90596-3).
- [OSI] OSI Optoelectronics, *Characteristics and Applications*, https://osioptoelectronics.com/standard-products/default.aspx?gclid=EAIAIQobChMIkYrLif_37QIVDNTtCh3NuwpkEAYASAAEgKMJ_D_BwE.
- [OSO17] OSOYOO, *CNC Shield V3.0*, OSOYOO (2017).
- [Pal07] Palomo, M., Peñalver, A., Aguilar, C. and Borrull, F., *Tritium Activity Levels in Environmental Water Samples from Different*

BIBLIOGRAPHY

- Origins*, Applied Radiation and Isotopes **65** (2007) 1048–1056, URL <http://dx.doi.org/10.1016/j.apradiso.2007.03.013>.
- [PET] PETsys, *PETsys Electronics*, <https://www.petsyselectronics.com/web/private/login>.
- [PF81] Pietrzak-Flis, Z., Radwan, I., Major, Z. and Kowalska, M., *Tritium Incorporation in Rats Chronically Exposed to Tritiated Food or Tritiated Water for Three Successive Generations*, Journal of Radiation Research **22** (1981) 434–442, URL <http://dx.doi.org/10.1269/jrr.22.434>.
- [Phi] Phillips Scientific, *Model 740 Quad Linear Fan-In/Out*, Phillips Scientific.
- [Phy] Physikalisch-Technische Bundesanstalt (PTB), <https://www.ptb.de/cms/>.
- [Plo] Plot Nuclear Data (NADS), *Physics Simulation Packages, CRY (Cosmic-Ray Particle Showers)*, <https://nuclear.llnl.gov/simulation/>.
- [Ras] Raspberry Pi Foundation, <https://www.raspberrypi.org/>.
- [Rat00] Ratnakaran, M., Revetkar, R. M., Samant, R. K. and Abani, M. C. (Eds.), *A Real-time Tritium-In-Water Monitor for Measurement Of Heavy Water Leak To The Secondary Coolant, SPECIAL NUCLEAR REACTORS AND ASSOCIATED PLANTS (S21)*, volume 32, International Atomic Energy Agency (IAEA), Japan Health Physics Society, Japan (2000), URL https://inis.iaea.org/search/search.aspx?orig_q=RN:32015986.
- [Red19] Red Eléctrica de España, *Informe del Sistema Eléctrico Español*, <https://www.ree.es/es/datos/\protect\discretionary{\char\hyphenchar\font{}{}{}}publicaciones/informe-anual-sistema/>

- {\protect\discretionary{\char\hyphenchar}{}}informe-del-sistema-electrico-espanol-2019 (2019).
- [Roi10] Roithner LaserTechnik GmbH, *LED435-03, 20 mW, 20 mA*, Roithner LaserTechnik GmbH (2010).
- [Ré18] Réseau National de mesures de la radioactivité de l'environnement, IRSN, *Bilan de l'État Radiologique de l'Environnement Français de 2015 à 2017*, Réseau National de mesures de la radioactivité de l'environnement, Institut de Radioprotection et de Sûreté Nucléaire, France (2018).
- [Sag12] Sagawa, H. and Urabe, I., *Estimation of Absorbed Dose Rates in Air Based on Flux Densities of Cosmic Ray Muons and Electrons on the Ground Level in Japan*, Journal of Nuclear Science and Technology **38** (2012) 1103–1108, URL <http://dx.doi.org/10.1080/18811248.2001.9715142>.
- [Saia] Saint-Gobain Crystals, <https://www.crystals.saint-gobain.com/#>.
- [Saib] Saint-Gobain Crystals, *BC-630, Silicone Optical Grease*, <https://www.crystals.saint-gobain.com/>.
- [Sai21a] Saint-Gobain Crystals, *Optical fiber BCF-98*, Saint-Gobain Crystals, United States (2021).
- [Sai21b] Saint-Gobain Crystals, *Scintillating Optical Fibers, It's What's Inside that Counts*, Saint-Gobain Crystals, United States (2021).
- [Sai21c] Saint-Gobain Crystals, *Scintillating Plastic Grown with Polymeric Method*, Saint-Gobain Crystals, United States (2021).
- [San] San Nopco Limited, *Wetting Agents*, <https://www.sannopco.co.jp/eng/products/function/function4.php>.

BIBLIOGRAPHY

- [SAS] SAS, M. T. C., *Tennelec Model TC 952 High Voltage Supply*, Mirion Technologies (Camberra) SAS.
- [Saw00] Sawodni, A., Pazdur, A. and Pawlyta, J., *Measurements of Tritium Radioactivity in Surface Water on the Upper Silesia Region*, Journal of Nuclear Fuel Cycle and Waste Technology **18** (2000) 23–28, URL <http://yadda.icm.edu.pl/baztech/element/bwmeta1.element.baztech-article-BAT3-0035-0005>.
- [Sen17] SensL sense light, *Introduction to the SPM Technical Note*, SensL sense light (2017).
- [Sha97] Shah, K. S., Gothoskar, P., Farrell, R. and Gordon, J., *High Efficiency Detection of Tritium Using Silicon Avalanche Photodiodes*, IEEE Transactions on Nuclear Science **44** (1997) 774–776, URL <http://dx.doi.org/10.1109/23.603750>.
- [Sig94] Sigg, R., McCarty, J., Livingston, R. and Sanders, M., *Real-time Aqueous Tritium Monitor Using Liquid Scintillation Counting*, Nuclear Instruments and Methods in Physics Research Section A: Accelerators, Spectrometers, Detectors and Associated Equipment **353** (1994) 494–498, URL [http://dx.doi.org/10.1016/0168-9002\(94\)91707-8](http://dx.doi.org/10.1016/0168-9002(94)91707-8).
- [Sin85] Singh, A., Ratnakaran, M. and Vohra, K., *An On-Line Tritium-in-Water Monitor*, Nuclear Instruments and Methods in Physics Research Section A: Accelerators, Spectrometers, Detectors and Associated Equipment **236** (1985) 159–164, URL [http://dx.doi.org/10.1016/0168-9002\(85\)90141-X](http://dx.doi.org/10.1016/0168-9002(85)90141-X).
- [Sol17] Soler Cambra, A., *Contribución al Desarrollo de un Prototipo de Detector de Fibras Centelleadoras para la Medición de Tritio en Agua* (2017), Trabajo final de grado (TFG) de la Universidad de Valencia.

- [Spi97] Spinelli, A. and Lacaita, A., *Physics and Numerical Simulation of Single Photon Avalanche Diodes*, IEEE Transactions on Electron Devices **44** (1997) 1931–1943, URL <http://dx.doi.org/10.1109/16.641363>.
- [SR15] Sáez-Rodríguez, D., Nielsen, K., Bang, O. and Webb, D. J., *Simple Room Temperature Method for Polymer Optical Fibre Cleaving*, Journal of Lightwave Technology **33** (2015) 4712–4716, URL <http://dx.doi.org/10.1109/JLT.2015.2479365>.
- [Str93] Straume, T. and Carsten, A. L., *Tritium Radiobiology and Relative Biological Effectiveness*, Health Physics **65** (1993) 657–72, URL <http://dx.doi.org/10.1097/00004032-199312000-00005>.
- [Szu15] Szucs, T. et al., *Cosmic-Ray-Induced Background Intercomparison with Actively Shielded HPGe Detectors at Underground Locations*, The European Physical Journal A **51** (2015), URL <http://dx.doi.org/10.1140/epja/i2015-15033-0>.
- [Tek21] Tektronix, Inc., *Mixed Signal Oscilloscope, Model MSO44*, Tektronix, Inc. (2021).
- [Tel17] Teledyne LeCroy, *WaveRunner 6 Zi Oscilloscopes 400 MHz – 4 GHz*, Teledyne LeCroy (2017).
- [Tex14] Texas Instruments, *Driver DRV8825 Stepper Motor Controller IC*, Texas Instruments (2014).
- [Tex15] Texas Instruments, *OPA656 Wideband, Unity-Gain Stable, FET-Input Operational Amplifier*, Texas Instruments, 09 (2015).
- [Tex16] Texas Instruments, *SN74LVC1G11DBVR Single 3-Input Positive-AND Gate*, Texas Instruments, 11 (2016).
- [Tex17] Texas Instruments, *SN74AHC1G32 Single 2-Input Positive-OR Gate*, Texas Instruments (2017).

BIBLIOGRAPHY

- [Thea] The International Atomic Energy Agency (IAEA), <https://www.iaea.org/>.
- [Theb] The United Nations Scientific Committee on the Effects of Atomic Radiation (UNSCEAR), <https://www.unscear.org/>.
- [The96] Theodórsson, P., *Measurement of Weak Radioactivity*, World Scientific (1996), URL <http://dx.doi.org/10.1142/2800>.
- [Thoal] Thorlabs, Inc., <https://www.thorlabs.com/>.
- [Thob] Thorlabs Inc., *BK5 - Black Nylon, Polyurethane-Coated Fabric, 5' × 9' (1.5m × 2.7m) × 0.005" (0.12 mm) Thick*, Thorlabs Inc.
- [Tho06] Thorlabs Inc., *Guide to Connectorization and Polishing Optical Fibers*, Thorlabs Inc. (2006).
- [Tho18] Thorlabs, Inc., *LED430L - 430 nm LED with a Glass Lens, 8 mW, TO-18*, Thorlabs, Inc. (2018).
- [Tri] Tritium Collaboration, *Tritium, Interreg Sudoe Program*, <https://www.interreg-sudoe.eu/gbr/projects/the-approved-projects/158-design-construction-and-commissioning-of-a-low-level-tr>
- [Val07] Valverde Hermosilla, M., *Interacción Neutrino-núcleo a Energías Intermedias*, Ph.D. thesis, University of Granada, Granada, Spain (2007).
- [Wen] Wenzel Electronik GmbH, *Model N 1330-4 High Voltage Power Supply*, Wenzel Electronik GmbH.
- [WHO17] WHO, *Guidelines for Drinking-Water Quality*, volume 1, World Health Organization, Geneva, 3 edition (2017).
- [Wor20] World Nuclear Association, *Three mile island accident*, <https://www.world-nuclear.org/>

- information-library/safety-and-security/
safety-of-plants/three-mile-island-accident.aspx
(2020).
- [Zyl20] Zyla, P.A. et al., *Particle Data Group, Review of Particle Physics*, Prog. Theor. Exp. Phys. **083C01** (2020) 1–2093, URL <http://dx.doi.org/10.1093/ptep/ptaa104>.